СИБИРСКИЙ ЖУРНАЛ НАУКИ И ТЕХНОЛОГИЙ
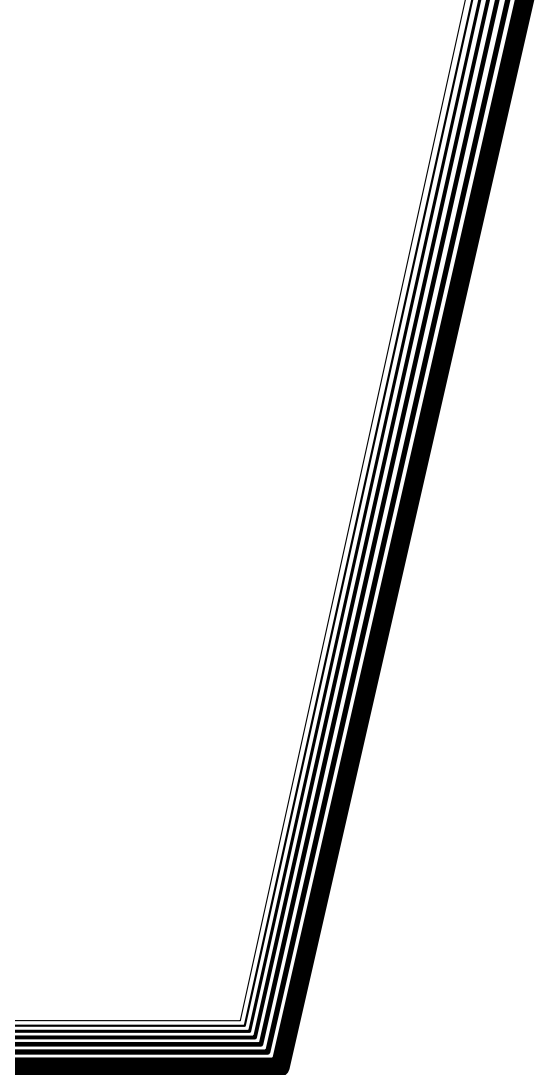
SIBERIAN JOURNAL OF SCIENCE AND TECHNOLOGY

Том 21, № 4
Vol.

СИБИРСКИЙ ЖУРНАЛ НАУКИ И ТЕХНОЛОГИЙ

Том 21, № 4

СИБИРСКИЙ ЖУРНАЛ НАУКИ И ТЕХНОЛОГИЙ

Том 21, № 4

СОДЕРЖАНИЕ

CONTENTS

PART 1. INFORMATICS, COMPUTER TECHNOLOGY AND MANAGEMENT

PART 2. AVIATION AND SPACECRAFT ENGINEERING

PART 3. TECHNOLOGICAL PROCESSES AND MATERIAL SCIENCE

ИНФОРМАТИКА,
ВЫЧИСЛИТЕЛЬНАЯ
ТЕХНИКА И УПРАВЛЕНИЕ

INFORMATICS,
COMPUTER TECHNOLOGY
AND MANAGEMENT

ALGORITHMIC AND SOFTWARE OF THE SYSTEM PROFILING THE ACTIONS OF USERS OF THE INFORMATION SYSTEM

E. V. Anashkin[*], M. N. Zhukova

Reshetnev Siberian State University of Science and Technology
31, Krasnoyarskii rabochii prospekt, Krasnoyarsk, 660037, Russian Federation
*E-mail: a.yegoriy@gmail.com

The paper describes the software of the system for profiling the actions of users of the information system. This profiling system is aimed at solving the problem of trust in users of information systems. The system should regulate access to protected resources by analyzing user behavior. The algorithmic component of the system is represented by a user behavior model and a general system operation algorithm. The user behavior model is based on the apparatus of Markov chains Software implementation allows in practice to obtain the foundations of the proposed approach to work. At the development stages, the choice of software architecture is carried out. The client-server architecture was chosen as a reasonable decision. The software component of the user activity profiling system consists of five separate software modules. At the end of development, a brief testing of the components is carried out. The novelty of this work lies in the proposal of an approach that uses the profiling of user actions as an additional determining factor in managing access to objects, as a way to strengthen the basic measures "Controlling access of subjects to access objects" in the order system of FSTEC of Russia.

Keywords: user behavior analysis, access control, UBA, information security software.

АЛГОРИТМИЧЕСКОЕ И ПРОГРАММНОЕ ОБЕСПЕЧЕНИЕ СИСТЕМЫ ПРОФИЛИРОВАНИЯ ДЕЙСТВИЙ ПОЛЬЗОВАТЕЛЕЙ ИНФОРМАЦИОННОЙ СИСТЕМЫ

Е. В. Анашкин[*], М. Н. Жукова

Сибирский государственный университет науки и технологий имени академика М. Ф. Решетнева
Российская Федерация, 660037, г. Красноярск, просп. им. газ. «Красноярский рабочий», 31
*E-mail: a.yegoriy@gmail.com

В работе приводится описание алгоритмического и программного обеспечения системы профилирования действий пользователей информационной системы. Данная система профилирования направлена на решение проблемы с доверием к пользователям информационных систем. Система должна регулировать доступ к защищаемым ресурсам путем анализа поведения пользователей. Алгоритмическая составляющая системы представлена моделью поведения пользователя и общим алгоритмом работы системы. Модель поведения пользователя строится на базе аппарата марковских цепей. Программная реализация позволяет на практике получить подтверждение работоспособности предлагаемого подхода. На этапах разработки осуществляется выбор архитектуры программного обеспечения. В качестве обоснованного решения выбрана архитектура типа «клиент – сервер». Программная составляющая системы профилирования действий пользователей состоит из пяти отдельных программных модулей. В конце разработки проводится краткое тестирование работы компонентов. Новизна данной работы заключается в предложении подхода, который использует профилирование действий пользователей как дополнительный определяющий фактор при управлении доступом к объектам, как способ усиления базовых мер «Управление доступом субъектов к объектам доступа» в системе приказов ФСТЭК России.

Ключевые слова: анализ поведения пользователей, контроль доступа, ПО СЗИ, UBA.

Introduction. The development of information security in information systems offers various options for solution to the issue of trust in system users.

In some information systems, the issue of trust in users is limited to the password authentication procedure. The system trusts a user if the user knows the password.

However, there are several cases where password authentication as a trust criterion is not enough. The first case is password theft or brute-force attack. The use of disgraced accounts is the second most popular method used by cybercriminals to conduct attacks aimed at stealing confidential data [1]. The second case is the presence of an internal attacker or insider on the information system. According to the study, 90 % of information leaks in Russia occur with an internal attacker (63.5 % in the world) [2].

Another option can be called a "communist" approach, which includes creating white and black lists: approved and prohibited programs, web resources, actions, etc. However, in the current conditions of development of information technologies, when new programs are being developed every day, new malicious resources are being created, and their tools are modified, it is problematic to create a full-fledged and comprehensive list. The same applies to business, the organizations themselves cannot always determine and fix the set of software, services and resources that they need to implement business processes today and tomorrow [3]. Even if a program is on the white list, it may have a vulnerability that could be exploited by a malefactor to circumvent restrictions of prohibitive policy. Thus, this approach is not sufficient to provide the environment for trust.

Another approach, called "ZeroTrust" [4], is based on distrust of the system components to each other, as well as the system does not trust the user. In this key, to confirm trust, it is proposed to use profiling of user actions in the system.

Profiling employee actions will make it possible to quickly identify all atypical actions that go beyond the usual behavior. This will help to identify the guilty party aiming at punishment or additional training. This will also allow detecting cases of the use of disgraced accounts, because, in order to circumvent behavioral analysis, a malefactor must accurately simulate all the actions of the employee who owned the disgraced account.

The scientific novelty of the work lies in the fact that among the scientific works that have appeared over the past 10 years, one can find a considerable number that affect user behavior for solving a different spectrum of tasks. To ensure enterprise protection, profiling of user actions occurs within the framework of access to the server [5]. In the paper [6], to protect cloud services, it is proposed to use fuzzy logic to calculate the level of trust in users based on their behavior. Another area of application for analysis of user behavior is security auditing and anomaly detection in databases [7]. In this paper a method of a one-class support vector machine is applied. Another work [8] is aimed at protecting information stored in databases. Its goal is to automate the adjustment of security policies and rules for accessing database tables. To do this, the operating rules are used, initially set by the security administrator to users, and user behavior is determined by access patterns. The following work analyzes, using Markov chains, the sequences of Unix-systems of variable length, which are entered by the user in the terminal server [9]. Also, user behavior is added to malware

detection [10]: wherefrom users download files, and wherefrom they lunch files, along with what file they lunch, that affects the calculation of the host's security level, as well as the accuracy of the detection system.

Nevertheless, despite the available variety of activities related to behavior profiling, there is a shortage of works that would fully cover user behavior in desktop operating systems for workstations. In this connection, this work proposes its own view of the system for profiling user actions in the OS of the Windows family.

The novelty of this work lies in the proposal of an approach that uses the profiling of user actions as an additional determining factor in managing access to objects, as a way to strengthen the basic measures "Controlling access of subjects to access objects" in the order system of FSTEC of Russia No. 17, 21, 31, 239 [11–14].

Description of the system profiling the actions of users. User actions profiling system (hereinafter referred to as UAPS) can have a different architecture and directivity, which depend on the protected object that is an information system (hereinafter referred to as IS). For example, for cloud ISs, UAPS is needed that supports a cloud architecture, and UAPS with an autonomous architecture is needed for an IS consisting of a single AWP.

In accordance with the official statistics for the regions of the Russian Federation for 2019, half of the employees at the enterprises are equipped with personal computers [15]. Therefore, the largest group is made up of ISs with a multiuser environment.

Tracking the actions of employees of the organization who are users of the IS, each of whom works at a separate personal computer, requires the installation of an UAPS on each of these computers. However, the computing power of these computers may either not meet the system requirements for installing a separate autonomous copy of the UAPS on them, or significantly affect the performance of the system and make it difficult to perform work duties and tasks.

To reduce system requirements and increase ergonomic parameters, the architecture of the "client-server" type was chosen as the architecture for the UAPS software. In this case, there is a separation of the functional capabilities of the UAPS into two components. The minimum required functionality is implemented in the client part. This reduces the system requirements for the personal computers of employees. Functions requiring high computing resources are moved to the server side. The server part allows performing centralized computing operations.

The UAPS architecture is shown in fig. 1

The client part consists of two mandatory components:

– agent programs;

– file system drivers.

The agent program has the following functional purpose:

– collection of system events from the Windows event service;

– interpretation of a system event into user action;

– recording user actions in the database;

– receiving control signals from the server;

– transmission of a control signal to the file system driver.

Mini-filter driver of the file system [16] is required to intercept operations with file resources and prohibit access to the resource in case of receiving a corresponding control signal from the agent program.

The server part includes the following components:

– database;

– web interface;

– the decision module.

The database stores the actions of all IS users that come from the installed agents.

The web interface serves for remote management and introduction to user profiles, their latest actions and other information.

The decision module calculates the correspondence of the current incoming user action with the profile. If the degree of compliance falls below the threshold value, the decision module sends a signal to the agent program to block access to the user.

Algorithmic support. Its own algorithmic support has been developed for the operation of the UAPS. The key element of the UAPS is the user behavior model, on the basis of which the UAPS makes decisions about the character of user actions. Markov chains are chosen as the mathematical apparatus used to construct a model of user behavior. The user behavior model consists of three Markov chains:

– "action-action" chain builds the probabilities of performing certain actions, after performing a certain action;

– "time-action" chain fixes the probabilities of performing actions at a certain time.

– "time-time" chain shows at what time the user is likely to take the next action.

To use the apparatus of Markov chains, a formula is needed that will correlate the probability of a state with the specificity of the user.

Several formulas have been proposed as options for a suitable formula:

$$H_t = H_{t-1} + \frac{e^{L_T} \cdot P_c}{e^{L_{\max}}} - \frac{L_A \cdot D}{L_T}, \tag{1}$$

$$H_t = H_{t-1} + P - \frac{L_A \cdot D}{L_{\max}}, \tag{2}$$

$$H_t = H_{t-1} + P - \frac{L_A \cdot D}{L_{\max} + L_T}, \tag{3}$$

$$H_t = H_{t-1} + \frac{L_T \cdot P}{L_{LA}} - \frac{L_A \cdot D}{L_{LT}}, \tag{4}$$

where H_t – current user specificity, H_{t-1} – specificity in the previous step, L_T – length of a chain of typical actions (number of typical actions in a row), L_A – the length of the current chain of atypical actions, $L_{\max}$ – maximum chain length (adjustable value: length of the sequence is enough to determine the specificity), P – probability of

such an action, L_A – length of the chain of atypical actions (the number of atypical actions in a row), D – reduction ratio (for example 0,1), L_{LA} – length of the last chain of atypical actions, L_{LT} – length of the last chain of typical actions.

The range of values of specificity H_t should lie in the segment [0; 1]: 1 – typical, 0 – not typical. The exponents in (1) are chosen to reduce the rate of increment of specificity to 1. Formulas (1), (2), (3) and (4) satisfy the following conditions:

– The longer the chain of typical user actions is, the higher and more stable the specificity should be. Resilience is a resistance to a sharp decrease in specificity in the event of an atypical action;

– the more likely the action, the higher the specificity;

– one atypical (but not dangerous) action should not invert the specificity.

After the development of the internal model of the UAPS, a general algorithm of the UAPS was designed. A diagram of the general algorithm of the UAPS operation is shown in fig. 2.

The work of the UAPS is carried out in two stages: the training stage and the working stage.

At the training stage, the system accumulates actions that the IS user performs. During this period, such components as the agent program on the client side and the database on the server side interact with each other.

After a time period of training, the UAPS administrator must initiate the creation of a profile for the user using the web service. When a profile is created, an interaction occurs between the web service and the database.

After creating the profile, the UAPS goes into the working stage. At this stage, all new incoming user actions are sent to the decision module. The decision module calculates the correspondence of the current user action with behavior profile. If the calculated compliance coefficient is less than the threshold value, then the decision module sends a control signal about the need to block access to controlled objects of the file system. Having received a control signal, the agent program sends a command to the file system driver to block access to controlled objects of the file system.

Agent component. The development of the Agent component was carried out in the C # programming language [17] in the Visual Studio Community 2019 development environment. The project name of the developed program is Julia Agent. The class diagram of the developed program is shown in fig. 3.

The agent program is installed on the system as a service that starts when a user logs on to the system. When installing the program, a script is also executed that configures the Windows audit policy and additionally installs the Sysmon service [18]. The agent program window at startup is shown in fig. 4.

The program window provides the following information:

– the server to which the agent has successfully connected;

– the name of the account whose activity is currently being tracked;

– the number of events received from the Windows event log.

When minimized, the program is hidden in the notification window.

Further, to assess the information technology aspect, we measured the impact of the Julia Agent program on the system resources. The measurements were carried out on a system with the configuration shown in tab. 1.

If there is no user activity, the program exerts the following average network load: 42 bytes per second sent, 26 bytes received per second.

When user activity appears, the network load increases.

In this case, the total network traffic averages 1250 bytes (1.226 KB) per second.

The average load on the CPU agent process is 0.08 %.

The amount of memory used when the program is running is 6,812 KB (6.65 MB).

When interacting with the hard disk, the program reads an average of 1089 bytes (1.65 Kb) per second.
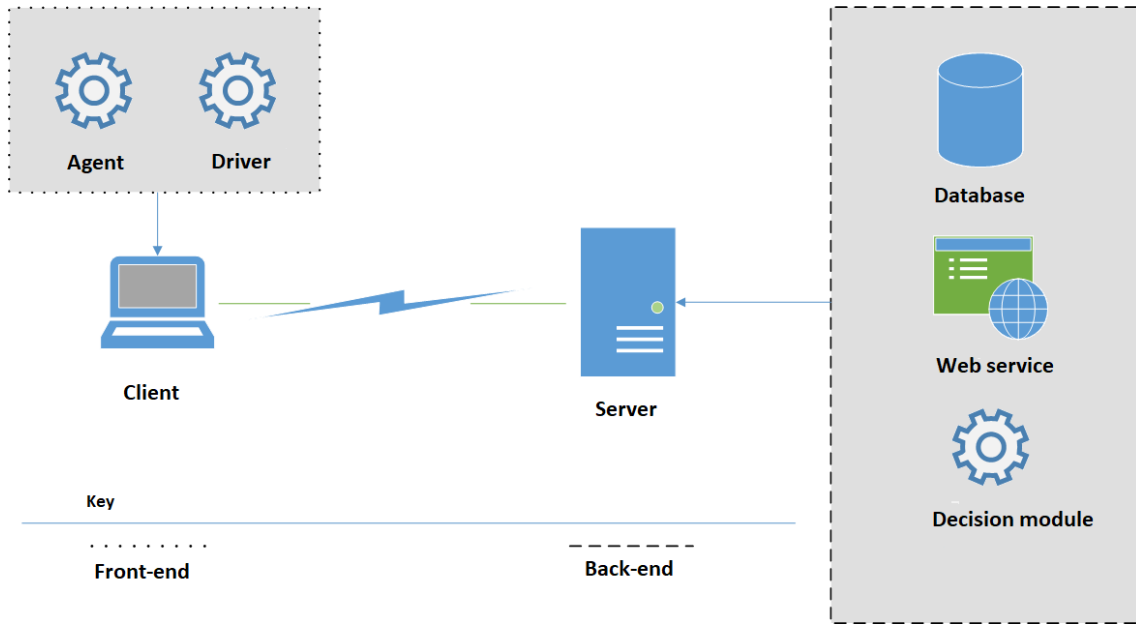
Fig. 1. Structural architecture of the user actions profiling system

Рис. 1. Структурная архитектура системы профилирования действий пользователя
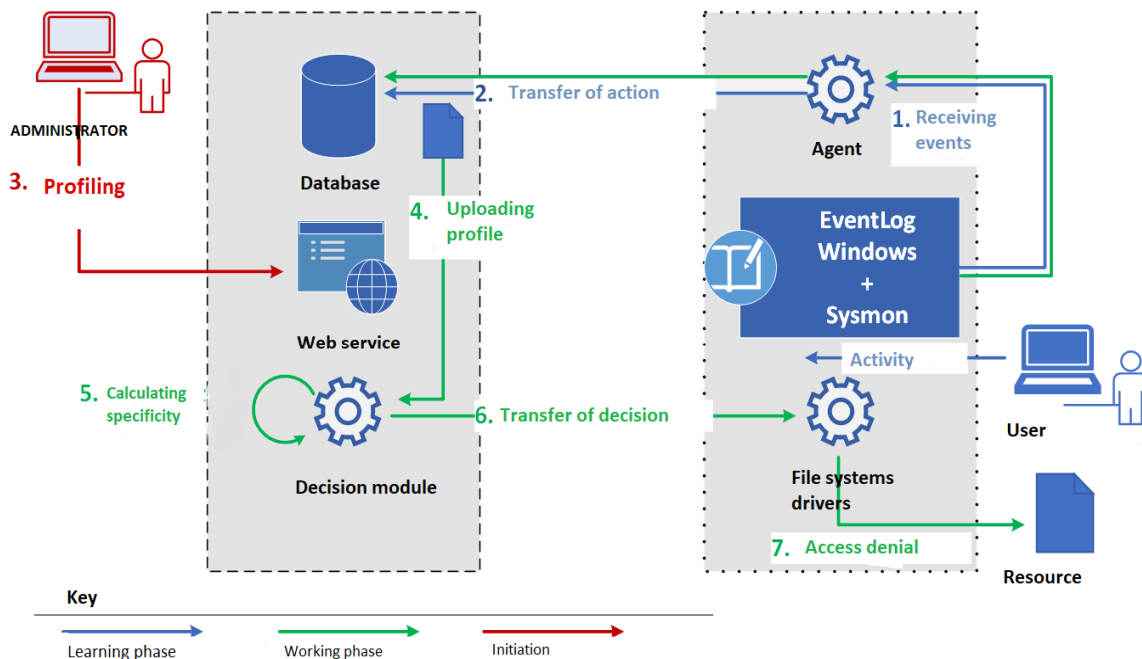
Fig. 2. General algorithm of the system for profiling user actions

Рис. 2. Общий алгоритм работы СПДП
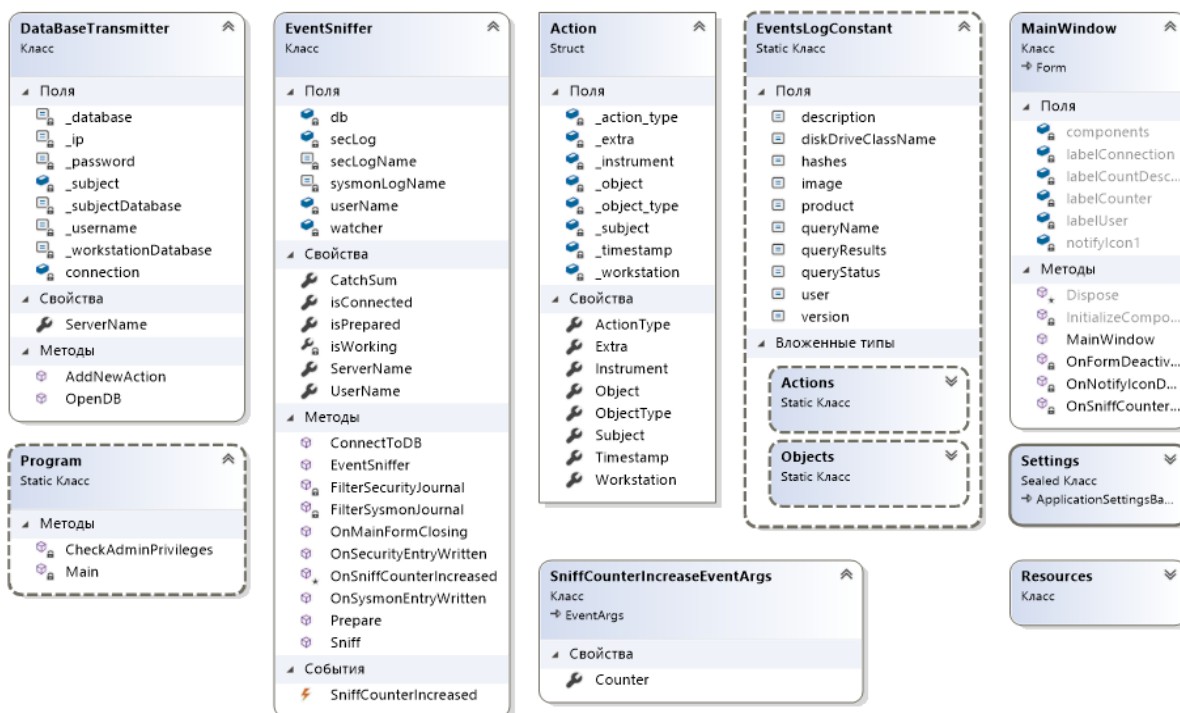
Fig. 3. Agent class diagram

Рис. 3. Диаграмма классов агента
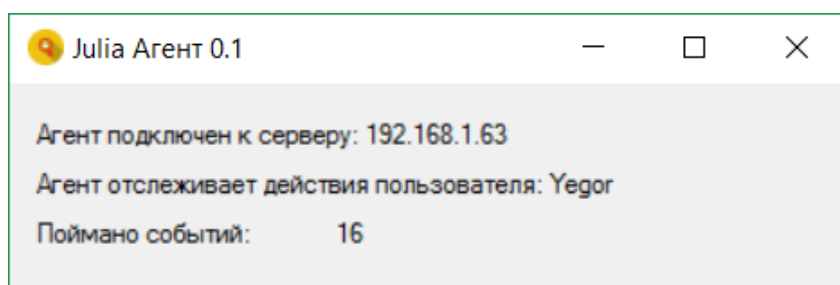
Fig. 4. The main window of the agent program

Рис. 4. Главное окно программы агента

The obtained average indicators of the use of PC resources are listed in tab. 2.

Thus, in all aspects, the program has a low consumption of system resources.

Web Service component. The development of the Web Service component was carried out in Python [19] in the PyCharm Community Edition development environment using the Django framework.

The web service designed for remote control of the UAPS by the security administrator provides the following set of capabilities:

– display of the latest actions of all users;
– displaying a list of all system users;
– formation and viewing of a user profile.

Fig. 5 shows the main page of the web service, which displays a list of recent user actions. The administrator can select the number of actions to display using the corresponding control located above the actions table.

When you select the "Users" item (Russian: Пользователи) in the administration panel menu, a page opens containing a list of users connected to the UAPS, which is shown in fig. 6. At the time of testing the Users component, two users have been registered in the system.

After selecting a specific user, the page of this user is opened. This page allows you to:

– see for how many days the statistics of actions were collected;
– generate a user profile if the profile does not exist yet;
– open user profile, if it exists;
– view recent user actions.

470
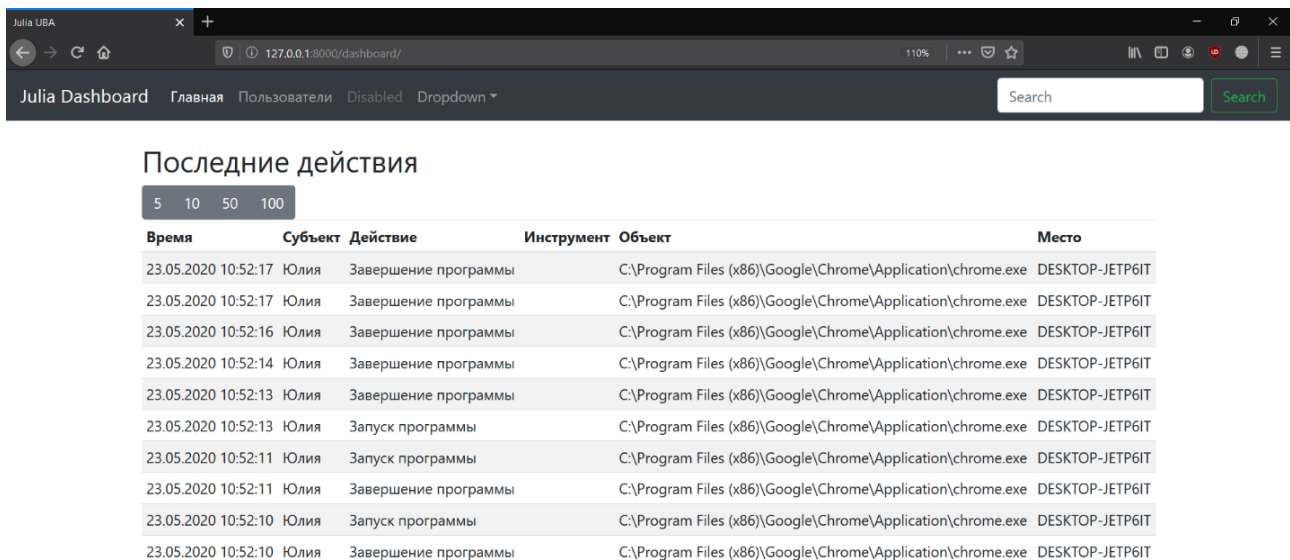
System characteristics for testing

System component	Characteristic
Central processing unit	AMD Ryzen 7 2700: 3.2 GHz 8 core
Random access memory (RAM)	16 Gbyte
Mass storage device	SSD Samsung 860 Evo 250 Gbyte HDD WD Blue 1 TByte
OS	Windows 10

Average indicators of resource use by the "Agent" component

Resource indicator	Average load value
Network load idle	42 byte/s – outcoming 26 byte/s – incoming
Network load when active	1250 byte/s
CPU utilization	0.08 %
Memory occupied by RAM	6.65 Mb
Hard disk load	1089 byte/s – reading

Fig. 5. Web service home page

Рис. 5. Главная страница веб-сервиса

Fig. 6. System users

Рис. 6. Пользователи системы

This page is shown in fig. 7.

After clicking the "To generate user profile" button (Russian: Сформировать профиль пользователя), the process of creating a user profile is started based on the currently available statistics. A profile consists of a visible and a hidden part. The displayed profile contains:

– a list of 10 most frequently used programs;

– a list of the 10 most frequently used network resources;

– a list of 10 most used files.

The top programs used by the user are shown in fig. 8.

The most used network resources are shown in fig. 9.

Top file resources used are shown in fig. 10.

The hidden part of the profile is a model of Markov chains written to a *JSON* file. The contents of the hidden part are shown in fig. 11.

Driver component. The development of the Driver component was carried out in the C programming language [20] in the Visual Studio Community 2019 development environment.

The driver reads from a special configuration file a list of file resources to which access must be controlled. Then the driver compares any access to the system files with the list of monitored resources. If the file is included in the set of controlled resources, then the driver further checks the value of the flag variable, which serves as an indicator of trust in the user. By default, the flag is not selected, which means trusting the user and granting access to resources. The "Agent" component can change the flag by sending the appropriate control signal to the driver.

To check the operation of the file system driver, a control signal has been simulated to deny access to the "New text document.txt" file (Russian: «Новый текстовый документ.txt»). The driver successfully blocked access to the text file, as shown in fig. 12.
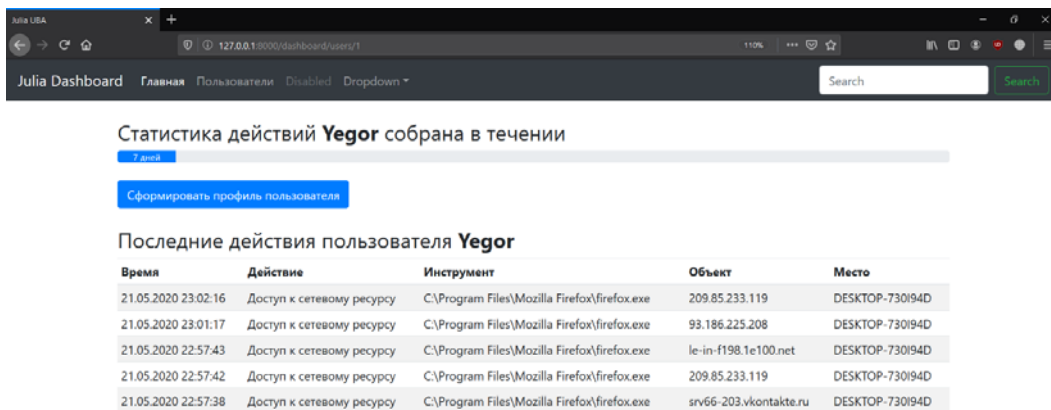
Fig. 7. User specific page

Рис. 7. Страница конкретного пользователя
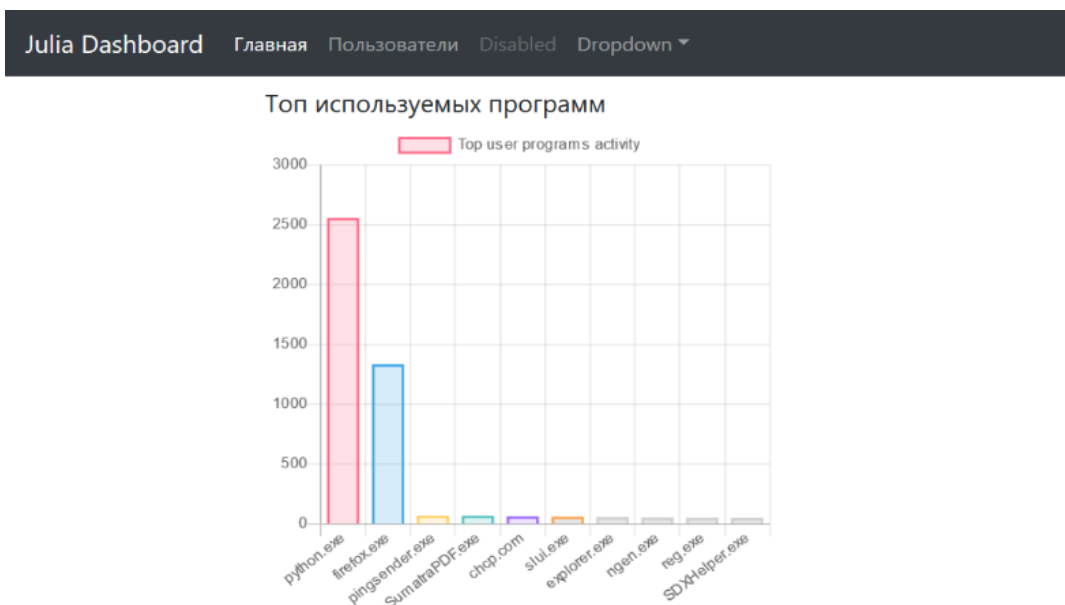
Fig. 8. Popular programs used

Рис. 8. Популярные используемые программы
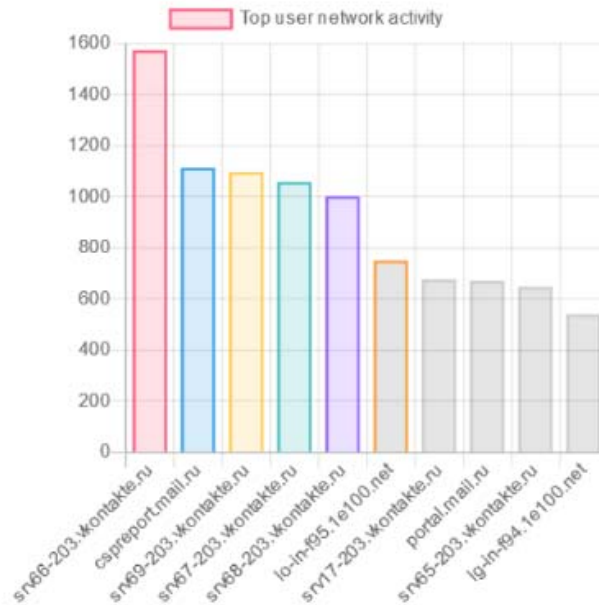
Fig. 9. Popular online resources

Рис. 9. Популярные сетевые ресурсы
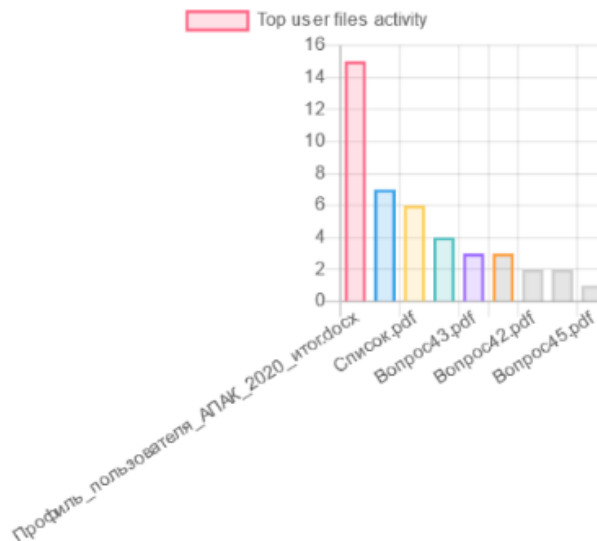
Fig. 10. Popular documents used

Рис. 10. Популярные используемые документы

Database component. A ready-made software product, PostgreSQL 12 DBMS [21] is used as the Database component.

To store data related to user activity, an uba database has been created, which has a structure in accordance with the diagram in fig. 13.

Database component implements the conceptual data model of user action, which has the following form: [TIME] [DATE] [SUBJECT] [ACTION] [OBJECT] from [LOCATION] using [TOOL].

Decision module component. The development of the Decision module component was carried out in Py-

thon in the PyCharm Community Edition development environment.

The decision module receives a notification from the database component if a new record (new user action) is added to the database. Then the decision module loads a new record from the database. From this entry, the decision module recognizes the user who performed the action. Then the decision module loads the profile of the given user.

The user profile is a calculated Markov chain. From the Markov chains, the decisive module learns the probability of such an action by a given user.

Thereafter the specificity of the user is calculated by the formula (1).

```
 1  ⊟(
 2      "action_to_action": {
 3          "Запуск программы C:\\Program Files (x86)\\ATI Technologies\\ATI.ACE\\Core-Static\\MMLoadDrv.exe": {
 4              "Запуск программы C:\\Program Files\\Mozilla Firefox\\firefox.exe": 0.25,
 5              "Создание файла C:\\Users\\Yegor\\Downloads\\лекции от\\-§ Средства коллективной и индивидуальной защиты работающих.doc": 0.16666666666666666,
 6              "Создание файла C:\\Users\\Yegor\\AppData\\Local\\Temp\\tmp56thnj\\gen_py\\__init__.py": 0.08333333333333333,
 7              "Создание файла C:\\Users\\Yegor\\AppData\\Local\\Temp\\tmpcybxfb\\gen_py\\__init__.py": 0.16666666666666666,
 8              "Создание файла C:\\Users\\Yegor\\AppData\\Local\\Temp\\tmpub8y56\\gen_py\\__init__.py": 0.08333333333333333,
 9              "Создание файла C:\\Users\\Yegor\\AppData\\Local\\Temp\\tmpry1vec\\gen_py\\__init__.py": 0.08333333333333333,
10              "Создание файла C:\\Users\\Yegor\\AppData\\Local\\Temp\\tmpzldv9x\\gen_py\\__init__.py": 0.08333333333333333,
11              "Создание файла C:\\Users\\Yegor\\AppData\\Local\\Temp\\tmpb_dnl1\\gen_py\\__init__.py": 0.08333333333333333
12          },
13          "Создание файла C:\\Users\\Yegor\\AppData\\Local\\Temp\\tmpexn7qa4cpycharm-management\\setuptools-40.8.0\\setuptools\\tests\\test_archive_util.py": {
14              "Создание файла C:\\Users\\Yegor\\AppData\\Local\\Temp\\tmpexn7qa4cpycharm-management\\setuptools-40.8.0\\setuptools\\tests\\test_dep_util.py": 1.0
15          },
16          "Доступ к сетевому ресурсу 104.244.42.193": {
17              "Доступ к сетевому ресурсу 152.199.19.161": 0.022727272727272728,
18              "Доступ к сетевому ресурсу ec2-44-227-11-155.us-west-2.compute.amazonaws.com": 0.13636363636363635,
19              "Доступ к сетевому ресурсу DESKTOP-5B1VQM7": 0.045454545454545456,
20              "Доступ к сетевому ресурсу portal.mail.ru": 0.022727272727272728,
21              "Доступ к сетевому ресурсу srv135-185-240-87.vk.com": 0.045454545454545456,
22              "Доступ к сетевому ресурсу srv51-203.vkontakte.ru": 0.045454545454545456,
23              "Запуск программы C:\\Program Files\\Mozilla Firefox\\firefox.exe": 0.3409090909090909,
24              "Доступ к сетевому ресурсу srv66-203.vkontakte.ru": 0.045454545454545456,
25              "Доступ к сетевому ресурсу cspreport.mail.ru": 0.06818181818181818,
26              "Доступ к сетевому ресурсу bar.love.mail.ru": 0.045454545454545456,
27              "Доступ к сетевому ресурсу 185.90.61.157": 0.045454545454545456,
28              "Доступ к сетевому ресурсу a88-221-216-200.deploy.static.akamaitechnologies.com": 0.022727272727272728,
29              "Доступ к сетевому ресурсу srv152-227.vkontakte.ru": 0.022727272727272728,
30              "Доступ к сетевому ресурсу lt-in-f19.1e100.net": 0.022727272727272728,
31              "Завершение программы C:\\Program Files (x86)\\Microsoft Visual Studio\\Installer\\resources\\app\\ServiceHub\\Services\\Microsoft.VisualStudio.Setup.Ser
32              "Доступ к сетевому ресурсу lq-in-f102.1e100.net": 0.022727272727272728,
33              "Доступ к сетевому ресурсу ec2-52-35-83-137.us-west-2.compute.amazonaws.com": 0.022727272727272728
34          },
```

Fig. 11. Snippet of hidden user profile

Рис. 11. Отрывок скрытого профиля пользователя
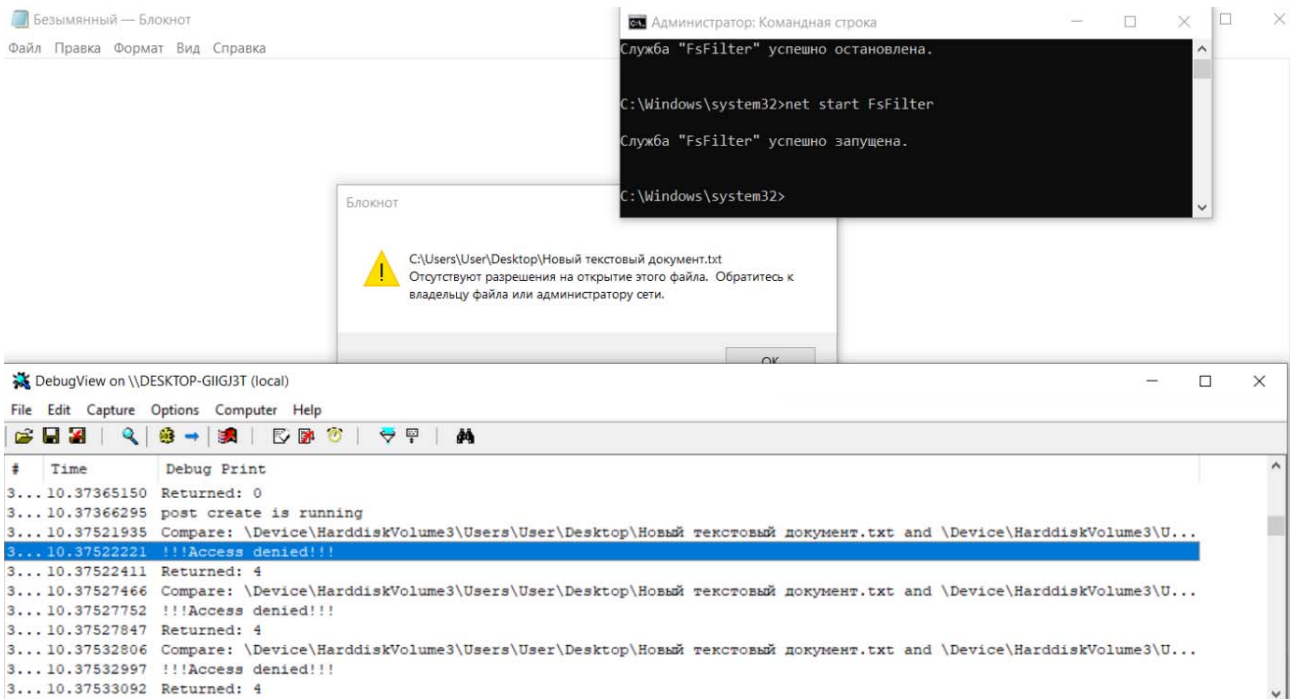
Fig. 12. The observed behavior of the file system driver confirms the correct operation of the component

Рис. 12. Наблюдаемое поведение драйвера файловой системы подтверждает корректность работы компонента
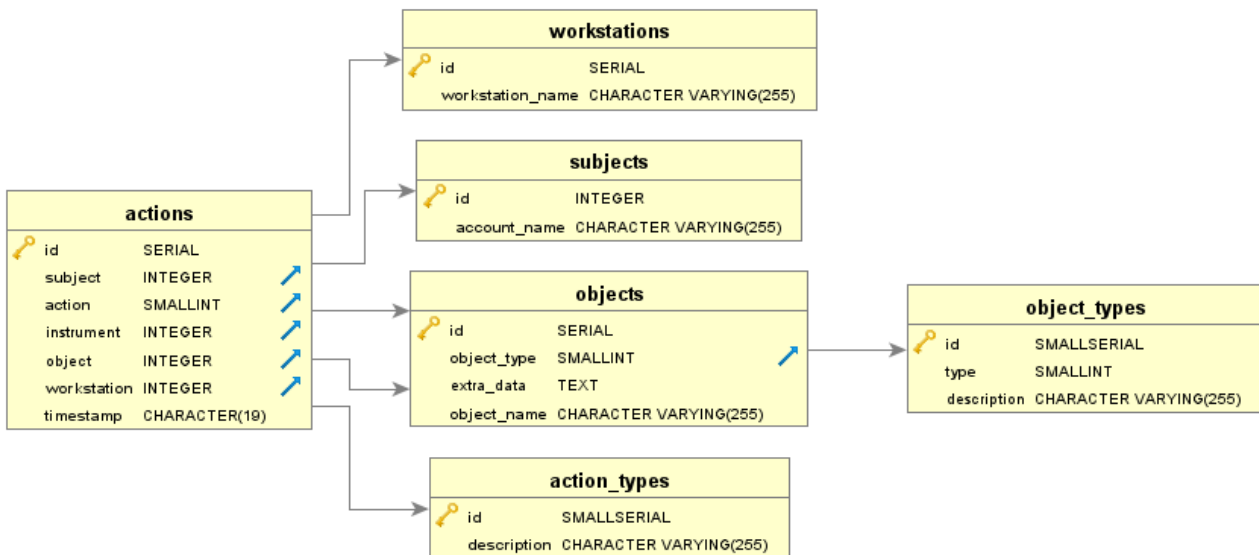
Fig. 13. Database component schema

Рис. 13. Схема компонента «База данных»

To apply formula (1), the decision module storages the following variables for each user:
– the last user action;
– the current specificity of the user;
– the length of the chain of typical actions;
– the length of the chain of atypical actions.
The parameters that are the same for all users are:
– the maximum chain length;
– the reduction factor.
These parameters in the decision module are specified as constant variables.

Conclusion. The client-server architecture was chosen as the software architecture for constructing a system for profiling user actions. The choice is based on the need to provide ergonomic parameters and statistics on the number of computerized workplaces in organizations. The system software is broken down into several main components:
– Agent;
– Driver;
– Database;
– Web Service;
– Decision module.

The software of each component has been successfully designed and developed. The development results have been verified. The software implementation of the components of the user profiling system has shown the viability of the proposed approach to access control based on user behavior analysis.

References

1. Data Breach Investigations Report. 2019, 78 p. Available at: https://enterprise.verizon.com/ resources/reports/2019-data-breach-investigations-report.pdf (accessed 14.09.2020).

2. *Utechki dannykh. Rossiya* [Analytical report GK Infowatch], Moscow, 2018 (In Russ). Available at: https://www.infowatch.ru/resources/analytics/reports/russia2018 (accessed 14.09.2020).

3. Lukatskiy A. V. *Novaya kontseptsiya kiberbezopasnosti Cisco Trusted Access* [New cybersecurity concept Cisco Trusted Access]. Samara, 2019, 55 p. (In Russ). Available at: https://www.slideshare.net/ lukatsky/zero-trust-196618076 (accessed 15.09.2020).

4. Kindervag J. No More Chewy Centers: The Zero Trust Model Of Information Security, Forrester, March 23, 2016. 18 p.

5. Shashanka M., Shen M., Wang J. User and Entity Behavior Analytics for Enterprise Security. *IEEE International Conference on Big Data (Big Data)*. 2016, P. 1867–1874. Doi: 10.1109/BigData.2016.7840805.

6. Alruwaythi M., Nygard K. E. Fuzzy logic Approach Based on User behavior Trust in Cloud Security. *2019 IEEE International Conference on Electro Information Technology (EIT)*. Brookings, SD, USA, 2019. Doi: 10.1109/EIT.2019.8834173.

7. Li Y., Zhang T. Anomaly Detection of User Behavior for Database Security Audit Based on OCSVM. *3rd International Conference on Information Science and Control Engineering*. Beijing, China, 2016, P. 214–219. Doi: 10.1109/ICISCE.2016.55.

8. Ghazinour K., Ghayoumi M. An Autonomous Model to Enforce Security Policies Based on User's Behavior. *Conf. 14th International Conference on Computer and Information Science (ICIS)*, Las-Vegas, USA, June 28 – July 1 2015, 6 p. Doi: 10.1109/ICIS.2015.7166576.

9. Xi X., Shu-tao X., Xin-guang T., Qi-bin Z. Anomaly detection of user behavior based on DTMC with states of variable-length sequences. *The Journal of China Universities of Posts and Telecommunication*. Vol. 18(6), P. 106–115. Doi: 10.1016/S1005-8885(10)60128-8.

10. Yang F., Wu J., Tang S., Zhang H. Dynamic Knowledge Repository-based Security Auxiliary System of User behavior. *Conf. IEEE International Conference on Green Computing and Communications and IEEE*

Internet of Things and IEEE Cyber, Physical and Social Computing, Beijing, China, 20–23 Aug. 2013. Doi: 10.1109/GreenCom-iThings-CPSCom.2013.390.

11. FSTEC of Russia. Acts. On approval of requirements for ensuring information security in automated production and technological process control systems at critical facilities, potentially dangerous facilities, as well as objects that pose an increased risk to human life and health and the environment : order of the FSTEC of Russia No. 31 : approved on March 14, 2014 : registered by the Ministry of justice of Russia on February 22, 2018, registration number 50118. Available at: https://fstec.ru/normotvorcheskaya/akty/53-prikazy/868-prikaz-fstek-rossii-ot-14-marta-2014-g-n-31 (accessed 15.09.2020).

12. FSTEC of Russia. Acts. On approval of requirements for ensuring the security of significant objects of critical information infrastructure of the Russian Federation: order of the FSTEC of Russia No. 239: approved on December 25, 2017: registered by the Ministry of justice of Russia on March 26, 2018, registration number 50524. Available at: https://fstec.ru/normotvorcheskaya/akty/53-prikazy/1592-prikaz-fstek-rossii-ot-25-dekabrya-2017-g-n-239 (accessed 15.09.2020).

13. FSTEC of Russia. Acts. On approval of requirements for the protection of information that does not constitute a state secret contained in state information systems: order of the FSTEC of Russia No. 17 : approved on February 11, 2013: registered by the Ministry of justice of Russia on may 31, 2013, registration number 28608. Available at: https://fstec.ru/normotvorcheskaya/akty/53-prikazy/702-prikaz-fstek-rossii-ot-11-fevralya-2013-g-n-17 (accessed 16.09.2020).

14. FSTEC of Russia. Acts. On approval of the composition and content of organizational and technical measures to ensure the security of personal data during their processing in personal data information systems: order FSTEC of Russia No. 21: approved on February 18, 2013: registered by the Ministry of justice of Russia on may 14, 2013, registration number 28375. Available at: https://fstec.ru/normotvorcheskaya/akty/53-prikazy/691-prikaz-fstek-rossii-ot-18-fevralya-2013-g-n-21 (accessed 16.09.2020).

15. Federal state statistics service. region of Russia. Socio-economic indicators-2019. Information and communication technologies. Number of personal computers per 100 employees: official website. Available at: https://gks.ru/bgd/regl/b19_14p/IssWWW.exe/Stg/d02/19-04.docx (accesed 16.09.2020).

16. Microsoft Docs. File System Minifilter Drivers: official documentation. Available at: https://docs.microsoft.com/en-us/windows-hardware/drivers/ifs/filter-manager-concepts (accessed 17.09.2020).

17. Shildt G. C# uchebnyy kurs [C# Training course]. St.Petersburg, Piter Publ., 2003, 20 p.

18. Microsoft Docs. Sysmon: official documentation. Available at: https://docs.microsoft.com/en-us/sysinternals/downloads/sysmon (accessed 17.09.2020).

19. Python: official site. Available at: https://docs.python.org/3/ (accessed 17.09.2020).

20. Kernigan, B.V. Yazyk Si [Language C]. Moscow, Williams Publ, 2017, 288 p.

21. PostgreSQL: The World's Most Advanced Open Source Relational Database. Available at: https://www.postgresql.org/ (accessed 18.09.2020).

Библиографические ссылки

1. Data Breach Investigations Report. 2019. 78 p. [Электронный ресурс]. URL: https://enterprise.verizon.com/resources/reports/2019-data-breach-investigations-report.pdf (дата обращения: 14.09.2020).

2. Утечки данных. Россия, 2018 // ГК Infowatch [Электронный текст]. URL: https://www.infowatch.ru/resources/analytics/reports/russia2018 (дата обращения 14.09.2020).

3. Лукацкий А. В. Новая концепция кибербезопасности Cisco Trusted Access: презентация. Самара, 2019. 55 слайдов [Электронный ресурс]. URL: https://www.slideshare.net/lukatsky/zero-trust-196618076 (дата обращения: 15.09.2020).

4. Kindervag J. No More Chewy Centers: The Zero Trust Model Of Information Security // Forrester. March 23, 2016. 18 p.

5. Shashanka M., Shen M., Wang J. User and Entity Behavior Analytics for Enterprise Security // 2016 IEEE International Conference on Big Data (Big Data). P. 1867–1874.

6. Alruwaythi M., Nygard K. E. Fuzzy logic Approach Based on User behavior Trust in Cloud Security // 2019 IEEE International Conference on Electro Information Technology (EIT).

7. Yong Li, Tao Zhang. Anomaly Detection of User Behavior for Database Security Audit Based on OCSVM // 3rd International Conference on Information Science and Control Engineering. P. 214–219.

8. Ghazinour K., Ghayoumi M. An Autonomous Model to Enforce Security Policies Based on User's Behavior // Conf. 14th International Conference on Computer and Information Science (ICIS), Las-Vegas, June 28 – July 1 2015. 6 p.

9. Xi X., Shu-tao X., Xin-guang T., Qi-bin Z. Anomaly detection of user behavior based on DTMC with states of variable-length sequences // The Journal of China Universities of Posts and Telecommunication. Vol. 18(6). P. 106–115.

10. Yang F., Wu J., Tang S., Zhang H. Dynamic Knowledge Repository-based Security Auxiliary System of User behavior // Conf. IEEE International Conference on Green Computing and Communications and IEEE Internet of Things and IEEE Cyber, Physical and Social Computing, 20–23 Aug. 2013.

11. ФСТЭК России. Акты. Об утверждении требований к обеспечению защиты информации в автоматизированных системах управления производственными и технологическими процессами на критически важных объектах, потенциально опасных объектах, а также объектах, представляющих повышенную опасность для жизни и здоровья людей и для окружающей природной среды : приказ ФСТЭК России № 31 : утвержден 14 марта 2014 года : зарегистрирован Минюстом России 22 февраля 2018 г., регистрационный № 50118 [Электронный ресурс].

URL: https://fstec.ru/normotvorcheskaya/akty/53-prikazy/ 868-prikaz-fstek-rossii-ot-14-marta-2014-g-n-31 (дата обращения 15.09.2020).

12. ФСТЭК России. Акты. Об утверждении требований по обеспечению безопасности значимых объектов критической информационной инфраструктуры российской федерации : приказ ФСТЭК России № 239 : утвержден 25 декабря 2017 года: зарегистрирован Минюстом России 26 марта 2018 г., регистрационный № 50524 [Электронный ресурс]. URL: https://fstec.ru/normotvorcheskaya/akty/53-prikazy/ 1592-prikaz-fstek-rossii-ot-25-dekabrya-2017-g-n-239 (дата обращения 15.09.2020).

13. ФСТЭК России. Акты. Об утверждении требований о защите информации, не составляющей государственную тайну, содержащейся в государственных информационных системах: приказ ФСТЭК России № 17 : утвержден 11 февраля 2013 года: зарегистрирован Минюстом России Минюсте России 31 мая 2013 г., регистрационный № 28608 [Электронный ресурс]. URL: https://fstec.ru/normotvorcheskaya/akty/53-prikazy/702-prikaz-fstek-rossii-ot-11-fevralya-2013-g-n-17 (дата обращения 16.09.2020).

14. ФСТЭК России. Акты. Об утверждении состава и содержания организационных и технических мер по обеспечению безопасности персональных данных при их обработке в информационных системах персональных данных: приказ ФСТЭК России № 21 : утвержден 18 февраля 2013 года: зарегистрирован Минюстом России Минюсте России 14 мая 2013 г., регистрационный № 28375 [Электронный ресурс]. URL: https://fstec.ru/normot-vorcheskaya/akty/53-prikazy/691-prikaz-fstek-rossii-ot-18-fevralya-2013-g-n-21 (дата обращения 16.09.2020).

15. Федеральная служба государственной статистики. Регионы России. Социально-экономические показатели – 2019. Информационные и коммуникационные технологии. Число персональных компьютеров на 100 работников: официальный сайт [Электронный ресурс]. URL: https://gks.ru/bgd/regl/ b19_14p/IssWWW.exe/Stg/d02/19-04.docx (дата обращения 16.09.2020).

16. Microsoft Docs. File System Minifilter Drivers: official documentation [Электронный ресурс]. URL: https://docs.microsoft.com/en-us/windows-hardware/ drivers/ifs/filter-manager-concepts (дата обращения 17.09.2020).

17. Шилдт Г. C# учебный курс. СПб. : Питер, 2003. 20 c.

18. Microsoft Docs. Sysmon: official documentation [Электронный ресурс]. URL: https://docs.microsoft.com/ en-us/sysinternals/downloads/sysmon (дата обращения 17.09.2020).

19. Python: official site [Электронный ресурс]. URL: https://docs.python.org/3/ (дата обращения 17.09.2020).

20. Керниган Б. В., Ричи Д. М. Язык Си. М. : Вильямс, 2017. 288 c.

21. PostgreSQL: The World's Most Advanced Open Source Relational Database [Электронный ресурс]. URL: https://www.postgresql.org/ (дата обращения 18.09.2020).

Anashkin Yegor Vadimovich – PhD student, assistant lecturer, department of Information technology security; Reshetnev Siberian State University of Science and Technology, Institute of Informatics and Telecommunications. E-mail: a.yegoriy@gmail.com.

Zhukova Marina Nikolaevna – Cand. Sc., associate professor of the department of Information technology security, Reshetnev Siberian State University of Science and Technology, Institute of Informatics and Telecommunications.

Анашкин Егор Вадимович – аспирант, ассистент кафедры безопасности информационных технологий; Сибирский государственный университет науки и технологий имени академика М. Ф. Решетнева, Институт информатики и телекоммуникаций. E-mail: a.yegoriy@gmail.com.

Жукова Марина Николаевна – кандидат технических наук, доцент кафедры безопасности информационных технологий; Сибирский государственный университет науки и технологий имени академика М. Ф. Решетнева, Институт информатики и телекоммуникаций.

STRUCTURE, NETWORK PROTOCOLS OF THE INTERNET OF THINGS FOR QUALITY PRODUCTION CONTROL

U. A. Vishnyakou*, B. H. Shaya, A. H. Al-Masri, S. H. Al-Hajj

Belarusian State University of Informatics and Radioelectronics
6, P. Brovky St., Minsk, 220600, Republic of Belarus
*E-mail: vish2002@list.ru

The subject of research is the model and structure of the Internet of things (IoT) network for product quality control in industry and agriculture. The purpose of the article is to analyze communication protocols and structures of IoT networks. The method of analysis and structural design of IoT networks is applied. The field of application is automation of monitoring products of enterprises of the aerospace industry. The article provides an overview and analysis of existing IoT technology; it considers the protocols and composition of IoT networks, and provides variations in the structures of building such networks. 4 levels of IoT architecture are described, as well as the communication protocols are used. The directions of building the Internet of things network for product quality control are defined. A multi-agent model of such system is presented, for the implementation of which the structure of the IoT network is given.

The structure of a multi-agent system (MAS) for monitoring product quality in industry and agriculture includes many agents, such as product quality agents, communication agents, database agents, agents for analyzing information received from sensor agents, and decision-making agents. This MAS implements functions to ensure the required class of product quality and it is based on building a local network of the Internet of things. The research proposes an algorithm for processing information in such an IoT network. Analyzers (sensors) product qualities will be periodically polled and their values will be recorded in the server database. The decision-making subsystem sends data on product quality compliance to the enterprise administrator on a mobile device. The server structure is implemented using cloud IoT platforms, for which a brief overview is provided. The one IoT network implementation is developed using LTE NB-IoT technology. This approach can be used in the aerospace industry for product quality control within automation 4.0.

Keyword: IoT network model and structure, monitoring the products quality of aerospace enterprises.

СТРУКТУРА, СЕТЕВЫЕ ПРОТОКОЛЫ СЕТИ ИНТЕРНЕТА ВЕЩЕЙ ДЛЯ КОНТРОЛЯ КАЧЕСТВА ПРОДУКЦИИ

В. А. Вишняков*, Б. Х. Шайя, А. Х. Аль-Масри, С. Х. Аль-Хаджи

Белорусский государственный университет информатики и радиоэлектроники
Республика Беларусь, 220600, г. Минск, ул. П. Бровки, 6
*E-mail: vish2002@list.ru

Предметом исследований является модель и структура сети Интернета вещей (ИВ) для контроля качества продукции в промышленности и сельском хозяйстве. Цель статьи – проанализировать протоколы коммуникации и структуры сетей ИВ. Применен метод анализа и структурного проектирования сетей ИВ. Областью применения является автоматизация мониторинга продукции предприятий аэрокосмической отрасли. В статье приведен обзор и анализ существующих технологий ИВ, рассмотрены протоколы и состав сетей ИВ, приведены вариации структур построения сети ИВ. Дано описание 4 уровней архитектур, а также использующихся протоколов связи. Определены направления построения сети ИВ для контроля качества продукции. Представлена многоагентная модель такой системы, для реализации которой приведена структура сети ИВ.

Структура мультиагентной системы (МАС) для мониторинга качества продукции в промышленности и сельском хозяйстве включает множество агентов, таких как агенты качества продукции, агенты связи, агенты базы данных, агенты анализа информации, полученной от агентов датчиков, агенты принятия решений. Данная МАС реализует функции по обеспечению требуемого класса качества продукции и основана на построении локальной сети ИВ. Предложен алгоритм обработка информации в такой сети IoT. Анализаторы (датчики) качества продукции будут периодически опрашиваться, их значения будут записываться в базу

данных сервера. Подсистема принятия решений будет выдавать данные о соответствии качества продукции администратору предприятия на мобильное устройство. Серверная структура реализуется с использованием облачных платформ интернета вещей, для которых приведен краткий обзор. Реализации сети IoT разрабатывается с использованием технологии LTE NB-IoT. Этот подход может быть использован в аэрокосмической отрасли для контроля качества продукции в рамках автоматизации 4.0.

Ключевые слова: модель и структура сети интернета вещей, мониторинг качества продукции предприятий аэрокосмической отрасли.

Introduction. Internet of Things (IoT) is a technology that automates input, processing, and optimization based on the obtained values of process characteristics reflected in indicators from industrial and home sensors. IoT technology allows a user to receive data and report on the status of equipment or processes in real time, track the work of industrial and agricultural enterprises [1]. There is a wide range of wireless connection standards available for IoT networks. Each of these standards and protocols has its own strengths and weaknesses [2; 3].

Communication in the IoT network consists of organizing an Internet connection with data storage facilities on a remote server and application software, for integrating wireless sensors and actuators with upper levels (servers, mobile devices). The received information is processed and analyzed using intelligent software in the cloud, that is on a remote multi-access server platform. The use of such cloud technology and services simplifies not only the software, but also the hardware implementation of IoT, deals with the issues of minimizing individual devices and increasing their energy efficiency [4–8].

Analysis of the use of IoT networks in the aerospace industry. Leaders in the aerospace and defense industries must work faster to meet the growing demands of modern reality. This follows from the increase in defense spending, the development of space technologies, and the geopolitical situation [9]. One of the breakthrough technologies in this direction is IoT. Augmented reality in integration with analytical data extracted from IoT data in real time allows developers to apply data analysis technologies where they are needed [9].

The use of IoT technologies in the aerospace industry is advisable in three main areas: using operational data in product development; providing high quality and timely data for maintenance and repair of equipment; optimizing the production process [10]. The approach discussed below can be applied in this industry.

Communication standards in IoT networks. At short distances, IoT networks use such communication standards as Bluetooth, ZigBee, and less popular protocols: Thread, WirelessHART, MiWi, SNAP, and others [2]. All of them use non-licensing bands of the radio frequency spectrum from the so-called ISM band (Industrial, Science, Medical), allocated for the needs of industry, medical equipment and scientific equipment. In practice, this frequency range, taking into account the restrictions adopted for it, is also used for organizing communication channels within cells and clusters of IoT cellular networks. For long distances, Wi-Max and LTE protocols are used (see table).

IoT network structures. IoT communication technologies that enable the exchange of information and management teams are diverse [4]. The 2.4 GHz region is used worldwide for Wi-Fi and other personal LAN protocols. The wireless communication standards used in this area (Bluetooth, ZigBee, Wi-Fi, and several others) have been popular in many areas for several years [3]. Implementation of such solutions is available because there are a large number of chips and complete modules that can be integrated and used in the development of an IoT device.

Most of the standards for short-range wireless communication systems relate to the organization of the so called «personal network» - the one that is built around a user. Such network is sometimes abbreviated as PAN (Personal Area Networks), although other names are common, for example, WLAN (Wireless Local Area Network). PAN is a data transmission network that connects personal electronic devices of one user (phones, pocket personal computers, smartphones, laptops, wireless headsets, and others.). Typically, such networks have a coverage radius of 10 to 30 meters (although in good conditions, all of them can provide a long range of communication).

Communication protocols used in IoT networks

Name of protocols	Transmission rate	Frequency band	Communication range
RFID	424 Kb/s	135 KHz	>50 sm
		13.56 MHz	>50 smм
		866–960 MHz	>3 m
		2.4 GHz	>1.5 m
NFC	106–6780 Kbod	13.56 MHz < 10 sm	13.56 MHz < 10 sm
ZigBee	20/256 Kb/s	900 МГц/ 2.4 ГГц	10 m
Bluetooth	1 Mb/s	2.4 GHz	10 m
BLE	10 Mb/s	2.4 GHz	>10 m
UWB	50 Mb/s	broadband	30 m
Wi-Fi (IEEE 802/11ac)	up to 6.77 Gb/s	2.4/5 GHz	100 m
Mobile networks 3G/4G (LTE)	up to 150 Mb/s	800/900/1800/2400 MHz	More ten Km

Devices for organizing a short-range personal network are sometimes optimized for certain applications using protocols called «application profiles» or using similar identifiers. These protocols are adapted to specific areas: health, sports, control and industrial automation, monitoring of buildings and structures, and others.

For simple point-to-point RF links, higher-level specifications have been developed: protocols for network, transport and even application layers. The final choice of wireless technologies will include software solutions related to the set end goal and the area of use of data from certain end sensors.

The disadvantage is that technologies with different communication protocols in the radio frequency environment are not reliable enough, since several devices use the same frequency spectrum band and interfere with each other.

The Internet of things belongs conceptually to the next generation of networks, so its structure is similar to the well-known four layer of NGN architecture, which includes smart sensors, transport environment, services and applications [1; 7; 8].

Large network sizes in IoT. A number of applications that use IoT networks require long distances from monitoring objects to processing services. Such networks with limited capacity and significant distances belong to the LPWAN class (Low-power Wide-area Network-energy-efficient long-range network) [11]. The areas of application of these networks are as follows: medicine (monitoring and diagnostics of patients at home or away), control of natural resources (water quality, indicators for oil and other minerals), industry and trade (monitoring and control in distributed organizations that occupy large territories), agriculture (condition and location of livestock, product quality, and control in crop production).

LoRaWAN network technology is used to transmit small amounts of information over long distances. The technology was developed for distributed control networks, machine-to-machine interaction (M2M). A network based on this technology is one of the most promising wireless implementations that support collecting information from sensors, devices, and sensors. In various regions, this network uses radio frequencies in the non-licensing range (30-300 MHz), (300 MHz – 3 GHz) and 800–930 MHz.

LoRa technology is more detailed at the physical levels that are the lowest in the network structure from both the LoRa consortium and the IoT technology. At the top levels of the network, the company defines specifications that depend on the implementation location. Information is transmitted via LoRa channels to the gateways to which sensors and devices are connected. IoT devices are connected to cloud or on servers via gateways.

LoRa defines testing and certification requirements for the compatibility of various LoRa devices on the network in order to implement a security policy. To maintain information security in the network in General and information in particular, LoRa technology uses special communication keys: at the network level, and at the level of software applications. This is due to the fact that radio signals are distributed over a large area of the network [11]. Although LoRa technology is relatively new for

developers, the latter are offered ready-made chips, individual modules, and a variety of test tools.

Two solutions are good suggestions for developers of IoT networks in the framework of fourth-generation LTE mobile communication technology: the relatively low-speed NB-IoT standard and the faster, but also expensive Cat-M1 standard. This gives flexibility to choose developers. NB-IoT technology is part of GSMA's Mobile IoT initiative and it is more suitable for our implementation.

Platform for Internet of things. IoT platforms are developed by large Internet companies to automate the creation of application projects for IoT networks. These platforms represent a service that manages network deployment, sensors, and transmitted data. IoT network platforms manage hardware and software components, support network security, implement authentication technology, and support user interaction. There are several hundred service providers on the IoT platform market with various offers, ranging from software and hardware to SDKs and APIs [12–14]. The typical composition of many IB platforms includes:

– IoT network gateway for converting the format of transmitted information;

– authentication and sensor management tools, user interfaces;

– cloud service models (infrastructure, platform, etc.)

– use of additional applications.

Models and structure of IoT network for production quality control. We use a multi-agent approach to create a model of IoT network for monitoring production quality for various companies [15]. In this multi-agent structure, we will distinguish a set of agents for production quality sensors, agents for converters, agents for storing quality production indicators, agents for processing production quality indicators to obtain conclusions, agents for monitoring these indicators and conclusions. This multi-agent model is represented by the set:

$$IoT_{ccm} = \{A_{pq}, A_c, A_{mq}, A_{pmq}, A_{dmq}, A_{imq}, M_{Ai}\},$$

where IoT_{ccm} – a IoT network model, A_{pq} – a set of sensor agents (from portable analyzers of production quality), A_c – the set of agents converters (gateways), A_{mq} – agents storage of quality indicators, A_{pmq} – agents of their processing, A_{dmq} –agents to make decisions about the quality of production, A_{imq} – agents interface to display indicators, M_{Ai} – monitoring agents (mobile devices to monitor production quality indices).

Based on this model, the structure of the production quality monitoring system network is developed [16]. It is composed of portable analyzers for production quality of the monitored industry (agricultural) companies. These analyzers usually output the results to a computer or printer via a serial port (avtomatization 3.0). In our structure, these indicators are fed to the gateways-converters. The latter are necessary for converting and transmitting the captured production quality indicators to the cloud environment (CC). Its structure realizes elements of avtomatization 4.0.

In the cloud environment, we use the server that contains databases and knowledge, tools of security, solver, and a notification service. The database stores data received from company, taken quality characteristics

by time (number, time of day, checked parameters and others), from different enterprisers. This data is sent to the database. The knowledge base contains rules for evaluating the quality of production. Data and knowledge bases are sent to the solver, which, based on the accepted indicators of the rules for processing quality indicators from the knowledge base, issues solutions for certain quality parameters. These decisions are also recorded in the database. The site serves as a means of displaying captured and obtained results on the quality of production for user.

On each of the mobile devices, specialists installed an application that allows them to display information of interest from the cloud database through the site. On a cloud server a user can install a software system for making decisions about changing the quality production content to improve its characteristics according to the rules from the knowledge base.

Conclusion.

1. The concepts, models, and IoT part show the variation of the architectures of network construction IoT. The research describes 4 levels of IoT architectures, as well as the communication protocols used for IoT networks. It also briefly analyses the use of IoT networks in the aerospace industry.

2. The model of multi-agent system for quality control of production is developed. The structure of the IoT network is proposed, which includes production quality analyzers, gateways and a cloud structure where the server platform is rented. The server database stores the quality indicators of control production. These indicators can be monitored from specialists' mobile devices.

3. The proposed system is realized on IoT platform. The most popular IoT cloud platforms are considered. As a communication network for transmitting information from company sensors to the cloud platform, the 4th generation LTE network with its variant for the IB-NB – IoT network is chosen. This approach can be used in aerospace industry enterprises.

References

1. Roslyakov A. V., Vanyashin S. V., Grebeshkov A. Yu. *Internet veshchey* [Internet of things]. Samara, PGUTiI Publ., 2015, 115 p.

2. Rentyuk V. [Brief guide to wireless technologies of the Internet of things. Part 1. Networks, gateways, clouds and protocols]. *Control Engineering Russia*. 2017, No. 6, P. 61–65 (In Russ.).

3. Rentyuk V. [Brief guide to wireless technologies of the Internet of things. Part 2. Short range]. *Control Engineering Russia.* 2018, No. 1, P. 51–57 (In Russ.).

4. Internet of things definition. Available at: https://www.hpe.com/us/en/what-is/internet-of-things.html (accessed 4.04.2020).

5. "IoT Signals" Summary of research learnings 2019. Available at: https://azure.microsoft.com/mediahandler/files/resourcefiles/iot-signals/IoT-Signals-Microsoft-072019.pdf (accessed 4.04.2020).

6. The Internet of Things (IoT) explained. Available at: https://www.dbbest.com/blog/the-internet-of-things/ (accessed 4.04.2020).

7. The Internet of Things: Today and Tomorrow. Available at: http://chiefit.me/wp-content/uploads/2017/03/HPE-Aruba_IoT_Research_Report.pdf (accessed 5.09.2020).

8. The Internet of Things, IoT, M2M would market Available at: http://www.tadviser.ru/a/302413 (accessed 5.09.2020).

9. The aerospace and defense industries are introducing Internet of things and augmented reality technologies. Available at: https://www.ptc.com/ru/industries/aerospace- and-defense/IoT-and-Augmented-Realit (accessed 11.10.2020).

10. Using the Internet of things and augmented reality in the aerospace industry. Available at: http://www.remmag.ru/upload_data/files/2018-0304/MONT-PTC1.pdf (accessed 11.10.2020).

11. Rentyuk V. [Brief guide to wireless technologies of the Internet of things. Part 4. Long range]. *Control Engineering Russia*. 2018, No. 3 (75), P. 82–87 (In Russ.).

12. Review of the best IoT platforms in 2019. Tips for choosing a cloud solution. Available at: https://www.edsson.com/ru/blog/article?id=iot-platforms (accessed 4.09.2020).

13. Twenty-one examples of IoT platforms. Available at: https://nag.ru/articles/article/32221/dvadtsat-odin-primer-iot-platform.html (accessed 14.09.2020).

14. How cloud-based Big Data IoT platforms work with the Internet of things. Available at: https://www.bigdataschool.ru/blog/iot-platform-big-data-cloud.html (accessed 14.09.2020).

15. Leyton-Brown K., Shoham Y. Multiagent Systems: Algorithmic, Game-Theoretic and Logical Foundations. London, Cambridge University Press, 2009, 513 p.

16. Visniakou U. A., Al-Masri A. H., Al-Hajj S. K. Organization of management and structure in local networks internet of things. *System analysis and application informatics*. 2020, No. 2, P. 11–16.

Библиографические ссылки

1. Росляков А. В., Ваняшин С. В., Гребешков А. Ю. Интернет вещей. Самара, ПГУТиИ, 2015. 115 с.

2. Рентюк В. Краткий путеводитель по беспроводным технологиям «Интернета вещей». Часть 1. Сети, шлюзы, облака и протоколы // Control Engineering Россия. 2017. № 6. С. 61–65.

3. Рентюк В. Краткий путеводитель по беспроводным технологиям «Интернета вещей». Ч. 2. Ближний радиус действия // Control Engineering Россия. 2018. № 1. С. 51–57.

4. Internet of things definition [Электронный ресурс]. URL: https://www.hpe.com/us/en/what-is/ internet-of-things.html (дата обращения: 4.04.2020).

5. "IoT Signals" Summary of research learnings 2019 [Электронный ресурс]. URL: https://azure.microsoft.com/mediahandler/files/resourcefiles/iot-signals/IoT-Signals-Microsoft-072019.pdf (дата обращения: 4.04.2020).

6. The Internet of Things (IoT) explained [Электронный ресурс]. URL: https://www.dbbest.com/blog/the-internet-of-things/ (дата обращения: 4.04.2020).

7. The Internet of Things: Today and Tomorrow [Электронный ресурс]. URL: http://chiefit.me/wp-content/

uploads/2017/03/HPE-Aruba_IoT_Research_Report.pdf (дата обращения: 5.09.2020).

8. The Internet of Things, IoT, M2M would market [Электронный ресурс]. URL: http://www.tadviser.ru/a/302413 (дата обращения: 5.09.2020).

9. Аэрокосмическая и оборонная отрасли внедряют Интернет вещей и технологии дополненной реальности. [Электронный ресурс]. URL: https://www.ptc.com/ru/industries/aerospace-and-defense/IoT-and-Augmented-Realit (дата обращения: 11.10.2020).

10. Использование Интернет вещей и дополнительной реальности в аэрокосмической отрасли [Электронный ресурс]. URL: http://www.remmag.ru/upload_data/files/2018-0304/MONT-PTC1.pdf (дата обращения: 11.10.2020).

11. Рентюк В. Краткий путеводитель по беспроводным технологиям «Интернета вещей». Часть 4. Дальний радиус действия // Control Engineering Россия. 2018. № 3(75). С. 82–87.

12. Обзор лучших IoT платформ в 2019 году. Советы по выбору облачного решения [Электронный ресурс]. URL: https://www.edsson.com/ru/blog/ article?id= iot-platforms (дата обращения: 4.09.2020).

13. Twenty-one examples of IoT platforms [Электронный ресурс]. URL: https://nag.ru/articles/article/32221/dvadtsat-odin-primer-iot-platform.html (дата обращения: 14.09.2020).

14. How cloud-based Big Data IoT platforms work with the Internet of things [Электронный ресурс]. URL: https://www.bigdataschool.ru/blog/iot-platform-big-data-cloud.html (дата обращения: 14.09.2020).

15. Leyton-Brown, K., Shoham Y. Multiagent Systems: Algorithmic, Game-Theoretic and Logical Foundations. London: Cambridge University Press. 2009. 513 p.

16. Visniakou U. A., Al-Masri A. H., Al-Hajj S. K. Organization of management and structure in local networks internet of things // System analysis and application informatics. 2020. No. 2. P. 11–16.

Vishniakou Vladzimir Anatolyevich – Dr. Sc., professor; Belarusian State University of Informatics and Radioelectronics. E-mail: vish2002@list.ru.

Shaya B. H. – master of technical science, PhD-student; Belarusian State University of Informatics and Radioelectronics.

Al-Masri A. H. – master of technical science, PhD-student; Belarusian State University of Informatics and Radioelectronics.

Al-Hajj S. H. – master of technical science, PhD-student; Belarusian State University of Informatics and Radioelectronics.

Вишняков Владимир Анатольевич – доктор технических наук, профессор; Белорусский государственный университет информатики и радиоэлектроники. E-mail: vish2002@list.ru.

Шайя Б. Х. – магистр технических наук, аспирант; Белорусский государственный университет информатики и радиоэлектроники.

Аль-Масри А. Х. – магистр технических наук, аспирант; Белорусский государственный университет информатики и радиоэлектроники.

Аль-Хаджи С. Х. – магистр технических наук, аспирант; Белорусский государственный университет информатики и радиоэлектроники.

METHOD OF EQUIVALENT STRENGTH CONDITIONS IN CALCULATIONS OF BODIES WITH INHOMOGENEOS REGULAR STRUCTURE

A. D. Matveev

Institute of Computational Modeling
50/44, Akademgorodok, Krasnoyarsk, 660036, Russian Federation
E-mail: mtv241@mail.ru

Plates, beams and shells with a non-uniform and micro-uniform regular structure are widely used in aviation and rocket and space technology. In calculating the strength of elastic composite structures using the finite element method (FEM) it is important to know the error of the approximate solution for finding where you need to build a sequence of approximate solutions that is connected with the procedure of crushing discrete models. Implementation of the procedure for grinding (within the micro-pass) discrete models of composite structures (bodies) requires large computer resources, especially for discrete models with a microinhomogeneous structure. In this paper, we propose a method of equivalent strength conditions (MESC) for calculating elastic bodies static strength with inhomogeneous and microinhomogeneous regular structures, which is implemented via FEM using multigrid finite elements. The calculation of composite bodies' strength according to MESC is limited to the calculation of elastic isotropic homogeneous bodies strength using equivalent strength conditions, which are determined based on the strength conditions set for composite bodies. The MESC is based on the following statement. For all composite bodies V_0, which are such a homogeneous isotropic body V^b and the number of p, if the safety factor n_b of the body V^b satisfies the equivalent conditions of strength $pn_1(1+\delta_\alpha) \le n_b(1-\delta_\alpha^2) \le pn_2(1-\delta_\alpha)$, the safety factor n_0 of the body V_0 meets the defined criteria for strength $n_1 \le n_0 \le n_2$, where n_1, n_2 specified, the safety factor n_0 (n_b) complies with the accurate (approximate) solution of elasticity theory problem is built for body V_0 (body V^b); $\delta_\alpha < (n_2 - n_1)/(n_2 + n_1)$; δ_α is the upper δ_b error estimation of the maximum equivalent body stress V^b, corresponding to approximate solution. When constructing equivalent strength conditions, i. e when finding the equivalence p coefficient, a system of discrete models is used, dimensions of which are smaller than the dimensions of the basic composite bodies models. The implementation of MESC requires small computer resources and does not use procedures for grinding composite discrete models. Strength calculations for bodies with a microinhomogeneous structure using MESC show its high efficiency. The main procedures for implementing the MESC are briefly described.

Keywords: elasticity, composites, equivalent strength conditions, multigrid finite elements, plates, beams, shells.

МЕТОД ЭКВИВАЛЕНТНЫХ УСЛОВИЙ ПРОЧНОСТИ В РАСЧЕТАХ ТЕЛ С НЕОДНОРОДНОЙ РЕГУЛЯРНОЙ СТРУКТУРОЙ

А. Д. Матвеев

Институт вычислительного моделирования СО РАН
Российская Федерация, 630036, г. Красноярск, Академгородок, стр. 50/44
E-mail: mtv241@mail.ru

Пластины, балки и оболочки с неоднородной, микронеоднородной регулярной структурой широко применяются в авиационной и ракетно-космической технике. В расчетах на прочность упругих композитных конструкций с помощью метода конечных элементов (МКЭ) важно знать погрешность приближенного решения, для нахождения которой необходимо построить последовательность приближенных решений, что связано с применением процедуры измельчения дискретных моделей. Реализация процедуры измельчения (в рамках микроподхода) дискретных моделей композитных конструкций (тел) требует больших ресурсов ЭВМ, особенно для дискретных моделей с микронеоднородной структурой. В данной работе предложен метод эквивалентных

условий прочности (МЭУП) для расчета на статическую прочность упругих тел с неоднородной и микронеоднородной регулярной структурой, который реализуется с помощью МКЭ с применением многосеточных конечных элементов. Расчет на прочность композитных тел по МЭУП сводится к расчету на прочность упругих изотропных однородных тел с применением эквивалентных условий прочности, которые определяются на основе условий прочности заданных для композитных тел. В основе МЭУП лежит следующее утверждение. Для всякого композитного тела V_0 существуют такое изотропное однородное тело V^b и число p, что если коэффициент запаса n_b тела V^b удовлетворяет эквивалентным условиям прочности вида

$$pn_1(1+\delta_\alpha) \le n_b(1-\delta_\alpha^2) \le pn_2(1-\delta_\alpha),$$ *то коэффициент запаса n_0 тела V_0 удовлетворяет заданным условиям прочности $n_1 \le n_0 \le n_2$, где n_1, n_2 заданы, коэффициент запаса n_0 (n_b) отвечает точному (приближенному) решению задачи теории упругости, построенному для тела V_0 (тела V^b), $\delta_\alpha < (n_2 - n_1)/(n_2 + n_1)$, δ_α – верхняя оценка погрешности δ_b максимального эквивалентного напряжения тела V^b, отвечающего приближенному решению. При построении эквивалентных условий прочности, т. е. при нахождении коэффициента эквивалентности p, используется система дискретных моделей, размерности которых меньше размерностей базовых моделей композитных тел. Реализация МЭУП требует малых ресурсов ЭВМ и не использует процедуры измельчения композитных дискретных моделей. С помощью расчетов показано, что эквивалентные условия прочности, построенные для конкретного нагружения композитного тела, можно использовать для определенного вида его нагружений. Расчеты на прочность тел с микронеоднородной структурой с помощью МЭУП показывают высокую его эффективность. Кратко изложены основные процедуры реализации МЭУП.*

Ключевые слова: упругость, композиты, эквивалентные условия прочности, многосеточные элементы, пластины, балки, оболочки.

Introduction. Structure strength calculation is one of the most important stages in the outline design of a structure based on a structure project feasibility study. As a rule, calculations for static strength, elastic structure (body) of a certain class (for example, elements or aircraft and rocket-space structures) are carried out according to safety requirements [1–3], and limited to the equivalent structure stress determination. In this case for the body V_0 the given strength conditions are $n_1 \le n_0 \le n_2$, where n_1, n_2 are given, n_0 is the body safety factor, V_0, $n_0 = \sigma_T / \sigma_0$, σ_T is the yield stress [1], σ_0 is the maximum equivalent stress corresponding to the exact solution of the elasticity problem (constructed for the body V_0). If the safety factor n_0 satisfies the given strength conditions, then it is suggested that the body V_0 does not collapse during operation. It should be noted that construction of analytical solutions of the three-dimensional problem of elasticity theory for composite bodies is associated with great difficulties. If the maximum equivalent stresses of the bodies is approximate, then in this case the corrected strength conditions are used [4], which pass the stress error. In the analysis of the stress-strain state (SSS), the finite element method (FEM) is widely used [5; 6]. Basic discrete models of bodies, accounting for their inhomogeneous and micro-inhomogeneous structures within the micro-approach [7], have a very high dimension. Implementation of FEM for such discrete models is very difficult, since it requires large computer resources. In addition, to determine the error in the solution, a sequence of approximate solutions constructed using refinement (within the micro approach) of discrete models is used. The grinding procedure is difficult to implement; it leads to a sharp increase in the discrete models size, making implementation of FEM challenging. To determine the SSS of composite bodies, the method of multi-grid finite elements (MFEM) [8–14] is effectively applied, which generates discrete models, dimensions of which are $10^3 \div 10^6$ times less than the base models dimensions. It should be noted that FEM is a special case of MFEM. If when solving boundary value problems by FEM, multigrid finite elements (MgFE) are used [8–22], then MFEM is implemented in this case.

In this work, for calculating the strength of solid composite bodies using equivalent strengths, the method of equivalent strength (MESC) is proposed, which means calculating the strength of isotropic homogeneous bodies using equivalent strengths [23]. In this paper in contrast to [24], a theorem is formulated and proved, which underlies the MESC. In addition, the following should be noted: equivalent strength conditions are based on specified strength conditions using the equivalence coefficient p. In fact, the construction of equivalent strength islimited to determining the coefficient p, which is determined for a given composite body loading. However, it is important to note that the equivalent strength conditions constructed using the coefficient p can be used in composite body strength calculations for a certain type of its loading.

To find the coefficient p, a system of homogeneous and composite discrete models is used, dimensions of which are less than the dimensions of composite bodies models. The analysis of SSS in discrete models is carried out using the MFEM, which generates discrete models of small dimension. The advantages of the MESC are that its implementation requires small computer resources and does not use the procedure for refining discrete models of composite bodies. The use of MESC in strength calculations of bodies with a micro-inhomogeneous regular structure shows its effectiveness.

1. Equivalent strength conditions and equivalent strength structures. Suppose two elastic structures V_1 and V_2 have the same shape, geometrical dimensions, fixings and static loading, but differ in elasticity modulus.

Suppose strength conditions n_1, n_2 are given for the safety factors, respectively of structures V_1, V_2

$$n_a^1 \le n_1 \le n_b^1, \qquad (1)$$

$$n_a^2 \le n_2 \le n_b^2, \qquad (2)$$

where $n_a^1, n_a^2 > 1$; $n_a^1, n_a^2, n_b^1, n_b^2$ – are given; safety factors n_1 (n_2) complie with the precise solution of elasticity theory, built for structures V_1 (V_2).

For structures V_1, V_2 the following two definitions are introduced:

Definition 1. Fulfillment of conditions (2) for the coefficient n_2 implies fulfillment of conditions (1) for the coefficient n_1 and vice versa, if the fulfillment of conditions (1) for the coefficient n_1 implies the fulfillment of conditions (2) for the coefficient n_2, then the strength conditions (1), (2) will be called equivalent strength conditions for structures V_2, V_1, respectively.

Definition 2. Suppose the structures V_1, V_2, for which respectively condition (2), (1) is equivalent to strength conditions do not collapse under the same operating conditions. Then the structures V_1, V_2 will be called strength equivalent.

In practice, the equivalence in strength of structures V_1, V_2 means that V_2 structure can be used instead of a working structure V_1, and vice versa. It should be noted that of the two structures equivalent in strength, it is advisable to use such a structure that is more technologically advanced in manufacturing, meets the specified technical requirements and more cost effective for manufacturing and operation.

2. Provisions of the method of equivalent strength conditions MESC are used to calculate the strength of structures (bodies) that satisfy the following:

Provision 1. Linearly elastic three-dimensional isotropic homogeneous bodies and bodies with an inhomogeneous, micro-inhomogeneous regular structure, which consist of plastic materials, have smooth boundaries and static loading are considered. The body loading functions are smooth functions. Solid boundaries do not degenerate into points.

Provision 2. Composite bodies consist of isotropic homogeneous bodies of different modulus, connections between which are ideal, that is, on common boundaries of homogeneous bodies of different modulus, the functions of displacements and stresses are continuous.

Provision 3. Displacements, deformations and stresses of heterogeneous isotropic homogeneous bodies correspond to the Cauchy relations and Hooke's law of the three-dimensional linear problem of elasticity theory [25]. Equivalent stresses for bodies are determined according to the 4th theory of strength [1].

Provision 4. The maximum equivalent stress of the basic discrete model of a composite body (which consists of a first-order FE of the cube shape, takes into account the inhomogeneous structure of the composite body and generates a three-dimensional uniform mesh) shows a small difference with the exact solution. It should be noted that due to the convergence of the FEM, such basic discrete models for composite bodies always exist.

Provision 5. For the typical dimensions of a composite body and its regular cell, the condition $d / B << 1$ is fulfilled, where d is the maximum typical size of the regular cell of the composite body, B is the minimum typical size of the composite body.

It should be noted that positions 4, 5, as a rule, are fulfilled for bodies with micro-inhomogeneous regular structure.

3. The main theorem of the method of equivalent strength conditions. Without losing shared judgments, we consider bodies with an inhomogeneous regular fibrous structure, which are widely used in practice. The MESC is based on the following theorem:

Theorem. Suppose the strength conditions of the form 3 are given to the safety factor of a composite body n_0 (fibrous structure).

$$n_1 \le n_0 \le n_2, \qquad (3)$$

where n_1, n_2 – are given, $n_1 > 1$, $n_0 = \sigma_T / \sigma_0$, σ_T – fiber yield stress, σ_0 – the maximum equivalent stress of the body V_0, which corresponds to the exact solution of the problem of the elasticity theory, constructed for the body V_0.

Then there is such an isotropic homogeneous body V^b and such a number $p > 0$ (equivalence coefficient) that if the body V^b safety factor n_b satisfies the corrected equivalent strength conditions

$$\frac{pn_1}{1-\delta_\alpha} \le n_b \le \frac{pn_2}{1+\delta_\alpha}, \qquad (4)$$

then, safety factor n_0 of the structure V_0 meets the strength requirements (3), where $n_b = \sigma_T / \sigma_b$, σ_b – the maximum equivalent stress of the body V^b, which corresponds to the approximate solution of the theory of elasticity problem, constructed for the body V^b,

$$\delta_\alpha < \frac{n_2 - n_1}{n_2 + n_1}, \qquad (5)$$

δ_α – upper bound on relative error, δ_b pressure σ_b of body V^b, $|\delta_b| \le \delta_\alpha$.

Deduction.

First, let us prove the existence of equivalent strength conditions for linearly elastic composite bodies. Suppose an elastic homogeneous isotropic body V^b and a composite body V_0 have the same shape, size, fixation and loading, but differ in elastic moduli. Suppose the elastic moduli of the body V^b and fiber be the same. The safety factors n_0, n_b^0 respectively bodies V_0, V^b are found by the formulas

$$n_0 = \frac{\sigma_T}{\sigma_0}, \qquad (6)$$

$$n_b^0 = \frac{\sigma_T}{\sigma_b^0}, \qquad (7)$$

where σ_T – fiber yield strength [1–3]; σ_b^0 – maximum equivalent body stress V^b, corresponding to the exact solution of the elasticity theory problem.

Suppose coefficient n_0 meets the requirements (3). Applying (6) to (3) we obtain

$$n_1 \le \frac{\sigma_T}{\sigma_0} \le n_2 . \qquad (8)$$

There is a number $p > 0$,

$$p = \frac{\sigma_0}{\sigma_b^0} . \qquad (9)$$

Considering (9) in (8), we obtain

$$pn_1 \le \frac{\sigma_T}{\sigma_b^0} \le pn_2 \qquad (10)$$

Applying (7) in (10), we obtain

$$pn_1 \le n_b^0 \le pn_2 . \qquad (11)$$

So, the safety factor n_b^0 of an isotropic homogeneous body V^b satisfies conditions (11). Conversely, suppose body V^b safety factor n_b^0 satisfy the strength conditions (11). Applying (7) in (11) considering (9), we obtain $pn_1 \le \frac{p\sigma_T}{\sigma_0} \le pn_2$. Whence, taking into account (6), follows the fulfillment of the strength conditions for the safety factor n_0 of the composite body V_0 (3). It is shown that each coefficient $n_b^0 \in (pn_1, pn_2)$ corresponds to a single coefficient $n_0 \in (n_1, n_2)$ found by formula (6), and vice versa. Further limiting cases are considered. Suppose $n_b^0 = pn_1$. Using relation (7) in the latter equation we obtain $p\sigma_T / \sigma_0 = pn_1$. Whence, taking into account (6) it follows $n_0 = n_1$. Similarly, one can show that if $n_b^0 = pn_2$, then $n_0 = n_2$. Suppose $n_0 = n_1$. Using (6), (9) in the latter equation, we obtain $\sigma_T / \sigma_b^0 = pn_1$. Now then, taking into account (7), it follows that $n_b^0 = pn_1$. Similarly, one can show that if $n_0 = n_2$, then $n_b^0 = pn_2$. Hence it follows that conditions (11), according to Definition 1, are equivalent strength conditions for a body V_0 .

Suppose for the body V^b the maximum equivalent stress has been defined as σ_b , corresponding to the approximate solution of the elasticity theory problem, such that

$$|\delta_b| \le \delta_\alpha < C_\alpha = \frac{n_2 - n_1}{n_1 + n_2} , \qquad (12)$$

where n_1 , n_2 – are given; $n_1 > 1$, $n_2 > n_1$, δ_b – relative stress error σ_b , i. e.

$$\delta_b = \frac{\sigma_b - \sigma_b^0}{\sigma_b^0} , \qquad (13)$$

where δ_α – upper bound for error δ_b .

From (13) it follows that $\sigma_b = (1 + \delta_b) \sigma_b^0$. Hence obtain

$$n_b^0 = (1 + \delta_b) n_b . \qquad (14)$$

Let us note that in (12) $C_\alpha < 1$. Suppose δ_0 is such that $\delta_0 = |\delta_b|$. Then due to (12) obtain

$$0 \le \delta_0 = |\delta_b| \le \delta_\alpha < 1 . \qquad (15)$$

Assuming in (14) consecutively $\delta_b = -\delta_0$, $\delta_b = \delta_0$, apply coefficients

$$n_1^r = (1 - \delta_0) n_b , \quad n_2^r = (1 + \delta_0) n_b , \qquad (16)$$

Then due to (14), (16) obtain

$$n_b^0 = n_1^r \quad \text{or} \quad n_b^0 = n_2^r . \qquad (17)$$

Apply coefficients n_1^d , n_2^d according to formulas

$$n_1^d = (1 - \delta_\alpha) n_b , \quad n_2^d = (1 + \delta_\alpha) n_b . \qquad (18)$$

Due to $0 \le \delta_\alpha < 1$, $n_b > 0$, from (18) it follows that

$$n_2^d \ge n_1^d . \qquad (19)$$

Equivalent strength conditions that take into account stress error, i. e., corrected equivalent strength conditions (4) are presented in the form

$$pn_1(1 + \delta_\alpha) \le n_b(1 - \delta_\alpha^2) \le pn_2(1 - \delta_\alpha) , \qquad (20)$$

where $n_b = \sigma_T / \sigma_b$, σ_T – fiber yield strength.

Suppose for coefficient n_b strength conditions are met (20), i. e. suppose $pn_1 \le (1 - \delta_g) n_b$, $(1 + \delta_g) n_b \le pn_2$. Hence for the coefficient n_1^d , n_2^d , taking into account (18), (19) inequation is done

$$pn_1 \le n_1^d \le n_2^d \le pn_2 . \qquad (21)$$

Comparing (16), (18) with respect to (15), equations $n_1^d \le n_1^r$, $n_2^r \le n_2^d$ follow. Hence, considering that according to (16) $n_1^r \le n_2^r$, we obtain

$$n_1^d \le n_1^r \le n_2^r \le n_2^d . \qquad (22)$$

Then, due to (21), (22) inequations are done

$$pn_1 \le n_1^r \le n_2^r \le pn_2 . \qquad (23)$$

From (23) taking into account (17), i. e. from meeting for the body V^b safety factor n_b (corresponding to the approximate solution) of the corrected equivalent strength conditions (20), that is (4), it follows that strength conditions (11) for the safety factor n_b^0 of the body V^b (corresponding to the exact solution) are met, therefore, satisfying the given strength conditions (3) for the safety factor n_0 of the composite body V_0 (corresponding to the exact solution). Constraints on the parameter δ_α are found from the assumption of strength conditions existence (4), i. e. suppose inequation $pn_1(1 + \delta_\alpha) \le pn_2(1 - \delta_\alpha)$ is done. Whence it follows that

$$\delta_\alpha < C_\alpha = \frac{n_2 - n_1}{n_1 + n_2} . \qquad (24)$$

It should be noted that, since $n_2 > n_1 \geq 1$, then from (24) it follows that $0 < C_\alpha < 1$. If $\delta_\alpha = C_\alpha$, then the range for varying values of the coefficient n_0 is zero, which is difficult to perform in practice. Now then $\delta_\alpha < C_\alpha$, it is possible to meet the equivalent strength conditions (11) for the coefficient n_b^0 applying corrected equivalent strength conditions (4) and the approximate solution that generates an error δ_b for the stress σ_b that $|\delta_b| \leq \delta_\alpha$. Note that meeting conditions (11) implies the fulfillment of the specified strength conditions (3). The theorem is proved.

Note that it follows from the theorem that if the safety factor n_b of the body V^b satisfies the corrected equivalent strength conditions (4), then this means that the error δ_b of the maximum equivalent stress σ_b of the body V^b is not greater than δ_α, i. e. $|\delta_b| \leq \delta_\alpha$.

4. Procedures for implementing the method of equivalent strength conditions. Implementation of the MESC is reduced to construction of equivalent strength conditions (4) applying the MFEM, that is, to determination of the equivalence coefficient p, and to determination of the maximum equivalent stress σ_b for the body V^b with an error $|\delta_b| < \delta_\alpha$, $n_b = \sigma_T / \sigma_b$. The coefficient p is determined by the formula (9), i. e.

$$p = \frac{\sigma_0}{\sigma_b^0}. \qquad (25)$$

Without losing shared judgments, for convenience and clarity of presentation, we will consider the basic procedures for the implementation of MESC using the example of calculating the strength of a composite beam (body) V_0 with dimensions $H \times L \times H$, where $H = 128h$, $L = 1536h$, h – is given, Fig. 1. The body V_0 is reinforced with continuous longitudinal fibers of constant cross-section with dimensions $h \times h$. The fibers have the same modulus of elasticity. When $y = 0$ the body is fixed and has loading $q_z(x, y)$ on the surface $z = H$. The inhomogeneous structure of the body V_0 is represented by regular cells G_0 with $8h \times 8h \times 8h$ size, fig. 2, the sections of 16 fibers are painted over. It is believed [26] that if the fiber thickness is less than 0.5 mm, then such fibers form a micro-inhomogeneous structure. Suppose $L = 600$ мм, $H = 50$ мм, then $h = 0.3906$ мм. In this case, the body V_0 has a micro-inhomogeneous regular structure.

It should be noted that since the filling factor of the composite body V_0 is small (equal to 0.25), it is difficult to determine the effective elastic moduli for the body V_0. The case when the filling coefficient is close to one was considered in [23].

Suppose the strength conditions (3) are given for the safety factor n_0 of the composite body V_0. The basic discrete V_0 body model $\mathbf{R}_0$ consists of finite elements (FE) of the 1st order of a cube shape with a side h [6], in which a three-dimensional SSS is realized, accounting for

the inhomogeneous structure of the beam and generates a basic uniform mesh with a step h with dimension $129 \times 1537 \times 129$.
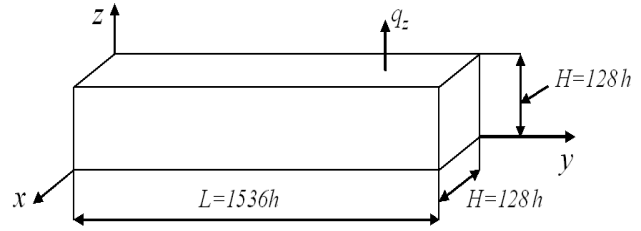
Fig. 1. The characteristic sizes of the beam (body) V_0

Рис. 1. Характерные размеры балки (тела) V_0
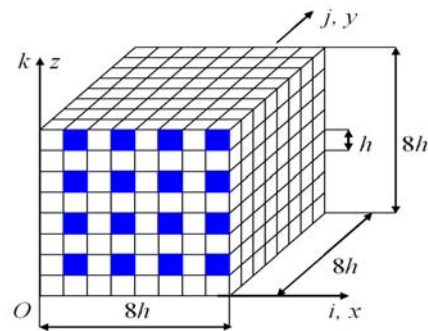
Fig. 2. Regular cell (body) G_0

Рис. 2. Регулярная ячейка (тело) G_0

Fig. 2 shows the basic grid G_0 of a regular dimension cell $9 \times 9 \times 9$; $i, j, k = 1, ..., 9$. The model $\mathbf{R}_0$ has $N_0 = 76681728$ nodal unknown FEM, system tape width of FEM equations is $b_0 = 50316$. The basic model $\mathbf{R}_0$ takes into account the micro-inhomogeneous structure of the body V_0 with high dimension, therefore we can assume that this model satisfies position 4. However, it is difficult to apply the discrete model $\mathbf{R}_0$ in calculations, since the implementation of the FEM for the $\mathbf{R}_0$ model requires essential computer resources.

According to the MESC, introduced is an isotropic homogeneous body V^b such that the bodies V^b, V_0 have the same shape, dimensions, specified fixing and loading, but differ in elastic moduli. The elastic moduli of the body V^b are equal to the elastic moduli of the body V_0 fiber. For the body V^b we define a discrete model V_n^b, which consists of an FE $V_e^{(n)}$ of the 1st order of a cube shape with a side h_n [6] and has a uniform mesh with a step h_n with dimension $n_1^{(n)} \times n_2^{(n)} \times n_3^{(n)}$, where

$$n_1^{(n)} = 8n + 1, \ n_2^{(n)} = 12 \times 8n + 1,$$
$$n_3^{(n)} = 8n + 1, \ n = 1, 2, 3, ... \qquad (26)$$

The steps of the fine mesh of the model V_n^0 along the axeses Ox, Oy, Oz equal $h_x^{(n)} = H/(8n)$, $h_y^{(n)} = L/(96n)$, $h_z^{(n)} = H/(8n)$. Since $L = 12H$, then $h_n = h_x^{(n)} = h_y^{(n)} = h_z^{(n)}$. Due to (26) we obtain $h_n = \beta_n h$, where β_n – scale factor, $\beta_n = 16/n$, $n = 1,2,3,...$. Under $n = 1,...,15$ we have $\beta_n > 1$, i. e. $h_n > h$. Under $n \to 16$ we have $\beta_n \to 1$, $\beta_{16} = 1$, $h_{16} = h$. Discrete model V_n^b of a finite number of bodies of the same shape G_n^b with dimensions $8h_n \times 8h_n \times 8h_n$, $n = 1,2,3,...$. The body and the regular cell G_0 have the same shape (cube shape), but differ in characteristic dimensions.

Let us introduce a composite body G_n^0 (cube shaped) with dimensions $8h_n \times 8h_n \times 8h_n$. Suppose the composite body G_n^0 consist of FE $V_e^{(n)}$ cube-shaped with the side h_n. The composite body G_n^0 is of fibrous structure, the same number of fibers (16 longitudinal fibers with a square cross section $h_n \times h_n$, the distance between the fibers equals h_n) and the same mutual arrangement as in the regular cell G_0 (the cell G_0 has 16 with dimensions $h \times h$, the distance between them equals h, fig. 2). $n = 1,2,3,...$. Inhomogeneous structure in the composite body G_n^0 is taken into account using FE $V_e^{(n)}$. Fibers and matrices of the bodies G_n^0, G_0 have the same elastic moduli. The bodies G_n^0, G_0 in fact differ only in scale, they can formally be written as $G_n^0 = (\beta_n)^3 G_0$. Under $n = 16$ we obtain $\beta_{16} = 1$, i. e. $G_{16}^0 = G_0$.

Using the bodies G_n^0 instead of the bodies G_n^b in the discrete model V_n^b we obtain a composite discrete model R_n^0, $n = 1,2,3,...$, which accounts for inhomogeneous structure. Composite body G_n^0 is, in fact, a regular cell for the model R_n^0, $n = 1,2,3,...$. Discrete model R_n^0 has the same uniform grid with step h_n and dimensions V_n^b. Under $n = 16$ the discrete models V_{16}^b, R_{16}^0 and $\mathbf{R}_0$ have the same shape, characteristic size and dimensions. Since $G_{16}^0 = G_0$, then under $n = 16$ models R_{16}^0 and $\mathbf{R}_0$ coincide, i. e. $R_{16}^0 = \mathbf{R}_0$. Thus, the discrete models V_n^0, R_n^0 possess the same shape , characteristic size and dimensions, the same fixing and loading, like a body (beam) V_0, but differ only in elastic moduli $n = 1,2,3,...$. It is important to note the following:

1. Dimensions of discrete models V_n^0, R_n^0 under $n = 1,...,15$, due to (26), are less than the dimensions of the basic discrete model $\mathbf{R}_0$ of a composite body V_0.

2. When constructing composite discrete models $\{R_n^0\}_{n=2}^{15}$, the procedure of grinding composite discrete models is not applied.

To reduce the dimensions of the models V_n^b, R_n^0 MgFE are used [8–22]. Since the models R_{16}^0, V_{16}^b have the same high dimension as the basic discrete body model $\mathbf{R}_0$, which has 76681728 nodal unknown FEM, we believe that the maximum equivalent stress σ_{16}^0 (stress σ_{16}^b) of the model R_{16}^0 (model V_{16}^b) differs a little from the exact stress σ_0 (σ_b^0). Therefore, we assume $\sigma_0 = \sigma_{16}^0$, $\sigma_b^0 = \sigma_{16}^b$.

We find the equivalence coefficient p by formula (25) accounting for the latter 2 equations, i. e.

$$p = \sigma_{16}^0 / \sigma_{16}^b. \qquad (27)$$

Taking into account in the formula $p_n = \sigma_n^0 / \sigma_n^b$, where σ_n^0 (σ_n^b) is the maximum equivalent stress of the model R_n^0 (model), which at $n \to 16$ we have $\sigma_n^0 \to \sigma_{16}^0$, $\sigma_n^b \to \sigma_{16}^b$, due to (27) we have $p_n \to p$ at $n \to 16$. Suppose p_n quickly converge to p. Let the value $\delta_n = |p_n - p_{n-1}|/p_n$ be small, where then we accept hat $p = p_n$. Applying the found coefficient p and parameter δ_α (δ_α specified and satisfies condition (5)) n_1 and n_2 specified in representation (4), we determine the corrected equivalent strength conditions, which accounts for the stress error. Suppose σ_n^b quickly converge to σ_b^0. Let the small value $\delta_n^\sigma = |\sigma_n^b - \sigma_{n-1}^b|/\sigma_n^b$ and $|\delta_n^b| \le \delta_\alpha$, where δ_n^b is the relative voltage error, σ_n^b δ_α is given, $\delta_\alpha < C_\alpha$ $n = 2,3,...,$. Then we accept that $\sigma_b = \sigma_n^b$, i. e., the maximum equivalent body V^b stress σ_b is found. Suppose the found safety factor n_b (where $n_b = \sigma_T / \sigma_b$, i. e. $n_b = \sigma_T / \sigma_n^b$) of an isotropic homogeneous body V^b (corresponding to an approximate solution) satisfy the constructed equivalent strength conditions (4). Then the safety factor n_0 of the composite body V_0 (which corresponds to the exact solution) satisfies the given strength conditions (3).

When calculating the composite bodies strength according to MESC, it is advisable to use MgFE [24]. In this case, the implementation of MESC requires small computer resources.

5. Application of the corrected equivalent strength conditions in the calculations of composite bodies with a certain type of loading. The calculations given below show that the corrected equivalent strength conditions (4), constructed for a specific body loading, can be used in the strength calculations of a composite body V_0 (fig. 1), for which a certain type of loading is specified.

In [24], an example of a cantilever beam V_0 (fig. 1) strength analysis according to MESC using three-mesh FE is considered in detail. The beam is reinforced with longitudinal fibers. The regular cell of the beam is shown in fig. 2. Under $y = 0$, $u = v = w = 0$, i. e in the xOz

plane the beam is fixed. For the safety factor n_0 of the beam, the given strength conditions have the form

$$1.3 \le n_0 \le 3.2 . \qquad (28)$$

In the calculations of the beam the following data were used:

$$h = 0.3906 ; \ \sigma_T = 5 ; \ E_v = 10 , \ E_c = 1 ,$$

$$\nu_c = \nu_v = 0.3, \ q_z = 0.0018, \qquad (29)$$

where E_c, E_v (ν_c, ν_v) – Young's moduli (Poisson's ratios) of the binder and fibers, respectively, σ_T is the yield stress q_z of the fiber, the load acts on the surface $z = H$, $0.5L \le y \le L$, fig. 1.

The equivalence factor p for the composite beam V_0 is determined using the procedure described above. Discrete models V_n^b, R_n^0, $n = 9, 11, 12$ are constructed using 3sFE (the construction procedure of which is described in detail in [24]) on the basis of basic regular partitions, respectively of dimensions: $73 \times 865 \times 73$, $89 \times 1057 \times 89$ and $97 \times 1153 \times 97$. The coefficients p_n are found by the formula $p_n = \sigma_n / \sigma_n^b$, where σ_n, σ_n^b are the maximum equivalent stresses, respectively of the models R_n^0, V_n^b, $n = 9, 11, 12$. As a result of calculations we get: $p_9 = 3.002$, $p_{11} = 3.000$, $p_{12} = 2.999$. The relative errors for the found coefficients p_9, p_{11}, p_{12} are

$$\delta_1(\%) = 100\,\% \times |\,p_{11} - p_9\,| / p_{11} =$$
$$= 100\,\% \times |\,3.002 - 3.000\,| / 3.000 = 0.066\,\%,$$

$$\delta_2(\%) = 100\,\% \times |\,p_{12} - p_{11}\,| / p_{12} =$$
$$= 100\,\% \times |\,3.000 - 2.999\,| / 2.999 = 0.033\,\%.$$

Since $p_9 > p_{11} > p_{12}$ and δ_2 is the smallest value, we consider, equivalent coefficient equals $p = p_{12} = 2.999$. Applying to (4) $\delta_\alpha = 0.15$, $n_1 = 1.3$, $n_2 = 3.2$, we obtain the corrected equivalent strength conditions expressed in terms of the equivalence coefficient p

$$1.5288 p \le n_b \le 2.7805 p . \qquad (30)$$

Applying to (30) $p = 2.999$, we obtain the following corrected equivalent strength conditions $4.584 \le n_b \le 8.339$, which in practice, in order to take

into account the error of computer calculations, is used in the following modified form

$$4.65 \le n_b \le 8.25 . \qquad (31)$$

Table 1 shows the results of calculations for five loadings q_z^n of the beam V_0, for which the equivalence coefficients p^n are found, where x, y, z are the coordinates of the points of the beam surface, on which a constant load q_z^n, $n = 1,...,5$ is applied. Loads q_z^n, $n = 1, 4, 5$ provide direct bending of the beam, loads q_z^2, q_z^3 – oblique bending of the beam. The relative error $\delta_n(\%)$ for the equivalence coefficient p_n, presented in table, is determined by the formula

$$\delta_n(\%) = 100\,\% \times |\,p - p_n\,| / p , \qquad (32)$$

where $p = 2.999$, $n = 1,...,5$.

Analysis of the calculation results shows that the equivalence coefficients p^n, $n = \overline{1.5}$ differ from the equivalence coefficient $p = 2.999$ by small values, which are $0.35\,\%$ less (see formula (32), tab. 1). According to (30), the corrected equivalent strength conditions for the equivalence coefficient p^n, $n = 1,...,5$ have the form

$$1.5288 p^n \le n_b \le 2.7805 p^n . \qquad (33)$$

Since the coefficients p^n, $n = 1,...,5$ have minor difference with p (see formula (32), fig. 1), then equivalent strength conditions (33) will differ a little from the equivalent strength conditions (30); moreover, we have

$$1.5288 p^n \le 4.65 \le n_b \le 8.25 \le 2.7805 p^n , \qquad (34)$$

where $n = 1,...,5$.

Fulfillment of (34) implies that the equivalence coefficients p^n, $n = \overline{1.5}$, in fact, generate corrected equivalent strength conditions (31).

Consequently, the results of the calculations show that when calculating the strength of a composite beam V_0 under the action of piecewise constant loads q_z^n on the surface $z = H$, $n = 1,...,5$ it is possible to use the corrected equivalent strength conditions (31) constructed for a beam V_0 with loading $q_z = 0.0018$ on the surface $0.5L \le y \le L$, $z = H$ i. e., constructed using the equivalence coefficient $p = 2.999$.

The results of calculations of the beam V_0

n	x	y	z	q_z^n	p^n	$\delta_n(\%)$
1	$0 \le x \le H$	$0 \le y \le L$	H	0.0078	2.997	0.066 %
2	$0 \le x \le H/2$	$0 \le y \le L/2$	H	0.543	2.991	0.267 %
3	$0 \le x \le H/2$	$0 \le y \le L$	H	0.125	2.989	0.333 %
4	$0 \le x \le H$	$0{,}998L \le y \le L$	H	2.8000	2.999	0.000 %
5	$0 \le x \le H$ $0 \le x \le H$	$0 \le y \le L/2$ $0{,}5L \le y \le L$	H	0.0145 0.0034	2.994	0.167 %

Now then, if a piecewise constant load q_z acts on the upper surface of the beam V_0, which provides direct or oblique bending of the beam, then when calculating the strength of the beam V_0, you can use the corrected equivalent strength conditions (31).

Given in [24] example of calculating the strength of a cantilever beam (having a micro-inhomogeneous regular fibrous structure) using the MESC shows its high efficiency.

Conclusion. The method of equivalent strength conditions is proposed for calculating the static strength of elastic bodies with an inhomogeneous, micro-inhomogeneous regular structure under given strength conditions. The proposed method is implemented applying FEM using multigrid finite elements and is limited to calculation of isotropic homogeneous bodies strength using equivalent strength conditions that account for solution errors. In the process of implementation, the method of equivalent strength conditions requires little time or computer resources and is exceptionally effective when calculating the strength of bodies that have a micro-inhomogeneous regular fibrous structure.

References

1. Pisarenko G. S., Yakovlev A. P., Matveev V. V. *Spravochnik po soprotivleniyu materialov* [Handbook of resistance materials']. Kiev, Nauk. Dumka Publ., 1975, 704 p.

2. Birger I. A., Shorr B. F., Iosilevich G. B. *Raschet na prochnost' detalej mashin* [Calculation of the strength of machine parts]. Moscow, Mashinostroenie Publ., 1993, 640 p.

3. Moskvichev V. V. *Osnovy konstrukcionnoj prochnosti tekhnicheskih sistem i inzhenernyh sooruzhenij* [Fundamentals of structural strength of technical systems and engineering structures]. Novosibirsk, Nauka Publ., 2002, 106 p.

4. Matveev A. D. [Calculation of elastic structures using the adjusted terms of strength]. *Izvestiya AltGU.* 2017, No. 4, P. 116–119 (In Russ.). Doi: 10.14258/izvasu(2017)4-21.

5. Norri D., de Friz Zh. *Vvedenie v metod konechnykh elementov* [Introduction to the finite element method]. Moscow, Mir Publ., 1981, 304 p.

6. Zenkevich O. *Metod konechnykh elementov v tekhnike* [Finite element method in engineering]. Moscow, Mir Publ., 1975, 544 p.

7. Fudzii T., Dzako M. *Mekhanika razrusheniya kompozicionnyh materialov* [Fracture mechanics of composite materials]. Moscow, Mir Publ., 1982.

8. Matveev A. D. [The method of multigrid finite elements in the calculations of three-dimensional homogeneous and composite bodies]. *Uchen. zap. Kazan. un-ta. Seriia: Fiz.-matem. Nauki.* 2016, Vol. 158, No. 4, P. 530–543 (In Russ.).

9. Matveev A. D. [Multigrid method for finite elements in the analysis of composite plates and beams]. *Vestnik KrasGAU.* 2016, No. 12, P. 93–100 (In Russ.).

10. Matveev A. D. Multigrid finite element method in stress of three-dimensional elastic bodies of heterogeneous structure. *IOP Conf, Ser.: Mater. Sci. Eng.* 2016, Vol. 158, No. 1, Art. 012067, P. 1–9.

11. Matveev A. D. [Multigrid finite element Method in the calculations of composite plates and beams of irregular shape]. *The Bulletin of KrasGAU.* 2017, No. 11, P. 131–140 (In Russ.).

12. Matveev A. D. [Multigrid finite element Method]. *The Bulletin of KrasGAU.* 2018, No. 2, P. 90–103 (In Russ.).

13. Matveev A. D. [The method of. multigrid finite elements of the composite rotational and bi-curved shell calculations]. *The Bulletin of KrasGAU.* 2018. No. 3, P. 126–137 (In Russ.).

14. Matveev A. D. [Method of. multigrid finite elements to solve physical boundary value problems]. *Ministry of information technologies and mathematical modeling.* Krasnoyarsk, 2017, P. 27–60.

15. Matveev A. D. [Some approaches of designing elastic multigrid finite elements]. *VINITI Proceedings.* 2000, No. 2990-B00, P. 30 (In Russ.).

16. Matveev A. D. [Multigrid modeling of composites of irregular structure with a small filling ratio]. *J. Appl. Mech. Tech. Phys.* 2004, No. 3, P. 161–171 (In Russ.).

17. Matveev A. D., Grishanov A. N. [Single- and double-grid curvilinear elements of three-dimensional cylindrical panels and shells]. *Izvestiya AltGU.* 2014, No. 1/1. P. 84–89 (In Russ.).

18. Matveev A. D., Grishanov A. N. [Multigrid curvilinear elements in three-dimensional analysis of cylindrical composite panels with cavities and holes]. *Proceedings of Kazan University.* 2014, Vol. 156, No. 4, P. 47–59 (In Russ.).

19. Matveev A. D., Grishanov A. N. [Three-dimensional Composite Multigrid Finite Shell-Type Elements]. *Izvestiya AltGU.* 2017, No. 4/1, P. 120–125 (In Russ.).

20. Matveev A. D. [The construction of complex multigrid finite element heterogeneous and micro-inhomogeneities in structure]. *Izvestiya AltGU.* 2014, No. 1/1, P. 80–83(In Russ.). Doi: 10.14258/izvasu(2014)1.1-18.

21. Matveev A. D. [Method of generating finite elements]. *The Bulletin of KrasGAU.* 2018, No. 6, P. 141–154 (In Russ.).

22. Matveev A. D. [Construction of multigrid finite elements to calculate shells, plates and beams based on generating finite elements]. *PNRPU Mechanics Bulletin.* 2019, No. 3, P. 48–57 (In Russ.). Doi: 10/15593/perm.mech/2019.3.05.

23. Matveev A. D. [Calculation of the strength of composite structures using equivalent strength conditions]. *The Bulletin of KrasGAU.* 2014, No. 11, P. 68–79 (In Russ.).

24. Matveev A. D. [The method of equivalent strength conditions in calculating composite structures regular structure using multigrid finite elements]. *Siberian Journal of Science and Technology.* 2019, Vol. 20, No. 4, P. 423–435 (In Russ.). Doi: 10.31772/2587-6066-2019-20-4-423-435.

25. Samul' V. I. *Osnovy teorii uprugosti i plastichnosti* [Fundamentals of the theory of elasticity and plasticity]. Moscow, Vysshaia shkola Publ., 1982, 264 p.

26. Golushko S. K., Nemirovskii Iu. V. *Priamye i obratnye zadachi mekhaniki uprugikh kompozitnykh plastin i obolochek vrashcheniia* [Direct and inverse problems of mechanics of elastic composite plates and shells of rotation]. Moscow, FIZMATLIT Publ., 2008, 432 p.

Библиографические ссылки

1. Писаренко Г. С., Яковлев А. П., Матвеев В. В. Справочник по сопротивлению материалов. Киев : Наук. думка, 1975. 704 с.

2. Биргер И. А., Шорр Б. Ф., Иосилевич Г. Б. Расчет на прочность деталей машин. М. : Машиностроение, 1993. 640 с.

3. Москвичев В. В. Основы конструкционной прочности технических систем и инженерных сооружений. Новосибирск : Наука, 2002. 106 с.

4. Матвеев А. Д. Расчет упругих конструкций с применением скорректированных условий прочности // Известия АлтГУ. 2017. № 4. С. 116–119. Doi: 10.14258/izvasu(2017)4-21.

5. Норри Д., Ж. де Фриз. Введение в метод конечных элементов. М. : Мир, 1981. 304 с.

6. Зенкевич О. Метод конечных элементов в технике. М. : Мир, 1975. 542 с.

7. Фудзии Т., Дзако М. Механика разрушения композиционных материалов. М. : Мир, 1982.

8. Матвеев А. Д. Метод многосеточных конечных элементов в расчетах трехмерных однородных и композитных тел. // Учен. зап. Казан. ун-та. Серия: Физ.-матем. науки. 2016. Т. 158, кн. 4. С. 530–543.

9. Матвеев А. Д. Метод многосеточных конечных элементов в расчетах композитных пластин и балок. // Вестник КрасГАУ. 2016. № 12. С. 93–100.

10. Matveev A. D. Multigrid finite element method in stress of three-dimensional elastic bodies of heterogeneous structure // IOP Conf. Ser.: Mater. Sci. Eng. 2016. Vol. 158, No. 1. P. 1–9.

11. Матвеев А. Д. Метод многосеточных конечных элементов в расчетах композитных пластин и балок сложной формы // Вестник КрасГАУ. 2017. № 11. С. 131–140.

12. Матвеев А. Д. Метод многосеточных конечных элементов // Вестник КрасГАУ. 2018. № 2. С. 90–103.

13. Матвеев А. Д. Метод многосеточных конечных элементов в расчетах композитных оболочек вращения и двоякой кривизны // Вестник КрасГАУ. 2018. № 3. С. 126–137.

14. Матвеев А. Д. Метод многосеточных конечных элементов в решении физических краевых задач. // Информационные технологии и математическое моделирование. Красноярск, 2017. С. 27–60.

15. Матвеев А. Д. Некоторые подходы проектирования упругих многосеточных конечных элементов // Деп. в ВИНИТИ. 2000. № 2990–В00. 30 с.

16. Матвеев А. Д. Многосеточное моделирование композитов нерегулярной структуры с малым коэффициентом наполнения // Прикладная механика и техническая физика. 2004. № 3. С. 161–171.

17. Матвеев А. Д., Гришанов А. Н. Одно- и двухсеточные криволинейные элементы трехмерных цилиндрических панелей и оболочек // Известия АлтГУ. 2014. № 1/1. С. 84–89.

18. Матвеев А. Д., Гришанов А. Н. Многосеточные криволинейные элементы в трехмерном анализе цилиндрических композитных панелей с полостями и отверстиями // Ученые записки Казанского университета. Серия: Физико-математические науки. 2014. Т. 156, кн. 4. С. 47–59.

19. Матвеев А. Д., Гришанов А. Н. Трехмерные композитные многосеточные конечные элементы оболочечного типа. // Известия АлтГУ. Серия: физико-математические науки. 2017. № 4/1. С. 120–125.

20. Матвеев А. Д. Построение сложных многосеточных конечных элементов с неоднородной и микронеоднородной структурой // Известия АлтГУ. Серия: Математика и механика. 2014. № 1/1. С. 80–83. Doi: 10.14258/izvasu(2014)1.1-18.

21. Матвеев А. Д. Метод образующих конечных элементов // Вестник КрасГАУ. 2018. № 6. С. 141–154.

22. Матвеев А. Д. Построение многосеточных конечных элементов для расчета оболочек, пластин и балок на основе образующих конечных элементов // Вестник Пермского национального исследовательского политехнического университета. Механика. 2019. № 3. С. 48-57. Doi: 10/15593/perm.mech/2019.3.05.

23. Матвеев А. Д. Расчет на прочность композитных конструкций с применением эквивалентных условий прочности // Вестник КрасГАУ. 2014. № 11. С. 68–79.

24. Матвеев А. Д. Метод эквивалентных условий прочности в расчетах композитных конструкций регулярной структуры с применением многосеточных конечных элементов // Сибирский журнал науки и технологий. 2019. Т. 20, № 4. С. 423–435. Doi: 10.31772/2587-6066-2019-20-4-423-435.

25. Самуль В. И. Основы теории упругости и пластичности. М. : Высшая школа, 1982. 264 с.

26. Голушко С. К., Немировский Ю. В. Прямые и обратные задачи механики упругих композитных пластин и оболочек вращения. М. : Физматлит, 2008. 432 с.

Matveev Alexander Danilovich – Cand. Sc., associate Professor, senior researcher; Institute of computational modeling SB RAS. E-mail: mtv241@mail.ru.

Матвеев Александр Данилович – кандидат физико-математических наук, доцент, старший научный сотрудник; Институт вычислительного моделирования СО РАН. E-mail: mtv241@mail.ru.

MODELS AND METHODS OF OPTIMAL CONTROL OF SOFTWARE AND TECHNICAL CONFIGURATION OF HETEROGENEOUS DISTRIBUTED INFORMATION PROCESSING SYSTEMS

G. A. Ontuzheva

Siberian Federal University
79, Svobodny Av., Krasnoyarsk, 660041, Russian Federation
E-mail: gontuzheva@sfu-kras.ru

The article discusses formalization of the problem of heterogeneous distributed information processing systems (HDIPS) software and hardware configuration management. A formal description of possible optimality criteria for the HDIPS software and hardware configuration is given. The HDIPS model in terms of queuing theory is proposed. The problem of allocating the HDIPS computational resources is formulated as a transport problem according to time criterion with atomic needs. The algorithm for solving this problem is proposed and the boundaries of its applicability to the HDIPS are determined. To meet the selected optimality criterion, the analysis of the HDIPS software and hardware configuration applying its formal model, using the queuing theory methods is presented. HDIPS is presented as a queuing network, where each computing node and route control unit is a mass service system. The problem of computing resource allocation in HDIPS is presented as a transport problem according to the time criterion with atomic needs. The least time algorithm for indivisible needs takes into account the indivisibility condition.

Keywords: distributed information processing systems, transport problem, queuing systems, software and hardware configuration, management of software and hardware resources, management optimization.

МОДЕЛИ И МЕТОДЫ ОПТИМАЛЬНОГО УПРАВЛЕНИЯ ПРОГРАММНО-ТЕХНИЧЕСКОЙ КОНФИГУРАЦИЕЙ ГЕТЕРОГЕННЫХ РАСПРЕДЕЛЕННЫХ СИСТЕМ ОБРАБОТКИ ИНФОРМАЦИИ

Г. А. Онтужева

Сибирский федеральный университет
Российская Федерация, 660041, г. Красноярск, просп. Свободный, 79
E-mail: gontuzheva@sfu-kras.ru

В статье рассматривается формализация задачи управления программно-технической конфигурацией гетерогенных распределенных систем обработки информации (ГРСОИ). Дано формальное описание возможных критериев оптимальности программно-технической конфигурации ГРСОИ. Предложена модель ГРСОИ в терминах теории массового обслуживания. Задача распределения вычислительных ресурсов ГРСОИ сформулирована в виде транспортной задачи по критерию времени с атомарными потребностями. Предложен алгоритм решения данной задачи и определены границы его применимости в ГРСОИ. Для достижения выбранного критерия оптимальности приведен анализ программно-технической конфигурации ГРСОИ при помощи ее формальной модели с применением методов теории массового обслуживания. ГРСОИ представлена как сеть массового обслуживания, где каждый вычислительный узел и блок управления маршрутом является системой массового облуживания. Задача распределения вычислительного ресурса в ГРОСИ представляется как транспортная задача по критерию времени с атомарными потребностями. С учетом условия атомарности был разработан алгоритм наименьшего времени для атомарных заявок.

Ключевые слова: распределенная системы обработки информации, транспортная задача, системы массового обслуживания, программно-техническая конфигурация, управление программно-техническими ресурсами, оптимизация управления.

Introduction. Heterogeneous distributed information processing systems (HDIPS) are information processing systems that are characterized by territorial distribution, a variety of software and hardware components and a heterogeneous nature of tasks being processed [1; 2]. Such systems are used in areas where it is necessary to receive and process primary data of a various nature in an automatic or automated mode. They combine computational nodes (CN) and data sources of various types, which make it possible to carry out the entire computation process in the system, from obtaining raw operational data obtained from one or several sources to delivering final information to decision-makers.

One of the HDIPS features as a class of systems is a heterogeneous nature of tasks simultaneously solved in the system. They may require various software and hardware resources, which increases the complexity of the most efficient software and hardware configuration choice. Due to the complexity of the HDIPS, a decision-making process for software and hardware configuration management is associated with a large amount of uncertainty, making decision-making on the design and modernization of the HDIPS software and hardware configuration laborious, and increases error probability. The number of HDIPS software and hardware configuration elements and permissible ways of connecting them into various structures, which perform computational functions, are great.

The more components a HDIPS contains, the higher the complexity of the interaction between them is, therefore special tools are needed to work with such a large amount of information.

Existing approaches are either intended for universal computing systems and do not take into account heterogeneity [3–7], or do not imply the possibility of changing the software and hardware configuration [8–10].

The inter-agency nature of some HDIPSs also complicates the system management. For example, in the event that a HDIPS was formed due to the merger of several departments or divisions, it is difficult to see the system "from above" without special tools, to assess its potential and the way to optimize the combined computing resource use by shifting from independent problem solving "old" subsystems to a shared computing space.

The aim of this work is to formalize the problem of HDIPS software and hardware configuration management. To achieve this goal, formalization of possible optimality criteria of HDIPS software and hardware configuration was carried out, a HDIPS model in terms of queuing theory was proposed, the problem of allocating HDIPS computing resources was formulated as a transport problem by the time criterion with atomic needs, the algorithm for its solution was proposed and its applicability boundaries were determined.

Optimality criteria for HDIPS software and hardware configuration. Software and hardware configuration is a set of functional parts of an information processing system, their software and connections between them, due to the main technical characteristics of these functional parts, as well as the requirements of the tasks to be solved [11].

The problem of HDIPS optimal configuration choice is the choice of such a set of CN P, which provides an acceptable level of the optimality criterion J for solving a set of computational problems E. In this case, the optimality criterion may differ depending on the purpose of a particular HDIPS [12]. Such criteria can be as follows:

1. Minimizing the CN utilization factor average value:

$$J^1 = \min\left(\overline{utilasid}\right).$$

In this case, we can assume that the computational load is evenly distributed and there are no overloaded nodes

2. Minimizing the total time on problem solving in the system

$$J^2 = \min\left(\sum_i^n T\left(e^i\right)\right),$$

where T – time spent on problem solving e^i, n – number of problems, calculated at the time of change. HDIPS can be used in areas where decision-making time is critical, in which case minimizing a problem processing time is more important than uniform load distribution.

3. Minimizing the probability of returning problem with CN due to a lack of computing resources:

$$J^3 = \min\left(\sum_i^n p_{return}^i\right).$$

In case of an incorrect combination of computational load, a number of CNs and algorithms for distributing the computing resource in the HDIPS, situations are possible when the task arrives at the CN, which does not have enough free resources to process it; in this case the task is returned to the routing agent. The likelihood of such returns must be minimized, since they indicate the non-optimal configuration of the HDIPS and increase the time spent on tasks in the computing system.

The choice of the efficiency criterion for the projected computing system is the first step in solving the problem of optimal HDIPS software and hardware configuration choice. To achieve the selected optimality criterion, it is proposed to analyze the HDIPS software and hardware configuration using its formal model, applying the queuing theory methods.

Representation of HDIPS in the form of a queuing network. HDIPS can be represented as a queuing network, where each CN and route control unit is a mass service system (QS). By a queuing network we mean a set of interconnected servicing devices with queues (queuing systems), in which requests pass from one device to another with a certain probability [13]. Each CN is represented as a multichannel QS without a queue, which returns a request for calculating a task to a routing agent if there is not enough computational resource for its execution.

Queues are accumulators for routing agents, while the probability of task transition to a specific CN is determined by the routing algorithm operation. A general scheme of the queuing network HDIPS is shown in fig. 1

The QS scheme of the CN is shown in fig. 2. Unserviced requests can arise in the QS of the CN in the event that upon the request receipt for the CN there is not enough resource to process it.
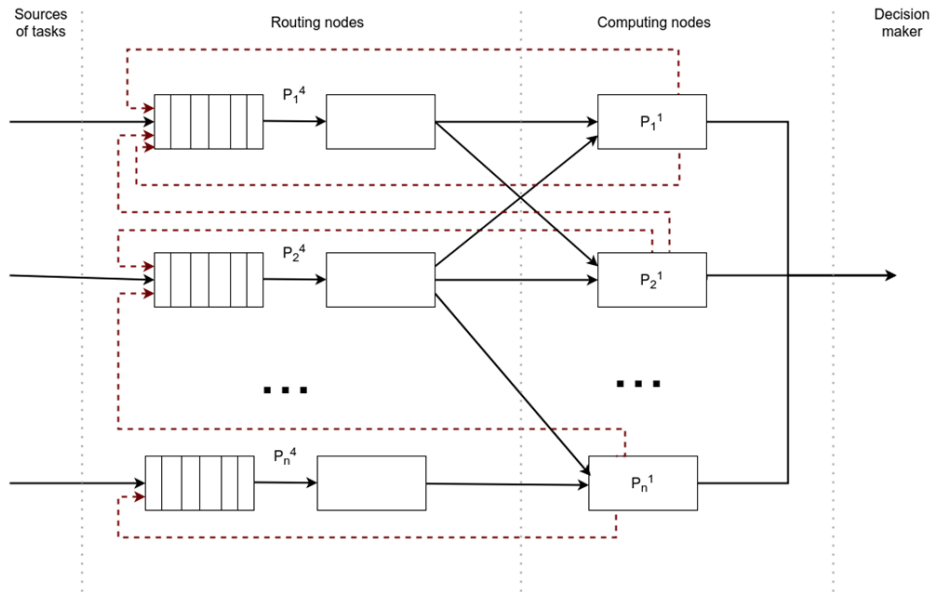
Fig. 1. A general scheme of the queuing network HDIPS

Рис. 1. Общая схема сети массового обслуживания ГРСОИ
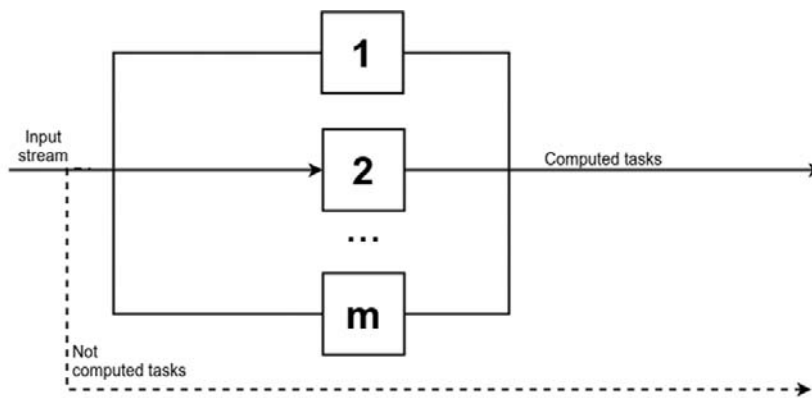
Fig. 2. The scheme of the queuing system computing node

Рис. 2. Схема системы массового обслуживания вычислительного узла

In this case, the probabilities of the task transition from the router p^4_i to the CN p^1_j is defined as the product request probability sending to this node in accordance with the routing algorithm operation and availability of the necessary software coefficient a^i_{task} in the software configuration of the control node a^j_{server}.

$$p_{ij} = p^{routing}_{ij} k_{ij},$$

where

$$k_{ij} = \begin{cases} 1, & \textit{if CN j is provided with required software,} \\ 0, & \textit{if CN j is not provided with required software.} \end{cases}$$

For each task subset requiring the same software set, only a CNs subset will be available that satisfies the condition of suitable software availability.

Thus, for a task from the A^k_{task} set, only a part of the queuing network elements will be available; therefore, it is advisable to calculate the average time spent on tasks in the system using the weighted average time spent in the task system for each type of software from A_{task}, subsets, where the weight will be the probability of the task appearance, requiring A^k_{task}, software in the system. Thus, it is possible to represent the efficiency criterion J^2 using the queuing theory instruments:

$$J^2 = \overline{T} = \frac{1}{\Lambda} \sum_{j=1}^{N} w_i \lambda_j \overline{t_{\Sigma_j}} \ ,$$

where Λ – total intensity of network input streams, $\overline{t_{\Sigma_j}}$ – average time spent by a task in j QS, λ_j – input flow rate j QS, w_i – weight of i task. To achieve the selected optimality criterion, in addition to enumerating different permissible combinations of software and hardware configurations of the system individual elements, it is necessary to determine the optimal algorithm for requests distribution for computations to computational nodes.

Transport task by the time criterion with atomic needs. The function that reflects the total time of data processing

problems at any finite time interval is presented in the form of a transport problem according to the time criterion [14].

There exists m of starting points (SP) A_1, …, A_m with margin a_1, …, a_m and n of destination points (DP) B_1, …, B_m with requests b_1, …, b_m the sum of margins equals the sum of requests:

$$\sum_{i=1}^{m} a_i = \sum_{j=1}^{n} b_j .$$

The times of transportation t_{ij} from each SP A_i to each DP B_j are given, it is assumed that they do not depend on the amount of the transported cargo.

It is required to choose transportation (x_{ij}) in such a way that the balance conditions are met

$$\begin{cases} \sum_{j=0}^{n} x_{ij} = a_i \;\; (i=1,…,m), \\ \sum_{i=0}^{m} x_{ij} = b_j \;\; (j=1,…,m), \end{cases}$$

and in addition, the end time of all transportations T turned at a minimum. Thus, it is necessary to find a transport plan (x_{ij}) for which the time T turns into a minimum:

$$T = \max_{x_{ij}>0} t_{ij} = \min .$$

The described problem can be used to select the optimal route for computing problems at time t^0 as follows. Computing nodes will be software A_1, …, A_m, and their free computing resource at the moment t^0 will be a stock in terms of transport problems. Moreover, each task will be a DP with a certain need for computing resources. This introduces an additional condition for transportation – each DP must be served by single software.

In order to support the heterogeneity of both computational tasks and software and hardware, computational tasks are considered as atomic – that is, indivisible between CNs. If a computation task is not atomic, it must be represented as a set of sequentially (or in parallel, depending on the nature of the task) of atomic applications running.

The condition on the atomicity of tasks introduces into the formulation of the transport problem the above-mentioned restriction that each DP must be serviced by a single software; in what follows, this type of transport problem will be called a transport problem by the time criterion with atomic needs.

The atomicity condition makes it possible not to consider the combination of servicing the DP by several softwares, which significantly reduces the complexity of the solution algorithm in comparison with the classical solution of the transport problem by the time criterion.

The transportation time (in terms of the model, the processing time of the task) t_{ij} is calculated as the sum of the task B_j delivery time forecast to the node A_i, the forecast of the calculation time, and the forecast of the delivery time of the received data to the destination.

If at time t^0 the computational task B_j is being processed at the node A_i, t_{ij} will express the remaining processing time + the time of data delivery to the end point.

For other nodes, the processing time for this task will include the cost of transferring the calculation from the current node to another.

If the CN A_i cannot process the task B_j, for example, does not have the necessary software, then we assume that the processing time t_{ij} is equal to infinity.

Least-time algorithm for atomic claims. The problem of choosing the most efficient computation route at time t^0 can be represented as a transport problem according to time criterion with atomic needs described above. Taking into account the condition that computational tasks are atomic, that is one task can be processed only on one node (in practice, this can be achieved by preliminary partitioning of complex calculations into a sequence of atomic tasks), the solution of a transport problem by the time criterion with atomic needs degenerate. The developed least-time algorithm for atomic claims (LTfAC) for the transport problem according to the time criterion with atomic needs can be represented as a diagram in fig. 3.

The algorithm works as follows. It is necessary to select a pair of DP and software with the smallest t_{ij}, provided that the software has all the necessary resources to service the DP, and then adjust the stock for software by the amount of DP and repeat the selection until all DP are served, or until no software will be able to serve the remaining DP. In this case, tasks for which a suitable computational node is determined are sent for computation, and the remaining tasks wait for the next iteration of the algorithm.

The efficiency of the developed algorithm was investigated on the HDIPS simulation model [15]. Fig. 4 shows a graph of the average computation time of tasks in the HDIPS dependence on its structure when using the LTfAC algorithm as an algorithm for computing resources distribution in HDIPS. For clarity, the axes of CN number and the number of tasks sources on the graph are inverted.

The developed algorithm provides the minimum average time for tasks completion and this time is fairly stable relative to the number of CNs. Thus, the developed algorithm is recommended to be used if the advantage from reducing the time of tasks calculations exceeds the cost of additional HDIPS computational load, thus the J^2 optimality criterion of the configuration is selected.

Conclusion. The following possible criteria for the optimality of the HDIPS software and hardware configuration were identified and formalized:

– minimizing the average value of the CN utilization factor;

– minimizing the total time for problem solving in the system;

– minimizing the probability of problem return with a CN due to a lack of computing resources.

To meet the selected optimality criterion it is proposed to analyze the HDIPS software and hardware configuration using its formal model applying queuing theory methods. HDIPS can be represented as a queuing network, where each CN and route control unit is a mass service system. In terms of the proposed formal model, a function is defined which expresses the probability of a task transition from a router to a computational node. The example of the presentation of the criterion "minimizing

the total time of problem solving in the system" in the formal model using the apparatus of the queuing theory is given.

The problem of computing resource allocation in HDIPS is presented as a transport problem according to the time criterion with atomic needs. The atomicity condi-

tion makes it possible not to consider the combination of serving one destination (in terms of the transport problem) by several starting points, which significantly reduces the complexity of the solution algorithm in comparison with the classical solution of the transport problem by the time criterion.
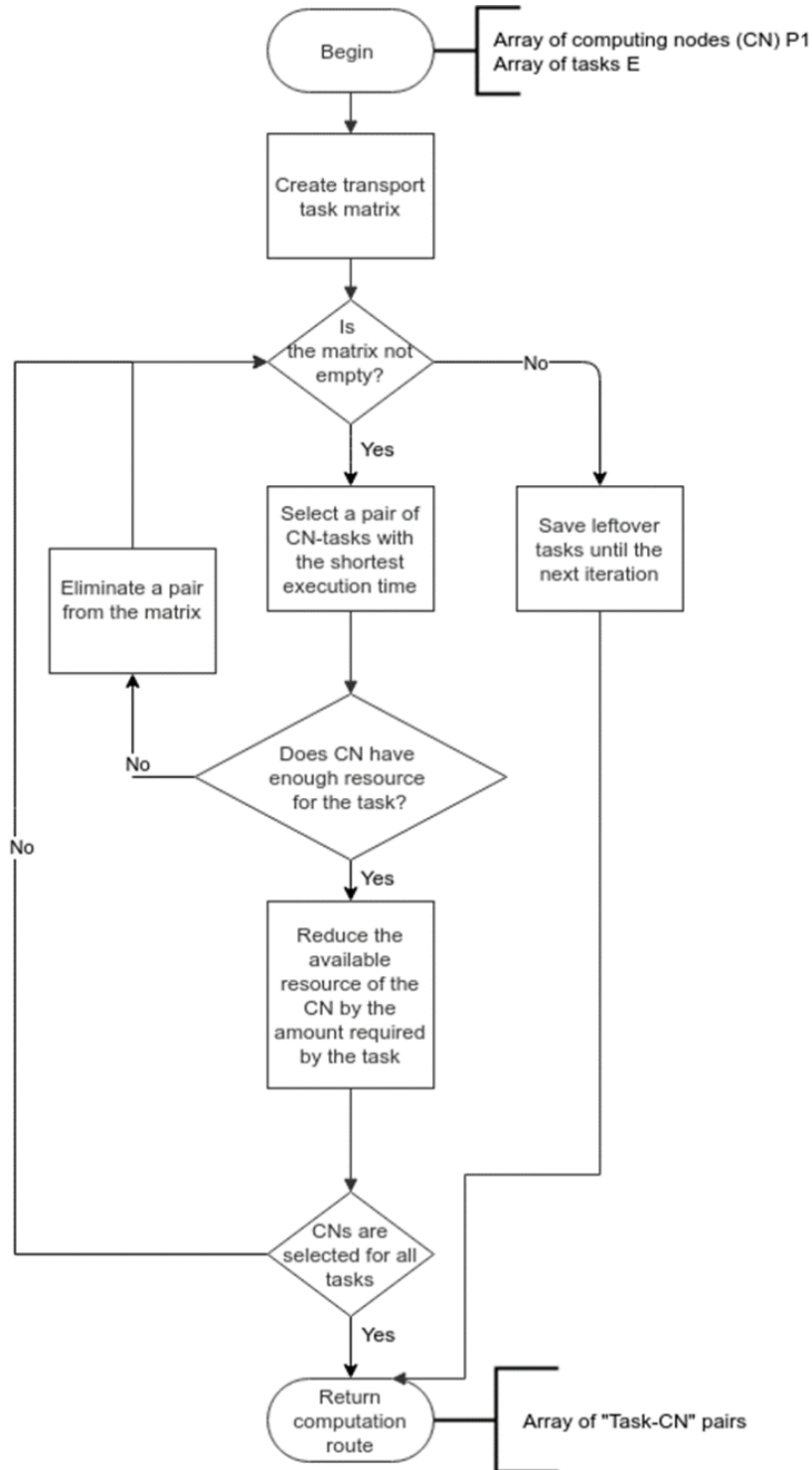
Fig. 3. Block diagram of the resource allocation algorithm via solving a transport problem by the time criterion with atomic needs using the LTfAC method

Рис. 3. Блок-схема алгоритма распределения ресурсов решением транспортной задачи по критерию времени с атомарными потребностями методом НВдАЗ
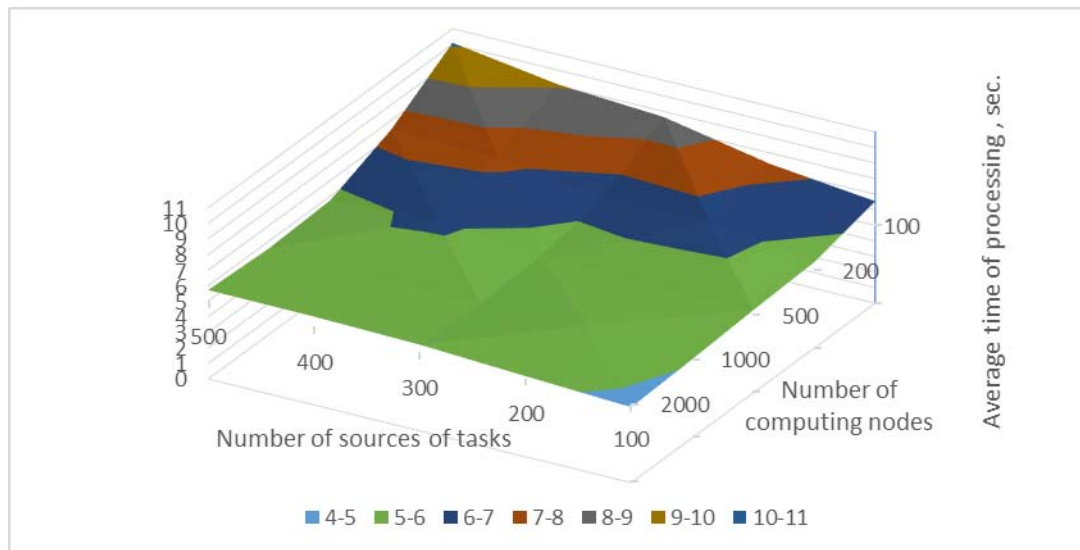
Fig. 4. Time of tasks processing when using the LTfAC algorithm for resource allocation

Рис. 4. Время обработки задач при использовании алгоритма НВдАЗ для распределения ресурсов

Taking into account the condition of atomicity, the least-time algorithm for atomic claims was developed. In comparison with other investigated algorithms, the developed algorithm provides the minimum average time for executing tasks and this time is fairly stable relative to the number of CNs. Thus, the developed algorithm is recommended to be used if the advantage from reducing the time for calculating the tasks exceeds the cost of the additional computational load of the HDIPS, that is, the criterion of optimality of the configuration "minimizing the total time for problem solving in the system" is selected.

References

1. Antamoshkin O. A., Kilochitskaya T. R., Ontuzheva G. A., Stupina A. A., Tynchenko V. S. Multicriterion problem of allocation of resources in the heterogeneous distributed information processing systems. *Journal of Physics: Conference Series*. 2018, Vol. 1015, P. 32162. Doi: 10.1088/1742-6596/1015/3/032162.

2. Antamoshkin O. A. [Multi-agent automation system for monitoring, forecasting and control in emergency situations]. *Mezhdunarodna nauchna shkola "Paradigma"* [Paradigma International Scientific School]. Varna, 2015, P. 18–28 (In Russ.).

3. Glazunov V. V., Kurochkin M. A., Popov S. G. [Method for evaluating message transmission routes in telematic networks of vehicles based on the logical-probabilistic method]. *Intellektual'nye tekhnologii na transporte*, 2015. Vol 1 (In Russ.). Available at: https://cyberleninka.ru/article/n/metod-otsenki-marshrutov-peredachi-soobscheniy-v-telematicheskih-setyah-transpotrnyh-sredstv-na-osnove-logiko-veroyatnostnogo-metoda (accessed: 25.10.2020).

4. Bigham J., Du L. Cooperative negotiation in a multi-agent system for real-time load balancing of a mobile cellular network *ACM*, 2003. P 568–575. Doi: 10.1145/860575.860666.

5. Kantamneni A., Brown L. E., Parker G., Weaver W. W. Survey of multi-agent systems for microgrid control. *Engineering applications of artificial intelligence*. 2015, Vol. 45, P. 192–203. Doi: 10.1016/j.engappai.2015.07.005.

6. Khritankov A. S. [Modeli i algoritmy raspredeleniya nagruzki]. *Informatsionnye tekhnologii i vychislitel'nye sistemy*. 2009, Vol. 2, P. 65–80 (In Russ.).

7. Skobelev P. O. [Intelligent resource management systems in real time: development principles, experience of industrial implementations and development prospects]. *Prilozhenie k teoreticheskomu i prikladnomu nauchno-tekhnicheskomu zhurnalu "Informatsionnye tekhnologii"*. 2013, No. 1, P. 1–32 (In Russ.).

8. Dmitriev V. N., Sorokin A. A., Kuok Ch. T. [Improving the efficiency of traffic management in heterogeneous data transmission systems under conditions of uncertainty]. *Vestnik Astrakhanskogo gosudarstvennogo tekhnicheskogo universiteta. Seriya: Upravlenie, vychislitel'naya tekhnika i informatika*. 2015, No. 3, P. 66–77 (In Russ.).

9. Krutolapov A. S. [Ensuring the quality of service in information exchange networks]. *Vestnik Voronezhskogo instituta GPS MChS Rossii*. 2013, No. 1, P. 18–22 (In Russ.).

10. Kammoun H. M., Kallel I., Casillas J., Abraham A., Alimi A. M. Adapt-Traf: An adaptive multiagent road traffic management system based on hybrid ant-hierarchical fuzzy model. *Transportation Research Part C: Emerging Technologies*. 2014, No. 42, P. 147–167. Doi.org: 10.1016/j.trc.2014.03.003.

11. *GOST 15971–90. Sistemy obrabotki informatsii. Terminy i opredeleniya* [State Standard 15971–90. Information processing systems. Terms and Definitions]. Moscow, Standartinform Publ., 1991, 12 p.

12. Ontuzheva G. A. [Methods for optimizing the distribution of resources of a geographically distributed multi-level computer network]. *Mezhdunarodna nauchna*

shkola "Paradigma" [Paradigma International Scientific School]. Varna, 2015, P. 185–190 (In Russ.).

13. Zhozhikashvili V. A., Vishnevskiy V. M. [Queuing networks: Theory and application to computer networks]. *Seti massovogo obsluzhivaniya: Teoriya i primenenie k setyam EVM*. Moscow, Radio i svyaz' Publ., 1988, 191 p.

14. Hammer P. L. Timeminimizing transportation problems. *Naval Research Logistics Quarterly*. 1969, No. 3 (16), P. 345–357. Doi:10.1002/nav.3800160307.

15. Ontuzheva G. A., Bruchanova E. R., Rudov I. N., Pikov N. O., Antamoshkin O. A. Simulation modelling of the heterogeneous distributed information processing systems. *In IOP Conference Series: Materials Science and Engineering*. 2018, Vol. 450, No. 5, P. 05. Doi: 10.1088/1757-899X/450/5/052018.

Библиографические ссылки

1. Multicriterion problem of allocation of resources in the heterogeneous distributed information processing systems / O. A. Antamoshkin, T. R. Kilochitskaya, G. A. Ontuzhevaet al. // Journal of Physics: Conference Series. 2018. Vol. 1015. P. 32162.

2. Антамошкин О. А. Мультиагентная система автоматизации мониторинга, прогнозирование и управления в чрезвычайных ситуациях // Международная научна школа «Парадигма». Лято-2015, 2015.

3. Глазунов В. В., Курочкин М. А., Попов С. Г. Метод оценки маршрутов передачи сообщений в телематических сетях транспотрных средств на основе логико-вероятностного метода [Электронный ресурс] // Интеллектуальные технологии на транспорте. 2015. № 1. URL: https://cyberleninka.ru/article/n/metod-otsenki-marshrutov-peredachi-soobscheniy-v-telematicheskih-setyah-transpotrnyh-sredstv-na-osnove-logiko-veroyatnostnogo-metoda (дата обращения: 25.10.2020).

4. Bigham J., Du L. Cooperative negotiation in a multi-agent system for real-time load balancing of a mobile cellular network ACM, 2003. P. 568–575.

5. Kantamneni A., Brown L. E., Parker G., Weaver W. W. Survey of multi-agent systems for microgrid control // Engineering applications of artificial intelligence. 2015. Vol. 45. P. 192–203.

6. Хританков А. С. Модели и алгоритмы распределения нагрузки // Информационные технологии и вычислительные системы. 2009. № 2. С. 65–80.

7. Скобелев П. О. Интеллектуальные системы управления ресурсами в реальном времени: принципы разработки, опыт промышленных внедрений и перспективы развития // Приложение к теоретическому и прикладному научно-техническому журналу «Информационные технологии. 2013. № 1. С. 1–32.

8. Повышение эффективности управления трафиком в гетерогенных системах передачи данных в условиях неопределенности / В. Н. Дмитриев, А. А. Сорокин, Ч. Т. Куок и др. // Вестник Астраханского гос. техн. ун-та. Серия: Управление, вычислительная техника и информатика. 2015. № 3. С. 66–77.

9. Крутолапов А. С. Обеспечение качества обслуживания в сетях информационного обмена // Вестник Воронежского ин-та ГПС МЧС России. 2013. № 1. С. 18–22.

10. Adapt-Traf: An adaptive multiagent road traffic management system based on hybrid ant-hierarchical fuzzy model / H. M. Kammoun, I. Kallel, J. Casillas et al. // Transportation Research Part C: Emerging Technologies. 2014. No. 42. P. 147–167.

11. ГОСТ 15971–90. Системы обработки информации. Термины и определения. Взамен ГОСТ 15971–84. Дата введения в действие: 01.01.1992. Статус документа – действующий. Дата издания: 11.01.1991. Дата последнего изменения: 19.04.2010. М. : Изд-во стандартов, 1991. 12 с

12. Онтужева Г. А. Методы оптимизации распределения ресурсов территориально распределенной многоуровневой вычислительной сети // Международная научна школа «Парадигма». Лято-2015, 2015. С. 185–190.

13. Жожикашвили В. А., Вишневский В. М. Сети массового обслуживания: Теория и применение к сетям ЭВМ. М. : Радио и связь, 1988.

14. Hammer P. L. Timeminimizing transportation problems // Naval Research Logistics Quarterly. 1969. № 3 (16). P. 345–357.

15. Simulation modelling of the heterogeneous distributed information processing systems / G. A. Ontuzheva, E. R. Bruchanova, I. N. Rudov et al. // In IOP Conference Series: Materials Science and Engineering. 2018. Vol. 450, No. 5. P. 05.

Ontuzheva Galina Aleksandrovna – Assistant of the Department of Information Technologies in Creative and Cultural Industries; Siberian Federal University. E-mail: gontuzheva@sfu-kras.ru.

Онтужева Галина Александровна – ассистент кафедры информационных технологий в креативных и культурных индустриях; Сибирский федеральный университет. E-mail: gontuzheva@sfu-kras.ru.

COMPOUND BENDING OF AN ORTHOTROPIC PLATE

R. A. Sabirov

Reshetnev Siberian State University of Science and Technology
31, Krasnoyarskii rabochii prospekt, Krasnoyarsk, 660037, Russian Federation
E-mail: rashidsab@mail.ru

The problem of longitudinal-transverse deformation and strength of an orthotropic plate on the action of a local transverse force and stretching along the contour of the membrane forces is studied. The direction of laying the fiber of a unidirectional composite that provides the lowest level of stress and deflection is determined.

In the zone of application of concentrated force in thin-walled structures, significant bending moments and shear forces occur, which are a source of stress concentration. To reduce stresses, the method of plate tension by membrane forces applied along the contour is chosen. The maximum possible order of membrane tension forces is selected, which provides conditions for the strength and rigidity of the solar panel plate structure, which has a hinge-fixed support along the contour. Pre-tensioning the plate web allows to reduce the stress by 50 times.

The problem of compound bending of isotropic and anisotropic plates when applying transverse and selection of longitudinal loads, with restrictions on strength and stiffness, can be called a problem of rational design of the structure. The resulting equations and calculation program can be used in the design of plate structures, as well as in the educational process.

Keywords: plate bending, longitudinal-transverse deformation.

СЛОЖНЫЙ ИЗГИБ ОРТОТРОПНОЙ ПЛАСТИНЫ

Р. А. Сабиров

Сибирский государственный университет науки и технологий имени академика М. Ф. Решетнева
Российская Федерация, 660037, г. Красноярск, просп. им. газ. «Красноярский рабочий», 31
E-mail: rashidsab@mail.ru

Изучается вопрос продольно-поперечного деформирования и прочности ортотропной пластины от воздействия локальной поперечной силы и растягивающих по контуру мембранных сил. Определено направление укладки волокна однонаправленного композита, обеспечивающего наиболее низкий уровень напряжений и прогиба.

В зоне приложения сосредоточенной силы в тонкостенных конструкциях возникают существенные изгибающие моменты и перерезывающие силы, являющиеся источником концентрации напряжений. Для уменьшения напряжений выбран прием натяжения пластины мембранными силами, приложенными по контуру. Подобран максимально возможный порядок мембранных сил натяжения, обеспечивающий условия прочности и жесткости конструкции пластины солнечной батареи, имеющей шарнирно-неподвижное опирание по контуру. Предварительное натяжение полотна пластины позволяет уменьшить напряжения в 50 раз.

Задачу сложного изгиба изотропных и анизотропных пластин при приложении поперечных и подборе продольных нагрузок с ограничениями прочности и жесткости можно назвать задачей рационального проектирования конструкции. Полученные уравнения и программа расчета могут быть использованы как при проектировании конструкций пластин, так и в учебном процессе.

Ключевые слова: изгиб пластины, продольно-поперечное деформирование.

Introduction. Space technology uses rectangular flexible plates with photovoltaic cells attached to its surface. Plates are attached to rigid ribs and pre-stretched using forces in its plane [1; 2].

Composites, often unidirectional, the physical properties of which sometimes differ 15 times, and the strength differ up to 40 times are used [3] as materials. Therefore, the plate material should be considered substantially

orthotropic. The task is to ensure the fulfillment of the required conditions for the rigidity and strength of the plate.

A pre-stretched plate (membrane) is subjected to a transverse load, which is classified under the concept of compound bending [4]. In compound bending, as in simple bending, we can consider the total action on the plate of a number of different transverse loads, equal to the sum of the actions on it of all loads separately, however, if the membrane forces themselves are functions of the transverse load, then the principle of additivity (superposition) does not apply [5].

The transverse loads acting on the plate are distributed over a substantially small surface. When calculating structures, real loads are replaced by idealized forces, dividing them into loads distributed over a large surface, and local loads acting in a small area. When the dimensions of the zone within which the load acts are significantly small compared to the dimensions of the entire surface of the structure, or, for example, when the diameter of the loaded zone is less than the thickness of the plate, the load can be considered as local, applied at one point [6]. In the area of application of a concentrated force in thin-walled structures, significant bending moments and shearing forces arise. These local forces are the source of stress concentration. One of the methods for reducing stresses can be the tension of the plate by membrane forces applied along the contour.

On the theory of compound bending of isotropic plates, the following works can be mentioned [7–9]; a review and analysis of deformation models is given in [10–16].

Work objective. It is required to choose a model for calculating thin plates from an orthogonal anisotropic material; to solve the problem of ensuring the rigidity and strength of a compound bending of an orthotropic plate for optimal orientation of the composite fibers located in a rectangular non-deformable contour, with a simultaneous application of transverse and longitudinal loads.

I. Statement of the problem of deformation of an orthotropic model of compound bending. A differential formulation of the problem of longitudinal-transverse bending of a plate is considered. Geometric nonlinear equations are simplified: they neglect the derivatives of the functions of membrane displacements of the basal surface. The resolving equilibrium equation is compiled according to the deformed scheme.

1. Physical equations. As the governing equations, we use Hooke's law for a body with orthogonal-anisotropic properties, compiled in the Cartesian coordinate system $Oxyz$ [17]

$$\begin{Bmatrix} \varepsilon_{xx} \\ \varepsilon_{yy} \\ \varepsilon_{xy} \end{Bmatrix} = \begin{bmatrix} c_{11} & c_{12} & 0 \\ c_{12} & c_{22} & 0 \\ 0 & 0 & c_{66} \end{bmatrix} \begin{Bmatrix} \sigma_x \\ \sigma_y \\ \tau_{xy} \end{Bmatrix}, \qquad (1)$$

where the components of the strain tensor ε_{xx}, ε_{yy}, ε_{xy} related to the stress tensor components σ_x, σ_y, τ_{xy} compliance coefficients:

$$c_{11} = 1/E_1, \quad c_{22} = 1/E_2, \quad c_{12} = -\nu_{21}/E_2,$$

$$c_{21} = -\nu_{12}/E_1, \ c_{66} = 1/G_{12}, \ (E_1\nu_{21} = E_2\nu_{12}). \quad (2)$$

Here E_1, E_2, ν_{12}, ν_{21}, G_{12} are elastic characteristics of rigidity (technical constants) of an orthotropic material determined for the principal directions of elastic symmetry *1–2*.

The inverse matrix of (1) matrix has the form:

$$\begin{Bmatrix} \sigma_x \\ \sigma_y \\ \tau_{xy} \end{Bmatrix} = \begin{bmatrix} b_{11} & b_{12} & 0 \\ b_{12} & b_{22} & 0 \\ 0 & 0 & b_{66} \end{bmatrix} \begin{Bmatrix} \varepsilon_{xx} \\ \varepsilon_{yy} \\ \varepsilon_{xy} \end{Bmatrix}. \qquad (3)$$

Here,

$$b_{11} = \frac{c_{22}}{c_{11}c_{22} - c_{12}^2}, \qquad b_{12} = b_{21} = -\frac{c_{12}}{c_{11}c_{22} - c_{12}^2},$$

$$b_{22} = \frac{c_{11}}{c_{11}c_{22} - c_{12}^2}, \qquad b_{66} = \frac{1}{c_{66}}. \qquad (4)$$

The coefficients of matrix (3), expressed in terms of technical constants (2), have the form:

$$\begin{Bmatrix} \sigma_x \\ \sigma_y \\ \tau_{xy} \end{Bmatrix} = \begin{bmatrix} \dfrac{E_1}{1-\nu_{12}\nu_{21}} & \dfrac{\nu_{21}E_1}{1-\nu_{12}\nu_{21}} & 0 \\ \dfrac{\nu_{12}E_2}{1-\nu_{12}\nu_{21}} & \dfrac{E_2}{1-\nu_{12}\nu_{21}} & 0 \\ 0 & 0 & G_{12} \end{bmatrix} \begin{Bmatrix} \varepsilon_{xx} \\ \varepsilon_{yy} \\ \varepsilon_{xy} \end{Bmatrix}. \qquad (5)$$

2. Geometric equations (deformations). We apply the geometrically nonlinear Love – Karman – Novozhilov – Papkovich equations [4; 7; 10]:

$$\varepsilon_{xx} = \frac{\partial u_0}{\partial x} + \frac{1}{2}\left(\frac{\partial w}{\partial x}\right)^2 - \frac{\partial^2 w}{\partial x^2}z, \qquad (6)$$

$$\varepsilon_{yy} = \frac{\partial v_0}{\partial y} + \frac{1}{2}\left(\frac{\partial w}{\partial y}\right)^2 - \frac{\partial^2 w}{\partial y^2}z, \qquad (7)$$

$$\varepsilon_{xy} = \frac{\partial u_0}{\partial y} + \frac{\partial v_0}{\partial x} + \frac{\partial w}{\partial x}\frac{\partial w}{\partial y} - 2\frac{\partial^2 w}{\partial x \partial y}z. \qquad (8)$$

In practical plate design, membrane displacements $u_0 = u(x,y)$, $v_0 = v(x,y)$ one to two orders of magnitude less deflections of the middle layer $w = w(x,y)$. Therefore, in equations (6)–(7), we can exclude the derivatives of membrane displacement functions, which gives:

$$\varepsilon_{xx} = \frac{1}{2}\left(\frac{\partial w}{\partial x}\right)^2 - \frac{\partial^2 w}{\partial x^2}z, \qquad (9)$$

$$\varepsilon_{yy} = \frac{1}{2}\left(\frac{\partial w}{\partial y}\right)^2 - \frac{\partial^2 w}{\partial y^2}z, \qquad (10)$$

$$\varepsilon_{xy} = \frac{\partial w}{\partial x}\frac{\partial w}{\partial y} - 2\frac{\partial^2 w}{\partial x \partial y}z. \qquad (11)$$

Equations (9)–(11) can be called quasi-nonlinear, since they contain squares and the product of the first derivatives of the deflection functions.

3. Stress and internal strength factors. Substituting (9)–(11) in (3), we obtain the stress values:

$$\sigma_x(x,y,z) = b_{11}\left[\frac{1}{2}\left(\frac{\partial w}{\partial x}\right)^2 - z\frac{\partial^2 w}{\partial x^2}\right] +$$

$$+ b_{12}\left[\frac{1}{2}\left(\frac{\partial w}{\partial y}\right)^2 - z\frac{\partial^2 w}{\partial y^2}\right], \tag{12}$$

$$\sigma_y(x,y,z) = b_{12}\left[\frac{1}{2}\left(\frac{\partial w}{\partial x}\right)^2 - z\frac{\partial^2 w}{\partial x^2}\right] +$$

$$+ b_{22}\left[\frac{1}{2}\left(\frac{\partial w}{\partial y}\right)^2 - z\frac{\partial^2 w}{\partial y^2}\right], \tag{13}$$

$$\tau_{xy}(x,y,z) = b_{66}\left(\frac{\partial w}{\partial x}\frac{\partial w}{\partial y} - 2\frac{\partial^2 w}{\partial x\partial y}z\right). \tag{14}$$

Integration of stresses (12)–(14) along the plate height h $(-h/2 \le z \le h/2)$ gives a group of internal force factors, membrane forces, bending moments and torque:

$$N_x = \frac{h}{2}\left[b_{11}\left(\frac{\partial w}{\partial x}\right)^2 + b_{12}\left(\frac{\partial w}{\partial y}\right)^2\right], \tag{15}$$

$$N_y = \frac{h}{2}\left[b_{12}\left(\frac{\partial w}{\partial x}\right)^2 + b_{22}\left(\frac{\partial w}{\partial y}\right)^2\right], \tag{16}$$

$$S_{xy} = b_{66}h\frac{\partial w}{\partial x}\frac{\partial w}{\partial y}, \tag{17}$$

$$M_x = -\frac{h^3}{12}\left(b_{11}\frac{\partial^2 w}{\partial x^2} + b_{12}\frac{\partial^2 w}{\partial y^2}\right), \tag{18}$$

$$M_y = -\frac{h^3}{12}\left(b_{12}\frac{\partial^2 w}{\partial x^2} + b_{22}\frac{\partial^2 w}{\partial y^2}\right), \tag{19}$$

$$H_{xy} = -2b_{66}\frac{h^3}{12}\frac{\partial^2 w}{\partial x\partial y}. \tag{20}$$

4. Equilibrium equation. The model of S. P. Timoshenko, in which the equilibrium equation [9] corresponds to the state of compound bending:

$$\frac{\partial^2 M_x}{\partial x^2} + 2\frac{\partial^2 H_{xy}}{\partial x^2} + \frac{\partial^2 M_y}{\partial y^2} =$$

$$= -q_z - N_x\frac{\partial^2 w}{\partial x^2} - N_y\frac{\partial^2 w}{\partial y^2} - 2S_{xy}\frac{\partial^2 w}{\partial x\partial y}. \tag{21}$$

Substituting moments (18)–(20) into (21), we obtain the resolving equation for calculating the orthotropic plate

$$B_{11}\frac{\partial^4 w}{\partial x^4} + B_{12}\frac{\partial^4 w}{\partial x^2\partial y^2} + B_{22}\frac{\partial^4 w}{\partial y^4} =$$

$$= q_z + N_x\frac{\partial^2 w}{\partial x^2} + N_y\frac{\partial^2 w}{\partial y^2} + 2S_{xy}\frac{\partial^2 w}{\partial x\partial y}, \tag{22}$$

in which the stiffness parameters are equal:

$$B_{11} = \frac{b_{11}h^3}{12}, \quad B_{12} = \frac{2b_{12}+4b_{66}}{12}h^3, \quad B_{22} = \frac{b_{22}h^3}{12}. \tag{23}$$

In the right part (22) $N_x = N_x(x,y)$, $N_y = N_y(x,y)$ и $S_{xy} = S_{xy}(x,y)$. At the first step of calculating a compound bend, these forces are assumed to be equal to the pretensioning forces. It can be assumed that if in the numerical analysis of the plate deformation it turns out that the forces calculated by formulas (15)–(17), depending only on the squares of the first derivatives of the deflection functions, will be comparable with the order of the applied membrane tension forces, then the calculation problem should be reformulated and considered as a boundary value problem with variable coefficients.

5. Transition from a continuous problem statement to a discrete (finite-difference) one. Discretization of equations (22) is carried out by the method of grids [18], replacing the differential operators with central differences. Finite-difference analogue of differential equation (22) for a uniform square grid $i = 1,2,...,n$, $j = 1,2,...,m$, with step λ is the following:

$$\left[\frac{6(B_{11}+B_{22})+4B_{12}}{\lambda^4} + \frac{2(N_x+N_y)}{\lambda^2}\right]w_{i,j} -$$

$$-\left(\frac{4B_{11}+2B_{22}}{\lambda^4} + \frac{N_x}{\lambda^2}\right)w_{i,j+1} - \left(\frac{4B_{11}+2B_{22}}{\lambda^4} + \frac{N_x}{\lambda^2}\right)w_{i,j-1} -$$

$$-\left(\frac{4B_{22}+2B_{12}}{\lambda^4} + \frac{N_y}{\lambda^2}\right)w_{i+1,j} - \left(\frac{4B_{22}+2B_{12}}{\lambda^4} + \frac{N_y}{\lambda^2}\right)w_{i-1,j} +$$

$$+\frac{B_{12}}{\lambda^4}w_{i+1,j+1} + \frac{B_{12}}{\lambda^4}w_{i+1,j-1} + \frac{B_{12}}{\lambda^4}w_{i-1,j-1} +$$

$$+\frac{B_{12}}{\lambda^4}w_{i-1,j+1} + \frac{B_{11}}{\lambda^4}w_{i,j+2} + \frac{B_{11}}{\lambda^4}w_{i,j-2} +$$

$$+\frac{B_{11}}{\lambda^4}w_{i+1,j} + \frac{B_{11}}{\lambda^4}w_{i-1,j} = \frac{P_{ij}}{\lambda^2}. \tag{24}$$

6. Internal force factors and stresses of a discrete problem. Internal force factors are calculated by the formulas (15)–(17):

$$N_x^{(i,j)} =$$

$$= \frac{h}{2}\left[b_{11}\left(\frac{w_{i,j+1}-w_{i,j-1}}{2\lambda_x}\right)^2 + b_{12}\left(\frac{w_{i+1,j}-w_{i-1,j}}{2\lambda_y}\right)^2\right], \tag{25}$$

$$N_y^{(i,j)} =$$

$$= \frac{h}{2}\left[b_{12}\left(\frac{w_{i,j+1}-w_{i,j-1}}{2\lambda_x}\right)^2 + b_{22}\left(\frac{w_{i+1,j}-w_{i-1,j}}{2\lambda_y}\right)^2\right], \tag{26}$$

$$S_{xy}^{(i,j)} = b_{66}h\frac{w_{i,j+1}-w_{i,j-1}}{2\lambda_x}\frac{w_{i+1,j}-w_{i-1,j}}{2\lambda_y}, \tag{27}$$

$$M_x^{(i,j)} = -\frac{h^3}{12}\left(b_{11}\frac{w_{i,j+1}-2w_{i,j}+w_{i,j-1}}{\lambda_x^2} +\right.$$

$$\left.+ b_{12}\frac{w_{i+1,j}-2w_{i,j}+w_{i-1,j}}{\lambda_y^2}\right), \tag{28}$$

501

$$M_y^{(i,j)} = -\frac{h^3}{12}\left(b_{12} \frac{w_{i,j+1} - 2w_{i,j} + w_{i,j-1}}{\lambda_x^2} + \right.$$

$$\left. + b_{22} \frac{w_{i+1,j} - 2w_{i,j} + w_{i-1,j}}{\lambda_y^2} \right), \qquad (29)$$

$$H_{xy}^{(i,j)} = -2 b_{66} \left(\frac{h^3}{12} \right) \frac{1}{4\lambda_x \lambda_y} \times$$

$$\times \left(w_{i+1,j+1} - w_{i-1,j+1} + w_{i-1,j-1} + w_{i+1,j-1} \right). \qquad (30)$$

Stresses are calculated at grid points: $\sigma_x^{max} = \pm M_x / h^2$, $\sigma_y^{max} = \pm M_y / h^2$, $\tau_{xy}^{max} = \pm H_{xy} / h^2$.

II. Calculations of the stiffness and strength of an orthotropic plate. The longitudinal-transverse deformation of an anisotropic plate is considered, and the strength is estimated. The level of membrane forces is determined, depending only on the squares of the first derivatives of the deflection functions. The calculations were performed on the basis of our own Maple program [19].

1. Given. Let us consider a plate $(1\,m \times 0.8\,m)$ made of unidirectional carbon fiber reinforced plastic [3] Tornel-300 (Carbon-fiber-reinforced-polymer (CFRP)),

thickness $h = 2$ mm. Strength of the material along the grain $\sigma_1^+ = 1400\,MPa$, across the grain $\sigma_2^+ = 34.5\,MPa$; shear strength $\tau_{12} = 74\,MPa$. Tensile modulus along fibers $E_1 = 142.8\,GPa$; tensile modulus across fibers $E_2 = 9.13\,GPa$; Poisson's ratios: $\nu_{21} = 0.32$, $\nu_{12} = 0.02$. Shear modulus is $G_{12} = 5.49\,GPa$. Maximum deflection boom $w^+ \leq 15\ mm$.

The plate is exposed to concentrated force $P = 1000N$ in the centre. A hinge-fixed support is specified along the contour.

2. Determination of the most favorable orientation of fibers of a unidirectional composite in terms of plate stiffness. Let us investigate the stress-strain state from the action of only a concentrated shear force P.

In fig. 1 let us consider the orientation of the composite in the global coordinate system of the plate (Oxy) and give the strength parameters with the stiffness characteristics in its own principal axes O12. Let's call these parameters and characteristics normative.

Let us show in fig. 2 options for the arrangement of fibers: we orient the composite of unidirectional CFRP with fibers parallel to the long side of the plate (fig. 2, a) and parallel to the short side of the plate (fig. 2, b).
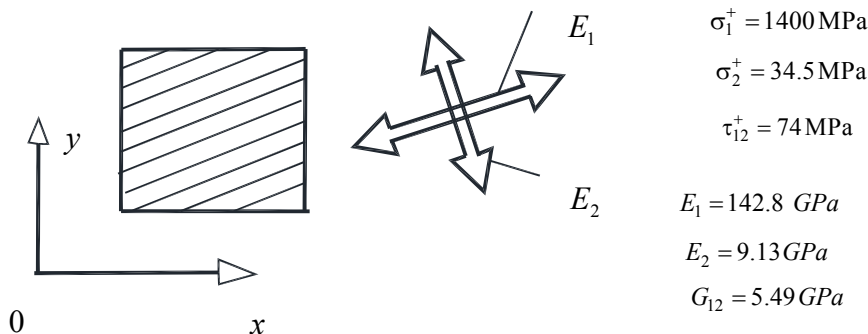
Fig. 1. Composite orientation in the global plate coordinate system (*0xy*)
and strength parameters with stiffness characteristics

Рис. 1. Ориентация композита в глобальной системе координат пластины (*0xy*)
и прочностные параметры с характеристиками жесткости

a   *b*
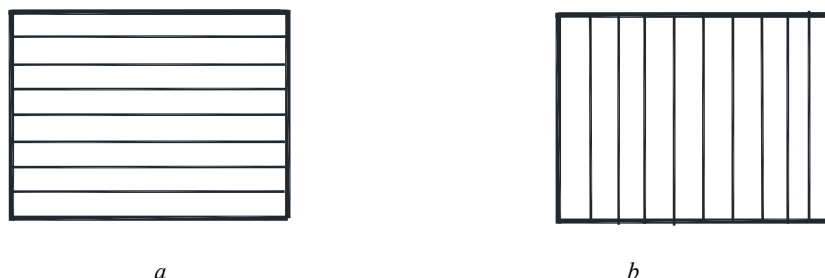
Fig. 2. Plates with two types of composite fiber orientation:
a – carbon fiber is located along the long side of the plate; *b* – carbon fiber is located along
the short side of the plate

Рис. 2. Пластины с двумя видами ориентации волокон композита:
а – волокна углепластика расположены вдоль длинной стороны пластины;
б – волокна углепластика расположены вдоль короткой стороны пластины

Let us write the physical law for the first orientation of the fibers along the long side of the plate (fig. 2, *a*):

$$\begin{Bmatrix} \varepsilon_{xx} \\ \varepsilon_{yy} \\ \varepsilon_{xy} \end{Bmatrix} = \begin{bmatrix} \dfrac{1}{142.8\,GPa} & -\dfrac{0.02}{9.13\,GPa} & 0 \\ -\dfrac{0,32}{142.8\,GPa} & \dfrac{1}{9.13\,GPa} & 0 \\ 0 & 0 & \dfrac{1}{5.49\,GPa} \end{bmatrix} \begin{Bmatrix} \sigma_x \\ \sigma_y \\ \tau_{xy} \end{Bmatrix}$$

and for the second orientation of fibers along the short side of the plate (fig. 2, *б*):

$$\begin{Bmatrix} \varepsilon_{xx} \\ \varepsilon_{yy} \\ \varepsilon_{xy} \end{Bmatrix} = \begin{bmatrix} \dfrac{1}{9.13\,GPa} & -\dfrac{0,32}{142.8\,GPa} & 0 \\ -\dfrac{0,02}{9.13\,GPa} & \dfrac{1}{142.8\,GPa} & 0 \\ 0 & 0 & \dfrac{1}{5.49\,GPa} \end{bmatrix} \begin{Bmatrix} \sigma_x \\ \sigma_y \\ \tau_{xy} \end{Bmatrix}.$$

Let's perform the calculations, the results are shown in fig. 3–7.

The most favorable orientation of the fibers of a unidirectional composite in terms of plate rigidity is the arrangement of the composite fibers along its short side. In this case, the deflections are less by 56 % than when the fibers are arranged along the long side. Normal stresses in both cases are greater than the normative ones, strength is not ensured. Stress regulation is required. Calculations for both fiber arrangements are discussed below.

3. Location of composite fibers along the long side of the plate. The loads $N_x = 10^5\,N/m$ and $N_y = 10^5\,N/m$ are applies. The calculation results are shown in fig. 8. The initial stresses from pre-tension are equal to: $\sigma_x^0 = N_x / h$ и $\sigma_y^0 = N_y / h$.

The results shown in fig. 8, *a* show that under tension $N_x = 10^5\,N/m$ deflection in the center of the plate $w^{max} = 20,8\,mm > w^+$ and stresses across the fibers, equal $\sigma_y^{max} = 130\,MPa > \sigma_2^+$, are above standard.

The results shown in fig. 8, *b* show that under tension $N_y = 10^5\,N/m$ deflection in the center of the plate $w^{max} = 10.05\,mm < w^+$, which satisfies the stiffness condition, and the stresses across the fibers $\sigma_y^{max} = 129.8\,MPa > \sigma_2^+$ remain above standard. Let's increase efforts of N_x and N_y by an order. The calculation results are shown in fig. 9.

When loading the plate with pretension $N_x = 10^6\,N/m$ (fig. 9, *a*), the stress acting across the fibers decreases from 474,6 MPa (at $N_x = 0$) to 31,9 MPa (at $N_x = 10^6\,Н/м$).

The applied force $N_y = 10^6\,N/m$ (fig. 9, *b*) by itself creates a preliminary tension across the fibers significantly more than the standard $\sigma_y^0 = 500\,MPa > \sigma_2^+$. As for the deflection, it is significantly less than the standard and equal to $w^{max} = 1.84\,mm < w^+$.

Let us present the diagrams of deflection and internal force factors for this loading case in fig. 10–14.

4. Location of composite fibers along the short side of the plate. The loads $N_x = 10^5\,N/m$ and $N_y = 10^5\,N/m$ are applied. The calculation results are shown in fig. 13. The initial stresses from pre-tension are equal to: $\sigma_x^0 = N_x / h$ и $\sigma_y^0 = N_y / h$.

The results presented in fig. 13 *a* show that when stretched by force $N_x = 10^5\,N/m$ deflection in the center of the plate $w^{max} = 11,3\,mm < w^+$ turned out to be of the same order of magnitude with the allowable deflection, and the stresses across the fibers, it is $\sigma_x^{max} = 130.9\,MPa > \sigma_2^+$, above the standard.

$P = 1kN$

$w^{max} = 437\,mm > w^+$
$\sigma_x^{max} = 1970\,MPa > \sigma_1^+$
$\sigma_y^{max} = 474,6\,MPa > \sigma_2^+$
$\tau_{xy}^{max} = 405\,MPa > \tau_{12}^+$

а

$P = 1kN$

$w^{max} = 280\,mm > w^+$
$\sigma_x^{max} = 438,9\,MPa > \sigma_2^+$
$\sigma_y^{max} = 1834,5\,MPa > \sigma_1^+$
$\tau_{xy}^{max} = 32,4\,MPa < \tau_{12}^+$

б
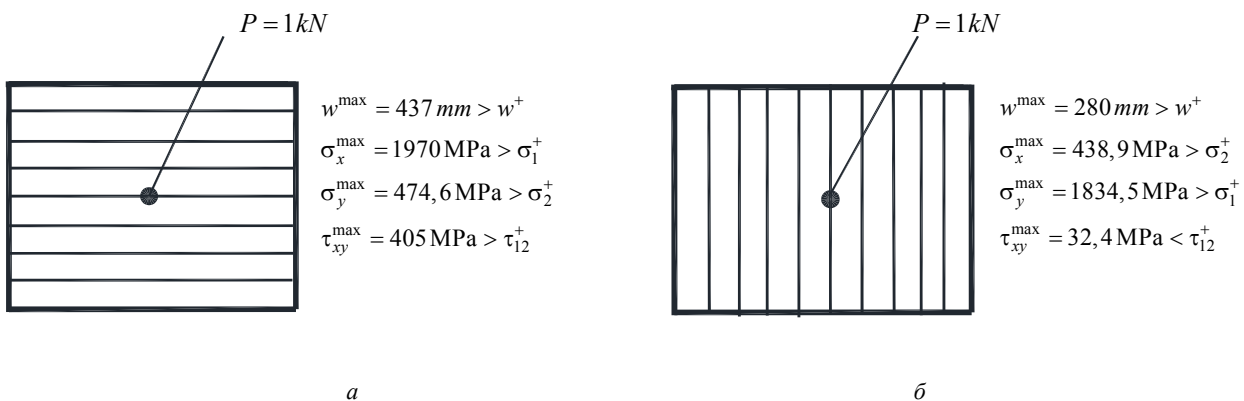
Fig. 3. Comparison of deflections and maximum stresses with standard:
a – fiber CFRP along the long sides of the plate; *b* – CFRP fibers are located along the short sides of the plate

Рис. 3. Сравнение прогибов и максимальных напряжений с нормативными:
а – волокна углепластика расположены вдоль длинной стороны пластины;
б – волокна углепластика расположены вдоль короткой стороны пластины

a

б
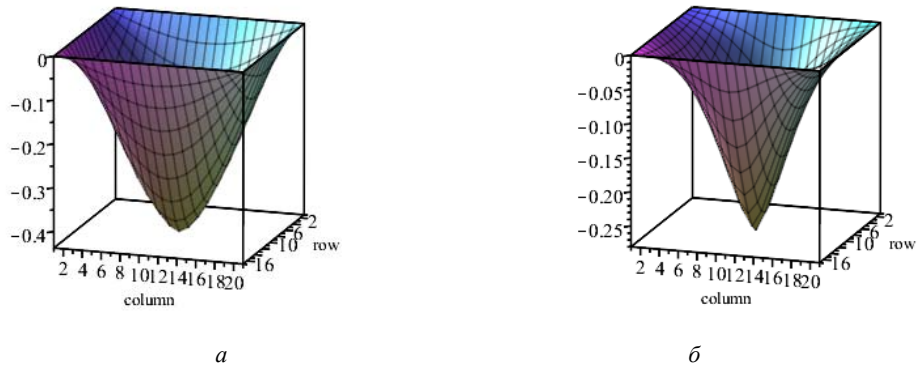
Fig. 4. Comparison plots of deflections:
a – fiber CFRP along the long sides of the plate; *b* – CFRP fibers are located along the short sides of the plate

Рис. 4. Сравнение эпюр прогибов:
a – волокна углепластика расположены вдоль длинной стороны пластины;
б – волокна углепластика расположены вдоль короткой стороны пластины

a

б
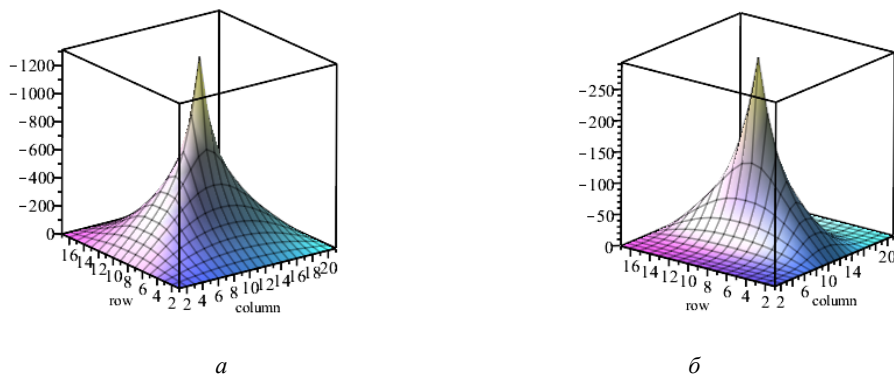
Fig. 5. Comparison of bending moments M_x:
a – CFRP fibers are located along the long side of the plate;
b – CFRP fibers are located along the short side of the plate

Рис. 5. Сравнение изгибающих моментов M_x:
a – волокна углепластика расположены вдоль длинной стороны пластины;
б – волокна углепластика расположены вдоль короткой стороны пластины

a

б
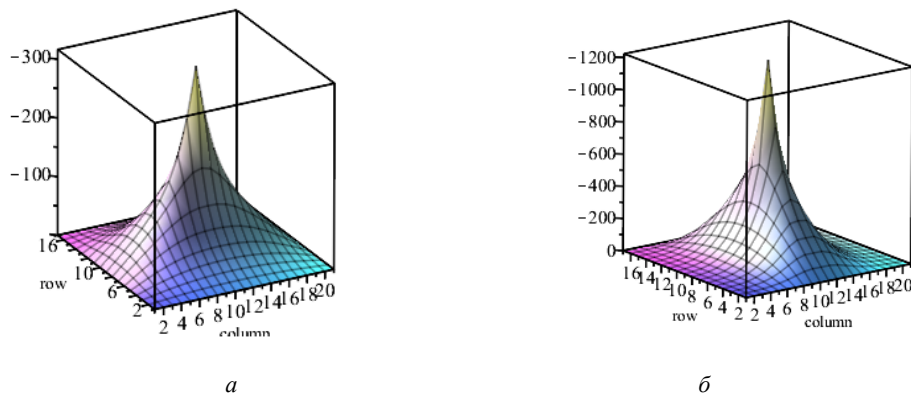
Fig. 6. Comparison of bending moments M_y:
a – CFRP fibers are located along the long side of the plate;
b – CFRP fibers are located along the short sides of the plate

Рис. 6. Сравнение изгибающих моментов M_y:
a – волокна углепластика расположены вдоль длинной стороны пластины;
б – волокна углепластика расположены вдоль короткой стороны пластины

Fig. 7. Comparison of torque H_{xy}:
a – CFRP fibers are located along the long side of the plate;
b – CFRP fibers are located along the short sides of the plate

Рис. 7. Сравнение крутящих моментов H_{xy}:
а – волокна углепластика расположены вдоль длинной стороны пластины;
б – волокна углепластика расположены вдоль короткой стороны пластины

$$w^{\max} = 20.8\,mm > w^+$$
$$\sigma_x^0 = 50\,\text{MPa} < \sigma_1^+$$
$$\sigma_y^0 = 0$$
$$\sigma_x^{\max} = 559\,\text{MPa} < \sigma_1^+$$
$$\sigma_y^{\max} = 130\,\text{MPa} > \sigma_2^+$$
$$\tau_{xy}^{\max} = 5.65\ \text{MPa} < \tau_{12}^+$$

$$w^{\max} = 10.05\,mm < w^+$$
$$\sigma_x^0 = 0$$
$$\sigma_y^0 = 50\,\text{MPa} > \sigma_2^+$$
$$\sigma_x^{\max} = 374.0\,\text{MPa} < \sigma_1^+$$
$$\sigma_y^{\max} = 129.8\ \text{MPa} > \sigma_2^+$$
$$\tau_{xy}^{\max} = 3.8\ \text{MPa} < \tau_{12}^+$$

a *б*

Fig. 8. Calculation results for a plate in which CFRP fibers are located along its long side:
a – pre – stretching by force $N_x = 10^5$ N/m ; *b* – pre-stretching by force $N_y = 10^5$ N/m

Рис. 8. Результаты расчета пластины, в которой волокна углепластика расположены
вдоль ее длинной стороны:
а – предварительное растяжение силой $N_x = 10^5$ Н/м ;

б – предварительное растяжение силой $N_y = 10^5$ Н/м

$$P = 1\,kN$$

$$N_y = 10^6\,\frac{N}{m}$$

$$N_x = 10^6\,\frac{N}{m}$$

$$P = 1\,kN$$

$w^{\max} = 3.72\,mm < w^+$

$\sigma_x^0 = 500\,\text{MPa} < \sigma_1^+$

$\sigma_y^0 = 0$

$\sigma_x^{\max} = 617\,\text{MPa} < \sigma_1^+$

$\sigma_y^{\max} = 31.9\,\text{MPa} < \sigma_2^+ = 34.5\,\text{MPa}$

$\tau_{xy}^{\max} = 0.96\,\text{MPa} < \tau_{12}^+$

$w^{\max} = 1.84\,mm < w^+$

$\sigma_x^0 = 0$

$\sigma_y^0 = 500\,\text{MPa} > \sigma_2^+$

$\sigma_x^{\max} = 121.6\,\text{MPa} < \sigma_1^+$

$\sigma_y^{\max} = 524.0\,\text{MPa} > \sigma_2^+$

$\tau_{xy}^{\max} = 0.76\,\text{MPa} < \tau_{12}^+$

а   *б*
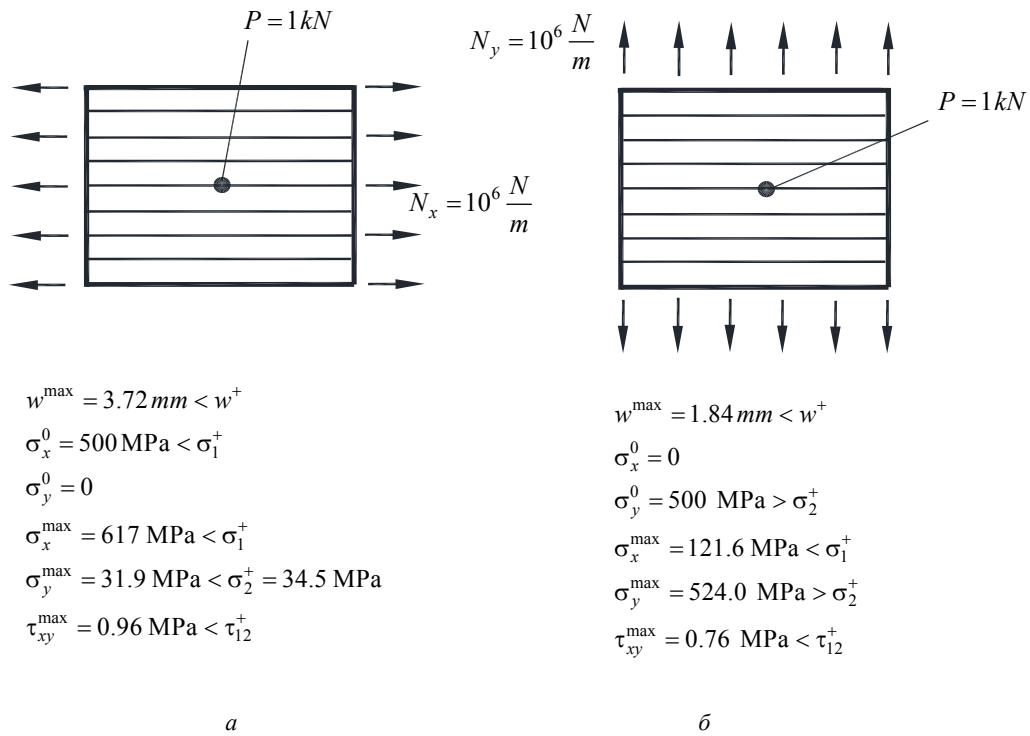
Fig. 9. Results of calculating a plate in which CFRP fibers are located along its long side:
a – pre – stretching by force $N_x = 10^6$ N/m ; b – pre-stretching is applied $N_y = 10^6$ N/m

Рис. 9. Результаты расчета пластины, в которой волокна углепластика расположены
вдоль ее длинной стороны:
a – предварительное растяжение силой $N_x = 10^6$ Н/м ;
$б$ – приложено предварительное растяжение $N_y = 10^6$ Н/м
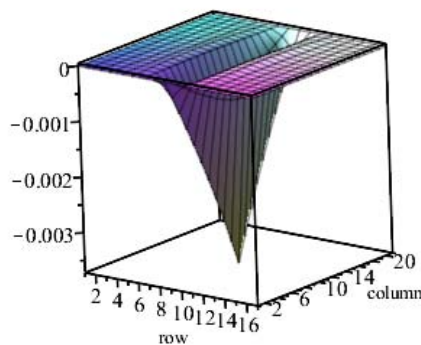
Fig. 10. Diagram of deflections for calculating
a plate in which CFRP fibers are located along
its long side $N_x = 10^6$ N/m and $P = 1\ kN$

Рис. 10. Эпюра прогибов расчета пластины,
в которой волокна углепластика расположены
вдоль ее длинной стороны при $N_x = 10^6$ Н/м
и $P = 1$ кН
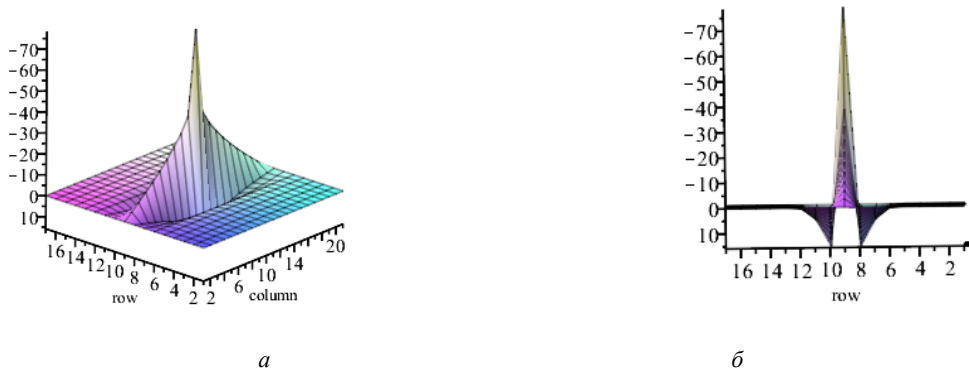
Fig. 11. Diagram of the bending moment M_x of a plate in which CFRP fibers are located along its

long side at $N_x = 10^6$ N/m and $P = 1$ kN :

a – general view of the diagram; b – view of the diagram in the $0yz$ plane

Рис. 11. Эпюра изгибающего момента M_x, в которой волокна углепластика расположены

вдоль длинной стороны при $N_x = 10^6$ Н/м и $P = 1$ кН :

a – общий вид эпюры; $б$ – вид эпюры в плоскости $0yz$

Fig. 12. Diagrams of moments of a plate in which CFRP fibers are located along

its long side at $N_x = 10^6$ N/m and $P = 1$ kN :

a – plot M_x; b – plot H_{xy}

Рис. 12. Эпюры моментов пластины, в которой волокна углепластика

расположены вдоль ее длинной стороны при $N_x = 10^6$ Н/м и $P = 1$ кН :

a – эпюра M_x; $б$ – эпюра H_{xy}

The results shown in fig. 13 b show that under tension $N_y = 10^5 \, N/m$ in the center of the plate deflection $w^{\max} = 18,16 \, mm > w^+ = 15 \, mm$, that does not satisfy the stiffness condition; also the stress across the fibers, equal to $\sigma_x^{\max} = 127,7 \, MPa > \sigma_2^+$, is higher than the standard.

Let's increase forces N_x and N_y to an order of magnitude. The calculation results are shown in fig. 14.

The pre-tension by force $N_x = 10^6 \, N/m$ gives tension across the fibers ($\sigma_x^0 = 500 \, MPa > \sigma_2^+$) more regulatory stress. The combined action of the shear force and the tensile force increased this stress ($\sigma_x^{\max} = 525.4 \, MPa > \sigma_2^+$).

When the plate is loaded (fig. 14, a) with a load acting across the fibers, the stress decreases from 474.6 MPa (at $N_x = 0$) to 31.9 MPa (at $N_x = 10^6 \, N/m$).

Applied effort $N_y = 10^6 \, N/m$ (fig. 14, b) meets all the criteria of rigidity and strength.

Let us present the diagrams of the deflection and internal force factors for this case of loading in fig. 15–17.

Left (a):
$P = 1\ kN$
$N_x = 10^5\ \dfrac{N}{m}$

$w^{\max} = 11.3\ mm < w^{+}$
$\sigma_x^0 = 50\ \text{MPa} > \sigma_2^{+}$
$\sigma_y^0 = 0$
$\sigma_x^{\max} = 130.9\ \text{MPa} > \sigma_2^{+}$
$\sigma_y^{\max} = 378.7\ \text{MPa} < \sigma_1^{+}$
$\tau_{xy}^{\max} = 3{,}77\ \text{MPa} < \tau_{12}^{+}$

a

Right (б):
$N_y = 10^5\ \dfrac{N}{m}$
$P = 1\ kN$

$w^{\max} = 18.16\ mm > w^{+}$
$\sigma_x^0 = 0$
$\sigma_y^0 = 50\ \text{MPa} < \sigma_1^{+}$
$\sigma_x^{\max} = 127.7\ \text{MPa} > \sigma_2^{+}$
$\sigma_y^{\max} = 552.0\ \text{MPa} < \sigma_1^{+}$
$\tau_{xy}^{\max} = 5.874\ \text{MPa} < \tau_{12}^{+}$

б
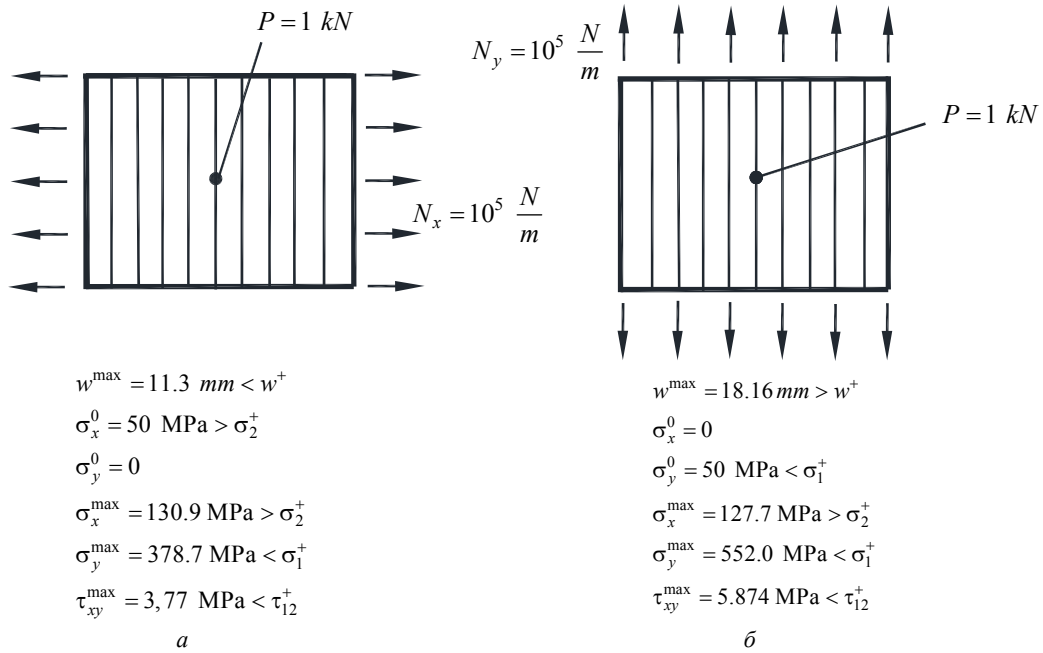
Fig. 13. Results of calculating a plate in which CFRP fibers are located along its short side:
A – pre – stretching is $N_x = 10^5$ N/m ; b – applied pre-stretching is $N_y = 10^5$ N/m

Рис. 13. Результаты расчета пластины, в которой волокна углепластика расположены
вдоль ее короткой стороны:
a – предварительное растяжение $N_x = 10^5$ Н/м ;
б – приложено предварительное растяжение $N_y = 10^5$ Н/м

Left (a):
$P = 1\ kN$
$N_x = 10^6\ \dfrac{N}{m}$

$w^{\max} = 2.08\ mm < w^{+}$
$\sigma_x^0 = 500\ \text{MPa} > \sigma_2^{+}$
$\sigma_y^0 = 0$
$\sigma_x^{\max} = 525.4\ \text{MPa} > \sigma_2^{+}$
$\sigma_y^{\max} = 124.9\ \text{MPa} < \sigma_1^{+}$
$\tau_{xy}^{\max} = 0.75\ \text{MPa} < \tau_{12}^{+}$

a

Right (б):
$N_y = 10^6\ \dfrac{N}{m}$
$P = 1\ kN$

$w^{\max} = 3{,}18\ mm < w^{+}$
$\sigma_x^0 = 0$
$\sigma_y^0 = 500\ \text{MPa} < \sigma_1^{+}$
$\sigma_x^{\max} = 29.86\ \text{MPa} < \sigma_2^{+} = 34.5\ \text{MPa}$
$\sigma_y^{\max} = 611.4\ \text{MPa} < \sigma_1^{+}$
$\tau_{xy}^{\max} = 0.97\ \text{MPa} < \tau_{12}^{+}$

б
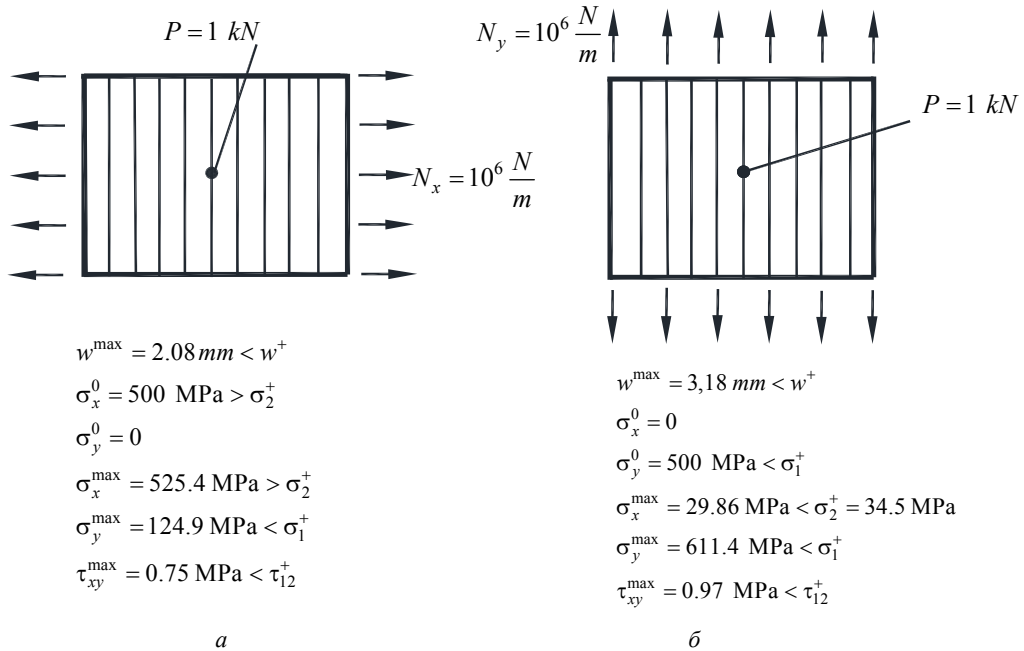
Fig. 14. Results of calculating a plate in which CFRP fibers are located along its short side:
a – applied pre – tension is $N_x = 10^6$ N/m ; *b* – applied pre-tension is $N_y = 10^6$ N/m

Рис. 14. Результаты расчета пластины, в которой волокна углепластика
расположены вдоль ее короткой стороны:
a – приложено предварительное растяжение $N_x = 10^6$ Н/м ;
б – приложено предварительное растяжение $N_y = 10^6$ Н/м
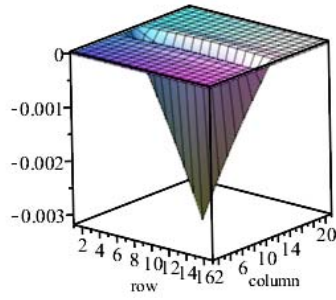
Fig. 15. Diagram of deflections of a plate in which
CFRP fibers are located along its short side
at $N_x = 10^6$ N/m and $P = 1\ kN$

Рис. 15. Эпюра прогибов пластины, в которой
волокна углепластика расположены вдоль
ее короткой стороны при $N_x = 10^6$ Н/м и $P = 1$ кН

а   *б*
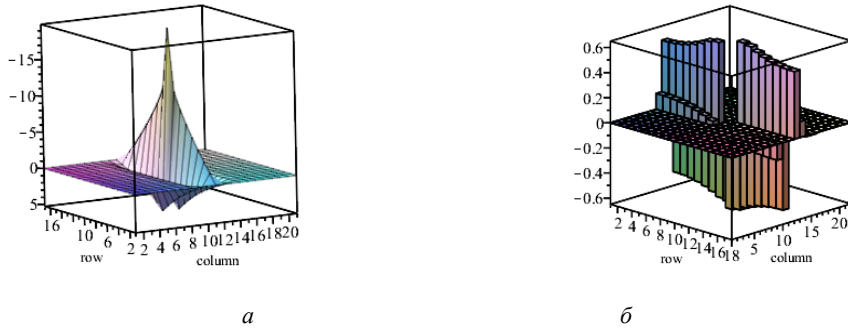
Fig. 16. Diagrams of moments of a plate in which CFRP fibers are located along its
short side of the short side at $N_y = 10^6$ N/m and $P = 1\ kN$:

$$a - M_x\ ;\ b - H_{xy}$$

Рис. 16. Эпюры моментов пластины, в которой волокна углепластика расположены
вдоль ее короткой стороны короткой стороны при $N_y = 10^6$ Н/м и $P = 1$ кН :

$$a - M_x\ ;\ \textit{б} - H_{xy}$$

а   *б*
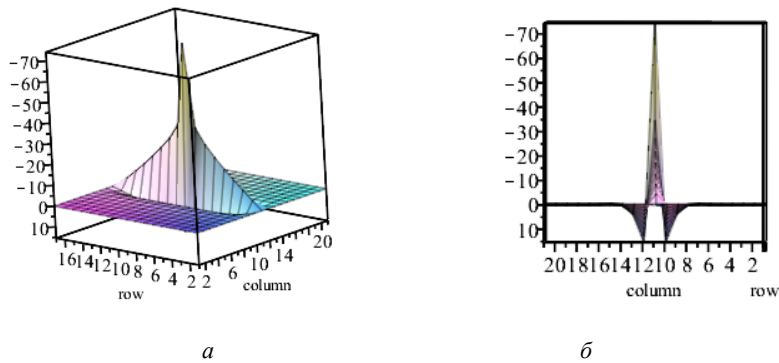
Fig. 17. Diagrams of moments of a plate in which CFRP fibers are located along
its short side at $N_y = 10^6$ N/m at and $P = 1\ kN$:

a – general view; *b* – view in the *0xz* plane

Рис. 17. Эпюры моментов пластины, в которой волокна углепластика расположены
вдоль ее короткой стороны при $N_y = 10^6$ Н/м и $P = 1$ кН :

a – общий вид; *б* – вид в плоскости *0xz*

According to the results of calculations of a plate reinforced along its long and short sides, it was found that, according to the required characteristics of rigidity and strength, both variants of tension by membrane forces are suitable N_x и N_y.

When reinforcing along the long side of the plate, the pretension by force $N_x = 10^6$ N/m reduces the stress acting along the fibers from 1970 MPa to 617 MPa (fig. 3, *a*), and the stress acting across the fibers, equal to 474.6 MPa, is reduced by the preliminary tension to 31.9 MPa (fig. 9, *a*).

For reinforcement on the short side, the pretension by force $N_y = 10^6 N/m$ reduces the stress acting across the fibers from 438 MPa to 29.86 MPa (fig. 3, *b*), and the stress acting along the fibers, equal to 1834.5 MPa, is reduced by the pretensioning to 611.44 MPa (fig. 14 *b*).

5. Simultaneous loading of plates with membrane forces N_x and N_y. In fig. 18 we present the results of calculating a plate in which the fibers of the composite are located along its long side (fig. 18, *a*), and a plate in which the fibers are located along its short side (fig. 18, *b*). In both cases, stretching by membrane forces is performed simultaneously by forces $N_x = 10^5 N/m$ and $N_y = 10^5 N/m$. Both types of loading do not satisfy the strength across the fibers. Let's increase the membrane tensile forces by 10 times (fig. 19).

Diagrams for a plate in which CFRP fibers are located along the short side of the plate are shown in fig. 20.

Both variants of loading the plates, in which the fibers are oriented both along the long and short sides, do not correspond to the strength across the fibers of the composite material. Therefore, it is necessary to select a material with increased strength in the direction of the anisotropy axis 2.

Stretching of a rectangular composite web simultaneously in two directions presents certain technological difficulties; therefore, this option of pretensioning should be abandoned.

$w^{max} = 5.25\,mm < w^+$
$\sigma_x^0 = 50$ MPa $< \sigma_1^+$
$\sigma_y^0 = 50$ MPa $> \sigma_2^+$
$\sigma_x^{max} = 265.4$ MPa $< \sigma_1^+$
$\sigma_y^{max} = 97.43$ MPa $> \sigma_2^+$
$\tau_{xy}^{max} = 2.4$ MPa $< \tau_{12}^+$

a

$w^{max} = 5.25\,mm < w^+$
$\sigma_x^0 = 50$ MPa $> \sigma_2^+$
$\sigma_y^0 = 50$ MPa $< \sigma_1^+$
$\sigma_x^{max} = 97.6$ MPa $> \sigma_2^+$
$\sigma_y^{max} = 265.9$ MPa $< \sigma_1^+$
$\tau_{xy}^{max} = 2.4$ MPa $< \tau_{12}^+$

б
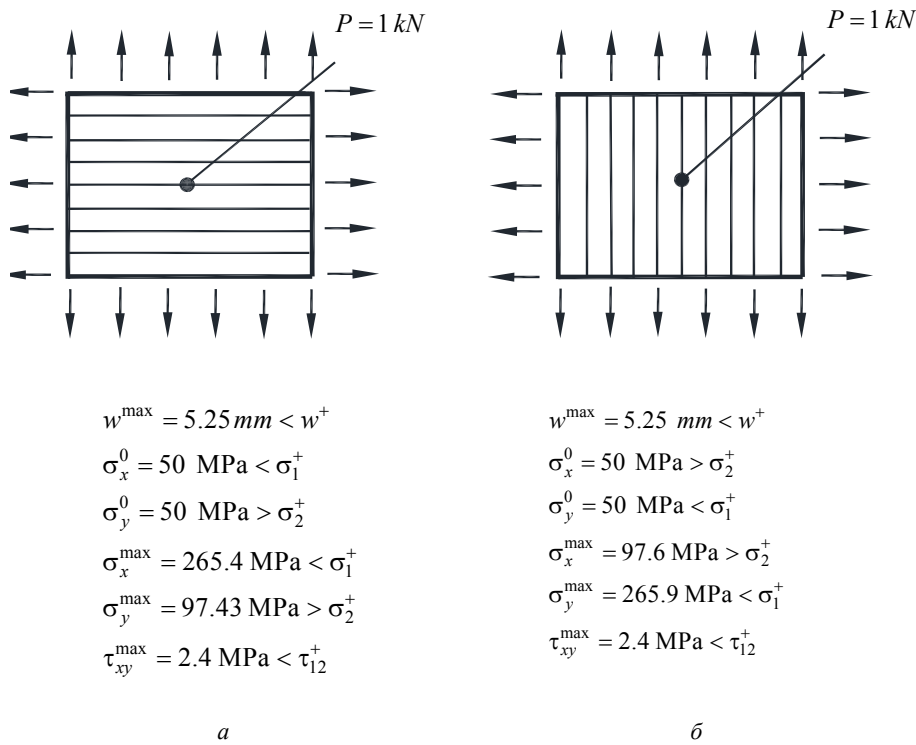
Fig. 18. Comparison of deflections and maximum stresses with standard ones when loads are applied simultaneously $N_x = 10^5$ N/m and $N_y = 10^5$ N/m:

a – CFRP fibers are located along the long side of the plate;
b – carbon fiber fibers are located along the short side of the plate

Рис. 18. Сравнение прогибов и максимальных напряжений с нормативными при одновременном приложении нагрузок $N_x = 10^5$ Н/м и $N_y = 10^5$ Н/м:

а – волокна углепластика расположены вдоль длинной стороны пластины;
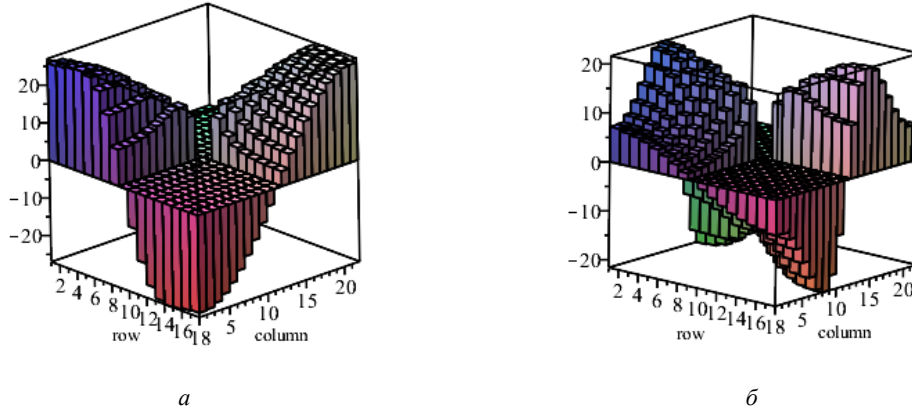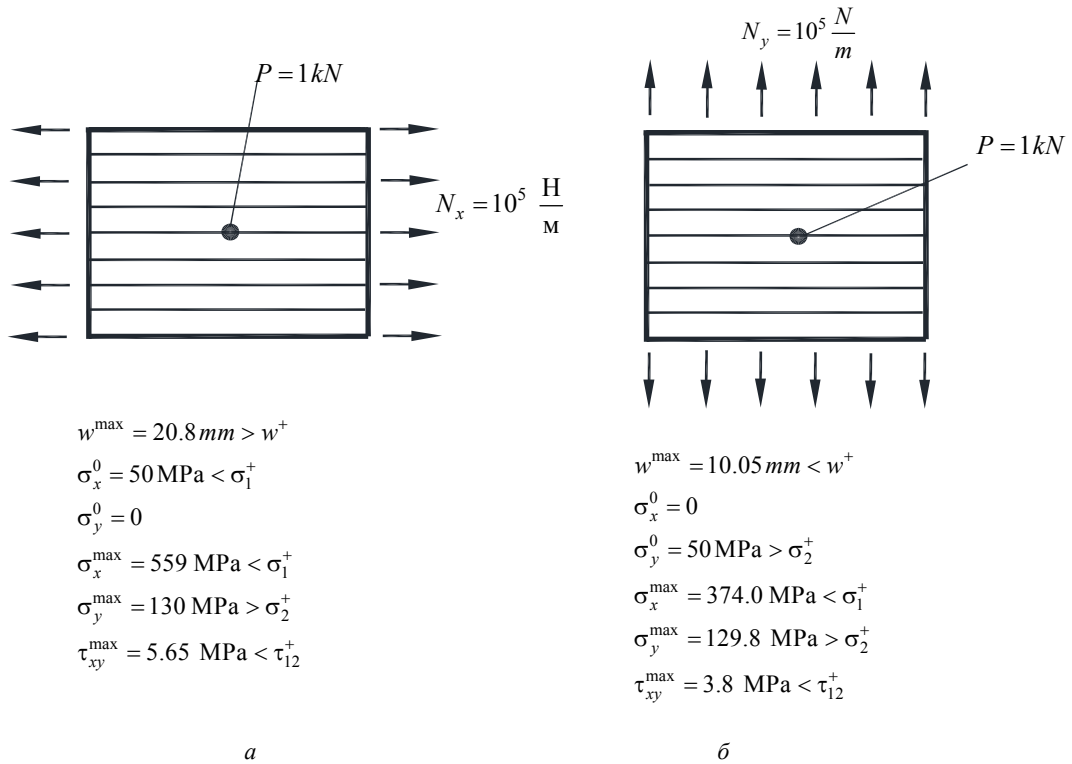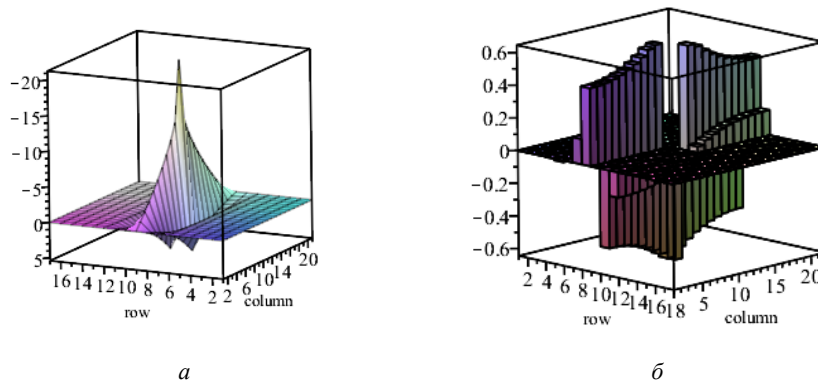*б* – волокна углепластика расположены вдоль короткой стороны пластины

$w^{\max} = 0.60 \ mm < w^+$

$\sigma_x^0 = 500 \ \text{MPa} < \sigma_1^+$

$\sigma_y^0 = 500 \ \text{MPa} > \sigma_2^+$

$\sigma_x^{\max} = 532.4 \ \text{MPa} < \sigma_1^+$

$\sigma_y^{\max} = 506.9 \ \text{MPa} > \sigma_2^+$

$\tau_{xy}^{\max} = 0.38 \ \text{MPa} < \tau_{12}^+$

$w^{\max} = 0.60 \ mm < w^+$

$\sigma_x^0 = 500 \ \text{MPa} > \sigma_2^+$

$\sigma_y^0 = 500 \ \text{MPa} < \sigma_1^+$

$\sigma_x^{\max} = 506.95 \ \text{MPa} > \sigma_2^+$

$\sigma_y^{\max} = 532.1 \ \text{MPa} < \sigma_1^+$

$\tau_{xy}^{\max} = 0.32 \ \text{MPa} < \tau_{12}^+$

а   *б*
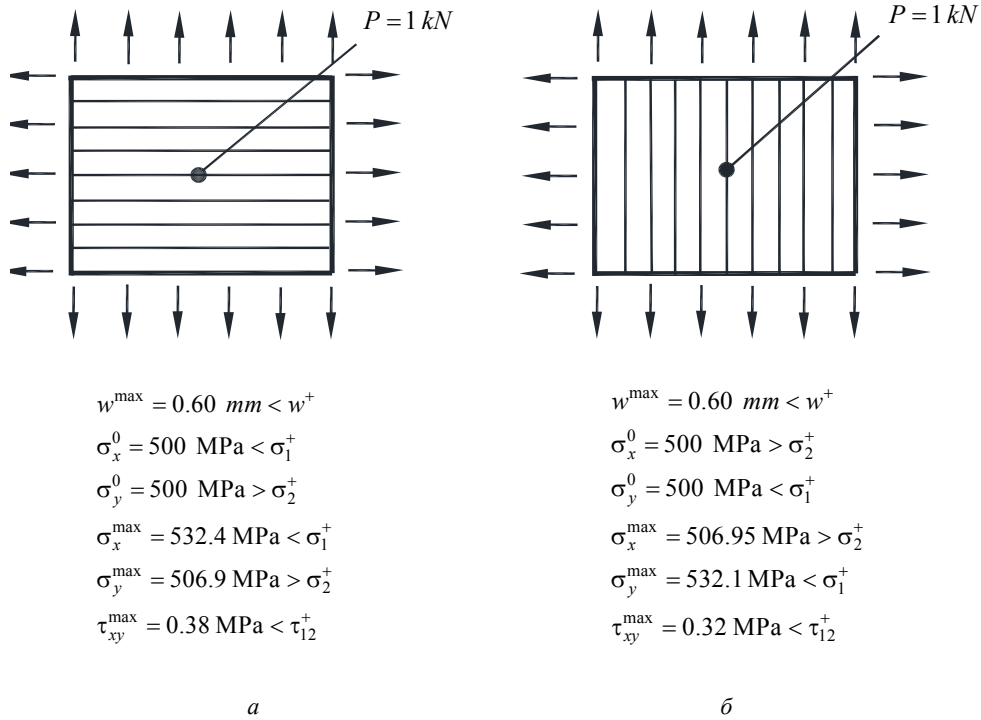
Fig. 19. Comparison of deflections and maximum stresses
with standard ones when loads are applied simultaneously
$N_x = 10^6 \ \text{N/m}$ and $N_y = 10^6 \ \text{N/m}$:

a – CFRP fibers are located along the long side of the plate;
b – CFRP fibers are located along the short side of the plate

Рис. 19. Сравнение прогибов и максимальных напряжений
с нормативными при одновременном приложении нагрузок
$N_x = 10^6 \ \text{Н/м}$ и $N_y = 10^6 \ \text{Н/м}$:

а – волокна углепластика расположены вдоль длинной стороны пластины;
б – волокна углепластика расположены вдоль короткой стороны пластины

a   *б*   *c*
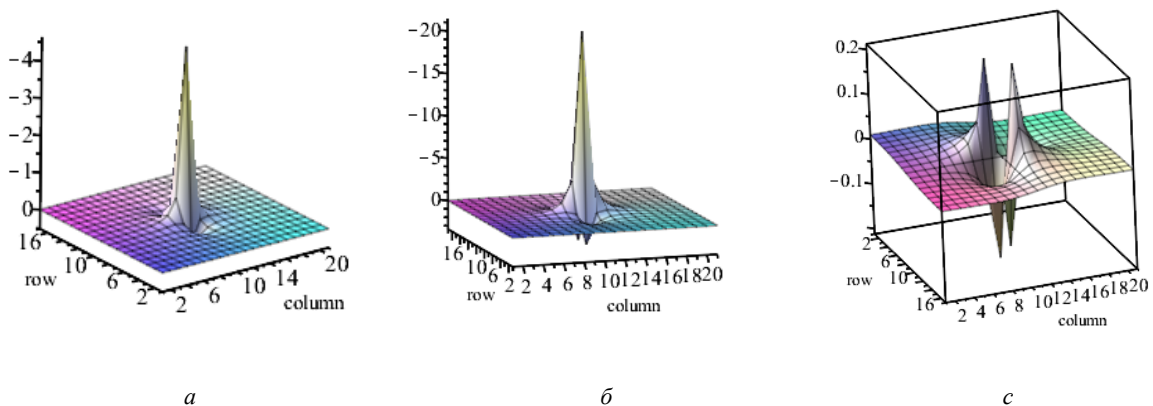
Fig. 20. Results of calculations of a plate in which CFRP fibers are located along the short side:
a – moment M_x; b – moment M_x; c – moment H_{xy}

Рис. 20. Результаты вычислений пластины, в которой волокна углепластика
расположены вдоль короткой стороны:
а – момент M_x; *б* – момент M_x; *с* – момент H_{xy}
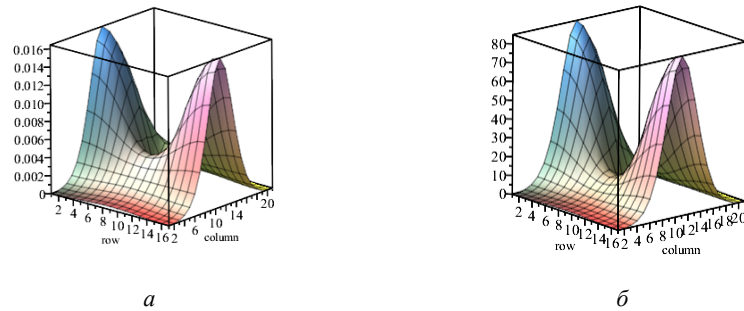
а   *б*

Fig. 21. Diagrams of calculated longitudinal forces

$$N_x = N_x(x, y) \text{ and } N_y = N_y(x, y):$$

a – diagram N_x; b – diagram N_y

Рис. 21. Эпюры вычисляемых продольных сил

$$N_x = N_x(x, y) \text{ и } N_y = N_y(x, y):$$

$а$ – эпюра N_x; $б$ – эпюра N_y

6. A numerical estimate of simplification of geometric equations of the boundary value problem. To estimate the level of efforts (15) and (16), which depend only on the squares of the first derivatives of the deflection functions, we consider the calculation data for an orthotropic plate. Compared with the specified longitudinal forces, the level of which was assigned from 10^5 to 10^6 N/m, which gives stresses of the order of 50 MPa to 500 MPa, the forces calculated by formulas (15) and (16) (fig. 21) give the maximum stresses up to 0.04 MPa. That is, the squares of the first derivatives of the deflection function $(\partial w / \partial x)^2$ and $(\partial w / \partial y)^2$ in (15) and (16) have little effect on the values of longitudinal membrane forces $N_x = N_x(x, y)$ and $N_y = N_y(x, y)$.

Thus, following the calculated results, it makes no sense to complicate the model of the longitudinal-transverse deformation of the plate under preliminary tension by membrane forces and to solve problem (22) with variable coefficients.

Conclusion. The selected deformation model, as *a model of a flexible plate of small deflection* made of an orthogonal anisotropic material, makes it possible to solve the problems of ensuring the rigidity and strength of compound longitudinal-transverse bending of an orthotropic plate.

For a rectangular plate, according to the selected deformation model, in order to ensure a minimum deflection from a concentrated force, it is more advantageous to install fibers of a unidirectional composite along the short side. Stress levels and deflection are reduced.

Significant bending moments arising in the zone of application of a concentrated force are a source of stress concentration. The pre-tension of the plate web allows the stress to be reduced by 50 times.

The problem of compound bending of isotropic and anisotropic plates when applying transverse and selecting longitudinal loads with constraints on strength and stiffness can be called the problem of rational design of a structure. The obtained equations and the calculation program can be used both in the design of plate structures and in the educational process.

References

1. Morozov E. V., Lopatin A. V. Analysis and design of the flexible composite membrane stretched on the spacecraft solar array frame. *Composite Structures.* 2012, No. 94, P. 3106–3114.

2. Lopatin A. V., SHumkova L. V., Gantovnik V. B. *Nelineynaya deformaciya ortotropnoj membrany, rastyanutoj na zhestkoj rame solnechnogo elementa. V: Protokol 49 konferencii AIAA / ASME / ASCE / AHS / ASC, strukturnoj dinamiki i materialov, 16 konferencii AIAA / ASME / AHS po adaptivnym strukturam. 10t, Schaumburg, IL: AIAA-2008-2302* [Nonlinear deformation of an orthotropic membrane stretched on a rigid frame of a solar cell. In: Minutes of the 49th AIAA / ASME / ASCE / AHS / ASC Conference, Structural Dynamics and Materials, 16th AIAA / ASME / AHS Conference on Adaptive Structures. 10t, schaumburg, il: aiaa-2008-2302]. april 7–10, 2008.

3. Vasil'ev V. V., Protasov V. D., Bolotin V. V. et al. *Kompozicionnye materialy: Spravochnik* [Composite materials: handbook]. Moscow, Mashinostroenie Publ., 1990, 512 p.

4. Papkovich P. F. *Stroitel'naya mekhanika korablya. CHast' II. Slozhnyy izgib, ustojchivost' sterzhney i ustojchivost' plastin* [Construction mechanics of the ship. Part II. Complex bending, stability of rods and stability of plates]. Leningrad, Sudpromgiz Publ., 1941, 960 p.

5. Papkovich P. F. *Stroitel'naya mekhanika korablya* [Construction mechanics of the ship]. Vol. 1. Iss. 1. Moscow, Morskoy transport Publ., 1945, 618 p.

6. Lukasevich S. *Lokal'nye nagruzki v plastinah i obolochkah* [Local loads in plates and shells]. Moscow, Mir Publ., 1982, 544 p.

7. Novozhilov V. V. *Osnovy nelinejnoj teorii uprugosti* [Fundamentals of the nonlinear theory of elas-

ticity]. Leningrad – Moscow, OGIZ-Gostekhizdat Publ., 1948, 212 p.

8. Timoshenko S. P. *Ustoychivost' uprugih system* [Stability of elastic systems]. Leningrad – Moscow, OGIZ-Gostekhizdat Publ., 1946, 532 p.

9. Timoshenko S. P., Yung D. *Inzhenernaya mekhanika* [Engineering mechanics]. Moscow, Mashgiz Publ., 1960, 508 p.

10. Lyav A. *Matematicheskaya teoriya uprugosti* [Mathematical theory of elasticity]. Moscow, ONTI Publ., 1935.

11. Vol'mir A. S. *Gibkie plastinki i obolochki* [Flexible plates and shells]. Moscow, Gostekhizdat Publ., 1956, 419 p.

12. Il'yushin A. A., Lenskiy V. S. *Soprotivlenie materialov* [Resistance of materials]. Moscow, Fizmatgiz Publ., 1959, 372 p.

13. Kauderer G. *Nelineynaya mekhanika* [Nonlinear mechanics]. Moscow, Izd-vo inostrannoy literatury Publ., 1961, 778 p.

14. Lejbenzon L. S. *Kurs teorii uprugosti* [Course of the theory of elasticity]. Leningrad – Moscow, OGIZ Publ., 1947, 465 p.

15. Lukash P. A. *Osnovy nelineynoy stroitel'noy mekhaniki* [Fundamentals of nonlinear construction mechanics]. Moscow, Stroyizdat Publ., 1978, 204 p.

16. Novackij V. *Teoriya uprugosti* [Theory of elasticity]. Moscow, Mir Publ., 1975, 872 p.

17. Lekhnickiy S. G. *Teoriya uprugosti anizotropnogo tela* [Theory of elasticity of an anisotropic body]. Moscow, Nauka Publ., 1977, 416 p.

18. Samarskij A. A. *Teoriya raznostnyh skhem* [Theory of difference schemes]. Moscow, Nauka Publ., 1977, 656 p.

19. Govoruhin V., Cybulin V. *Komp'yuter v matematicheskom issledovanii. Uchebnyy kurs* [Computer in mathematical research: training course]. St. Petersburg, Piter Publ., 2001, 624 p.

Библиографические ссылки

1. Morozov E. V., Lopatin A. V. Analysis and design of the flexible composite membrane stretched on the spacecraft solar array frame // Composite Structures. 2012. No. 94. P. 3106–3114.

2. Лопатин А. В., Шумкова Л. В., Гантовник В. Б. Нелинейная деформация ортотропной мембраны, растянутой на жесткой раме солнечного элемента. В: Протокол 49-й конференции AIAA / ASME / ASCE / AHS / ASC, структурной динамики и материалов, 16-й конференции AIAA / ASME / AHS по адаптивным структурам. 10t, Schaumburg, IL: AIAA-2008-2302; 7–10 апреля 2008 г.

3. Композиционные материалы : справочник / В. В. Васильев, В. Д. Протасов, В. В. Болотин и др. М. : Машиностроение, 1990. 512 с.

4. Папкович П. Ф. Строительная механика корабля. Ч. II. Сложный изгиб, устойчивость стержней и устойчивость пластин. Ленинград : СУДПРОМГИЗ, 1941. 960 с.

5. Папкович П. Ф. Строительная механика корабля. Ч. 1. Т. 1. М. : Морской транспорт, 1945. 618 с.

6. Лукасевич С. Локальные нагрузки в пластинах и оболочках. М. : Мир, 1982. 544 с.

7. Новожилов В. В. Основы нелинейной теории упругости. Л.-М. : ОГИЗ-Гостехиздат. 1948. 212 с.

8. Тимошенко С. П. Устойчивость упругих систем. М.-Л. : ОГИЗ-Гостехиздат, 1946. 532 с.

9. Тимошенко С. П., Юнг Д. Инженерная механика. М. : Машгиз, 1960. 508 с.

10. Ляв А. Математическая теория упругости. М. : ОНТИ, 1935.

11. Вольмир А. С. Гибкие пластинки и оболочки. М. : Гостехиздат, 1956. 419 с.

12. Ильюшин А. А., Ленский В. С. Сопротивление материалов. М. : Физматгиз, 1959. 372 с.

13. Каудерер Г. Нелинейная механика. М. : Изд-во иностранной лит-ы, 1961. 778 с.

14. Лейбензон Л. С. Курс теории упругости. М.-Л. : ОГИЗ, 1947. 465 с.

15. Лукаш П. А. Основы нелинейной строительной механики. М. : Стройиздат, 1978. 204 с.

16. Новацкий В. Теория упругости. М. : Мир, 1975. 872 с.

17. Лехницкий С. Г. Теория упругости анизотропного тела. М. : Наука, 1977. 416 с.

18. Самарский А. А. Теория разностных схем. М. : Наука, 1977. 656 с.

19. Говорухин В., Цыбулин В. Компьютер в математическом исследовании : учебный курс. СПб. : Питер, 2001. 624 с.

Rashid Altavovich Sabirov – Ph. D., Associate Professor; Reshetnev Siberian State University of Science and Technology. E-mail: rashidsab@mail.ru.

Сабиров Рашид Альтавович – кандидат технических наук, доцент, доцент кафедры технической механики; Сибирский государственный университет науки и технологий имени академика М. Ф. Решетнева. E-mail: rashidsab@mail.ru.

ON REMOTE SENSING OF THE EARTH BY SPACECRAFT

A. A. Shlepkin[1], T. A. Shiryaeva[2], A. K. Shlepkin[2*], K. A. Filippov[2], O. V. Pashkovskaya[3]

[1] Siberian Federal University
70, Svobodny Av., Krasnoyarsk, 660074, Russian Federation
[2]Krasnoyarsk Sate Agrarian University
90, Mira Av., Krasnoyarsk, 660049, Russian Federation
[3] Reshetnev Siberian State University of Science and Technology
31, Krasnoyarskii rabochii prospekt, Krasnoyarsk, 660037, Russian Federation
*E-mail: ak_kgau@mail.ru

Remote sensing is a process which implies collecting information about an object. Due to their properties, satellite images are widely used in both practical and scientific fields.

Satellite imagery is used in research aimed at the comprehensive study of natural resources, the dynamics of natural phenomena, and in the tasks of environmental protection. Special attention is paid to the use of space information for daily operational monitoring of the state of the environment in the implementation of geo-ecological monitoring of regions. In particular, this poses the problem to find the regions of the earth's surface with the characteristics determined by the considered parameters using the values of established parameters at certain points of the earth's surface. In this paper, we consider the special case of this problem when the given four points of the earth's surface determine the regions of the earth's surface (the so-called kernels of generalized squares) that have a specified configuration (square).

Keywords: spacecraft, remote sensing, generalized square.

О ДИСТАНЦИОННОМ ЗОНДИРОВАНИИ ЗЕМЛИ КОСМИЧЕСКИМИ АППАРАТАМИ

А. А. Шлепкин[1], Т. А. Ширяева[2], А. К. Шлепкин[2*], К. А. Филиппов[2], О. В. Пашковская[3]

[1]Сибирский федеральный университет
Российская Федерация, 660074, г. Красноярск, просп. Свободный, 70
[2]Красноярский государственный аграрный университет
Российская Федерация, 660049, г. Красноярск, просп. Мира, 90
[3]Сибирский государственный университет науки и технологий имени академика М. Ф. Решетнева
Российская Федерация, 660037, г. Красноярск, просп. им. газ. «Красноярский рабочий», 31
*E-mail: ak_kgau@mail.ru

Дистанционное зондирование представляет собой процесс, посредством которого собирается информация об объекте. Благодаря своим свойствам космические снимки находят широкое применение как в практической, так и в научной сферах.

Космическую съемку применяют в исследованиях, направленных на всестороннее изучение природных ресурсов, динамики природных явлений, в задачах охраны окружающей среды. Особое место отводится применению космической информации для повседневного оперативного контроля за состоянием окружающей среды при осуществлении геоэкологического мониторинга регионов. В частности, возникает задача по значению заданных параметров в определенных точках земной поверхности найти области земной поверхности с характеристиками, определяемыми рассматриваемыми параметрами. В настоящей работе рассмотрен частный случай данной задачи, когда по заданным четырем точкам земной поверхности определяются области земной поверхности (так называемые ядра обобщенных квадратов), имеющие заданную конфигурацию (квадрат).

Ключевые слова: космический аппарат, дистанционное зондирование, обобщенный квадрат.

Introduction. Remote sensing of a territory is a process which implies collecting information about a territory without direct contact with it [1–6]. In connection with the widespread reduction of the programmes for aerial photography of the earth's surface, satellite imagery of the earth's surface is acquiring special interest. Due to their properties, space images are widely used in both practical and scientific fields [7; 9–11]. Materials of Earth research from space are widely used in Earth sciences. Space imagery is used in research aimed at the comprehensive study of natural resources, the dynamics of natural phenomena, in the tasks of environmental protection. Diverse and widespread use of remote sensing data is especially found in cartography, they serve as sources for the compilation and operational updating of general geographic and thematic maps [8]. Special attention is paid to the use of space information for current operational control over the state of the environment during geoecological monitoring of regions. The main advantages of using remote sensing data for mapping are the following: relevance of data at the time of research, high accuracy in determining the boundaries of objects [12–15]. In particular, this poses the problem in the value of the given parameters at certain points of the earth's surface to find areas of the earth's surface with characteristics determined by the parameters under consideration. In this paper, we consider the special case of this problem when the given four points of the earth's surface determine the regions of the earth's surface (the so-called kernels of generalized squares) that have a specified configuration (square).

Statement of problems, definitions, designations. Mathematical model of the problem. Let a Cartesian coordinate system be given on the plane and $A = A(x_A; y_A)$, $B = B(x_B; y_B)$, $C = C(x_C; y_C)$, $D = D(x_D; y_D)$ are four different points on the plane, L_A, L_B, L_C, L_D are straight lines passing through the points A, B, C, D respectively. Let us denote by V_{AC} the point of intersection of the straight lines L_A and L_C, V_{AD} – the point of intersection of the straight lines L_A and L_D, V_{BC} – the point of intersection of the straight lines L_B and L_C, V_{BD} – the point of intersection of the straight lines L_B and L_D, $|V_{AD}; V_{BD}|$ – the distance between the points V_{AD} and V_{BD}, $|V_{BC}; V_{BD}|$ – the distance between the points V_{BC} and V_{BD}.

The generalized square is a set of lines $K_{ABCD} = \{L_A, L_B, L_C, L_D\}$ with the property that L_A is parallel to L_B, L_C is parallel L_D, L_A is perpendicular to L_C, and $|V_{AD}; V_{BD}| = |V_{BC}; V_{BD}|$. The generalized square kernel is a square with the set of vertices $\{V_{AD}, V_{BD}, V_{BC}, V_{AC}\}$ (fig. 1).

Question 1. Does the generalized square $K_{ABCD} = \{L_A, L_B, L_C, L_D\}$ always exist at the random selection of the points $A = A(x_A; y_A)$, $B = B(x_B; y_B)$, $C = C(x_C; y_C)$, $D = D(x_D; y_D)$?

Question 2. If question 1 is answered negatively, what are the necessary and sufficient conditions for its positive solution?

Question 3. If for the set of the points $A = A(x_A; y_A)$, $B = B(x_B; y_B)$, $C = C(x_C; y_C)$, $D = D(x_D; y_D)$ the generalized square $K_{ABCD} = \{L_A, L_B, L_C, L_D\}$ exists, how many such generalized squares are there?
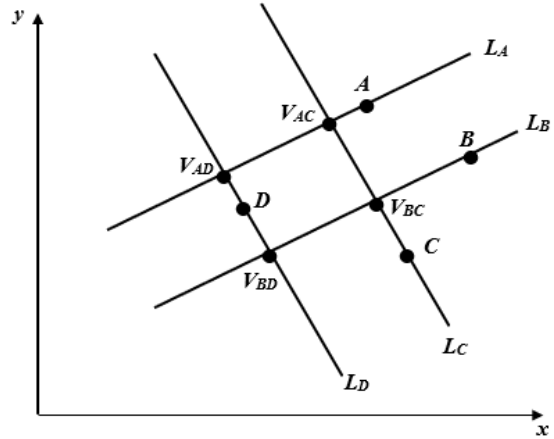
Fig. 1. Generalized square

Рис. 1. Обобщенный квадрат

Partial solution to question 2 and full solution to question 3. In accordance with the above notations, $A = A(x_A; y_A)$, $B = B(x_B; y_B)$, $C = C(x_C; y_C)$, $D = D(x_D; y_D)$ are four different points on the plane, L_A, L_B, L_C, L_D – straight lines that pass through the points A, B, C, D respectively. Let us write the equations of these sides according to [16]:

– $L_A : y = kx + b_A$ – equation of the straight line passing through the point $A = A(x_A; y_A)$,

– $L_B : y = kx + b_B$ – equation of the straight line passing through the point $B = B(x_B; y_B)$,

– $L_C : y = -\frac{1}{k}x + b_C$ – equation of the straight line passing through the point $C = C(x_C; y_C)$,

– $L_D : y = -\frac{1}{k}x + b_D$ – equation of the straight line passing through the point $D = D(x_D; y_D)$.

According to the notation introduced above, we write down the set of equations for finding the points $V_{AC}, V_{BC}, V_{BD}, V_{BC}$ and distances $|V_{AD}; V_{BD}|$, $|V_{BC}; V_{BD}|$.

$$V_{AC} : \begin{cases} y = kx + b_A, \\ y = \dfrac{-1}{k}x + b_C, \end{cases}$$

where $b_A = y_A - kx_A, b_C = y_C + \frac{1}{k}x_C$.

$$V_{AC}:\begin{cases} y=kx+\left(y_A-kx_A\right), \\ y=-\dfrac{1}{k}x+\left(y_C+\dfrac{1}{k}x_C\right), \end{cases}$$

$$V_{AC}=\begin{cases} x=\dfrac{k^2x_A+k\left(y_C-y_A\right)+x_C}{1+k^2}, \\ y=\dfrac{k^2y_C+k\left(x_C-x_A\right)+y_A}{1+k^2}; \end{cases}$$

$$V_{BC}:\begin{cases} y=kx+b_B, \\ y=-\dfrac{1}{k}x+b_C, \end{cases}$$

$$V_{BC}=\begin{cases} x=\dfrac{k^2x_B+k\left(y_C-y_B\right)+x_C}{1+k^2}, \\ y=\dfrac{k^2y_C+k\left(x_C-x_B\right)+y_B}{1+k^2}; \end{cases}$$

$$V_{AD}:\begin{cases} y=kx+b_A, \\ y=-\dfrac{1}{k}x+b_D, \end{cases}$$

$$V_{AD}=\begin{cases} x=\dfrac{k^2x_A+k\left(y_D-y_A\right)+x_D}{1+k^2}, \\ y=\dfrac{k^2y_D+k\left(x_D-x_A\right)+y_A}{1+k^2}; \end{cases}$$

$$V_{BD}:\begin{cases} y=kx+b_B, \\ y=-\dfrac{1}{k}x+b_D, \end{cases}$$

$$V_{BD}=\begin{cases} x=\dfrac{k^2x_B+k\left(y_D-y_B\right)+x_D}{1+k^2}, \\ y=\dfrac{k^2y_D+k\left(x_D-x_B\right)+y_B}{1+k^2}; \end{cases}$$

$$\left|V_{AD};V_{BD}\right|=\left[\left(k^2\left(x_A-x_B\right)+k\left(y_B-y_A\right)\right)^2+\right.$$

$$\left.+\left(k\left(x_B-x_A\right)+\left(y_A-y_B\right)\right)^2\right]^{\frac{1}{2}}\cdot\dfrac{1}{1+k^2},$$

$$\left|V_{BC};V_{BD}\right|=\left[\left(k^2\left(y_C-y_D\right)+k\left(x_C-x_D\right)\right)^2+\right.$$

$$\left.+\left(k\left(y_C-y_D\right)+\left(x_C-x_D\right)\right)^2\right]^{\frac{1}{2}}\cdot\dfrac{1}{1+k^2}.$$

Since the sides of the square are equal, we search for k from the condition $\left|V_{AD};V_{BD}\right|=\left|V_{BC};V_{BD}\right|$:

$$\left[\left(k^2\left(x_A-x_B\right)+k\left(y_B-y_A\right)\right)^2+\right.$$

$$\left.+\left(k\left(x_B-x_A\right)+\left(y_A-y_B\right)\right)^2\right]^{\frac{1}{2}}=$$

$$\left[\left(k^2\left(y_C-y_D\right)+k\left(x_C-x_D\right)\right)^2+\right.$$

$$\left.+\left(k\left(y_C-y_D\right)+\left(x_C-x_D\right)\right)^2\right]^{\frac{1}{2}}.$$

Squaring both sides of the above equation, we obtain:

$$k^4\left(x_A-x_B\right)^2+2k^3\left(x_A-x_B\right)\left(y_B-y_A\right)+k^2\left(y_B-y_A\right)^2+$$

$$+k^2\left(x_B-x_A\right)^2+2k\left(x_B-x_A\right)\left(y_A-y_B\right)+\left(y_A-y_B\right)^2=$$

$$=k^4\left(y_C-y_D\right)^2+2k^3\left(y_C-y_D\right)\left(x_C-x_D\right)+$$

$$+k^2\left(x_C-x_D\right)^2+k^2\left(y_C-y_D\right)^2+$$

$$+2k\left(y_C-y_D\right)\left(x_C-x_D\right)+\left(x_C-x_D\right)^2.$$

After reducing the similar terms with respect to k, we obtain the biquadratic equation:

$$k^4\left[\left(x_A-x_B\right)^2-\left(y_C-y_D\right)^2\right]+$$

$$k^3\left[2\left(x_A-x_B\right)\left(y_B-y_A\right)-2\left(y_C-y_D\right)\left(x_C-x_D\right)\right]+$$

$$k^2\left[\left(y_B-y_A\right)^2+\left(x_B-x_A\right)^2-\left(x_C-x_D\right)^2-\left(y_C-y_D\right)^2\right]+$$

$$k\left[2\left(x_B-x_A\right)\left(y_A-y_B\right)-2\left(y_C-y_D\right)\left(x_C-x_D\right)\right]+$$

$$\left[\left(y_A-y_B\right)^2-\left(x_C-x_D\right)^2\right]=0.$$

Dividing both sides of this equation by the coefficient at k^4, we obtain the following equation:

$$k^4+k^3\left[\dfrac{2\left(x_A-x_B\right)\left(y_B-y_A\right)-2\left(y_C-y_D\right)\left(x_C-x_D\right)}{\left(x_A-x_B\right)^2-\left(y_C-y_D\right)^2}\right]+$$

$$k^2\left[\dfrac{\left(y_B-y_A\right)^2+\left(x_B-x_A\right)^2-\left(x_C-x_D\right)^2-\left(y_C-y_D\right)^2}{\left(x_A-x_B\right)^2-\left(y_C-y_D\right)^2}\right]+$$

$$k\left[\dfrac{2\left(x_B-x_A\right)\left(y_A-y_B\right)-2\left(y_C-y_D\right)\left(x_C-x_D\right)}{\left(x_A-x_B\right)^2-\left(y_C-y_D\right)^2}\right]+$$

$$+\left[\dfrac{\left(y_A-y_B\right)^2-\left(x_C-x_D\right)^2}{\left(x_A-x_B\right)^2-\left(y_C-y_D\right)^2}\right]=0.$$

This yields the partial solution to question 2 and the full solution to question 3.

Partial solution to question 2 (sufficient condition for the existence of a generalized square). To make the equation have a real root, it is sufficient to satisfy the inequality:

$$\dfrac{\left[\left(y_A-y_B\right)^2-\left(x_C-x_D\right)^2\right]}{\left[\left(x_A-x_B\right)^2-\left(y_C-y_D\right)^2\right]}\le 0.$$

Solution to question 3. According to [17], this equation has no more than 4 different real roots. Since with the considered situation we can consider a certain case L_A is parallel to L_C and a certain case L_A is parallel to L_D, then the total number of generalized squares for a fixed set of points $A=A\left(x_A;y_A\right)$, $B=B\left(x_B;y_B\right)$, $C=C\left(x_C;y_C\right)$, $D=D\left(x_D;y_D\right)$ is no more than 12. It is obvious that the estimate is accurate.

Case Study. As our example we take the following: $A(x_A; y_A) = (5;6)$, $B(x_B; y_B) = (7;5)$, $C(x_C; y_C) = (4;3)$, $D(x_D; y_D) = (3;4)$ and we consider three different situations.

1. L_A is parallel to L_B

After substituting the coordinates of the given points into the formula (8), we obtain the equation

$$3k^4 + 6k^3 + 3k^2 + 6k = 0.$$

We find the roots of this equation: $k_1 = 0$, $k_2 = -2$, $k_3 = i$, $k_4 = -i$, $where \, i^2 = -1$.

We calculate the coordinates of the vertices of the generalized square for the root $k = k_1 = 0$ using the formulae:

$$V_{AC} = \begin{cases} x = \dfrac{k^2 x_A + k(y_C - y_A) + x_C}{1 + k^2}, \\ y = \dfrac{k^2 y_C + k(x_C - x_A) + y_A}{1 + k^2}, \end{cases}$$

$V_{AC}(x_C; y_A) = V_{AC}(4;6)$,

$$V_{BC} = \begin{cases} x = \dfrac{k^2 x_B + k(y_C - y_B) + x_C}{1 + k^2}, \\ y = \dfrac{k^2 y_C + k(x_C - x_B) + y_B}{1 + k^2}, \end{cases}$$

$V_{BC}(x_C; y_B) = V_{BC}(4;5)$,

$$V_{AD} = \begin{cases} x = \dfrac{k^2 x_A + k(y_D - y_A) + x_D}{1 + k^2}, \\ y = \dfrac{k^2 y_D + k(x_D - x_A) + y_A}{1 + k^2}, \end{cases}$$

$V_{AD}(x_D; y_A) = V_{AD}(3;6)$,

$$V_{BD} = \begin{cases} x = \dfrac{k^2 x_B + k(y_D - y_B) + x_D}{1 + k^2}, \\ y = \dfrac{k^2 y_D + k(x_D - x_B) + y_B}{1 + k^2}, \end{cases}$$

$V_{BD}(x_D; y_B) = V_{BD}(3;5)$.

Direct calculation shows that

$$\left| V_{AC}; V_{BC} \right| = \left| V_{BC}; V_{BD} \right| = \left| V_{BD}; V_{AD} \right| = \left| V_{AD}; V_{AC} \right| = 1.$$

It follows that the quadrangle with the vertices $V_{AD}, V_{BD}, V_{BC}, V_{AC}$ is a square (fig. 2).

We calculate the coordinates of the vertices of the generalized square for the root $k = k_2 = -2$ using the formulae:

$$V_{AC} = \begin{cases} x = \dfrac{k^2 x_A + k(y_C - y_A) + x_C}{1 + k^2} = \\ = \dfrac{(-2)^2 \, 5 + (-2)(3-6) + 4}{1 + (-2)^2} = \dfrac{30}{5}, \\ y = \dfrac{k^2 y_C + k(x_C - x_A) + y_A}{1 + k^2} = \\ = \dfrac{(-2)^2 \, 3 + (-2)(4-5) + 6}{1 + (-2)^2} = \dfrac{20}{5}, \end{cases} \quad V_{AC}(6;4);$$

$$V_{BC} = \begin{cases} x = \dfrac{k^2 x_B + k(y_C - y_B) + x_C}{1 + k^2} = \\ = \dfrac{(-2)^2 \, 7 + (-2)(3-5) + 4}{1 + (-2)^2} = \dfrac{36}{5}, \\ y = \dfrac{k^2 y_C + k(x_C - x_B) + y_B}{1 + k^2} = \\ = \dfrac{(-2)^2 \, 3 + (-2)(4-7) + 5}{1 + (-2)^2} = \dfrac{23}{5}, \end{cases} \quad V_{BC}(7.2;4.6);$$

$$V_{AD} = \begin{cases} x = \dfrac{k^2 x_A + k(y_D - y_A) + x_D}{1 + k^2} = \\ = \dfrac{(-2)^2 \, 5 + (-2)(4-6) + 3}{1 + (-2)^2} = \dfrac{27}{5}, \\ y = \dfrac{k^2 y_D + k(x_D - x_A) + y_A}{1 + k^2} = \\ = \dfrac{(-2)^2 \, 4 + (-2)(3-5) + 6}{1 + (-2)^2} = \dfrac{26}{5}, \end{cases} \quad V_{AD}(5.4;5.2);$$

$$V_{BD} = \begin{cases} x = \dfrac{k^2 x_B + k(y_D - y_B) + x_D}{1 + k^2} = \\ = \dfrac{(-2)^2 \, 7 + (-2)(4-5) + 3}{1 + (-2)^2} = \dfrac{33}{5}, \\ y = \dfrac{k^2 y_D + k(x_D - x_B) + y_B}{1 + k^2} = \\ = \dfrac{(-2)^2 \, 4 + (-2)(3-7) + 5}{1 + (-2)^2} = \dfrac{29}{5}, \end{cases} \quad V_{BD}(6.6;5.8).$$
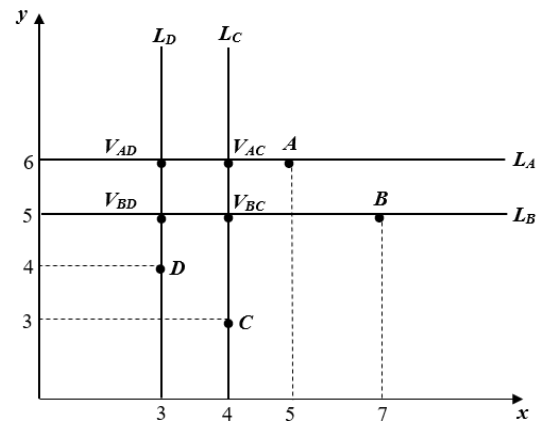
Fig. 2. Generalized square for the root $k_1 = 0$

Рис. 2. Обобщенный квадрат для корня $k_1 = 0$

Direct calculation shows that

$$0 \left| V_{AD}; V_{BD} \right| = \left| V_{BD}; V_{BC} \right| = \left| V_{BC}; V_{AC} \right| = \left| V_{AC}; V_{AD} \right| = \dfrac{3}{\sqrt{5}}.$$

It follows that the quadrangle with the vertices $V_{AD}, V_{BD}, V_{BC}, V_{AC}$ is a square (fig. 3).

Fig. 3. Generalized square for the root $k_2 = -2$

Рис. 3. Обобщенный квадрат для корня $k_2 = -2$

2. The straight line L_A is parallel to the straight line L_C

The general equations of required sides in this case are the following:

$L_A : y = kx + b_A$ – equation of the straight line passing through the point $A(x_A; y_A)$;

$L_B : y = -\dfrac{1}{k}x + b_B$ – equation of the straight line passing through the point $B(x_B; y_B)$;

$L_C : y = kx + b_C$ – equation of the straight line passing through the point $C(x_C; y_C)$;

$L_D : y = -\dfrac{1}{k}x + b_D$ – equation of the straight line passing through the point $D(x_D; y_D)$.

Let us write down the set of equations for finding the vertices of the square in this case:

$$V_{AB} : \begin{cases} y = kx + b_A, \\ y = \dfrac{-1}{k}x + b_B, \end{cases}$$

where $b_A = y_A - kx_A, b_B = y_B + \dfrac{1}{k}x_B$;

$$V_{AB} : \begin{cases} y = kx + (y_A - kx_A), \\ y = -\dfrac{1}{k}x + \left(y_B + \dfrac{1}{k}x_B\right), \end{cases}$$

$$V_{AB} = \begin{cases} x = \dfrac{k^2 x_A + k(y_B - y_A) + x_B}{1 + k^2}, \\ y = \dfrac{k^2 y_B + k(x_B - x_A) + y_A}{1 + k^2}. \end{cases}$$

$$V_{BC} : \begin{cases} y = kx + b_C, \\ y = -\dfrac{1}{k}x + b_B, \end{cases}$$

$$V_{BC} = \begin{cases} x = \dfrac{k^2 x_C + k(y_B - y_C) + x_B}{1 + k^2}, \\ y = \dfrac{k^2 y_B + k(x_B - x_C) + y_C}{1 + k^2}. \end{cases}$$

$$V_{AD} : \begin{cases} y = kx + b_A, \\ y = -\dfrac{1}{k}x + b_D, \end{cases}$$

$$V_{AD} = \begin{cases} x = \dfrac{k^2 x_A + k(y_D - y_A) + x_D}{1 + k^2}, \\ y = \dfrac{k^2 y_D + k(x_D - x_A) + y_A}{1 + k^2}. \end{cases}$$

$$V_{CD} : \begin{cases} y = kx + b_C, \\ y = -\dfrac{1}{k}x + b_D, \end{cases}$$

$$V_{CD} = \begin{cases} x = \dfrac{k^2 x_C + k(y_D - y_C) + x_D}{1 + k^2}, \\ y = \dfrac{k^2 y_D + k(x_D - x_C) + y_D}{1 + k^2}. \end{cases}$$

After substituting the coordinates of the points into the formula, we obtain the equation

$$2k^3 + k^2 + 2k + 1 = 0.$$

We find the roots of this equation $k_1 = -\dfrac{1}{2}, k_2 = -i, k_3 = i$, where $i^2 = -1$. We calculate the coordinates of the vertices of the generalized square for a real root $k = k_1 = -\dfrac{1}{2}$ according to the formulae presented above.

$$V_{AB} = \begin{cases} x = \dfrac{k^2 x_A + k(y_B - y_A) + x_B}{1 + k^2} = \\ = \dfrac{\left(-\dfrac{1}{2}\right)^2 5 - \dfrac{1}{2}(5 - 6) + 7}{1 + \left(-\dfrac{1}{2}\right)^2} = 7, \\ y = \dfrac{k^2 y_B + k(x_B - x_A) + y_A}{1 + k^2} = \\ = \dfrac{\left(-\dfrac{1}{2}\right)^2 5 - \dfrac{1}{2}(7 - 5) + 6}{1 + \left(-\dfrac{1}{2}\right)^2} = 5, \end{cases} \qquad V_{AB}(7;5).$$

$$V_{BC} = \begin{cases} x = \dfrac{k^2 x_C + k(y_B - y_C) + x_B}{1 + k^2} = \\ = \dfrac{\left(-\dfrac{1}{2}\right)^2 4 - \dfrac{1}{2}(5 - 3) + 7}{1 + \left(-\dfrac{1}{2}\right)^2} = \dfrac{28}{5}, \\ y = \dfrac{k^2 y_B + k(x_B - x_C) + y_C}{1 + k^2} = \\ = \dfrac{\left(-\dfrac{1}{2}\right)^2 5 - \dfrac{1}{2}(7 - 4) + 3}{1 + \left(-\dfrac{1}{2}\right)^2} = \dfrac{11}{5}, \end{cases} \qquad V_{BC}(5.6; 2.2).$$

$$V_{AD} = \begin{cases} x = \dfrac{k^2 x_A + k\left(y_D - y_A\right) + x_D}{1+k^2} = \\ \quad = \dfrac{\left(-\dfrac{1}{2}\right)^2 5 - \dfrac{1}{2}(4-6) + 3}{1 + \left(-\dfrac{1}{2}\right)^2} = \dfrac{21}{5}, \\ y = \dfrac{k^2 y_D + k\left(x_D - x_A\right) + y_A}{1+k^2} = \\ \quad = \dfrac{\left(-\dfrac{1}{2}\right)^2 4 - \dfrac{1}{2}(3-5) + 6}{1 + \left(-\dfrac{1}{2}\right)^2} = \dfrac{32}{5}, \end{cases} \qquad V_{AD}\,(4.2;6.4).$$

$$V_{CD} = \begin{cases} x = \dfrac{k^2 x_C + k\left(y_D - y_C\right) + x_D}{1+k^2} = \\ \quad = \dfrac{\left(-\dfrac{1}{2}\right)^2 4 - \dfrac{1}{2}(4-3) + 3}{1 + \left(-\dfrac{1}{2}\right)^2} = \dfrac{14}{5}; \\ y = \dfrac{k^2 y_D + k\left(x_D - x_C\right) + y_D}{1+k^2} = \\ \quad = \dfrac{\left(-\dfrac{1}{2}\right)^2 4 - \dfrac{1}{2}(3-4) + 3}{1 + \left(-\dfrac{1}{2}\right)^2} = \dfrac{18}{5}; \end{cases} \qquad V_{CD}\,(2.8;3.6).$$

Direct calculation shows that

$$\left|V_{AB};V_{BC}\right| = \left|V_{BC};V_{DC}\right| = \left|V_{AD};V_{DC}\right| = \left|V_{AD};V_{AB}\right| = \frac{7}{\sqrt{5}}.$$

Consequently, the quadrangle with the vertices $V_{AB}, V_{DC}, V_{BC}, V_{AD}$ is a square (fig. 4).
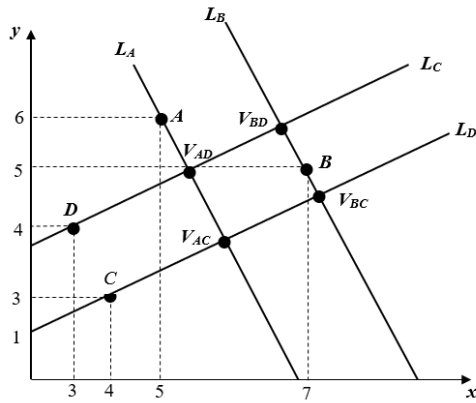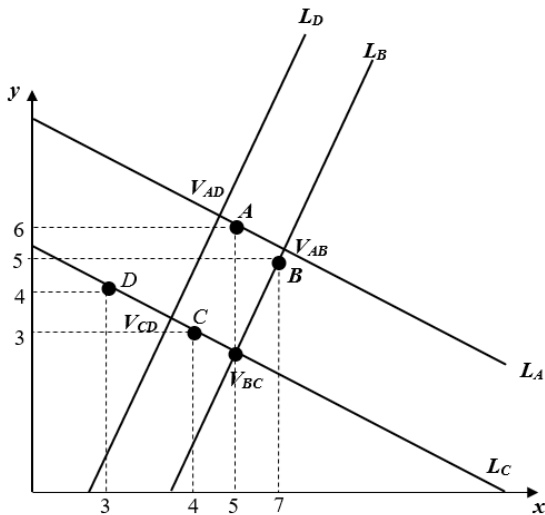

Fig. 4. Generalized square for the root $k = -1/2$

Рис. 4. Обобщенный квадрат для корня $k = -1/2$

3. The straight line L_A is parallel to the straight line L_D

Let us write down the general equations of required sides in case when the straight line L_A is parallel to the straight line L_D, in this instance:

$L_A : y = kx + b_A$ – equation of the straight line passing through the point $A(x_A; y_A)$;

$L_B : y = -\dfrac{1}{k}x + b_B$ – equation of the straight line passing through the point $B(x_B; y_B)$;

$L_C : y = -\dfrac{1}{k}x + b_C$ – equation of the straight line passing through the point $C(x_C; y_C)$;

$L_D : y = kx + b_D$ – equation of the straight line passing through the point $D(x_D; y_D)$.

The system of equations for finding the vertices of a square in this case is written as follows:

$$V_{AC} : \begin{cases} y = kx + b_A, \\ y = \dfrac{-1}{k}x + b_C, \end{cases}$$

where $b_A = y_A - kx_A, b_C = y_C + \dfrac{1}{k}x_C$.

$$V_{AC} : \begin{cases} y = kx + \left(y_A - kx_A\right), \\ y = -\dfrac{1}{k}x + \left(y_C + \dfrac{1}{k}x_C\right), \end{cases}$$

$$V_{AC} = \begin{cases} x = \dfrac{k^2 x_A + k\left(y_C - y_A\right) + x_C}{1+k^2}, \\ y = \dfrac{k^2 y_C + k\left(x_C - x_A\right) + y_A}{1+k^2}. \end{cases}$$

$$V_{DC} : \begin{cases} y = kx + b_D, \\ y = -\dfrac{1}{k}x + b_C, \end{cases}$$

$$V_{DC} = \begin{cases} x = \dfrac{k^2 x_D + k\left(y_C - y_D\right) + x_C}{1+k^2}, \\ y = \dfrac{k^2 y_C + k\left(x_C - x_D\right) + y_D}{1+k^2}. \end{cases}$$

$$V_{BD} : \begin{cases} y = kx + b_D \\ y = -\dfrac{1}{k}x + b_B \end{cases},$$

$$V_{BD} = \begin{cases} x = \dfrac{k^2 x_D + k\left(y_B - y_D\right) + x_B}{1+k^2} \\ y = \dfrac{k^2 y_B + k\left(x_B - x_D\right) + y_D}{1+k^2} \end{cases}.$$

Let us find the distance between the points.

$$\left|V_{AB};V_{DB}\right| = \Big[\big(k^2(x_A - x_D) + k(y_D - y_A)\big)^2 +$$

$$+ \big(k(x_D - x_A) + (y_A - y_D)\big)^2\Big]^{\frac{1}{2}} \cdot \frac{1}{1+k^2}.$$

$$\left| V_{DC}; V_{DB} \right| = \left[\left(k^2 \left(y_C - y_B \right) + k \left(x_C - x_B \right) \right)^2 + \right.$$

$$\left. + \left(k \left(y_C - y_B \right) + \left(x_C - x_B \right) \right)^2 \right]^{\frac{1}{2}} \cdot \frac{1}{1+k^2}.$$

Let us define k from the condition $\left| V_{AB}; V_{DB} \right| = \left| V_{DC}; V_{DB} \right|$:

$$\left[\left(k^2 \left(x_A - x_D \right) + k \left(y_D - y_A \right) \right)^2 + \right.$$

$$\left. + \left(k \left(x_D - x_A \right) + \left(y_A - y_D \right) \right)^2 \right]^{\frac{1}{2}} =$$

$$= \left[\left(k^2 \left(y_C - y_B \right) + k \left(x_C - x_B \right) \right)^2 + \right.$$

$$\left. + \left(k \left(y_C - y_B \right) + \left(x_C - x_B \right) \right)^2 \right]^{\frac{1}{2}}.$$

Let us square both sides of the resulting equality:

$$k^4 \left(x_A - x_D \right)^2 + 2k^3 \left(x_A - x_D \right) \left(y_D - y_A \right) +$$
$$+ k^2 \left(y_D - y_A \right)^2 + k^2 \left(x_D - x_A \right)^2 + 2k \left(x_D - x_A \right) \left(y_A - y_D \right) +$$
$$+ \left(y_A - y_D \right)^2 = k^4 \left(y_C - y_B \right)^2 + 2k^3 \left(y_C - y_B \right) \left(x_C - x_B \right) +$$
$$+ k^2 \left(x_C - x_B \right)^2 + k^2 \left(y_C - y_B \right)^2 +$$
$$+ 2k \left(y_C - y_B \right) \left(x_C - x_B \right) + \left(x_C - x_B \right)^2.$$

After reducing the terms in regard to the power of k of additive components, we obtain the following equation:

$$k^4 \left[\left(x_A - x_D \right)^2 - \left(y_C - y_B \right)^2 \right] +$$
$$+ k^3 \left[2 \left(x_A - x_D \right) \left(y_D - y_A \right) - 2 \left(y_C - y_B \right) \left(x_C - x_B \right) \right] +$$
$$+ k^2 \left[\left(y_D - y_A \right)^2 + \left(x_D - x_A \right)^2 - \left(x_C - x_B \right)^2 - \left(y_C - y_B \right)^2 \right] +$$
$$+ k \left[2 \left(x_D - x_A \right) \left(y_A - y_D \right) - 2 \left(y_C - y_B \right) \left(x_C - x_B \right) \right] = 0.$$

We substitute the coordinates of the points into the equation and we obtain the equation with numerical coefficients:

$$20k^3 + 12k^2 + 20k + 5 = 0.$$

We find the roots of this equation $k_1 = -0,28$, $k_2 = 0,16 + 0,94i$, $k_3 = 0,16 - 0,94i$.

We calculate the coordinates of the vertices of the generalized square for a real root $k = k_1 = -0,28$ according to the formulae presented above:

$$V_{AC} = \begin{cases} x = \dfrac{k^2 x_A + k \left(y_C - y_A \right) + x_C}{1+k^2} = \\ = \dfrac{(-0.28)^2 \, 5 + (-0.28)(3-6) + 4}{1+(-0.28)^2} = 4.85; \\ y = \dfrac{k^2 y_C + k \left(x_C - x_A \right) + y_A}{1+k^2} = \\ = \dfrac{(-0,28)^2 \, 3 + (-0,28)(4-5) + 6}{1+(-0,28)^2} = 6,08; \end{cases}$$

$V_{AC} \left(4.85; 6.08 \right).$

$$V_{DC} = \begin{cases} x = \dfrac{k^2 x_D + k \left(y_C - y_D \right) + x_C}{1+k^2} = \\ = \dfrac{(-0.28)^2 \, 3 + (-0.28)(3-4) + 4}{1+(-0,28)^2} = 4.51; \\ y = \dfrac{k^2 y_C + k \left(x_C - x_D \right) + y_D}{1+k^2} = \\ = \dfrac{(-0.28)^2 \, 3 + (-0.28)(4-3) + 4}{1+(-0.28)^2} = 3.66; \end{cases}$$

$V_{DC} \left(4.51; 3.66 \right).$

$$V_{AB} = \begin{cases} x = \dfrac{k^2 x_A + k \left(y_B - y_A \right) + x_B}{1+k^2} = \\ = \dfrac{(-0.28)^2 \, 5 + (-0.28)(5-6) + 7}{1+(-0.28)^2} = 7.1; \\ y = \dfrac{k^2 y_B + k \left(x_B - x_A \right) + y_A}{1+k^2} = \\ = \dfrac{(-0.28)^2 \, 5 + (-0.28)(7-5) + 6}{1+(-0.28)^2} = 5.4; \end{cases}$$

$V_{AB} \left(7.1; 5.4 \right).$

$$V_{BD} = \begin{cases} x = \dfrac{k^2 x_D + k \left(y_B - y_D \right) + x_B}{1+k^2} = \\ = \dfrac{(-0.28)^2 \, 3 + (-0.28)(5-4) + 7}{1+(-0.28)^2} = 6.4; \\ y = \dfrac{k^2 y_B + k \left(x_B - x_D \right) + y_D}{1+k^2} = \\ = \dfrac{(-0.28)^2 \, 5 + (-0.28)(7-3) + 4}{1+(-0.28)^2} = 3.96; \end{cases}$$

$V_{BD} \left(6.4; 3.96 \right).$

Direct calculation shows that

$$\left| V_{AC}; V_{DC} \right| = \left| V_{AC}; V_{BA} \right| = \left| V_{BD}; V_{DC} \right| = \left| V_{BA}; V_{BD} \right| = 2.25$$

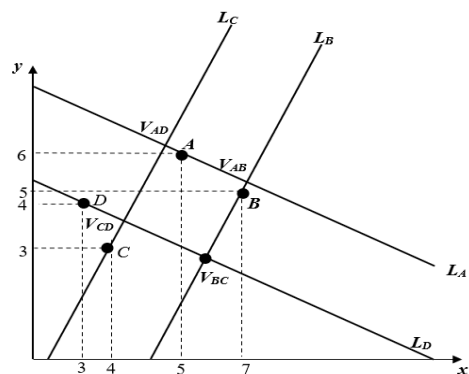Consequently, the quadrangle with the vertices $V_{AC}, V_{DC}, V_{BA}, V_{BD}$ is a square.

Fig. 5. Generalized square for the root $k = -0.28$

Рис. 5. Обобщенный квадрат для корня $k = -0,28$

Thus, for a given set of points, there are 4 generalized squares shown in fig. 2–5.

Conclusion. Remote sensing by spacecraft is a rapidly developing technology-based field. One of the most important components ensuring this development is the mathematical apparatus underlying the operation of the algorithms incorporated into the operation of spacecraft and providing the required parameters for sensing the earth's surface. The problem being considered in this work is devoted to this issue.

Sensing algorithms built on its basis will effectively obtain information about the state and boundaries of individual sections of the earth's surface within a short time (depending on the values of a finite number of specified parameters). The method being considered can naturally be expanded by changing the conditions imposed on the form of lines (not necessarily straight) passing through selected points on the earth's surface and intersecting under the conditions that are different from those given in the work under consideration.

References

1. *Laboratoriya distantsionnykh metodov i geoinformatsionnykh sistem (LDM GIS)* [Laboratory of remote sensing methods and geoinformation systems (LDM GIS)]. Available at: http://www.hydrology.ru/ ru/ structure/laboratoriya-distancionnyh-metodov-i-geoinformacionnyh-sistem (accessed 20.10.2020).

2. Labutina I. A., Baldina E. A. *Ispol'zovanie dannykh distantsionnogo zondirovaniya dlya monitoringa ekosistem OOPT* [Using remote sensing data for monitoring ecosystems of protected areas]. Moscow, 2011, 88 p.

3. Tokareva O. S. *Obrabotka i interpretatsiya dannykh distantsionnogo zondirovaniya Zemli* [Processing and interpretation of Earth remote sensing data]. Tomsk, Izd-vo Tom. politekh. un-ta Publ., 2010, 148 p.

4. Savinykh V. P., Tsvetkov V. Ya. *Geoinformatsionnyy analiz dannykh distantsionnogo zondirovaniya* [Geoinformation analysis of remote sensing data]. Moscow, Kartgeotsentr-Geodezizdat Publ., 2001, 228 p.

5. Koshkin V. B., Sukhonin A. I. *Distantsionnoe zondirovanie Zemli iz kosmosa. Tsifrovaya obrabotka izobrazheniy* [Remote sensing of the Earth from space. Digital image processing]. Moscow, Logos Publ., 2001, 264 p.

6. Egorov V. A. et at. [Possibilities of building automated systems for processing satellite data]. *Sovremennye problemy distantsionnogo zondirovaniya Zemli iz kosmosa : Fizicheskie osnovy, metody i tekhnologii monitoringa okruzhayushchey sredy, potentsial'no opasnykh ob"ektov i yavleniy.* Moscow, Poligrafservis Publ., 2004, P. 431–436.

7. Trifonova T. A., Mishchenko N. V., Krasnoshchekov A. N. *Geoinformatsionnye sistemy i distantsionnoe zondirovanie v ekologicheskikh issledovaniyakh* [Geographic information systems and remote sensing in environmental research]. Moscow, Akademicheskiy proekt Publ., 2005, 350 p.

8. Chandra A. M., Gosh S. K. *Distantsionnoe zondirovanie i geograficheskie informatsionnye sistemy* [Remote sensing and geographic information systems]. Moscow, Tekhnosfera Publ., 2008, 312 p.

9. Campell J. B. Introduction to remote sensing. London, The Guilford Press, 1966, P. 120–549.

10. Dr. Kelso T. S. Basics of the Geostationari Orbit. Available at: http://www.celestrak.com/columns (accessed 20.10.2020).

11. *Dogovor o printsipakh deyatel'nosti gosudarstv po issledovaniyu i ispol'zovaniyu kosmicheskogo prostranstva, vklyuchaya Lunu i drugie nebesnye tela* [Treaty on the principles of the activities of states in the exploration and use of outer space, including the Moon and other celestial bodies]. Available at: https://www.un.org/ru/ documents/decl_conv/conventions/outer_space_ governing.shtml (accessed 20.10.2020).

12. Fateev V. F., Min'kov S. [New direction of development of small spacecraft for remote sensing of the Earth]. *Izv. vuzov. Priborostroenie.* 2004, Vol. 47, No 3, P. 18–22 (In Russ.).

13. Lebedev A. A., Nesterenko O. P. *Kosmicheskie sistemy nablyudeniya. Sintez i modelirovanie* [Cosmic observation systems. Synthesis and modeling]. Moscow, Mashinostroenie Publ., 1991, 224 p.

14. Pod"ezdkov Yu. A. *Kosmicheskaya s"emka Zemli 2006–2007 gg.* [Space imagery of the Earth 2006–2007]. Moscow, Radiotekhnika Publ., 2008, 275 p.

15. Nevdyaev L. M., Smirnov A. A. *Personal'naya sputnikovaya svyaz'* [Personal satellite communications]. Moscow, Eko-Trendz Publ., 1998, 216 p.

16. Pogorelov A. V. *Analiticheskaya geometriya* [Analytic geometry]. Moscow, Nauka Publ., 1968, 176 p.

17. Tabachnikov S. L., Fuks D. B. *Matematicheskiy divertisment* [Mathematical divertissement]. Moscow, MTsNMO Publ., 2011, 512 p.

Библиографические ссылки

1. Лаборатория дистанционных методов и геоинформационных систем (ЛДМ ГИС) [Электронный ресурс]. URL: http://www.hydrology.ru/ru/structure/ laboratoriya-distancionnyh-metodov-i-geoinformacionnyh-sistem (дата обращения 20.10.2020).

2. Лабутина И. А., Балдина Е. А. Использование данных дистанционного зондирования для мониторинга экосистем ООПТ. М. : 2011. 88 с.

3. Токарева О. С. Обработка и интерпретация данных дистанционного зондирования Земли. Томск : Изд-во Том. политех. ун-та, 2010. 148 с.

4. Савиных В. П., Цветков В.Я. Геоинформационный анализ данных дистанционного зондирования. М. : Картгеоцентр-Геодезиздат, 2001. 228 с.

5. Кошкин В. Б., Сухонин А. И. Дистанционное зондирование Земли из космоса. Цифровая обработка изображений. М. : Логос, 2001. 264 с.

6. Возможности построения автоматизированных систем обработки спутниковых данных / В. А. Егоров и др. // Современные проблемы дистанционного зондирования Земли из космоса : Физические основы, методы и технологии мониторинга окружающей среды, потенциально опасных объектов и явлений. М. : Полиграфсервис, 2004. С. 431–436.

7. Трифонова Т. А., Мищенко Н. В., Краснощеков А. Н. Геоинформационные системы и дистанционное зондирование в экологических исследованиях. М. : Академический проект, 2005. 350 с.

8. Чандра А. М., Гош С. К. Дистанционное зондирование и географические информационные системы. М. : Техносфера, 2008. 312 с.

9. Campell J. B. Introduction to remote sensing. London : The Guilford Press, 1966. P. 120–549.

10. Dr. Kelso T. S. Basics of the Geostationari Orbit [Электронный ресурс]. URL: http://www.celestrak.com/columns (дата обращения 20.10.2020).

11. Договор о принципах деятельности государств по исследованию и использованию космического пространства, включая Луну и другие небесные тела (1967) [Электронный ресурс] / офиц. сайт ООН. URL: https://www.un.org/ru/documents/decl_conv/conventions/outer_space_governing.shtml (дата обращения 20.10.2020).

12. Фатеев В. Ф., Миньков С. Новое направление развития МКА дистанционного зондирования Земли. // Изв. вузов. Приборостроение. 2004. Т. 47, № 3. С. 18–22.

13. Лебедев А. А., Нестеренко О. П. Космические системы наблюдения. Синтез и моделирование. М. : Машиностроение, 1991. 224 с.

14. Подъездков Ю. А. Космическая съемка Земли 2006–2007 гг. М. : Радиотехника, 2008. 275 с.

15. Невдяев Л. М., Смирнов А. А. Персональная спутниковая связь. М. : Эко-Трендз, 1998. 216 с.

16. Погорелов А. В. Аналитическая геометрия. М. : Наука, 1968. 176 с.

17. Табачников С. Л., Фукс Д. Б. Математический дивертисмент. М. : МЦНМО, 2011. 512 с.

Shlepkin Aleksey Anatolevich – Cand. Sc., associate Professor, Siberian Federal University.

Shiryaeva Tamara Alekseevna – Cand. Sc., associate Professor; Krasnoyarsk state agrarian University. E-mail: tas_sfu@mail.ru.

Shlepkin Anatoliy Konstantinovich – D. Sc., Professor, Krasnoyarsk state agrarian University. E-mail: ak_kgau@mail.ru.

Filippov Konstantin Anatol'evich – D. Sc., associate Professor, Krasnoyarsk state agrarian University. E-mail: filippov_kostya@mail.ru.

Pashkovskaya Olga Vladimirovna – Cand. Sc., associate Professor, Reshetnev Siberian State University of Science and Technology. E-mail: pashkovskaya@sibsau.ru.
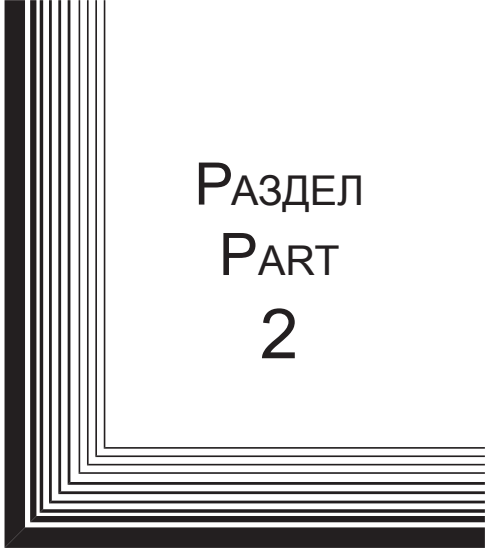
Шлепкин Алексей Анатольевич – кандидат физико-математических наук, доцент, Сибирский федеральный университет.

Ширяева Тамара Алексеевна – кандидат физико-математических наук, доцент; Красноярский государственный аграрный университет. E-mail: tas_sfu@mail.ru.

Шлепкин Анатолий Константинович – доктор физико-математических наук, профессор, Красноярский государственный аграрный университет. E-mail: ak_kgau@mail.ru.

Филиппов Константин Анатольевич – доктор физико-математических наук, доцент, Красноярский государственный аграрный университет. E-mail: filippov_kostya@mail.ru.

Пашковская Ольга Владимировна – кандидат физико-математических наук, доцент, Сибирский государственный университет науки и технологий имени академика М. Ф. Решетнева. E-mail: pashkovskaya@sibsau.ru.

АВИАЦИОННАЯ
И РАКЕТНО-
КОСМИЧЕСКАЯ ТЕХНИКА

AVIATION
AND SPACECRAFT
ENGINEERING

INFLUENCE OF PLASMA JETS OF ELECTRIC JET ENGINES ON SPACECRAFT FUNCTIONAL CHARACTERISTICS

A. B. Nadiradze[1], S. G. Kochura[2], I. A. Maximov[2], R. E. Tikhomirov[2], S. V. Balashov[2]

[1]Moscow aviation institute (national research university)
4, Volokolamskoe highway, Moscow, 125993, Russian Federation
[2]JSC Academician M. F. Reshetnev "Information satellite systems"
52, Lenin St., Zheleznogorsk, Krasnoyarsk region, 662972, Russian Federation
E-mail: tikhroman@gmail.com

The issues of compatibility of correcting electric jet engines (EJE) and large-size transformable antennas (LTA) used in high-orbit communication satellites are considered. The paper deals with the erosive and polluting effect of EJE jets interacting with knitted mesh material (grid mesh), which is used for manufacturing LTA reflectors. The erosive effect of the EJE jets on the LTA mesh is characterized by the fact that the angles of ions incidence on the surface of the threads in the mesh are in the range from 0 to 90°, i. e. such effect takes place at practically any angle of ions incidence on the mesh surface. The research includes both mathematical description of physical processes and conducting a wide series of experiments, which makes it possible to achieve the necessary reliability of the results. It has been established that the effect of plasma jets of correcting engines can lead to significant sputtering of the reflecting coating from the surface of a large-size antenna reflector. The authors obtained experimental data on the degradation of the reflection coefficient of electromagnetic radiation from the mesh, depending on the degree of plasma jet influence.

It was found that the sputtering of reflecting coating from the surface of threads does not significantly affect the reflection coefficient. The sputtering of the coating at the points of threads contact is much more significant. Strong dependence of the reflection coefficient on the type of mesh weaving was also found. The mechanism of sputtering products deposition on reflecting coatings of the thermal control system radiators was investigated. The results of calculations of the sputtering coefficient and the sputtering indicatrix of the reflecting coating applied to the mesh threads were obtained. The degradation of the functional characteristics of thermoregulatory coatings (TRC) during the deposition of thin films of gold, which is one of the possible materials for a reflecting coating, was experimentally determined. Estimates of the maximum permissible level of TRC contamination were obtained. It is shown that, subject to the relevant design rules, it is possible to use EJE and LTA together in high-orbit communication satellites.

Keywords: electric jet engines, large-size transformable antennas, mesh, contamination, plasma, thermoregulatory coatings.

ИССЛЕДОВАНИЕ ВЛИЯНИЯ ПЛАЗМЕННЫХ СТРУЙ ЭЛЕКТРОРАКЕТНЫХ ДВИГАТЕЛЕЙ НА ФУНКЦИОНАЛЬНЫЕ ХАРАКТЕРИСТИКИ КОСМИЧЕСКИХ АППАРАТОВ

А. Б. Надирадзе[1], Р. Е. Тихомиров[2], С. Г. Кочура[2], И. А. Максимов[2], С. В. Балашов[2]

[1]Московский авиационный институт (национальный исследовательский университет)
Российская Федерация, 125993, г. Москва, Волоколамское шоссе, 4
[2]АО «Информационные спутниковые системы» имени академика М. Ф. Решетнёва»
Российская Федерация, 662972, г. Железногорск Красноярского края, ул. Ленина, 52
E-mail: tikhroman@gmail.com

Рассмотрены вопросы совместимости электроракетных двигателей (ЭРД) коррекции и крупногабаритных трансформируемых антенн (КГА), применяемых на высокоорбитальных спутниках связи. В работе рассмотрено эрозионное и загрязняющее воздействие струй ЭРД при взаимодействии с трикотажным сетчатым материалом (сетеполотном), который применяется для изготовления рефлекторов КГА. Эрозионное воздействие струй ЭРД на сетеполотно КГА характеризуется тем, что углы падения ионов на поверхность нитей

находятся в диапазоне от 0 до 90°, т. е. практически при любом угле падения ионов на поверхность сетеполотна. Исследование, проведенное авторами, включало в себя как математическое описание физических процессов, так и проведение широкой серии экспериментов, что позволило добиться необходимой достоверности результатов. В работе установлено, что воздействие плазменных струй двигателей коррекции может приводить к значительному распылению отражающего покрытия с поверхности рефлектора крупногабаритной антенны. Получены экспериментальные данные о деградации коэффициента отражения электромагнитного излучения сетеполотна в зависимости от степени воздействия плазменной струи. Установлено, что распыление отражающего покрытия с поверхности нитей не оказывает существенного влияния на коэффициент отражения. Более значимым является распыление покрытия в точках контакта нитей. Также была обнаружена сильная зависимость коэффициента отражения от типа плетения сетеполотна. Исследован механизм осаждения продуктов распыления на отражающие покрытия радиаторов системы терморегулирования. Получены результаты расчетов коэффициента распыления и индикатрисы распыления отражающего покрытия, наносимого на нити сетеполотна. Экспериментально определена деградация функциональных характеристик терморегулирующих покрытий (ТРП) при осаждении на них тонких пленок золота, являющегося одним из возможных материалов отражающего покрытия. Получены оценки предельно допустимого уровня загрязнения ТРП. Показано, что при соблюдении соответствующих правил проектирования возможно совместное использование ЭРД и КГА на высокоорбитальных спутниках связи.

Ключевые слова: электроракетные двигатели, крупногабаритные трансформируемые антенны, сетеполотно, загрязнение, плазма, терморегулирующие покрытия.

Introduction. The main operational characteristic of any satellite system is its durability, i.e. the ability to fulfill the assigned target tasks during the required active life (RAL) by all spacecraft (SC) included in its composition.

A modern SC includes hundreds of radio-electronic units, optical devices and working surfaces, thousands of structural elements and cable assemblies. This entire technical complex must function for a long RAL (up to 15 years) under the conditions of the negative impact of space environment.

The range of factors affecting a SC during its orbital operation is extremely wide. As a result of their impact, various physicochemical processes occur in the materials of a SC structure and elements of onboard equipment (OE), leading to the deterioration of their operational parameters, as well as to the occurrence of abnormal situations in the operation of a SC and catastrophic failures of SC onboard systems. Therefore, one of the main problems in the field of applied cosmophysics when creating and ensuring the reliable functioning of SC is the problem of ensuring its resistance to the effects of space factors and factors of a technogenic nature.

Research on the influence of the space environment on SC in the world and in our country has been carried out for several decades. JSC "ISS" has many years of experience in the space environment study, the result of which is the refinement of the physics and mechanisms of the impact of the space environment on SC, the development and testing of methods and means of protection, the use of which allows ensuring a long active life of the SC being developed [1–17]. The work is carried out in close cooperation with such leading Russian research institutes as MAI, Research Institute of Nuclear Physics of Moscow State University, NSU, TPU, etc.

Modern trends in the development of space communication systems require the creation of large-size transformable antennas (LTA) with a diameter of 5–10 m and more, installed on SC board. The reflectors of such antennas are made of mesh materials knitted from metal threads and covered with thin electrically conductive films to ensure the required values of the reflection coefficient in the operating frequency range.

Electric jet engines (EJE) with a high specific impulse are used as correcting engines (CE) to correct the orbit of communication satellites operating in geostationary orbits. It allows saving the mass of the working flood of the engines and obtaining a significant (hundreds of kilograms) gain in SC payload mass.

However, design practice shows that when the EJE and LTA are used together in communication satellites, situations may arise when plasma jets of the EJE hit the antenna reflectors, causing a number of negative effects that can significantly affect the normal SC functioning. The most significant effects include the erosion of the reflecting coating and the contamination of the SC optical surfaces with the products of sputtering of the coating and the mesh cloth warp. Erosion of the reflecting coating can lead to decreasing the reflection coefficient of electromagnetic radiation of the LTA reflector. Contamination of the SC optical surfaces leads to degradation of their operating characteristics and, as a consequence, to the disruption of the normal operation of the SC onboard systems.

Erosion of mesh when exposed to a plasma jet. The mechanisms of the erosive effect of plasma jets of EJE on the SC were discussed in detail in [1; 18]. A peculiarity of the erosive effect of the EJE jets on the LTA mesh is that the angles of incidence of ions on the surface of the threads are in the range from 0 to 90° at practically any angle of incidence of ions on the surface of the LTA mesh θ [19]. To illustrate this effect, fig. 1 shows the results of calculating the depth of erosion of a reflecting coating at different values of the angle θ.

Fig. 1 shows that the nature of the coating wear weakly depends on θ. Erosion occurs almost uniformly over the entire irradiated surface of the threads, which is due to the nature of the dependence of the sputtering relative coefficient of a continuous surface on the angle of ions incidence $S(\theta)$ [20]. At the points of the threads facing the engine, $\theta = 0$ (if a thread is perpendicular to the jet axis) and $S(\theta) = 1$.

θ = 0°　　　　　　　　θ = 30°　　　　　　　　θ = 60°
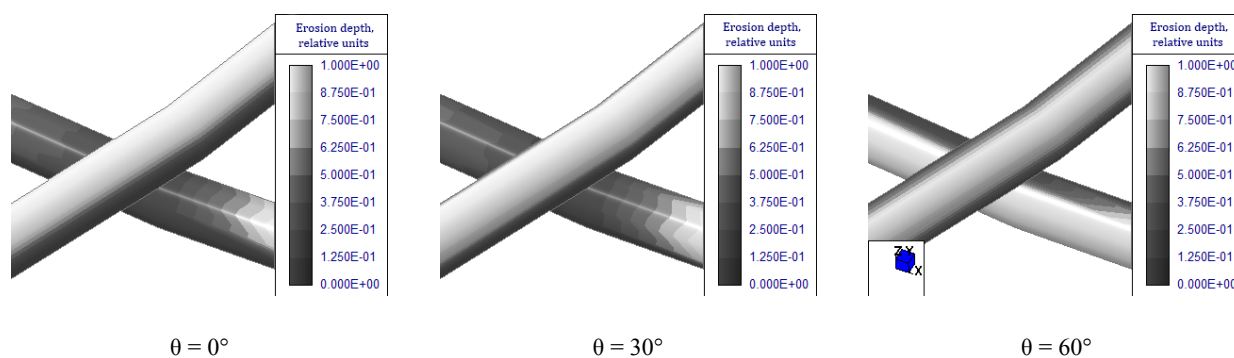
Fig. 1. Erosion depth of conducting coating (in fractions of thickness) for different angles
of ion incidence on the mesh surface θ (axis Y – erosion depth)

Рис. 1. Глубина эрозии проводящего покрытия (в долях толщины слоя) при различных углах падения ионов
на поверхность сетеполотна θ

a　　　　　　　　　　　　　　　　*b*
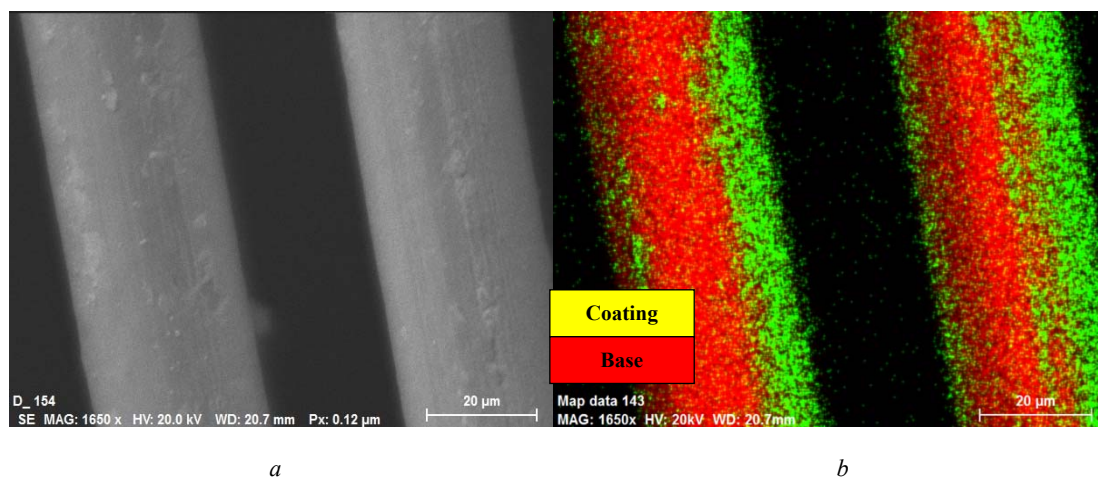
Fig. 2. Micrographofmesh threads (*a*) and a map of the elemental composition of their surface (*b*) in the vicinity
of the point of complete sputtering of the reflecting coating

Рис. 2. Микрофотография нитей сетеполотна (*a*) и карты элементного состава их поверхности (*б*)
вблизи точки полного распыления отражающего покрытия

On the lateral surface of the threads θ increases, and the ion flux density decreases proportionally to cos (θ). But in this case S (θ) increases, which compensates for the decrease in the current density. Thus, over most of the irradiated surface of the threads, the sputtering rate changes insignificantly.

This type of wear leads to the fact that at some point of time the reflective coating disappears immediately from almost the entire irradiated surface of the threads; thereafter the wear of the base begins.

Fig. 2 shows a micrograph of the surface and a map of the elemental composition of the mesh threads in the vicinity of the point of complete sputtering of the reflecting coating, obtained by SEM.

As it can be seen from fig. 2, the boundary of the complete sputtering of the reflecting coating is rather sharp, which confirms the conclusion about the complete coating sputtering from the entire irradiated surface of the thread.

Degradation of the mesh reflection coefficient. The degradation of the mesh reflection coefficient when the reflecting coating is sputtered is associated with decreasing the conductivity of the surface layer and increasing the contact resistance of the threads. In a complete formulation, the construction of a mathematical model of this effect is an extremely difficult task; therefore, in the framework of this work, the dependence of the reflection coefficient on the degree of exposure to the plasma jet of the EJE was determined experimentally.

Measurements of the reflection coefficient of the mesh samples in the operating frequency range were carried out before and after the impact of the jet. The degree of jet impact on the mesh was determined by calculation. In this case, the following parameters of the reflecting coating wear were used:

$$\vartheta_s = \frac{Area\ of\ complete\ coating\ sputtering}{Initial\ surface\ area\ of\ reflecting\ coating}, \quad (1)$$

$$\vartheta_m = \frac{Sputtered\ reflecting\ coating\ mass}{Initial\ mass\ of\ reflecting\ coating}, \quad (1.a)$$

$$\vartheta_b = \frac{Maximum\ erosion\ depth\ of\ reflecting\ coating}{Initial\ reflecting\ coating\ thickness}, \quad (1.b)$$

where ϑ_s is wear rate for area; ϑ_m is wear rate for mass; ϑ_b is wear rate for thickness.

The calculation of ϑ_s and ϑ_m was carried out by integrating the corresponding parameters over the surface of the threads on the area of a fragment containing a sufficiently large number of mesh cells. The calculation took into account the mutual shielding of the threads. The value ϑ_h was determined from the ratio of the maximum erosion length (the depth of erosion of a semi-infinite target) to the initial layer thickness h_0. The calculated dependences of the wear degree of the reflecting coating on the exposure time at different angles of ions incidence are shown in fig. 3.
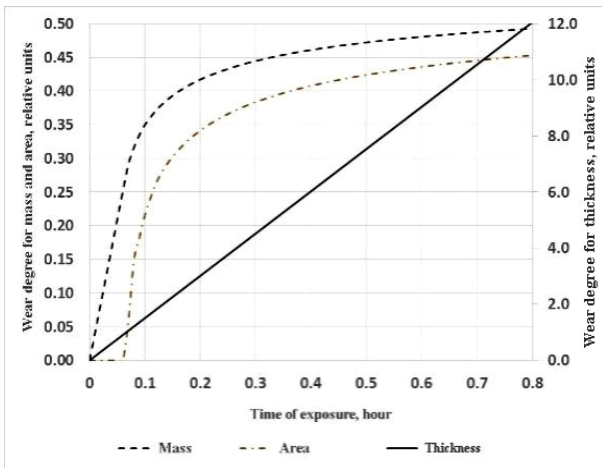

Fig. 3. Dependence of wear degree of reflective coating on the time of exposure to a plasma jet

Рис. 3. Зависимость степени износа отражающего покрытия от времени воздействия плазменной струи

Fig. 3 shows that the degrees of wear for area and mass asymptotically approach their limiting value of 0.5, and the degree of wear for thickness increases linearly with time. The degree of wear for area does not start to change immediately, but only after some time, corresponding to the sputtering of the reflecting coating to the entire depth, i. e. when $\vartheta_h \approx 1$. The wear degree for mass initially grows rapidly, but the growth rate slows down after sputtering a significant part of the coating.

It should be noted that 80 % of wear for mass is achieved when the reflecting coating is sputtered to a depth of about (2–3) h_0, and 80 % of wear for area is achieved when the reflecting coating is sputtered to a depth of about $6h_0$. This indicates that the side surfaces of the threads are sputtered much more slowly than the surfaces facing the engine. Apparently, the coating at the points of threads contactis sprayed even more slowly.

The analysis showed that the degree of wear for thickness ϑ_h is the most suitable for constructing an empirical

dependence of the reflection coefficient on the degree of reflecting coating wear. Application of ϑ_s and ϑ_m leads to significant errors, since the calculation of ϑ_s, ϑ_m near their limiting value (at $\vartheta_h \gg 1$) is inaccurate due to the inaccuracy of the geometric model of the mesh.

Fig. 4 shows the results of measurements of the mesh reflection coefficient depending on the degree of wear for the reflecting coating thickness. In the experiment the ion current density and the time of exposure to the samples were varied. In total, 18 samples were irradiated. Values of ϑ_h from 0.5 to 44 were realized on them.

Taking into account the large variations in the measured values of the reflection coefficient, the following function was used to approximate the dependence of the reflection coefficient of the electromagnetic radiation of the LTA reflector mesh on the degree of the reflecting coating wear (in fig. 4 it is shown by a dotted line):

$$\Delta R = R_{max}\left\{1 - \exp\left(-\beta \cdot \vartheta_h\right)\right\}, \quad (2)$$

where ΔR_{max} is the maximum degradation of the reflection coefficient of the mesh electromagnetic radiation; β is an adjustable parameter determined from the experiment.

As it can be seen from fig. 4, the value of $\Delta R \approx R_{max}$ is achieved at $\vartheta_h \gg 1$. Allowable ΔR values were maintained at $\vartheta_h < 15$–20 depending on the signal frequency. In this case ϑ_s and $\vartheta_m \approx 0.5$. This fact suggests that the sputtering of reflecting coating from the surface of the threads does not significantly affect the reflection coefficient. Apparently, sputtering of the coating at the points of threads contacts is more significant. This hypothesis is confirmed by a significant change in the reflection coefficient when changing ϑ_h from 5 to 44 (see fig. 4).

In addition, strong dependence of the reflection coefficient on the type of mesh weaving was found during the experiment. Fig. 5 shows the values of $\Delta R/R_{max}$ of two mesh samples differing in the type of weaving.

Fig. 5 shows that the mesh of type 1 has significantly higher resistance to the effect of a plasma jet than the mesh of type 2. The reason for such strong difference is, apparently, the different degree of protection of the points of threads contacts from the action of ions. Hence it follows that the type of weaving is an important parameter and it must be taken into account when choosing mesh and assessing the resistance of LTA to the effect of plasma jets of an EJE. To confirm the durability of the mesh, it is necessary to test it.

Since the effect of the plasma jet on the LTA occurs unevenly over the surface of the reflector and, accordingly, the degree of wear is different for each section of the reflector, the calculation of the change in the LTA reflection coefficient as a whole is performed by averaging over all sections:

$$R = \frac{1}{S_{tot}}\sum_i R_i S_i, \quad (3)$$

where S_{tot} is the total area of the reflector; S_i is the area of the section; R_i is the reflection coefficient of the section (calculated by the formula (2) for the estimated degree of wear of the section ϑ_{hi}).

The authors calculated the wear degree of the LTA reflector mesh of the experimental SC. The calculation was carried out for the case of the simultaneous action of two CEs (correcting engines) located on opposite sides of the SC body and installed at different angles. The operating time of both engines corresponded to the SC RAL.

In the course of the calculation it was found that at the end of the RAL the reflecting coating will be completely sputtered over about 35 % of the reflector area. The reflecting coating remains on the rest of the surface. The maximum degree of the coating wearin depth reaches 17, the wear of the base is less than 1 %.

At this level of exposure, the change in the reflection coefficient at the point with the maximum coating wear ($\vartheta_h \approx 17$) is close to the maximum permissible value of ΔR_{per}. But since the coating wear is much less on most of the reflector, the degradation of the antenna reflection coefficient as a whole is guaranteed not to exceed ΔR_{per}.

However with a different structural-layout scheme (SLS) of the SC the impact on the LTA may be critical, therefore, the problem of choosing the SC SLS in which the effect of the CE plasma jet on the LTA will not exceed the permissible level is very urgent.

The TRC contamination with the products of the mesh sputtering. Particles of metal, mainly reflecting coating, sputtered from the surface of the mesh threads, can be deposited on the surface of the TRC changing their thermo-optical characteristics. In this regard it becomes necessary to determine the thickness of the contamination films formed on the surface of the TRC during the entire time of the SC operation in orbit, as well as the optical properties of these films and their influence on the thermo optical characteristics of the TRC.

The deposition fluxes of particles on the TRC surface are calculated by integrating the sputtering fluxes over the entire surface of the LTA exposed to the plasma jet:

$$nv_c = \int_s \frac{nv_s}{\pi |\vec{r}_{AB}|^2} I\,n\,d\left(\theta_A, \vec{r}_{AB}\right)\cos\left(\vartheta_b\right)dS, \quad (4)$$

where $\vec{r}_{AB}$ is the radius vector connecting the point of the sputtered surface "A" and the point of the surface on which the sputtered products "B" are deposited; nvc is flux density of sputtered particles at point "A"; θA is the angle of incidence of ions on the sputtered surface at point "A"; θB is the angle of incidence of sputtered particles at point "B"; $I\,n\,d\left(\theta_A, \vec{r}_{AB}\right)$ is the sputtering indicatrix. In its turn, nvs is calculated as:

$$nv_s = \frac{J_i\cos\left(\theta_A\right)}{b}\int_0^\infty f(E)\cdot S(E,\theta_A)dE, \quad (5)$$

where J_i is the ion current density; E is the ion energy; $f(E)$ is the ion distribution function according to energy; $S(E,\theta_A)$ is the dependence of the sputtering coefficient on the energy and the angle of ions incidence; e is the electron charge.

Thus, to calculate nv_c in addition to the parameters of the plasma jet, it is necessary to know the characteristics of the mesh sputtering, namely, the sputtering indicatrix $I\,n\,d\left(\theta_A, \vec{r}_{AB}\right)$ and the sputtering coefficient $S(E,\theta_A)$.

Just as for smooth solid surfaces, the coefficient of sputtering of the mesh surface can be defined as the ratio $S = \frac{N_a}{N_i}$, where N_a is the number of atoms sputtered from the surface of the mesh threads per unit time; $N_i = J_i\cos(\theta)/e$ is the number of ions falling on the reflector surface.

However, unlike smooth surfaces N_a is calculated by integrating the flux density of sputtered particles nv_S over the surface of the threads.
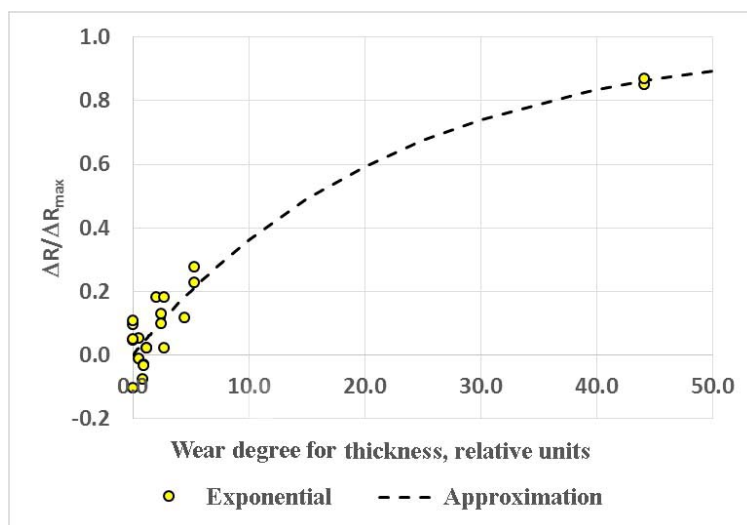
Fig. 4. Change in the mesh reflection coefficient depending
on the degree the reflective coating wear

Рис. 4. Изменение коэффициента отражения сетеполотна в зависимости
от степени износа отражающего покрытия
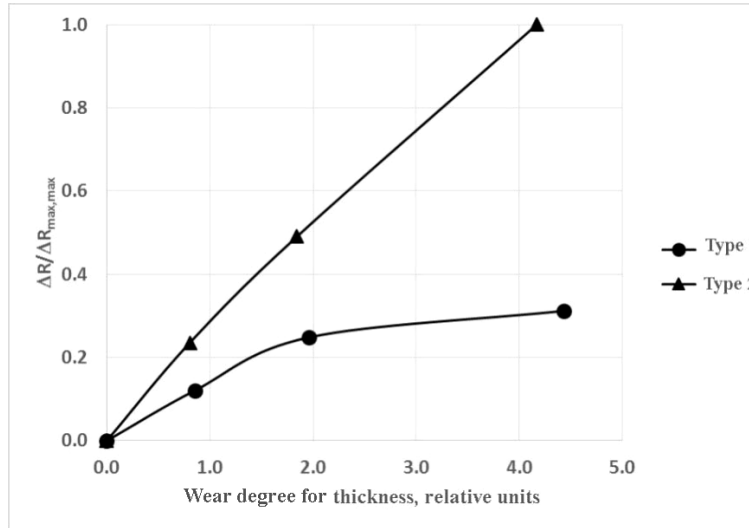
Fig. 5. Influence of weaving type on the change of the mesh reflection coefficient (values at all points are normalized by maximum value $\Delta R/R_{\max}$), axis Y – degree of wear for thickness

Рис. 5. Влияние типа плетения на изменение коэффициента отражения сетеполотна (значения во всех точках нормированы по максимальному значению $\Delta R_{\max,\max}$)
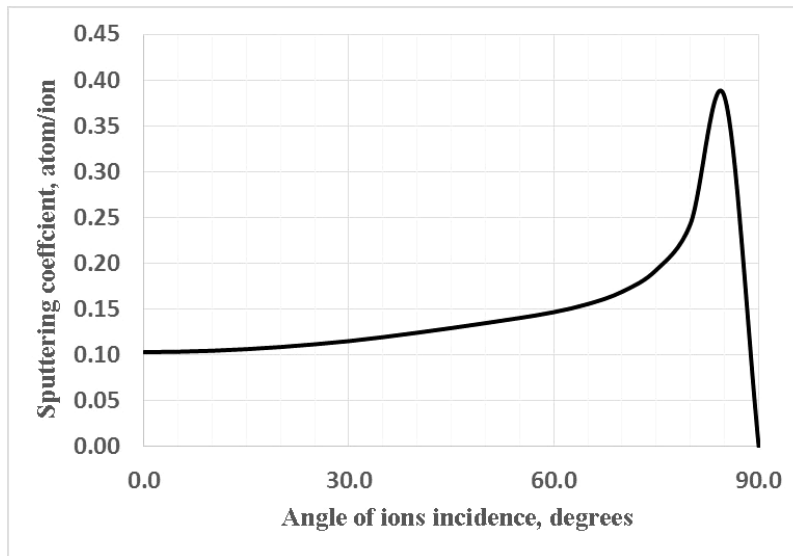
Fig. 6. Dependence of the mesh sputtering coefficient on the angle of ions incidence

Рис. 6. Зависимость коэффициента распыления сетеполотна от угла падения ионов

A three-dimensional computational model of the mesh containing a sufficiently large number of elementary cells is used to calculate nv_S.

Fig. 6 shows the calculated dependence of the mesh sputtering coefficient when it is exposed to a plasma jet of the EJE.

As you can see from fig. 6, the angular dependence of the mesh sputtering coefficient differs significantly from the angular dependence of a solid surface [20]. At $\theta < 60$–$70°$ the ion flux N_i decreases proportionally to $\cos(\theta)$, while N_a changes only slightly, since the total cross section of threads interacting with the flux remains almost unchanged.

At $\theta > 60$–$70°$ the mesh geometric transmittance tends to zero and almost all the ions of the jet fall on the surface of the threads. Therefore, there is a rapid growth of S here. At $\theta = 90°$ $N_i = 0$ and, correspondingly, $S = 0$.

Let us note that the mesh sputtering coefficient at $\theta = 0$ corresponds to the sputtering coefficient of the solid material, corrected for the mesh geometric transmittance:

$$S \approx S_{Au} \cdot (1 - T), \qquad (6)$$

where T is the mesh geometric transmittance.

The mesh sputtering indicatrix (fig. 7) also has a number of significant differences from the sputtering indicatrix of smooth materials.

From fig. 7 it can be seen that at sliding angles of incidence, most of the mesh sputtering products are directed towards the ion source, while on smooth surfaces it is directed away from the source. This is due to the fact that the sections of the threads that are directed to the source are sputtered at an oblique incidence of ions.

It should also be noted that when sputtering mesh surfaces, the streams of sputtered particles also spread to the rear hemisphere, since particles from the surface of the threads are emitted in almost all directions.

The calculation of the contamination of the of the surfaces of the experimental SC developed by JSC Academician M. F. Reshetnev "Information Satellite Systems" by sputtering products of the reflecting coating of the LTD reflectorwas carried out.

Calculations show that the maximum thickness of the deposited film on the side surface of the SC body is about 1.5 nm, and the surface density of contaminants is $3 \cdot 10^{-6}$ g / cm^2. It should be noted that the film will consist not only of gold atoms, but also of the mesh base atoms (tungsten or molybdenum), as well as of particles of its own external atmosphere [3], captured by the film.

Changes in the characteristics of TRCdepending on the level of contamination will be considered in the next section.

Degradation of the TRC thermo-optical characteristics. The deposition of thin metal films (products of the sputtering of the reflecting coating and the base of the mesh threads) on the surface of the TRC can lead to a significant change in their thermo-optical characteristics. Experiments to determine the dependence of the solar radiation absorption coefficient – A_s and the emissivity (emissivity factor) – ε on the thickness of the deposited gold film on the surface of the TRC were carried out to study this issue at the PP-2 stand of Moscow Aviation Institute. A detailed description of these experiments and the data obtained is given in [21]. The objects of research were "mirror" coating of the OSO-S type and a film coating of the PM-OA type. The use of gold as a metal for deposition is due to the fact that it does not form oxide films in air. Films of other metals are rapidly oxidized, while their properties change greatly.

Mirror coating OSO-S is a thin plate made of K-208 glass with one-sided deposition of a layer of silver, glued to the metal plate with glass outside. Initial characteristics of the coating: $A_s = 0.08$; ε = 0.85. The PM-OA film coating is made on the basis of the PM-1EU polyimide film with one-sided aluminum sputtering. Coating initial characteristics: $A_s = 0.31$; ε = 0.68.

The samples were rectangular plates 20x20 mm in size (OSO-S) and 30 × 25 mm (PM-OA), onto which thin gold films with a thickness of 1 to 24 nm were deposited by cathodic sputtering.

To apply the films, the TRC samples were placed in a protective casing (fig. 8), which protected the samples from sputtering products from the walls of the vacuum chamber.

The sputtering target was also placed inside the casing and was protected from sputtering products from the walls of the vacuum chamber. The jet ions passed through a special collimating hole (ceramics) and hit the target. A Hall engine of the M50 type was used as an ion source, accelerating xenon ions to the energy of ~ 300 eV. For the gas (recombined xenon ions) to escape from the casing, holes were made in its side walls, covered with plates, excluding the direct visibility of the target and samples from the side of the vacuum chamber. The sputtering products of the target were deposited on the TRC samples located immediately in front of it. The control of the mass deposited on the TRC samples was carried out using a quartz microbalance with a resonance frequency of 6 MHz (sensitivity $1.1 \cdot 10^{-8}$ g / cm^2 / Hz). The sputtering process continued until the change in the frequency of the quartz resonator reaches a predetermined value.

Fig. 9 shows the results of measuring the thermo-optical characteristics of TRC with deposited gold films of various thicknesses.

It can be seen from these graphs that the nature of the change in the coefficients A_s and ε, depending on the thickness of the contamination film d, is the same for both types of TRC. In the range d from 0 to 4 nmε practically does not change. At $d > 4$ nm, ε rapidly decreases and at $d = 24$ nm reaches values comparable to ε of a monolithic material (for polished gold from 0.018 to 0.035).

The A_s behavior is more complex. At d from 0 to 3 nm, a sharp increase in A_s is observed, in the range from 3 to 7 nm A_s reaches maximum and reaches a plateau, and at $d > 7$ nm it gradually decreases to values comparable to the A_s of a monolithic material.

Such an unusual behavior of A_s and ε is explained by the fact that the gold film with a thickness of up to 3–5 nm is granular. This is confirmed by the AFM images shown in fig. 10.

From fig. 10 it can be seen that at $d = 2.7$ nm almost all the granules have coalesced, and at $d \geq 6$ nm, the film is almost a monolithic substance. With a small film thickness, while the granules have not coalesced yet, the film has very low conductivity. As d increases, the granules coalesce and the conductivity of the film rapidly increases, reaching the level of a monolithic material.

The presence of a thick reflective film leads to the fact that thermal radiation does not leave the material and its ε is comparable to ε of the film material. As long as the reflecting layer is not formed, the value of ε remains practically unchanged and is equal to ε of an uncontaminated TRC.

The nature of A_s change is completely different. The rapid growth of A_s at d from 0 to 3 nm is associated with resonant absorption of radiation arising on the grid structure of the film. With further increase in d, the value of the A_s coefficient gradually decreases, approaching the A_s of gold on the substrate.

Since the degradation of TRC is characterized by a change not in the individual As or ε, but in the As/ε ratio, films with thickness of less than 2–3 nm are critical for TRC, when a significant increase in As occurs with relatively small changes in ε.
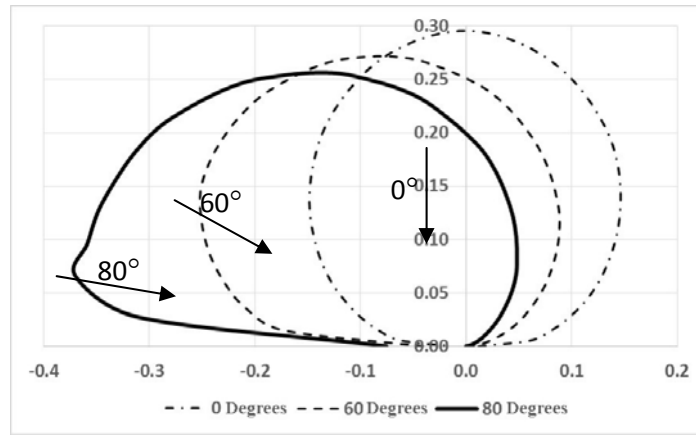
Fig. 7. Indicatrix of the mesh sputtering for different angle of incidence of ions

Рис. 7. Индикатриса распыления сетеполотна при различных углах падения ионов

a

b
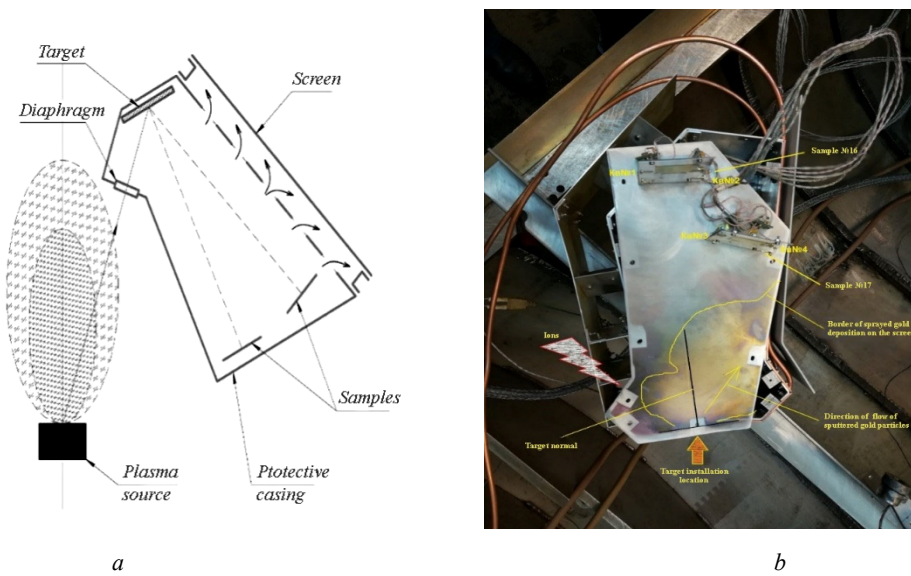
Fig. 8. The scheme of the deposition of gold films on the TRC samples (*a*) and the appearance
of the protective casing with the samples (*b*)

Рис. 8. Схема напыления пленок золота на образцы ТРП (*а*) и внешний вид защитного кожуха с образцами (*б*)

a

b
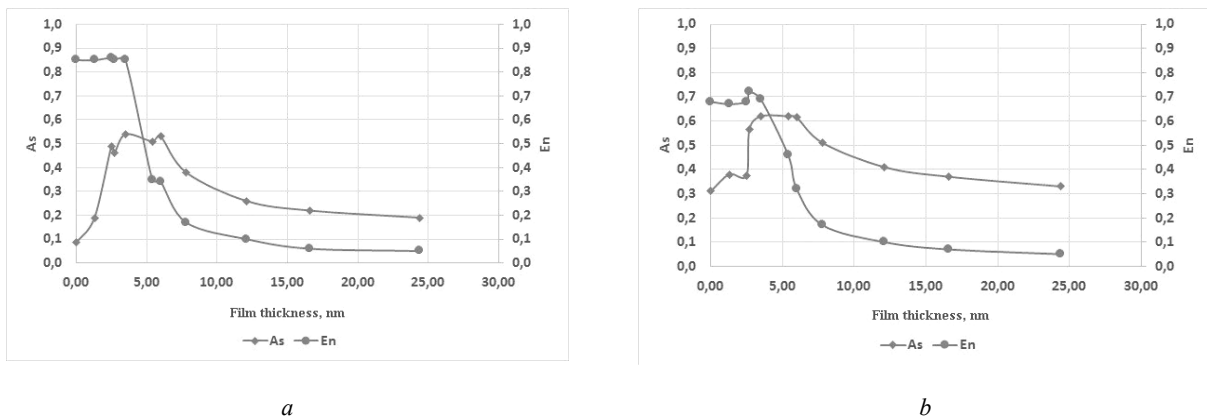
Fig. 9. Change of TRC optical characteristics depending on gold film thickness:
a – OSO-S; *b* – PM-OA

Рис. 9. Изменение оптических характеристик ТРП в зависимости от толщины пленки золота:
а – ОСО-С; *б* – ПМ-ОА
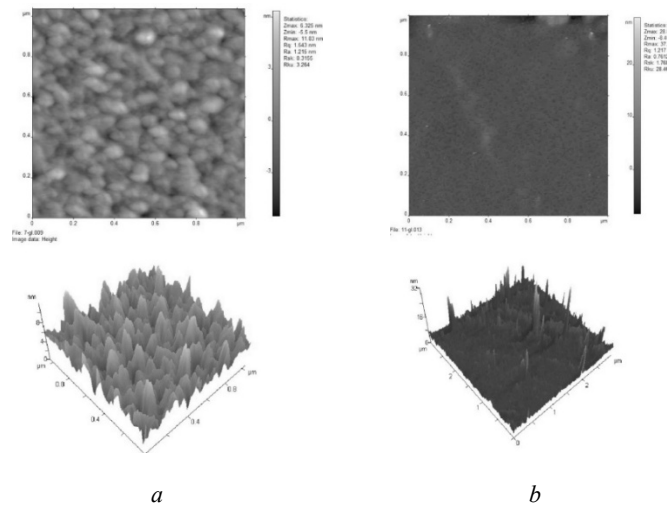
Fig. 10. AFM-images of contamination films on the OSO-S surface with
a film thickness of 2.7 nm (*a*) and 6 nm (*b*)

Рис. 10. АСМ-изображения пленок загрязнения на поверхности ОСО-С
при толщине пленки 2,7 нм (*а*) и 6 нм (*б*)

If we assume that the change in the ratio As/ε of TRC should not exceed 50 % of the initial value, from the data obtained it can be found that the permissible level of contamination of OSO-S with gold films is dlim = 0.3 nm ($6 \cdot 10^{-7}$ g / cm^2), and PM-OA – dlim = 1.7 nm ($3.5 \cdot 10^{-6}$ g / cm^2).

When thicker films are deposited ($d > 10^{-5}$ g / cm^2), the characteristics of the TRC change catastrophically. The emissivity decreases to 0.3, and the absorption coefficient increases 2–3 times. In this case, the *As*/ε ratio can increase by a factor of 5–10.

It should be noted that since under real SC operating conditions, pollution films contain not only metals, but also other particles (carbon, silicon, organic matter), the conductivity of the films and, accordingly, the change in the As coefficient will be less than that of films made of pure metal. Therefore, the above dlim estimates are worst case estimates.

Conclusion. As a result of a set of theoretical and experimental work to determine the effect of the plasma jet of correcting electric jet engines on the functional characteristics of spacecraft, results were obtained that are of significant interest and practical importance in the field of designing and ensuring the resistance of modern automatic spacecraft to the impact of man-made factors.

It has been established in this work that the effect of plasma jets of correcting engines can lead to significant sputtering of the reflective coating from the surface of the reflector of a large-size antenna.

It has been shown experimentally that the sputtering of the coating at the points of contact and interweaving of the threads under the action of the jet plasma of the engines occurs much less intensively, which causes relatively high values of the reflection coefficients measured on the samples of the mesh with high degrees of wear.

It has been established that the contamination of the optically sensitive SC surfaces with the products of LTA sputtering can be significant and should be taken into account when choosing the structural-layout scheme (SLS) of the SC.

The paper shows the fundamental possibility of creating modern automatic spacecraft, which include large-size antennas and electric jet engines. The implementation of this opportunity can be achieved by the appropriate choice of the SLS, taking into account this impact.

References

1. Testoyedov N. A., Kochura S. G., Maksimov I. A. [Study of the mechanisms and levels of the impact of the space environment on the spacecraft]. *Vestnik SibGAU* 2016, No. 6, P. 77–90 (In Russ.).

2. Maksimov I. A., Kochura S. G. *Issledovaniye vliyaniya faktorov kosmicheskogo prostranstva i tekhnogennykh faktorov na kosmicheskiye apparaty, razrabotka metodov i sredstv zashchity* [Study of the influence of space factors and man-made factors on spacecraft development of methods and means of protection]. Krasnoyarsk, 2011, 182 p.

3. Novikov L. S., Mileev V. N. et al. [Spacecraft charging in the magnetospheric plasma]. *Model kosmosa,* 2007, Vol. 2, 1127 p. (In Russ.).

4. Testoyedov N. A., Kochura S. G., Maksimov I. A. et al. [Erosion impact of plasma jets of electric propulsion engines on the network of large-size aerials of automatic spacecraft]. *Naukoyemkiye tekhnologii.* 2016, No. 7, P. 17 (In Russ.).

5. Vlasova N. A., Getselev I. V., Ivanova T. A. et al. [Monitoring the level of radiation conditions on high-apogee spacecraft]. *Kosmonavtika i raketostroenie.* 2003, No. 1(30), 6 p. (In Russ.).

6. Sosnovets E. N., Vlasova N. A., Ivanova T. A. et al. [Control of the level of radiation impact of cosmic radiation on geostationary spacecraft Express-A2, A3 in maximum of 23th solar activity cycle (2000–2002)]. *Voprosy atomnoy nauki i tekhniki. Seriya: fizika radiat-*

sionnogo vozdeystviya na radioelektronnuyu apparaturu. 2003, No. 1–2, P. 3–7 (In Russ.).

7. Nadiradze A. B., Rakhmatullin R. R., Kochura S. G. et al. [Features of the experimental determination of the resistance of composite materials to the erosion effect of STP]. *Vestnik SibGAU.* 2012, No. 1 (41), P. 91–96 (In Russ.).

8. Tverskaya L. V., Balashov S. V., Veden'kin N. N. et al. [Outer radiation belt of relativistic electrons in the 23rd solar cycle minimum]. *Geomagnetizm i aeronomiya.* 2012, Vol. 52, No. 6, P. 779–784 (In Russ.).

9. Ivanov V. V., Maksimov I. A., Nadiradze A. B. et al. [Methodology for ensuring the durability of onboard equipment and the spacecraft as a whole under SPT plasma conditions]. *Vestnik SibGAU.* 2006, No. 1 (8), P. 76–81 (In Russ.).

10. Nadiradze A. B., Maksimov I. A., Smirnov V. A. et al. [An experimental study of the contaminating effect of its own external atomosphere at the stage of orbital operation of a spacecraft]. *Vestnik SibGAU,* 2006, No. 1 (8), P. 91–96 (In Russ.).

11. Smirnov V. A., Shatrov A. K., Maksimov I. A. et al. [Study of the polluting effect of its own external atmosphere and plasma of SPT on spacecraft Express-AM]. *Vestnik SibGAU.* 2006, No. 2 (9), P. 46–50 (In Russ.).

12. Nadiradze A. B., Chirov A. A., Shaposhnikov V. V. et al.[Computional model of plasma penetration of electric propulsion engines into instrumental compartments of spacecraft]. *Vestnik SibGAU.* 2006, No. 3 (10), P. 49–52 (In Russ.).

13. Nadiradze A. B., Chirov A. A., Shaposhnikov V. V. et al. [Evaluation of the degassing time of a leaking equipment compartment]. *Vestnik SibGAU.* 2007, No. 1 (14). P. 95–99 (In Russ.).

14. Maksimov I. A., Smirnov V. A., Ivanov V. V., Nadiradze A. B. [Increasing the reliability of the leaky compartment of the spacecraft]. *Vestnik SibGAU.* 2007, No. 1 (14), P. 88–91 (In Russ.).

15. Smirnov V. A., Tibil'deyeva V. V., Maksimov I. A. et al. [Study of impact of SPT jets on structural elements of large-sized antennas]. *Vestnik SibGAU.* 2007, No. 1 (14), 7 p. (In Russ.).

16. Ivanov V. V., Maksimov I. A., Nadiradze A. B., Shaposhnikov V. V. [Mechanisms of the effect of the plasma of electric rocket engines on the operation of the onboard equipment of spacecraft]. *Vestnik SibGAU.* 2007, No. 3 (16), P. 87–91 (In Russ.).

17. Nadiradze A. B., Shaposhnikov V. V., Maksimov I. A. et al. [Selection of a ctriterion and cosiderration of the composition of pollution films when assessing the joint polluting effect of its own external atmosphere and stationary plasma engines]. *Vestnik SibGAU.* 2007, No 4 (17), P. 91–94 (In Russ.).

18. Nadiradze A. B., Shaposhnikov V. V., Smirnov V. A. et al. [Study of the erosion effect of jets of SPT on radio-reflecting set-cloth of large-sized aerials of spacecraft]. *Vestnik SibGAU.* 2008, No. 4 (21), P. 120–124 (In Russ.).

19. Ivanov V. V., Maksimov I. A., Nadiradze A. B., Shaposhnikov V. V., Smirnov V. A. [Model of penetration of plasma formations formed during the operation of electric propulsion engines into non-hermetic equipment compartment of spacecraft]. *Materialy mezhdunarodnoy konferentsii "Aviatsiya i kosmonavtika".* Moscow, 2006, P. 357 (In Russ.).

20. Kim V. P., Nadiradze A. B., Popov G. A. et al. [Problems of using electric rocket engines on spacecraft]. *V kn. "Model' kosmosa", Vol. 2 «Vozdeystviye kosmicheskoy sredy na materialy i oborudovaniye kosmicheskikh apparatov».* Ed. L. S. Novikova. Moscow, Universitet Publ., 2007, P. 615–659.

21. Balashov S. V., Blyakharskiy Ya. S., Nadiradze A. B. [Calculation of sputtering characteristics of mesh surfaces when exposed to them by plasma jets of SPT]. *tezisy dokladov XXI Mezhdunarodnoy konferentsii po Vychislitel'noy mekhanike i sovremennym pricladnym programmnym systemam* (VMSPPS'2019). 2019, Alushta (In Russ.).

Библиографические ссылки

1. Тестоедов Н. А., Кочура С. Г., Максимов И. А. Исследование механизмов и уровней воздействия космической среды на космический аппарат // Вестник СибГАУ. 2016. № 6. С. 77–90.

2. Максимов И. А., Кочура С. Г. Исследование влияния факторов космического пространства и техногенных факторов на космические аппараты, разработка методов и средств защиты : монография / СибГАУ. Красноярск, 2011. 182 с.

3 Модель Космоса. Т. 2, гл. 1.1 Моделирование процессов формирования СВА и загрязнения поверхности КА / А. Б. Надирадзе, В. В. Шапошников, В. В. Хартов и др. М. : Университет, 2007. 20 с.

4. Эрозионное воздействие плазменных струй электрореактивных двигателей на сетеполотно рефлекторов крупногабаритных антенн автоматических космических аппаратов / Н. А. Тестоедов, С. Г. Кочура, И. А. Максимов и др. // Наукоемкие технологии. 2016. Т. 17. С. 46–49.

5. Контроль радиационной обстановки на высокоапогейных космических аппаратах / Н. А. Власова, И. В. Гецелев, Т. А. Иванова и др. // Космонавтика и ракетостроение. 2003. Вып. 1(30). 6 с.

6. Контроль уровня радиационного воздействия космических излучений на геостационарные КА «Экспресс-А2, А3» в максимуме 23-го цикла солнечной активности (2000-2002 гг.) / Э. Н. Сосновец, Н. А. Власова, Т. А. Иванова и др. // Вопросы атомной науки и техники. Серия: физика радиационного воздействия на радиоэлектронную аппаратуру. 2003. № 1–2. С. 3–7.

7. Особенности экспериментального определения стойкости композиционных материалов к эрозионному воздействию струй стационарных плазменных двигателей / А. Б. Надирадзе, Р. Р. Рахматуллин, С. Г. Кочура и др. // Вестник СибГАУ. 2012. № 1 (41). С. 91–96.

8. Внешний радиационный пояс релятивистских электронов в минимуме 23-го цикла солнечной активности / Л. В. Тверская, С. В. Балашов, Н. Н. Веденькин и др. // Геомагнетизм и аэрономия. 2012. Т. 52, № 6. С. 779–784.

9. Методология обеспечения стойкости бортовой аппаратуры и космического аппарата в целом в условиях плазмы, формируемой стационарными плазменными двигателями / В. В. Иванов, И. А. Максимов,

А. Б. Надирадзе и др. // Вестник СибГАУ. 2006. № 1 (8). С. 76–81.

10. Экспериментальное исследование загрязняющего воздействия собственной внешней атмосферы на этапе орбитальной эксплуатации космического аппарата / А. Б. Надирадзе, И. А. Максимов, В. А. Смирнов и др. // Вестник СибГАУ. 2006. № 1 (8). С. 91–96.

11. Исследование загрязняющего воздействия собственной внешней атмосферы и плазмы стационарных плазменных двигателей на КА «Экспресс-АМ» / В. А. Смирнов, А. К. Шатров, И. А. Максимов и др. // Вестник СибГАУ. 2006. № 2 (9). С. 46–50.

12. Расчетная модель для оценки проникания плазмы электроракетных двигателей в приборные отсеки космического аппарата / В. В. Иванов, И. А. Максимов, А. Б. Надирадзе и др. // Вестник СибГАУ. 2006. № 3 (10). С. 49–52.

13. Оценка времени обезгаживания негерметичного приборного отсека космического аппарата / А. Б. Надирадзе, А. А. Чиров, В. В. Шапошников и др. // Вестник СибГАУ. 2007. № 1 (14). С. 95–99.

14. Повышение надежности негерметичного отсека космического аппарата / И. А. Максимов, В. А. Смирнов, В. В. Иванов, А. Б. Надирадзе // Вестник СибГАУ. 2007, № 1 (14). С. 88–91.

15. Исследование воздействия струй электроракетных двигателей на элементы конструкции крупногабаритных антенн / В. А. Смирнов, В. В. Тибильдеева, И. А. Максимов и др. // Вестник СибГАУ. 2007. Прилож. к № 1 (14). 7 с.

16. Механизмы воздействия плазмы электроракетных двигателей на работу бортовой аппаратуры космических аппаратов / В. В. Иванов, И. А. Максимов, А. Б. Надирадзе, В. В. Шапошников // Вестник СибГАУ. 2007. № 3 (16). С. 87–91.

17. Выбор критерия и учет состава пленок загрязнения при оценках совместного загрязняющего воздействия собственной внешней атмосферы и стационарных плазменных двигателей / А. Б. Надирадзе, В. В. Шапошников, И. А. Максимов и др. // Вестник СибГАУ. 2007. № 4 (17). С. 91–94.

18. Исследование эрозийного воздействия струй стационарных плазменных двигателей на радиоотражающее сетеполотно крупногабаритных антенн космических аппаратов / А. Б. Надирадзе, В. В. Шапошников, В. А. Смирнов и др. // Вестник СибГАУ. 2008. № 4 (21). С. 120–124.

19. Модель проникания плазменных образований, формируемых при работе электроракетных двигателей, в негерметичные приборные отсеки космических аппаратов / В. В. Иванов, И. А. Максимов, А. Б. Надирадзе и др. // Авиация и космонавтика : материалы международ. конф. М., 2006. С. 357.

20. Проблемы применения электроракетных двигателей на космических аппаратах : в кн. «Модель космоса» ; 8-е изд. Т. 2 «Воздействие космической среды на материалы и оборудование космических аппаратов» / В. П. Ким, А. Б. Надирадзе, Г. А. Попов и др. ; под ред. проф. Л. С. Новикова. М. : Университет, 2007. С. 615–659.

21. Балашов С. В., Бляхарский Я. С., Надирадзе А. Б. Расчет характеристик распыления сетчатых поверхностей при воздействии на них плазменных струй электроракетных двигателей // Тез. докладов XXI Междунар. конф. по вычислительной механике и современным прикладным программным системам (ВМСППС'2019). 24–31 мая 2019 г. Алушта, Крым.

Nadiradze Andrey Borisovich – Dr. Sc., professo; Moscow aviation institute (national research university). E-mail: nadiradze@mai.ru.

Tikhomirov Roman Evgen'evich – head of the group; JSC Academician M. F. Reshetnev "Information satellite systems". E-mail: tikhroman@iss-reshetnev.ru.

Maximov Igor Aleksandrovich – Dr. Sc., head of the department; JSC Academician M. F. Reshetnev "Information satellite systems". E-mail: mia@iss-reshetnetv.ru.

Kochura Sergey Grigor'evich – Cand. Sc., deputy general designer; JSC Academician M. F. Reshetnev "Information satellite systems". E-mail: kochura@iss-reshetnev.ru.

Balashow Sergey Vladimirovich – head of the sector; JSC Academician M. F. Reshetnev "Information satellite systems". E-mail: balashow@iss-reshetnev.ru.

Надирадзе Андрей Борисович – доктор технических наук, профессор; Московский авиационный институт (национальный исследовательский университет). E-mail: nadiradze@mai.ru.

Тихомиров Роман Евгеньевич – начальник группы; АО «Информационные спутниковые системы» имени академика М. Ф. Решетнёва». E-mail: tikhroman@iss-reshetnev.ru.

Максимов Игорь Александрович – доктор технических наук, начальник отдела; АО «Информационные спутниковые системы» имени академика М. Ф. Решетнёва». E-mail: mia@iss-reshetnetv.ru.

Кочура Сергей Григорьевич – кандидат технических наук, заместитель генерального конструктора по электрическому проектированию и системам управления КА; АО «Информационные спутниковые системы» имени академика М. Ф. Решетнёва». E-mail: kochura@iss-reshetnev.ru.

Балашов Сергей Владимирович – начальник сектора; АО «Информационные спутниковые системы» имени академика М. Ф. Решетнёва». E-mail: balashow@iss-reshetnev.ru.

IMPACT OF THE REINFORCEMENT TECHNIQUE ON CHARACTERISTICS OF COMPOSITE TUBULAR STRUCTURES

E. A. Trifonova[1]*, A. V. Zhukov[1], V. V. Savitsky[1], V. V. Batrakov[2]

[1]JSC Academician M. F. Reshetnev "Information satellite systems"
52, Lenin St., Zheleznogorsk, Krasnoyarsk region, 662972, Russian Federation
[2] Kazan National Research Technical University named after A. N. Tupolev
10, K. Marks St., Kazan, Republic of Tatarstan, 420111, Russian Federation
*E-mail: trifonova@iss-reshetnev.ru

Different composite elements including tubular structures are used as support structures in spacecraft optical systems. The compliance with the specified dimensional stability over a wide temperature range, in particular from –269 up to 100 °C, is important for the design of tubular structures. The promising method of manufacturing tubular structures of CM – radial braiding combined with RTM molding method is discussed in this paper. In addition, the paper describes the method of determining the optimal reinforcement technique for a braided perform which allows to reduce geometrical deflections occurring during a molding process. The impact of the reinforcement technique on the dimensional stability of tubular structures is illustrated in this paper by the example of several reinforcement techniques and manufacturing methods. The paper also contains the analysis of these techniques and the determination of the optimal one to comply with the specified characteristics.

Keywords: dimensional stability, composite materials, reinforcement technique, preform.

ВЛИЯНИЕ СХЕМЫ АРМИРОВАНИЯ НА ХАРАКТЕРИСТИКИ КОМПОЗИЦИОННЫХ ТРУБЧАТЫХ КОНСТРУКЦИЙ

Е. А. Трифонова[1], А. В. Жуков[1], В. В. Савицкий[1], В. В. Батраков[2]

[1] АО «Информационные спутниковые системы» имени академика М. Ф. Решетнёва»
Российская Федерация, 662972, г. Железногорск Красноярского края, ул. Ленина, 52
[2]Казанский национальный исследовательский технический университет имени А. Н. Туполева – КАИ
Российская Федерация, 420111, Республика Татарстан, г. Казань, ул. К. Маркса, 10
E-mail: trifonova@iss-reshetnev.ru

В оптических системах космических аппаратов в качестве опорных конструкций применяются различные композитные элементы, в том числе и трубчатые. При проектировании трубчатых элементов актуальным является вопрос обеспечения заданной размеростабильности в широком диапазоне температур, а именно от –269 до +100 °C. В работе рассматривается перспективный способ изготовления трубчатых элементов из КМ – радиального плетения в сочетании с RTM методом формования. Помимо этого, в данной работе изложена методика определения оптимальной схемы армирования плетеной преформы, позволяющая снизить возникающие в процессе формования геометрические отклонения. Влияние схемы армирования на размеростабильность трубчатых конструкций рассматривается на примере нескольких схем армирования и способов изготовления, проводится анализ этих схем и определение оптимальной для обеспечения заданных характеристик.

Ключевые слова: размеростабильность, композитные материалы, схема армирования, преформа.

Introduction. Composite materials (CM) occupy a significant part among materials used in the manufacture of spacecraft structures. Their advantages over traditional materials are the combination of such properties as high strength, stiffness, low coefficient of thermal expansion. The use of CM in spacecraft design has made it possible to significantly reduce the weight characteristics of modern spacecraft, and it has expanded the capabilities

of designers in the search of new solutions and design features in the development of a spacecraft body, assemblies and critical parts.

A distinctive feature of CM structures is that the material and structure are manufactured simultaneously. Therefore, the technological features of the production of the material, which make it possible to provide the specified parameters, are taken into account in the process of developing a composite structure. Thus, the CM manufacturing technology is an integral part of a composite structure design process.

Currently, Russian and foreign specialists are working on the creation of space observatories. Modern space observatories are designed to undertake studies of various types of objects in the Universe with ultra-high sensitivity (in single-telescope mode) and record high angular resolution (in ground-space interferometer mode) in the millimeter and infrared wavelength ranges. The ultra-high sensitivity of a space telescope operating in deep vacuum and ultra-low temperatures is achieved by actively cooling the mirror system and receiving equipment to the temperature of 4.5 K. The record resolution of the cryogenic space telescope is achieved by its joint work with large ground-based telescopes in interferometer mode in an ultra-long working orbit in the vicinity of the L2 Lagrange point in the Sun – Earth system that is located at the distance of 1.5 million km from the Earth. In this case, the distance between the Earth and the space observatory will reach 2 million km. The space observatory includes a two-mirror cryogenic space telescope with a main parabolic mirror with a diameter of 10 m deployable in the specified orbit, consisting of 24 deployable lobes and a stationary central mirror of 3 m in diameter. This telescope is installed on the space platform through a transitional truss and central power structures: reflector supporting truss, cooling support and unrefrigerated container. The working ranges of the wavelengths of the cryogenic space telescope are 0.02–3 mm and 0.3–16 mm and they determine the requirements for the cryogenic space telescope precision and the space platform: the accuracy of the working surface (standard deflection) of the main parabolic mirror (after its opening) is 10 μm; the accuracy of orientation and stabilization of a space platform with a cryogenic space telescope should be no worse than 1 "and 0.2", respectively [1].

The quality of data obtained from outer space depends, among other things, on the accuracy of the mutual positioning of the components of the telescope (including the counter-reflector relative to the reflector). The layout chart of the shape and size-stable tubular elements (rods) in the structure of the space observatory, providing positioning of the reflector and counter-reflector, is shown in fig. 1.

To ensure the functioning of the telescope in case of failure of orbital alignment mechanisms, the supporting elements of a counter-reflector structure must ensure the accuracy of the position of the main elements of the optical system after launching spacecraft into orbit. The design of a supporting tubular structure should exclude the occurrence of deformations leading to twisting around its longitudinal axis by more than 1' in the operating temperature range.

To ensure the structural rigidity at the stage of launching, it is advisable to fix screen lobes to the telescope counter-reflector [2]. Based on the task of the supporting tubular structure of a counter-reflector, they need to have high strength and stiffness characteristics, such as:

– elasticity modulus in the direction along its axis of a supporting tubular structure must be at minimum 200 GPa;

– ultimate compression strength in the direction along the axis must be at minimum 800 MPa;

– the coefficient of linear thermal expansion along the axis of a supporting tubular structure should be no more than $|0,8 \times 10{-}6|$ 1/°C in the temperature range from minus 269 to plus 100 °C.

Thus, one of the main elements being investigated in this work are tubular structures – rods made of composite material with high requirements for rigidity, strength, and shape stability.

The overview of the methods of manufacturing tubular structures. The analysis of the factors influencing dimensional stability. Currently, the main methods for the manufacture of tubular structures made of CM are:

– contact molding with the laying of a resin-impregnated fibrous canvas on the mold;

– winding resin-impregnated fiber onto a cylindrical shape;

– pultrusion or molding of shaped products by pulling a fiber through a polymer bath and a gage die hole;

– radial braiding in combination with RTM technology [3–8].

Radial braiding is the most suitable method to manufacture tubular products that meet specified parameters. The product is usually obtained by braiding the mandrel. Unlike threads during winding, during radial braiding threads are intertwined. This ensures that the braided part resists twisting and shearing.

The result is a seamless design with high structural integrity. In the course of its development, the technology of the braiding process has shown its advantages, such as reducing production costs due to the mechanization of the process and reducing the share of manual labor, the possibility of using it in serial production. The braiding process is shown in fig. 2.

Typical reinforcement of braided preforms can be biaxial and triaxial (fig. 3, *a*). At triaxial braiding (fig. 3, *b*), the third thread is added in the longitudinal direction, along the braiding axis.

At biaxial braiding, the braiding angle can vary from 10 to 85 degrees. Parts with small braiding angles are characterized by high axial strength and rigidity, while parts with large braiding angles have high circumferential strength.

This technology allows us to braid any type of reinforcing material – carbon fiber, glass fiber, aramid fiber, natural fiber, etc., as well as to combine various types of fibers [9–12].

The RTM molding method is the process of impregnating a reinforcing material with a binder substance that is injected under excessive pressure (up to 10 bar) into a closed rigid mold. The process allows us to achieve high precision manufacturing of parts. This method makes it

possible to manufacture parts with volumetric filling with a reinforcing material 55 ± 5%. The scheme of the method is shown in fig. 4.

One of the most important indicators of the shape stability of tubular structures is the minimization of their rotation along the axis.

In theory, a properly designed tubular structure with an ideal reinforcing structure should not twist when thermally loaded. However, in practice, it is almost impossible to obtain such an element. Twisting of tubular structures can occur both due to structural and technological imperfections.

Constructive imperfections include deflection from symmetry in the laying, the presence of additional elements, etc. Accordingly, the most advanced design is a cylindrical tubular structure without fittings and flanges with a constant wall thickness and balanced quasi-isotropic laying. However, in this case, it will be impossible to obtain required axial physical and mechanical characteristics and a low CLTE (coefficient of linear thermal expansion). As a rule, when designing a supporting tubular structure, it is necessary to find a reasonable compromise between stiffness, strength, CLTE, shape stability, integrity, and manufacturability.
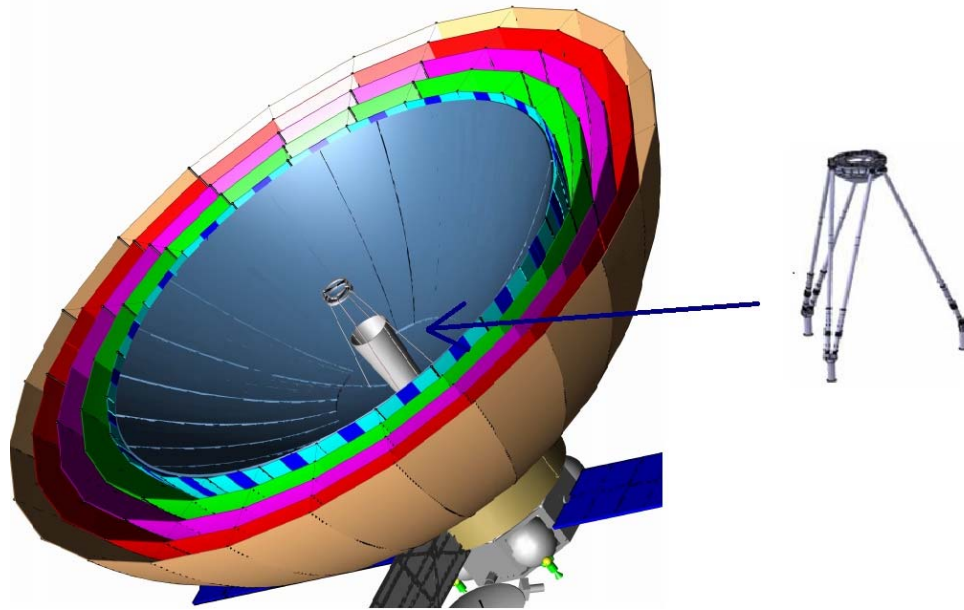

Fig. 1. Layout chart of the supporting tubular structure in the construction of space observatory

Рис. 1. Схема расположения опорного трубчатого элемента
в конструкции космической обсерватории

Fig. 2. Process of radial braiding of a tubular structure

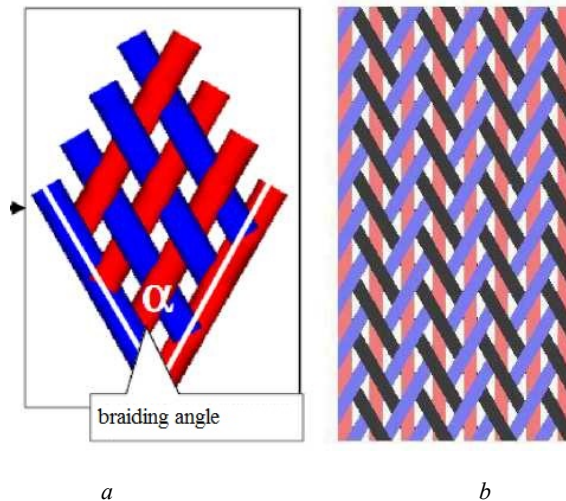Рис. 2. Процесс плетения трубчатого элемента

Fig. 3. Type of braiding:
a – biaxial braiding; *b* – triaxle braiding

Рис. 3. Виды плетения:
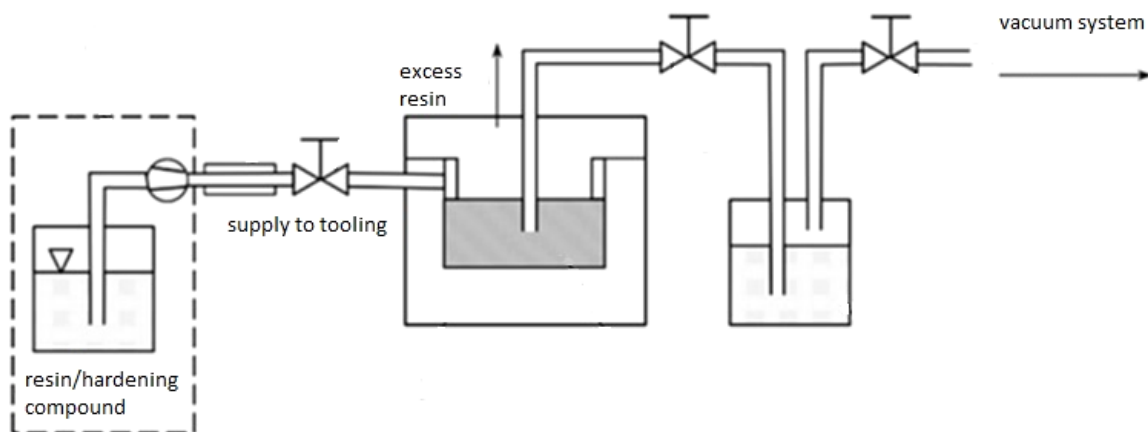*а* – двухосное плетение; *б* – трехосное плетение

Fig. 4. RTM molding method diagram

Рис. 4. Схема метода формования RTM

Even if the design of a tubular structure has no flaws, certain deflections necessarily occur during its manufacture. The deflections may include:

– unevenness and deflection from a given angle of reinforcement;

– uneven filling ratio;

– difference in properties of reinforcing fibers from different batches;

– the influence of molding equipment during heating and cooling.

The manufacture of a shape-stable tubular structure requires solutions that are clearly verified at every stage.

In this work, the following main proposals of a constructive and technological nature are made:

– the layers of the reinforcing structure of a supporting tubular structure must have a symmetrical – balanced triaxial structure;

– technological slope for mandrel extraction should be minimal;

– the reinforcement scheme should provide the least sensitivity of shape stability to technological deflections, while maintaining the required physical and mechanical characteristics;

– deflections from the nominal reinforcement angle and the filling factor should be minimized;

– when designing supporting tubular structures, it is necessary to take into account the probability of micro-cracking during thermal cycling [13–15].

Developing a method for calculating the deformations of a supporting tubular structure when subjected to thermal loadings. The purpose of the calculation is to determine the optimal reinforcement scheme in which the effect of structural and technological imperfections on the value of the angle of twisting of a

supporting tubular structure relative to the longitudinal axis will be minimal.

For the triaxial reinforcement scheme 0±φ°, where φ is the angle of symmetric oblique fibers, the following problems were solved:

1) the angles of rotation of a supporting tubular structure relative to the longitudinal axis are determined for the angles of oblique symmetrical fibers 5–90 ° with an error of the braiding angles of longitudinal and oblique fibers equal to 0.5 ° and 1.0 ° for their ratios of 7, 15 and 20 %, and for temperature gradients −100/+20, −100/+100 and +20/–269 °C;

2) the dependences of the longitudinal modulus of elasticity, strength and coefficient of linear thermal expansion (CLTE) on the ratio of longitudinal and oblique symmetric fibers for the optimal reinforcement angle were determined;

The design of a supporting tubular structure is shown in fig. 5.

The calculation was carried out in the Femap with NX Nastran program. The finite element mesh of the models of the supporting tubular structure is shown in fig. 6. The temperature loading was set in the form of a temperature difference and fixing along one of the ends with a restriction of 6 degrees of freedom (rigid restraint) was performed.

To calculate a supporting tubular structure, the shell elements PLATE and LAMINATE from the Femap with NX Nastran finite element library were used.

PLATE is a combined flat shell element (fig. 7, *a*) that bears membrane, shear and bending loads. It is used for any structures consisting of thin plates or shells.

Setting the desired direction of material properties is carried out by rotating the axis of orientation of the Xm material.

LAMINATE (layered) is similar to an element of type PLATE and consists of one or more layers (fig. 7, *b*). It is used for modeling multilayer composite plates and shells. The internal coordinate system is similar to the elements of the PLATE type. Setting the desired direction of mate-

rial properties is carried out by rotating the axis of orientation of Xm material properties.

The direction of the Z axis is taken as the zero direction of fibers (fig. 7). Counterclockwise direction is taken as a positive angle.

The following model of a composite with a reinforcing filler made by the radial braiding method was taken. The wall of the supporting tubular structure with total thickness h consists of n layers. One layer conventionally represents interlaced fibers with the orientation of 0° (along the generatrix of the cylinder) and ±φ° (oblique fibers) and has a total thickness t. Each of the n layers of thickness t was divided into 5 more sublayers with an average sublayer with the orientation of 0° and extreme sublayers ± φ ° to balance the package (fig. 8, *a*).

To take into account the volume ratio of longitudinal and oblique fibers vf0 and vfφ %, respectively, the thicknesses of sublayers were set in proportion to this ratio: 0,01·vf0·t – 0° sublayer; 0,01·vf0·t – sublayers ±φ °.

The scheme for determining the angles φ of symmetric oblique fibers and the deflection error Δ is shown in fig. 8, *b*.

The characteristics of carbon fiber-reinforced plastics with M46J fibers and the characteristics of carbon fiber-reinforced plastics with T300 fibers are presented in table.

Calculation of the axial twist of a supporting tubular structure depending on the reinforcement error. Let us determine the angles of rotation of a supporting tubular structure relative to the longitudinal axis for different angles of reinforcement with the axial fibers M46J and oblique fibers T300, depending on the error of braiding angles, the ratio of longitudinal and oblique fibers, and the temperature gradient.

The wall thickness of the supporting tubular structure is *h* = 3.5 mm. The number of layers *n* = 14.

To take into account the ratio of longitudinal and oblique fibers equal to 93 and 7 %, respectively, the thicknesses of the sublayers were set in proportion to this ratio: 0.2325 mm – 0° sublayer; 4×0.004375 mm – sublayers ±φ °.

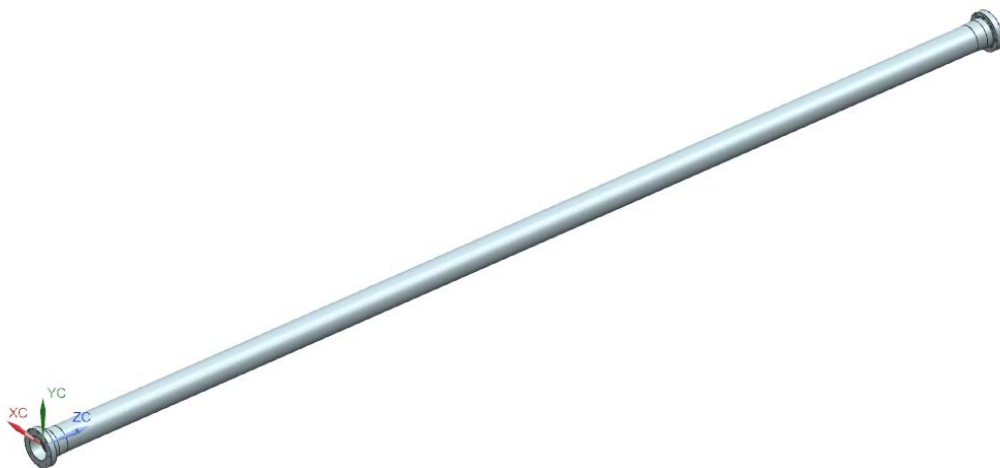Fig. 5. Construction of a supporting tubular structure

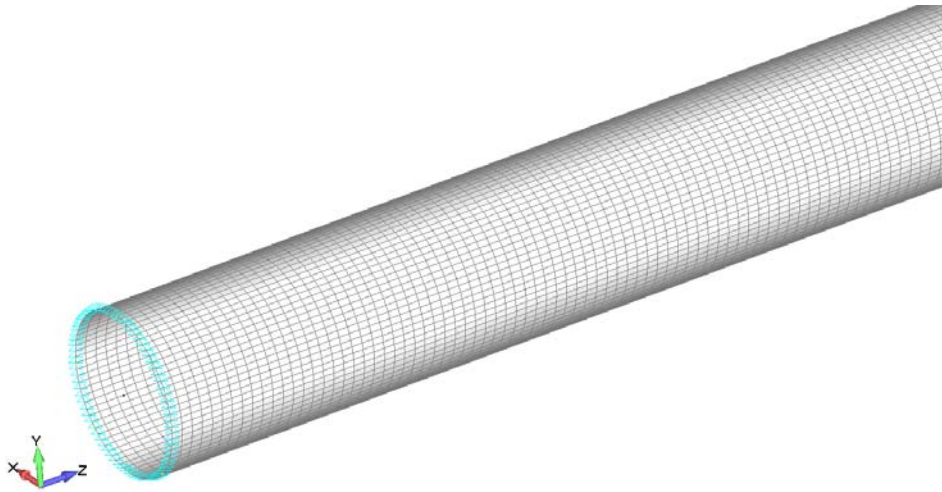Рис. 5. Конструкция опорного трубчатого элемента

Fig. 6. Finite-element model mesh of a supporting tubular structure without flange

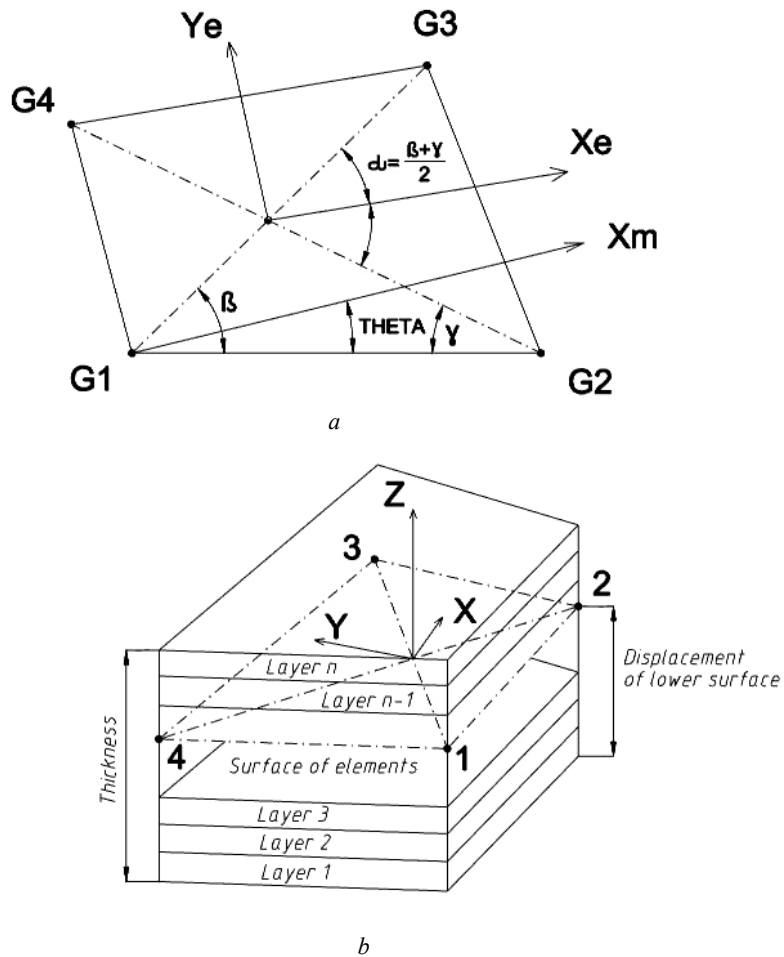Рис. 6. Конечно-элементная сетка модели опорного трубчатого элемента без фланца

a

b

Fig. 7. Shell element:
a – PLATE type; *b* – LAMINATE type

Рис. 7. Оболочечный элемент:
a – типа PLATE; *б* – типа LAMINATE
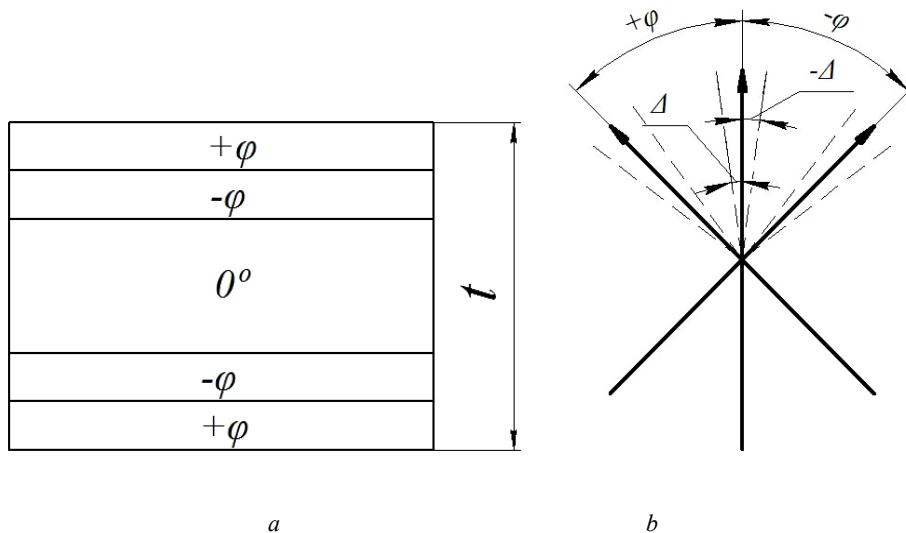
a   *b*

Fig. 8. Single layer scheme, scheme for determining the angles of oblique fibers and errors:
a – one layer; *b* – location of oblique fibers

Рис. 8. Схема одного слоя, схема определения углов косых волокон и погрешностей:
а – один слой; *б* – расположение косых волокон

Characteristics of carbon fiber-reinforced plastics used for calculation

Modulus of elasticity	Parameter	Carbon fiber M46J	Carbon fiber T300
Modulus of tension (0°)	E_1, Pa	2.45E+11	1.25E+11
Modulus of tension (90°)	E_2, Pa	6.9E+9	7.8E+9
Modulus of shear	G_{12}, Pa	3.9E+9	4.4E+9
Poison's ratio	μ_{12}	0.87	0.79
Longitudinal strength (0°)	σ^+_{B1}, Pa	2.16E+9	1.76E+9
Longitudinal strength (90°)	σ^+_{B2}, Pa	45000000	80000000
Compression strength (0°)	σ_{B1}, Pa	980000000	1.57E+9
Compression strength (90°)	σ_{B2}, Pa	0 (no information available)	0 (no information available)
In-plane shear strength	τ_{B12}, Pa	59000000	98000000
Interlaminar shear strength	$\tau13$, Pa	83000000	108000000
Monolayer thickness	δ, m	0.00025	–
CLTE of fiber (longitudinal direction)	$\alpha1$, 1/C°	–4,E-7	9,E-7
CLTE of matrices (orthogonal direction)	$\alpha2$, 1/C°	3.75E-5	3.75E-5

For the ratio of longitudinal and oblique fibers equal to 85 and 15 %, respectively, the thickness of the sublayers: 0.2125 mm – 0° sublayer; 4×0.0375 mm – sublayers ±φ°.

For the ratio of longitudinal and oblique fibers equal to 80 and 20 %, respectively, the thickness of the sublayers: 0.2 mm – 0° sublayer; 4×0.05 mm – sublayers ±φ°.

The total number of layers was 14×5 = 70 in all cases.

The possibility of deflection of longitudinal and oblique fibers in one direction or in opposite directions was taken into account.

The calculation results are shown in fig. 9–12.

Determination of the optimal reinforcement scheme. Based on the analysis of the graphs in fig. 9–12, the following conclusions can be drawn:

– the swirl angle of the supporting tubular structure increases when increasing the deflection error of longitudinal and oblique symmetrical fibers;

– when the longitudinal and oblique fibers are deflected in one direction at the reinforcement angles ±φ° up to 40°, the swirl angle of the supporting tubular structure increases when increasing the proportion of oblique fibers;

– when the longitudinal and oblique fibers are deflected in one direction at the reinforcement angles ±φ° more than 40°, the swirl angle of the rod decreases when increasing the proportion of oblique fibers;

– when the longitudinal and oblique fibers are deflected in opposite directions at the reinforcement angles ±φ° up to 70°, the swirl angle of the supporting tubular structure increases when decreasing the proportion of oblique fibers;

– when the longitudinal and oblique fibers are deflected in opposite directions at reinforcement angles ±φ° more than 70°, the swirl angle of the supporting tubular element decreases when decreasing the proportion of oblique fibers;

– with a certain proportion of oblique symmetric fibers, there are two values of the reinforcement angles at which the swirl angle of the supporting tubular structure will be zero for the case of deflection of longitudinal and oblique fibers in opposite directions;

– at the reinforcement angles $\pm\varphi° = 60°$, it is optimal if two types of error appear – when longitudinal and oblique fibers deflect in one direction or in the opposite direction.

Determination of the reinforcement scheme that meets the requirements for the physical and mechanical characteristics of the material of the supporting tubular structure. Using the Femap with NX Nastran program, the dependence of the axial modulus Ez of elasticity and axial CLTE αz on the volume fraction of oblique symmetric fibers (fig. 13, 14) was determined for the following design:

– wall thickness of the supporting tubular element h = 3.5 mm;

– number of layers n = 14;

– laying 0 ± 60 ° with axial fibers M46J and oblique T300, respectively, with the composite volumetric filling of 60%.

Using the Femap with NX Nastran program, the dependence of the axial modulus Ez of elasticity and axial CLTE αz on the volume fraction of oblique symmetric fibers (fig. 15, 16) was determined for the following design:

– wall thickness of the supporting tubular structure h = 3.5 mm;

– number of layers n = 14;

– laying 0 ± 4 ° with M46J fibers with a composite volumetric filling of 60 %.

The following conclusions can be drawn from the analysis of the graphs:

– laying $0 \pm 60°$ with M46J and T300 fibers allows obtaining the required axial CLTE αz with the fraction of oblique fibers up to 48 %, but the required axial modulus of elasticity Ez with the fraction of oblique fibers may only be up to 20 %;

– laying 0 ± 14 ° with M46J fiber allows to obtain the required axial CLTE αz with the proportion of oblique fibers up to 23 % (taking into account technological limitations, the amount of oblique fibers is 50.75 %), the required axial modulus of elasticity Ez with the proportion of oblique fibers is up to 75 %;

– laying $0 \pm 60°$ with M46J and T300 fibers is less sensitive to the influence of structural and technological imperfections on the value of the swirl angle of the supporting tubular structure relative to the longitudinal axis;

– laying $0 \pm 60°$ with M46J and T300 fibers meets the requirements for axial modulus of elasticity and CLTE with oblique fibers up to 20 % and has approximately 2 times less torsion around the longitudinal axis compared to the laying $0 \pm 14°$.

Fig. 9. Swirl angle at deflection of longitudinal and oblique fibers in one direction by 0.5 and 1.0 degrees. Temperature range +20/–269 °C

Рис. 9. Угол закрутки при отклонении продольных и косых волокон в одном направлении на 0,5° и на 1,0°. Диапазон температур +20/–269 °C
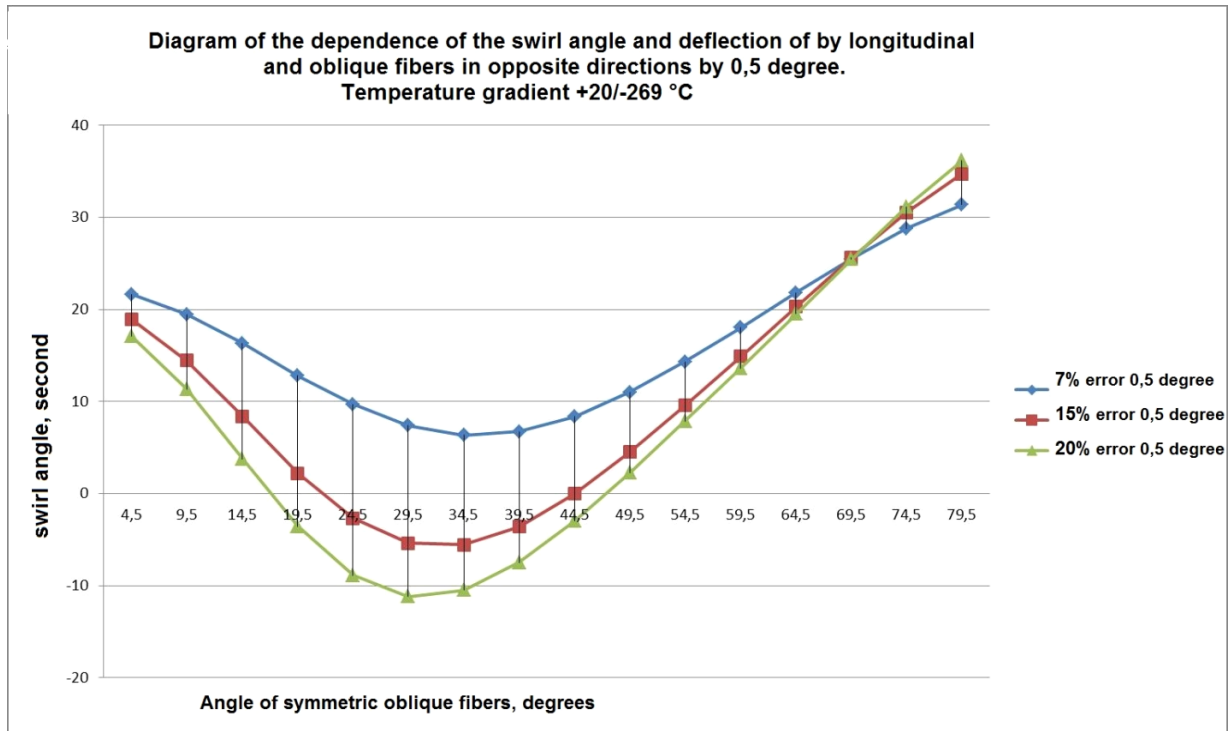
Fig. 10. Swirl angle at deflection of longitudinal and oblique fibers in opposite directions by 0,5 degree.
Temperature range +20/–269 °C

Рис. 10. Угол закрутки при отклонении продольных и косых волокон в противоположных направлениях на 0,5°.
Диапазон температур +20/–269 °C
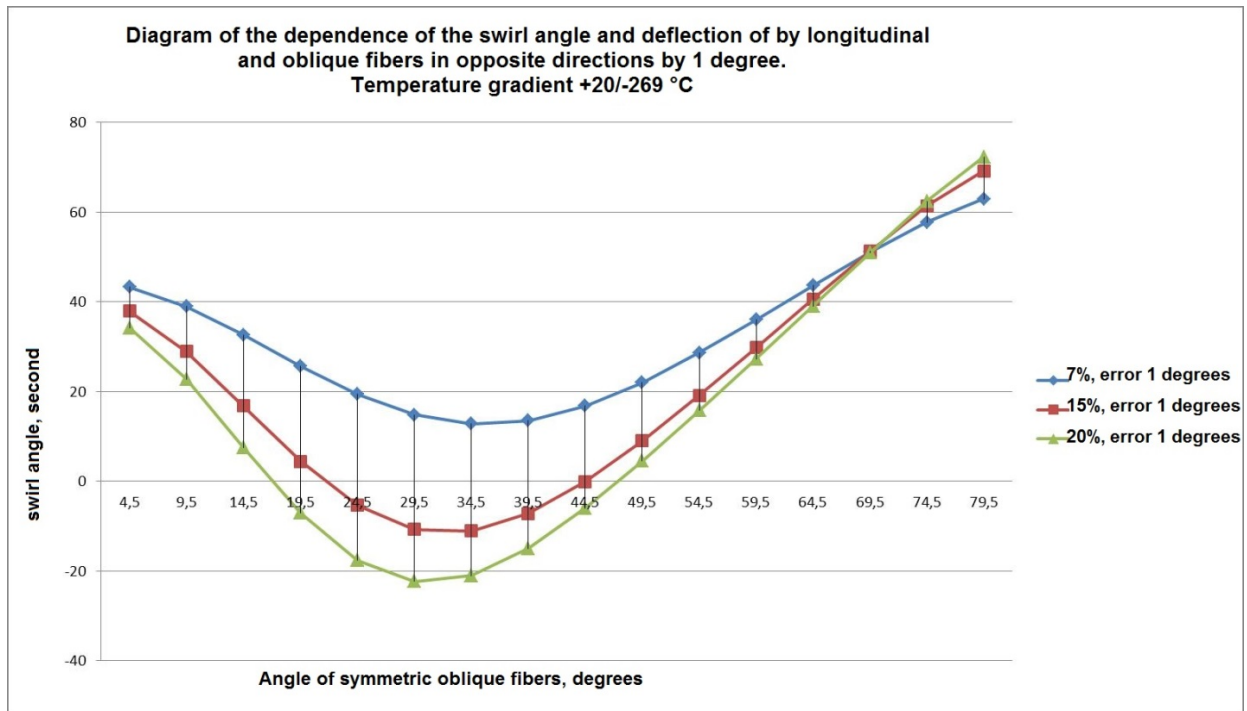
Fig. 11. Swirl angle at deflection of longitudinal and oblique fibers in opposite directions by 1 degree.
Temperature range +20/–269 °C

Рис. 11. Угол закрутки при отклонении продольных и косых волокон в противоположных направлениях на 1,0°.
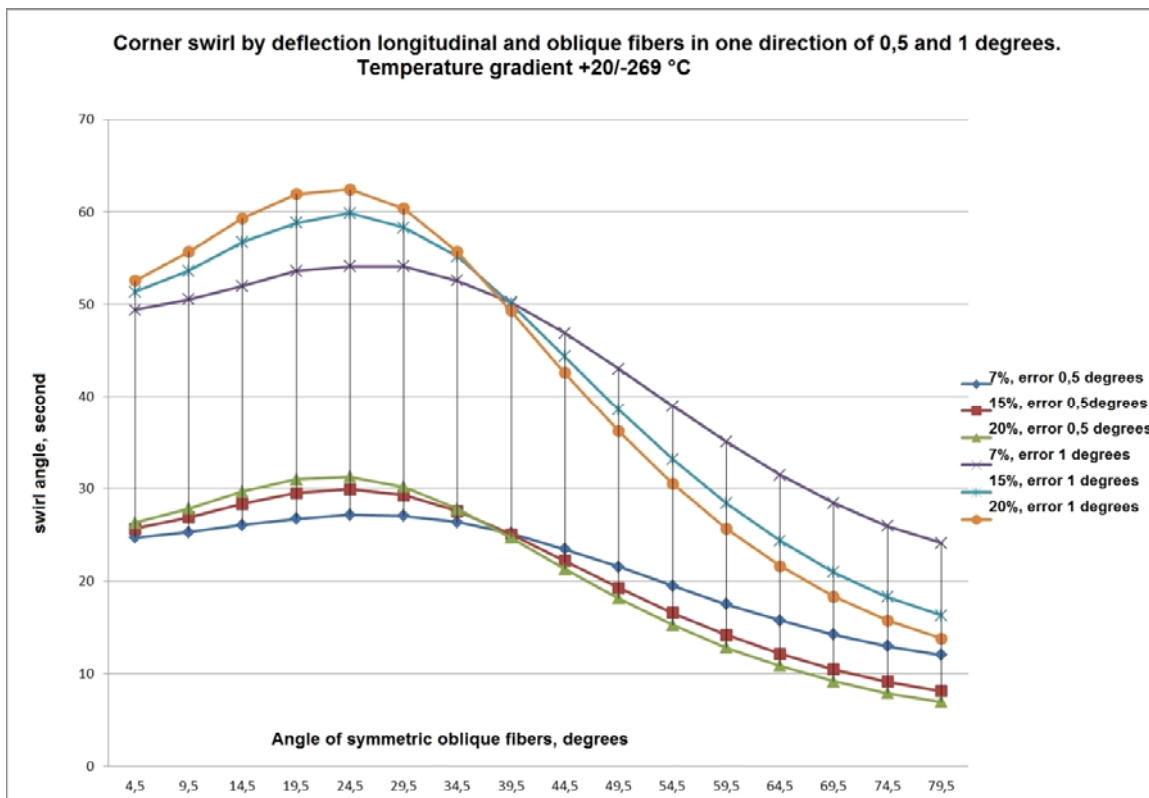Диапазон температур +20/–269 °C
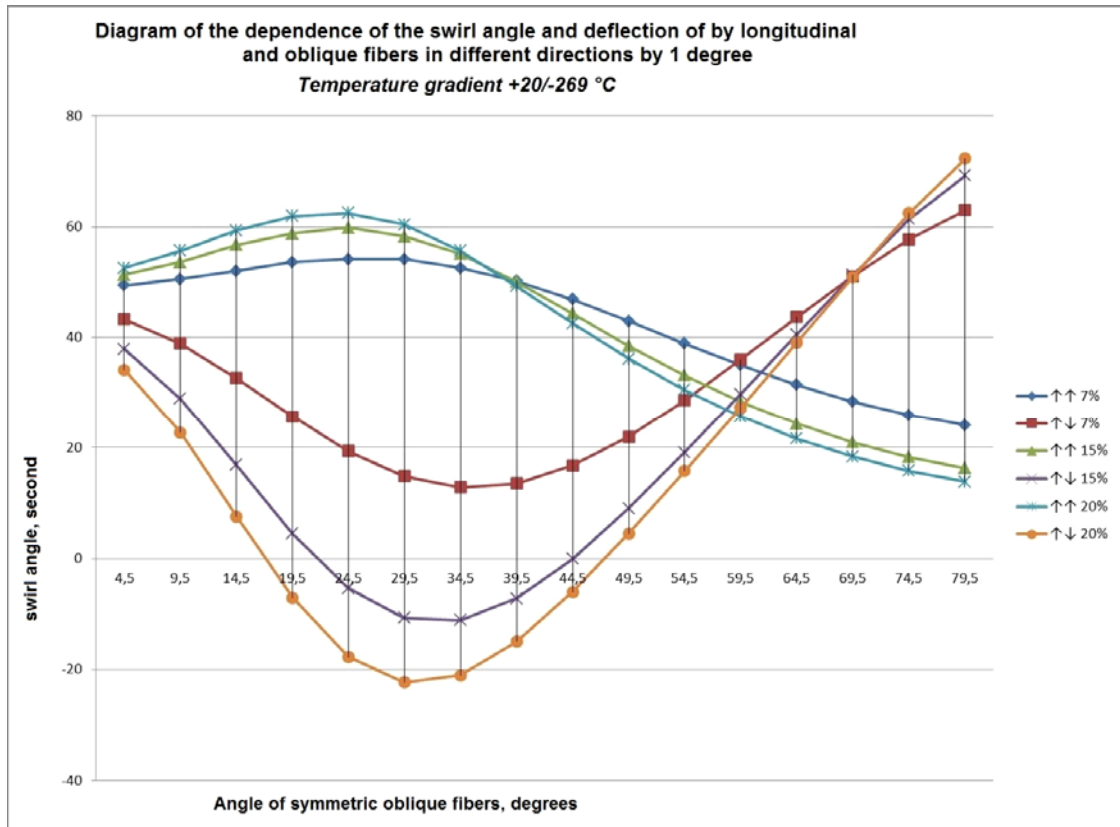
Fig. 12. Swirl angle at deflection of longitudinal and oblique fibers in different directions by 1 degree.
Temperature range +20/–269 °C

Рис. 12. Угол закрутки при отклонении продольных и косых волокон в различных направлениях на 1,0°.
Диапазон температур +20/–269 °C
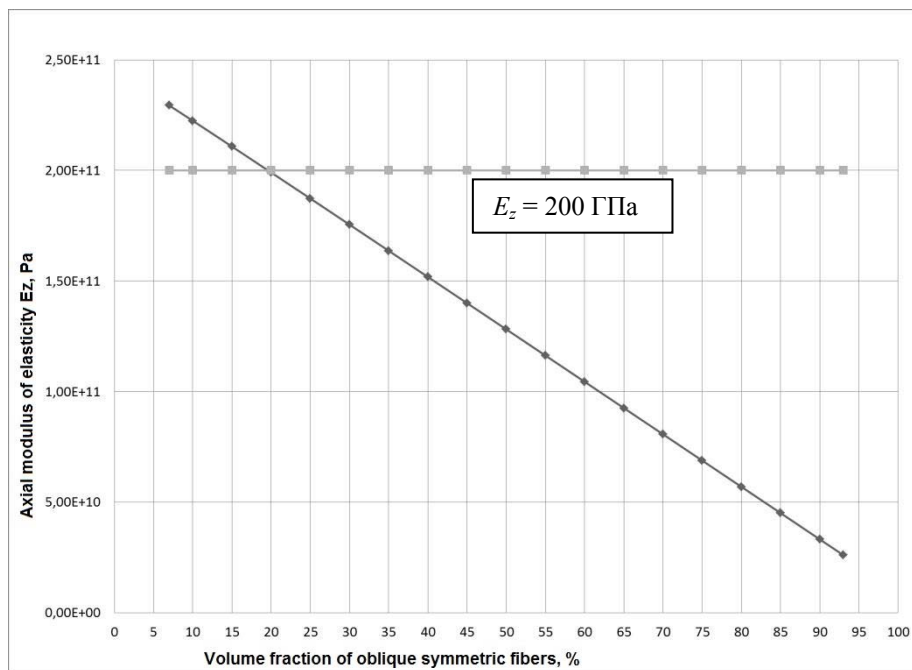
Fig. 13. Diagram of the dependence of the axial modulus of elasticity *Ez* on volume fraction of
oblique symmetric fibers for braiding scheme 0 ± 60° with M46J, T300 fiber types

Рис. 13. Зависимость осевого модуля *Ez* упругости от объемной доли косых симметричных
волокон для укладки 0 ± 60° с волокнами M46J и T300
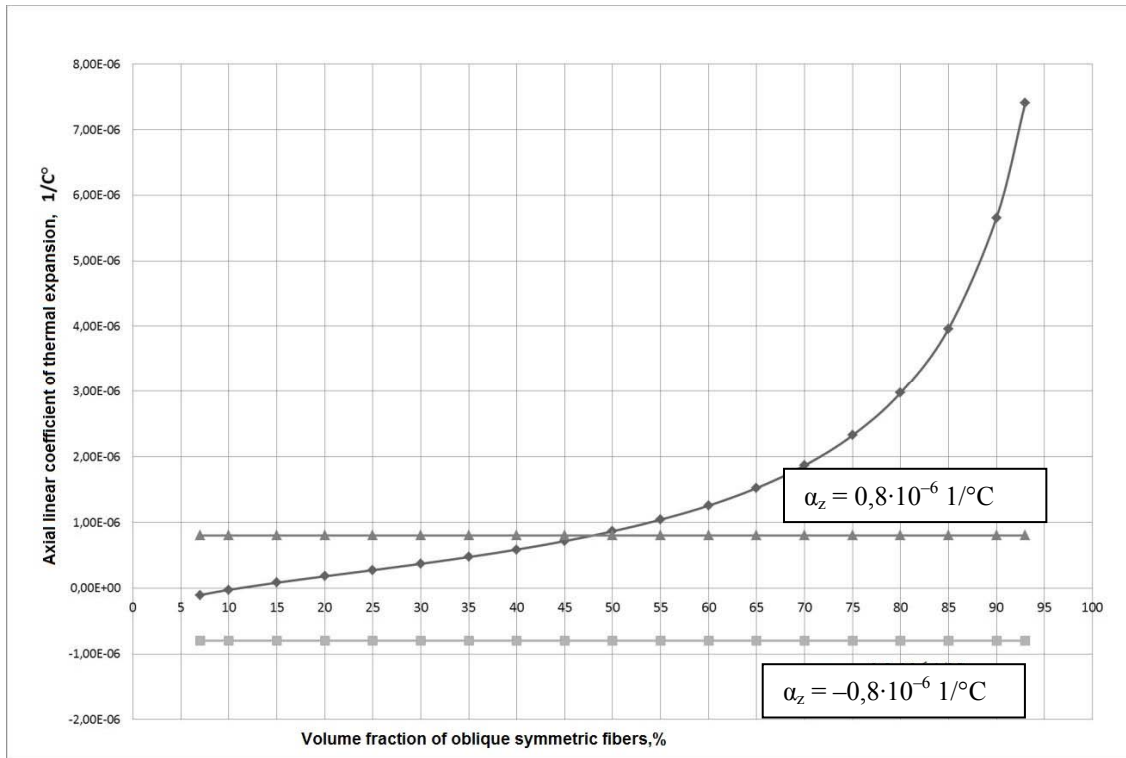
Fig. 14. Diagram of the dependence of the axial CLTE αz on volume fraction of oblique symmetric
fibers for braiding scheme 0 ± 60° with M46J, T300 fiber types

Рис. 14. Зависимость осевого КЛТР αz от объемной доли косых симметричных волокон
для укладки 0 ± 60° с волокнами М46J и Т300
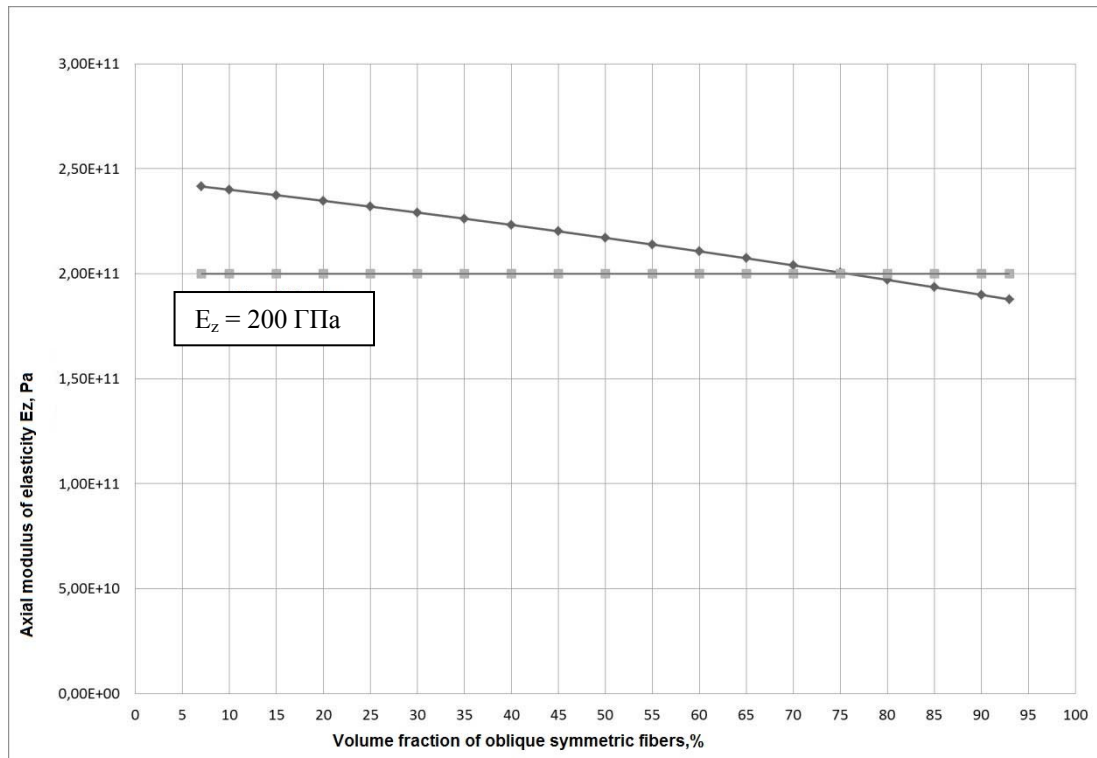
Fig. 15. Diagram of the dependence of the axial modulus of elasticity Ez on volume fraction
of oblique symmetric fibers for braiding scheme 0 ± 14° with M46J fiber type

Рис. 15. Зависимость осевого модуля упругости Ez от объемной доли косых симметричных
волокон для укладки 0 ± 14° с волокном М46J

Fig. 16. Diagram of the dependence of the axial CLTE αz on volume fraction of oblique
symmetric fibers for braiding scheme 0 ± 14° with M46J fiber type

Рис. 16. Зависимость осевого КЛТР αz от объемной доли косых симметричных волокон
для укладки 0 ± 14° с волокном M46J

Conclusion. On the basis of the considered methods of manufacturing supporting tubular structures, in order to ensure the requirements of sh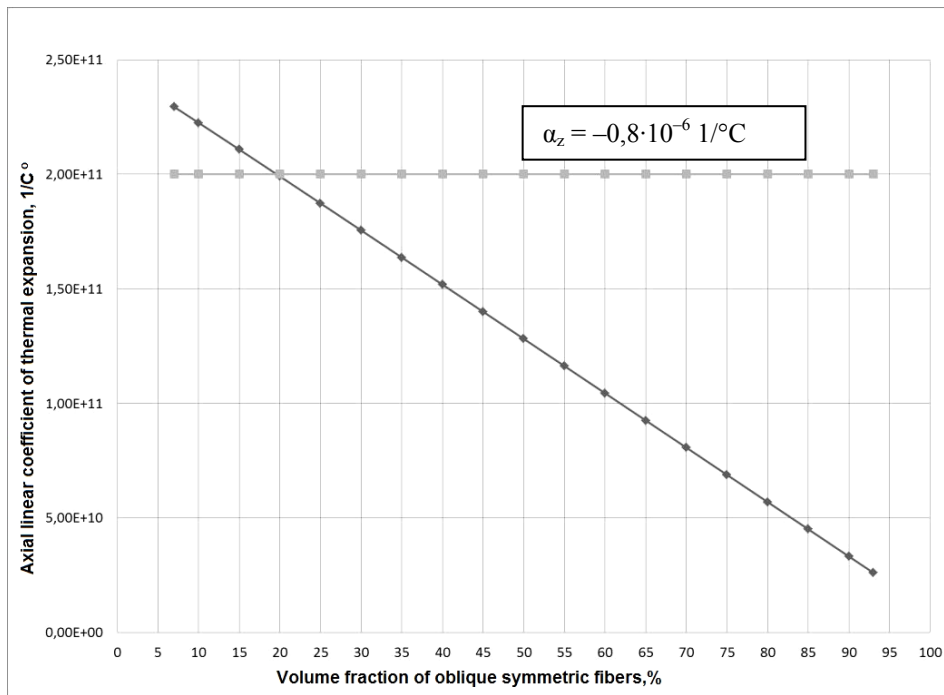ape stability, it is advisable to use the method of radial braiding in combination with the RTM technology of molding a product. The analysis of the considered preform reinforcement schemes shows that to ensure the specified parameters, the optimal one is braiding with the fiber laying of 0 ± 60° with the volume fraction of oblique fibers up to 20 %.

References

1. Kardashev N. S., Novikov I. D., Lukash V. N. [Overview of scientific task for the Millimertron observatory]. *Uspekhi fizicheskikh nauk.* 2014, No. 12, P. 1319–1352 (In Russ.).

2. *Federal'noe kosmicheskoe agentstvo* [Space observatory Millimertron] (In Russ.). Available at: http://millimetron.ru/index.php/ru/ (accessed 16.03.2020).

3. Mikhaylin Yu. A. *Spetsial'nye polimernye kompozitsionnye materialy* [Special polymer materials]. St.Petersburg, Nauch. osnovy i tekhnologii Publ., 2009, 658 p.

4. Kirillov V. N., Startsev O. V., Efimov V. A. [Climatic resistance and damageability of polymer composite materials, problems and solutions]. *Aviatsionnye materialy i tekhnologii.* 2012, No. S, P. 412–423 (In Russ.).

5. Mikhaylin Yu. A. *Konstruktsionnye polimernye kompozitsionnye materialy* [Structural polymer composite materials]. St.Petersburg, Nauch. osnovy i tekhnologii Publ., 2008, 820 p.

6. Maksimov G. Yu. *Teoreticheskie osnovy razrabotki kosmicheskikh apparatov* [Theoretical foundations of

spacecraft development]. Moscow, Nauka Publ., 1980, 320 p.

7. Smerdov A. A., Tairova L. P., Timofeev A. N. [Method of design and experimental development of dimensionally stable tubular rods made of carbon fiber]. *Konstruktsii iz kompozitsionnykh materialov.* 2006, No. 3, P. 12–23 (In Russ.).

8. Mikhaylov V. V. *K voprosu o mekhanike razrusheniya pri rastyazhenii elementov iz vysokoprochnykh armirovannykh plastikov s poverkhnostnymi i skvoznymi treshchinami* [On the issue of tensile fracture mechanics of high-strength reinforced plastic elements with surface and through cracks]. Moscow, Nauka Publ., 1981, P. 278–281.

9. Samipur S. A., Khaliulin V. I., Batrakov V. V. [Development of a technology for the manufacture of composite tubular elements for aerospace purposes by the method of radial braiding]. *Problemy mashinostroeniya i nadezhnosti mashin.* 2018, No. 3, P. 90–95 (In Russ.).

10. Meleshko A. I., Polovnikov S. P. *Uglerod, uglerodnye volokna, uglerodnye kompozity* [Carbon, carbon fibers, carbon composites]. Moscow, Sayns Press Publ., 2007, 189 p.

11. Tkachuk A. I., Grebeneva T. A., Chursova L. V., Panina N. N. [Thermoplastic binder. Present and future]. *Trudy VIAM.* 2013, No. 11. (In Russ.). Available at: http//www.viam-works.ru (accessed 13.03.2020).

12. Kozhanov D. A. [Modelling tensile behavior of flexible woven composites]. *Nizhniy Novgorod, NIIM NU,* 2017, 117 p.

13. Endruweit A., Ermanni P. The in-plane permeability of sheared textiles. Experimental observations

and a predictive conversion model. *Composites. Part A.* 2004, No. 35 P. 439–451. Doi: 10.1016/j.compositesa.2003.11.002.

14. Vernet N., Ruiz E., Advani S. Experimental determination of the permeability of engineering textiles. *Composites. Part A.* 2014, No. 61 P. 172–184. Doi: 10.1016/j.compositesa.2014.02.0101359-835X/.

15. Robert S. Pierce, Brian G. Falzon, Mark C. Thompson Permeability Characterization of Sheared Carbon Fiber Textile Preform POLYMER COMPOSITES, 2018, P. 2287–2298.

Библиографические ссылки

1. Обзор научных задач для обсерватории Миллиметрон / Н. С. Кардашев, И. Д. Новиков, В. Н. Лукаш и др. // Успехи физических наук. 2014. № 12. С. 1319–1352.

2. Федеральное космическое агентство [Электронный ресурс]. URL: http://millimetron.ru/index.php/ru/ (дата обращения: 16.03.2020).

3. Михайлин Ю. А. Специальные полимерные композиционные материалы. СПб. : Науч. основы и технологии, 2009. 658 с.

4. Кириллов В. Н., Старцев О. В., Ефимов В. А. Климатическая стойкость и повреждаемость полимерных композиционных материалов, проблемы и пути решения // Авиационные материалы и технологии. 2012. № S. C. 412–423.

5. Михайлин Ю. А. Конструкционные полимерные композиционные материалы. СПб. : Науч. основы и технологии, 2008 . 820 с.

6. Максимов Г. Ю. Теоретические основы разработки космических аппаратов. М. : Наука, 1980. 320 с.

7. Методика проектирования и экспериментальной отработки размеростабильных трубчатых стержней из углепластика / А. А. Смердов, Л. П. Таирова, А. Н. Тимофеев и др. // Конструкции из композиционных материалов. 2006. № 3. С. 12–23.

8. Михайлов В. В. К вопросу о механике разрушения при растяжении элементов из высокопрочных армированных пластиков с поверхностными и сквозными трещинами. М. : Наука, 1981. С. 278–281.

9. Самипур С. А., Халиулин В. И., Батраков В. В. Разработка технологии изготовления композитных трубчатых элементов авиакосмического назначения методом радиального плетения // Проблемы машиностроения и надежности машин. 2018. № 3. С. 90–95.

10. Мелешко А. И., Половников С. П. Углерод, углеродные волокна, углеродные композиты. М. : Сайнс-Пресс, 2007. 189 с.

11. Термопластичные связующие. Настоящее и будущее / А. И. Ткачук, Т. А. Гребенева, Л. В. Чурсова, Н. Н. Панина // Труды ВИАМ. 2013. № 11. С. 07. [Электронный ресурс]. URL: http//www.viam-works.ru (дата обращения: 13.03.2020).

12. Кожанов Д. А. Моделирование поведения гибких тканых композитов при растяжении : дис. … канд физ.-мат. наук. Нижний Новгород : НИИМ НУ, 2017. 117 с.

13. Endruweit A., Ermanni P. The in-plane permeability of sheared textiles. Experimental observations and a predictive conversion model. *Composites. Part A.* 2004. No. 35. P. 439–451.

14. Vernet N., Ruiz E., Advani S. Experimental determination of the permeability of engineering textiles. *Composites. Part A.* 2014. No. 61. P. 172–184.

15. Robert S. Pierce, Brian G. Falzon, Mark C. Thompson Permeability Characterization of Sheared Carbon Fiber Textile Preform POLYMER COMPOSITES. 2018. P. 2287–2298.

Trifonova Ekaterina Aleksandrovna – design engineer; JSC Academician M. F. Reshetnev "Information satellite systems". E-mail: trifonova@iss-reshetnev.ru.

Zhukov Andrey Viktorovich – deputy chief; JSC Academician M. F. Reshetnev "Information satellite systems". E-mail: zhav@iss-reshetnev.ru.

Savitsky Vyacheslav Vasil'evich – department head; JSC Academician M. F. Reshetnev "Information satellite systems". E-mail: savs@iss-reshetnev.ru.
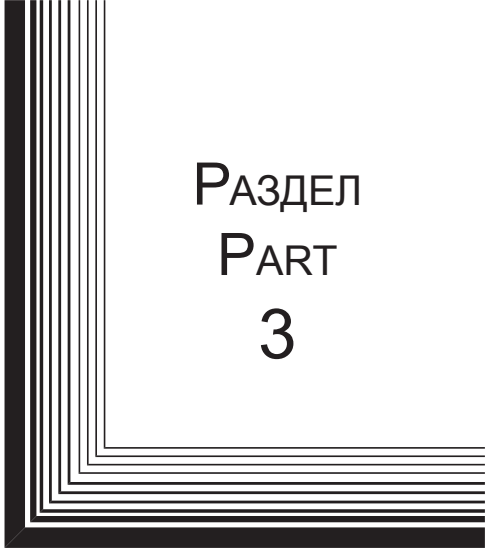
Batrakov Vladimir Vladimirovich – Head of Composite Technology Laboratory; Kazan National Research Technical University named after A. N. Tupolev E-mail: wwba@list.ru.

Трифонова Екатерина Александровна – инженер-конструктор 1 категории; АО «Информационные спутниковые системы» имени академика М. Ф. Решетнева». E-mail: trifonova@iss-reshetnev.ru.

Жуков Андрей Викторович – заместитель начальника отдела 309; АО «Информационные спутниковые системы» имени академика М. Ф. Решетнева». E-mail: zhav@iss-reshetnev.ru.

Савицкий Вячеслав Васильевич – начальник отдела 309; АО «Информационные спутниковые системы» имени академика М. Ф. Решетнева». E-mail: savs@iss-reshetnev.ru.

Батраков Владимир Владимирович – кандидат технических наук, руководитель лаборатории технологии композитов; Казанский национальный исследовательский технический университет имени А. Н. Туполева – КАИ. E-mail: wwba@list.ru.

ТЕХНОЛОГИЧЕСКИЕ ПРОЦЕССЫ И МАТЕРИАЛЫ

TECHNOLOGICAL PROCESSES AND MATERIALS SCIENCE

LABORATORY SEPARATOR OF BULK MATERIALS

E. G. Danilenko[*], S. V. Telegin

Reshetnev Siberian State University of Science and Technology
31, Krasnoyarskii rabochii prospekt, Krasnoyarsk, 660037, Russian Federation
*E-mail evg.danilenko@mail.ru

New materials for spacecraft radiation screens engineering require a fine classification of powder materials by particle size. The article concerns the construction of powder materials laboratory separator. This type of material separation is related to gravity methods. The Moseley laboratory separator serves as the prototype of the construction with table longitudinal shaking and diametrical vibrations by means of buffers during the separation process. The unbalanced oscillator yields deck separation surface harmonic vibrations in all directions. The unbalanced oscillator DC motor voltage control gradually alters the vibration frequency and supports finer separation of the material. A power pipe enables to conduct perpetual separation process. In prototype, in contrast, up to 100 g weight is processed for up to 5 minutes. To improve the materials fine and small classes separation efficiency, riffles are made on the separation surface, which determine the places of concentration of material particles. As a result of the conducted researches for elimination of the secondary circulation flows, a system of diametrical reefing is worked out: the riffle is approximately equal to the maximum particle size of the separated material and is equal to 0.2 mm in this construction; the distance between riffles is equal to 50 mm, the tilt angle is 80 degrees relative to the deck longitudinal side. The particle motion depends on the inclination angle of the separation surface. Large particles move upwards at angles of up to 5 degrees, and downwards at angles higher than 5 degrees. Vibration frequency and amplitude alteration, as well as adjusting the inclination angle of separation surface enables to move and adjust the speed of different properties and sizes of test material. The laboratory separator work is based on the physical effects, which enable to vary the location of the power pipe. This fact allows the construction to be adapted to a variety of specific conditions and expands the construction sphere. The separator construction is simple for production and operation, and can be quickly reconfigured if necessary. The separator portability allows it to be transported.

Keywords: shielding, composite material, separator, fractional composition, boron carbide.

ЛАБОРАТОРНЫЙ СЕПАРАТОР СЫПУЧИХ МАТЕРИАЛОВ

Е. Г. Даниленко[*], С. В. Телегин

Сибирский государственный университет науки и технологий имени академика М. Ф. Решетнева
Российская Федерация, 660037, г. Красноярск, просп. им. газ. «Красноярский рабочий», 31
*E-mail evg.danilenko@mail.ru

Разработка новых материалов для радиационных экранов космических аппаратов требует тонкой классификации порошковых материалов по размеру частиц. В статье рассмотрена конструкция лабораторного сепаратора порошковых материалов. Данный вид разделения материала относится к гравитационным методам. За прототип конструкции выбран лабораторный сепаратор Мозли, у которого процесс сепарации осуществляется продольным встряхиванием стола и поперечными колебаниями посредством буферов. Дебалансный вибратор позволил получать гармонические колебания поверхности сепарации деки во всех направлениях. Регулировка напряжения двигателя постоянного тока дебалансного вибратора плавно изменяет частоту вибрации, что способствует более тонкому разделению материала. Введением питающего патрубка реализована возможность непрерывного ведения процесса разделения, в отличие от прототипа, где навеска до 100 г обрабатывается до 5 мин. Для повышения эффективности разделения тонких и мелких классов материалов на поверхности сепарации выполнены рифли, определяющие места концентрации частиц материала. В результате проведенных исследований для исключения вероятности возникновения вторичных циркуляционных потоков была разработана система поперечных нарифлений: высота рифлей примерно равна максимальному размеру частиц разделяемого материала, в данной конструкции 0,2 мм; расстояние между рифлями 50 мм, угол наклона составил 80 градусов относительно продольной стороны деки. Движение частиц зависит от угла наклона

поверхности сепарации. При углах до 5 градусов крупные частицы движутся вверх, при больших – вниз. За счет изменения частоты и амплитуды вибрации, а также регулирования угла наклона поверхности сепарации, возможно перемещение и регулирование скорости движения разного по свойствам и размерам исследуемого материала. Физические эффекты, на которых основана работа лабораторного сепаратора, дают возможность варьировать и место размещения в нем питающего патрубка. Это позволяет приспособить конструкцию к разнообразным конкретным условиям, что расширяет область применения устройства. Конструкция сепаратора проста в изготовлении и эксплуатации, при необходимости ее можно быстро переналадить. Компактность сепаратора позволяет транспортировать его.

Ключевые слова: экранирование, композитный материал, сепаратор, фракционный состав, карбид бора.

Introduction. In materials science, composite materials are a separate sphere with their own industries and markets. Nano sized and ultrafine powders are mainly used as fillers for the composite materials production [1–3].

Shielding is considered to be one of the main means of protection against ionizing radiation effects on the Earth's orbit [4–6].

The most sensitive to ionizing radiation are semiconductor and optical materials, then go polymeric materials and metals have the highest resistance.

Aluminum and its alloys is the main material in the production of passive protective screens against ionizing radiation of devices and precision devices in space technology [7].

The AeroCube 8 project (4 vehicles A, B, C, D, also known as IMPACT) tested a radiation shielding material based on CNT / PEEK (Poly-ether-ether-ketone with the addition of carbon nanotubes) on board [8]. The Oufti-2 mission, scheduled for launching in 2021, is preparing an experiment as an additional payload to test the effectiveness of a multi-layer laminated coating on the basis of resins with additives and a tungsten alloy [9].

Ultrafine powders can improve the quality of materials used in rocket and mechanical engineering. Ultra dispersed metal powders are used for creation substances such as rocket fuel, explosives, pressed and sintered products. Some powders are used as fillers, they allow to obtain effective tread, antifriction, antiwear, resource-saving, hydrophobic, self-cleaning and bio inert composite materials [4].

The efficiency of the screens declines sharply at thicknesses over 1 cm, since the interaction of charged particles with the nuclei of the screen material produces intense electromagnetic bremsstrahlung radiation, which has a high penetrating ability [10]. An increase in the mass of protective screens leads to an increase in the cost of launching satellites into orbit by 25–50 % [11–12]. Therefore, an actual question about the development and creation of a new type of protection based on a multi-layer structure, where the first layer is made of a composite material, arises.

In the course of studying the effect of the fractional composition on the properties of composites weakening ionizing radiation, it became necessary to classify more finely the initial boron carbide powder.

Fraction is composed of particles of the size range between their maximum and minimum values. The shape and size of particles significantly affects the technological properties of composites and, through them, the density, strength, and uniformity of material properties [13].

Historically, manual stripping of minerals was the earliest form of processing, followed by primitive forms of gravity beneficiation. They were known more than 2 thousand years ago, the first descriptions were found in the works of Pliny [14] and then Agricola [15]. Gravity methods remained prevailing until the 20th century.

Gravity separation technologies allow to conduct separation or beneficiation using highly efficient and not complex equipment with minimal energy consumption in comparison with other beneficiation processes. Gravitational enrichment is a physical process in which the separation of one mineral from another depends on their relative movement under the influence of gravity and some other forces [16]. The main parameters which determine the movement of particles are their mass, size, volume and density. If these parameters differ significantly from each other, then separation takes place relatively easily. It must also be taken into consideration that if two particles have the same density, then a particle of a larger diameter has a higher final velocity and this is the characteristic of a homogeneous material, and if two particles have the same diameter, then a heavier particle has a higher final velocity, what takes place during enrichment.

There is a wide variety of equipment, but it can be divided into two general classes: those related to particle motion in the vertical plane – enrichment in the pulp volume; and related to the motion of particles along an inclined plane – separation in a thin layer. The efficiency of sizing is an important factor in the final product. Thus, an ideal gravity separation process would separate 100 % of one product size in one fraction and 100 % of excellent size in another.

In laboratory conditions, concentration tables are mainly used. The particles of the material are given periodical movements, caused by the movement of the working surface - the deck. Under the influence of the cross flow of the pulp and the longitudinal vibrations of the deck, the particles move in the longitudinal and transverse directions. Each particle of the separated material, depending on its density and size, acquires a certain speed and direction of movement relative to the deck of the concentration table.

There is a laboratory separator Moseley, which consists of a separation surface, inclined in one direction and performing simple harmonic oscillations [17]. Separation of material with a particle size from 10 to 200 microns is carried out by longitudinal shaking and lateral vibrations using buffers. The buffers are pulled from the rod by a cam mechanism and roller system and returned by a spring. Samples weighing 5–100 g are placed in the upper part of the tray, damp and vibrate on the working surface

for 3–5 minutes. Heavy particles remain on the separation surface or (with a type of end impact) move slowly upward. Light particles flow down into the discharge container under the influence of a small stream of spray water. Depending on the desired result, a longitudinal slope of 1.75–3 ° is selected, the oscillation frequency is 60–110 min − 1, the amplitude is 6–15 mm, and the irrigation fluid flow consumption is about 3 l / min.

Experimental part. Production, assembly and refinement were carried out with the Spektr design bureau of the REC IKIVT SibGU named after M. F. Reshetnev participation.

The aim of the work was simplifying the design and redaction the time of separation. The schematic diagram of the separator is shown in fig. 1.

Working surface *2* is a polished copper plate (fig. 1), not rigidly attached to the base *1* by hinges *6*, along which the powder, depending on the vibration frequency, is transported down, up and across. The unbalanced vibrator *3* sets the vibration frequency of the working surface. With the help of the adjusting screw *4*, the angle of inclination of the working surface is changed. Buffer *5* creates an additional impact on the separation surface.

The device works as follows. The feed pipe *7* is located above the vibrating working surface *2* between 8.1 and 8.2 grooves (fig. 2) from the upper edge at a height of 3–5 cm, and the material to be separated is fed. On the rear side of the working surface, an unbalanced vibrator is rigidly fixed, which is an unbalanced rotor driven by a DC motor. By controlling the engine speed, the vibration frequency of the working surface is achieved, at which the particle flow begins to split into two or more streams, depending on the separation requirements. Streams can form from the supply pipe upwards, above the 8.1th riffle; right or left between 8.1 and 8.2, 8.2 and 8.3, 8.3 and 8.4 riffles and down – below 8.4 riffles.

The study of the dependence of the amplitude of oscillations of the free end of the working surface and its frequency on the voltage supplied to the motor of the vibration drive (fig. 3) on the powder B4C is carried out.

Several experiments were carried out at different voltages on the vibrating motor. The amplitude of vibrations of the working surface was measured by a microscope, and the frequency – by a frequency meter. The graph (fig. 3) shows that at a voltage of 11 to 13 V, a plateau in amplitude with two surges up to 0.25 mm is observed. There is also an outburst in the range from 5 to 7 V, but it does not lead to the separation of particles into fractions, the B4C powder actually rolls down the plate.

The process of separating particles in the proposed device is continuous. Particle movement depends on the angle of inclination of the working surface. At angles up to 5 degrees, large particles move upward, and small particles move downward, at large angles – in the opposite direction.
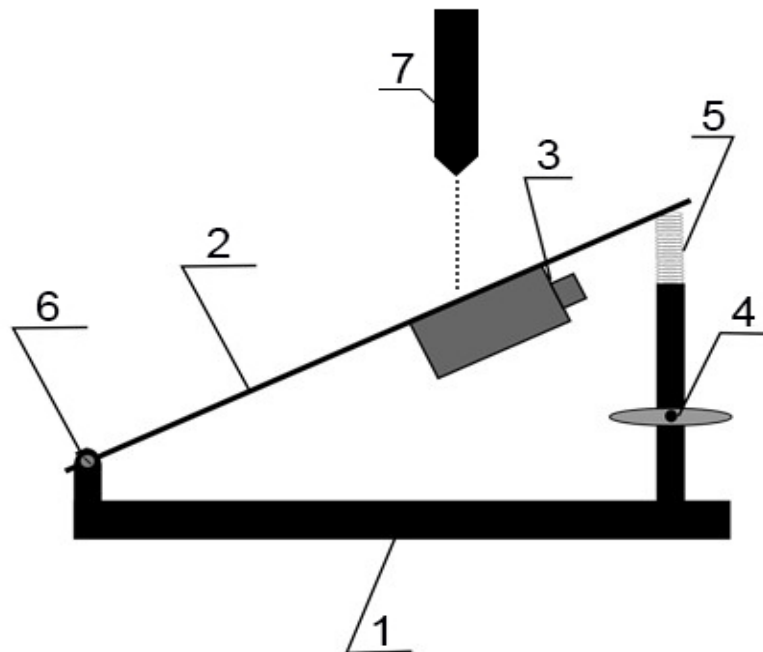
Fig. 1. Separator scheme:
1 – base; *2* – working surface; *3* – unbalanced vibrator;
4 – adjusting screw; *5* – buffer; *6* – joint; *7* – nutrient nozzle

Рис. 1. Схема сепаратора:
1 – основание; *2* – рабочая поверхность; *3* – дебалансный вибратор;
4 – регулировочный винт; *5* – буфер; *6* – шарнир;
7 – питающий патрубок
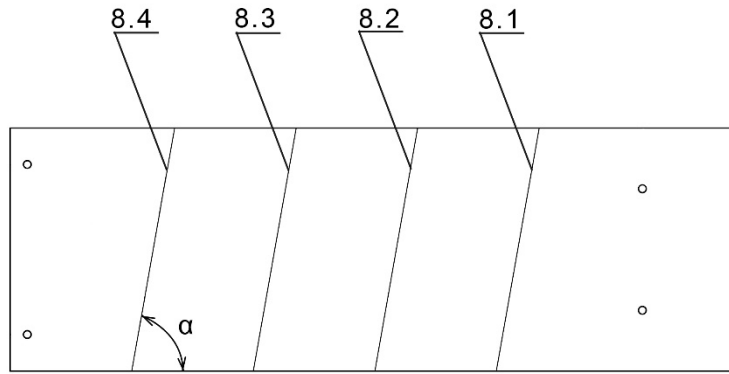
Fig. 2. Scheme rifle

Рис. 2. Схема нарифлений
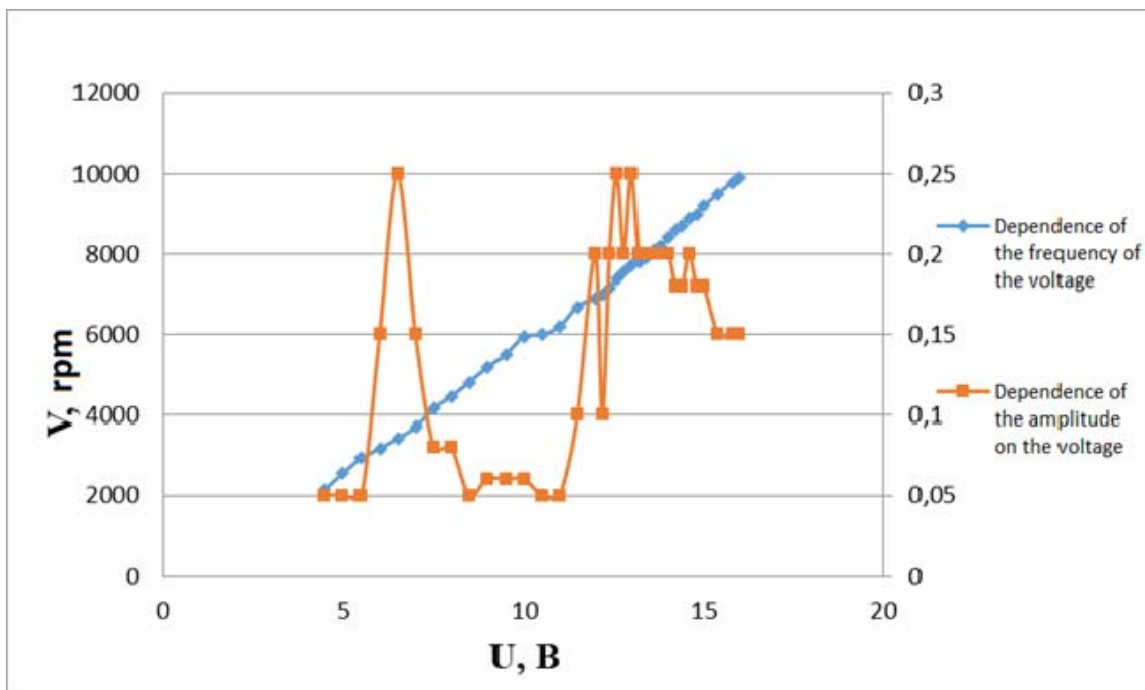
Fig. 3. Dependence of the amplitude and frequency of oscillations of the working
surface on the voltage on the vibration motor

Рис. 3. Зависимость амплитуды и частоты колебаний рабочей
поверхности от напряжения на вибромоторе

The area of particles passed through different streams under different modes

U, B	Bottom	Middle 1	Middle 2	Top
11	–	–	–	–
11.2	29–40 mkm^2	20–30 mkm^2	–	5–19 mkm^2
11.6	12–40 mkm^2	5–23 mkm^2	–	–
11.8	17–40 mkm^2	11–29 mkm^2	–	5–22 mkm^2
12.5	27–40 mkm^2	14–32 mkm^2	9–23mkm^2	5–16 mkm^2
13.5	26–40 mkm^2	18–29 mkm^2	10–23 mkm^2	5–17 mkm^2
13.5; angle 16°	30–40 mkm^2	16–30 mkm^2	10–18 mkm^2	5–14 mkm^2
14.2	–	–	–	–

To increase the efficiency of separation of thin and small classes of materials, riffles are made on the working surface (fig. 2), which serve as a place of concentration of particles of a certain size. The design of the working surface should be made in such a way, which would allow to exclude the likelihood of secondary circulation flows in the interstitial spaces [18].

As a result of the experiments carried out, a reefing system 8 was developed: the riffle height is approximately equal to the maximum particle size of the separated material, in this design it is 0.2 mm; the distance between the grooves is 50 mm, the angle of inclination α is 80 degrees; the riffle shape is round (fig. 3).

The research was carried out on the B4C powder of fraction F150 in the state of delivery, in which, in addition to particles with a size of 63–106 microns, there were also smaller particles up to 15 % by weight. By preliminary separation carried out on the same separator, a part of the powder with a size of 5 to 40 microns was isolated.

When working on a laboratory installation, the powder falling out of the hopper branch pipe is divided into several streams in different parts of the working surface, from which samples for fractional analysis were taken. The angle of inclination of the working surface is 12 degrees.

The analysis was carried out on a Levenhuk DTX 30 microscope at x230 increase with the MicroCapture Plus software, included in the set of delivery of the microscope, application. The analysis results are shown in table.

As seen from Table 1, the optimum vibrator voltage is 11.2 V. Under other voltages, an overlap of particle size is observed in different samples. At 11 and 14.2 B separation does not occur. The angle of inclination of the working surface increase up to 16 degrees made it possible to select a narrower fraction of 5–14 microns. The powder consumption is 100 g / min.

By changing the frequency and amplitude of vibration, as well as adjusting the angle of inclination of the working surface made it possible to move and regulate the speed of movement of the test material of different properties and sizes.

Conclusion. The studies carried out allowed: to simplify the design of the separator by introducing an unbalanced vibrator; to reduce the analysis time, excluding the operation of drying the material; to carry out powder classification continuously by installing a hopper with a branch pipe.

The physical effects, on which work of the laboratory separator is based on, make it possible to vary the location of the supply pipe in it. This allows the design to be adapted to a variety of specific conditions, what broadens the sphere of the device application. The design of the device is simple in production and operation; in case of necessity it is possible to adjust the work of the device quickly.

References

1. Suzdalev I. *Nanotekhnologiya: fiziko-khimiya nanoklasterov, nanostruktur i nanomaterialov* [Nanotechnology: physical chemistry of nanoclusters, nanostructures and nanomaterials]. In 2 books. Moscow, ComBook Publ., 2006, 592 p.

2. Novikov L. S. *Radiatsionnye vozdeystviya na materialy kosmicheskikh apparatov* [Radiation effects on materials of spacecraft: a tutorial]. Moscow, University book Publ., 2010, P. 4–5.

3. *Perspektivnye materialy. Struktura i metody issledovaniya* [Advanced materials. Research structure and methods]. Ed. D. L. Meersona. Togliatti: TSU, MISIS Publ., 2006, 536 p.

4. Bezrodnykh I. P., Morozova E. I., Petrukovich A. A., Kazantsev S. G., Kochetov I. V., Semenov V. T. [Bremsstrahlung of electrons in the substance of the spacecraft. Calculation method]. *Voprosy elektromekhaniki. Tr. NPP VNIIEM.* 2011, Vol. 120, No 1, P. 37–44 (In Russ.).

5. Gusev N. G., Klimanov V. A., Mashkovich V. P., Suvorov A. P. *Zashchita ot ioniziruyushchikh izlucheniy* [Protection against ionizing radiation]. In 2 books. Moscow, Energoatomizdat Publ., 1989.

6. Ying Wang, Guangke Wang, Tao Hu, Shipeng Wen, Shui Hu, Li Liu. Enhanced photon shielding efficiency of a flexible and lightweight rare earth/polymer composite: A Monte Carlo simulation study. *Nuclear Engineering and Technology.* 2020, Vol. 52, No. 7, P. 1565–1570

7. Kuznetsov N. V. *Radiatsionnaya opasnost' na okolozemnykh orbitakh i mezhplanetnykh traektoriyakh kosmicheskikh apparatov* [Radiation hazard in near-earth orbits and interplanetary trajectories of spacecraft]. Available at: http://nuclphys.sinp.msu.ru/crd/crd3.htm (accessed 19.10.2020).

8. Richard P. Welle, David Hinckley Aerospace Nano / Picosatellites Program. Available at: https://space.skyrocket.de/doc_sdat/aerocube-8-impact.htm (accessed 20.10.2020).

9. Guillaume T. OUFTI-2 educational CubeSat project of University of Liège , Belgium OUFTI-2 educational CubeSat project of University of Liège, Belgium 2017. May.

10. Bezrodnykh E. I. Morozova A. A. [Petrukovich and others. Radiation conditions in geostationary]. *Voprosy elektromekhaniki. Tr. NPP VNIIEM.* 2010, Vol. 117, No 4, P. 33–42 (In Russ.).

11. Daniel Dupont. Nuclear explosions in orbit. *In the world of science (Scientific American)* 2004, No. 9, P. 62–70.

12. Lobanovskiy Yu. I. *Tsena kosmosa: skol'ko stoit vykhod na orbitu?* [Cost of space: how much does it cost to enter orbit?]. Available at: http://www.synerjetics.ru/article/cost.pdf. (accessed 25.10.2020).

13. Vaytuzin O. P., Kuznetsov A. A. *Izuchenie mikrostkury metallov metodom komp'yuternoy opticheskoy mikroskopii* [Study of the microstructure of metals by the method of computer optical microscopy]. Krasnoyarsk, Siberian state aerospace un-t Publ., 2006, 100 p.

14. Pliny, C. P. S. (circa 70). Natural History Book 33, 21.

15. Agricola, G. (1556). De Re Metallica Trans Hoover, H. C. and Hoover, L. H., Dover Publications, N. Y. 1950, Book XIII.

16. Bert R. O., Millza K. *Tekhnologiya gravitatsionnogo obogashcheniya* [Gravity separation technology]. Moscow, Bosom Publ., 1990, 574 p.

17. Anon (1979). British-developed laboratory separator aids small-scale mineral studies. Min. Mag, Jan. 45–48.

18. Shokhin V. N., Lopatin A. G. *Gravitatsionnye protsessy obogashcheniya* [Gravitational enrichment processes]. Moscow, Bosom Publ., 1980, P. 256–257.

Библиографические ссылки

1. Суздалев И. Нанотехнология: физикохимия нанокластеров, наноструктур и наноматериалов. В 2 кн. Кн. 2. М. : КомКнига, 2006. 592 с.

2. Новиков Л. С. Радиационные воздействия на материалы космических аппаратов. М. : Университетская книга, 2010. С. 4–5.

3. Перспективные материалы. Структура и методы исследования / под ред. Д. Л. Меерсона. Тольятти : ТГУ ; МИСиС, 2006. 536 с.

4. Тормозное излучение электронов в веществе космического аппарата. Методика расчёта / И. П. Безродных, Е. И. Морозова, А. А. Петрукович и др. // Вопросы электромеханики. Тр. НПП ВНИИЭМ. 2011. Т. 120, № 1. С. 37–44.

5. Защита от ионизирующих излучений / Н. Г. Гусев, В. А. Климанов, В. П. Машкович, А. П. Суворов В 2 т. М. : Энергоатомиздат, 1989.

6. Enhanced photon shielding efficiency of a flexible and lightweight rare earth/polymer composite: A Monte Carlo simulation study / Ying Wang, Guangke Wang, Tao Hu et al. // Nuclear Engineering and Technology. 2020. Vol. 52, No. 7. P. 1565–1570.

7. Кузнецов Н. В. Радиационная опасность на околоземных орбитах и межпланетных траекториях космических аппаратов [Электронный ресурс]. URL: http://nuclphys.sinp.msu.ru/crd/crd3.htm (дата обращения: 19.10.2020).

8. Велле Р. П., Хинкли Д. Программа аэрокосмических нано / пикоспутников [Электронный ресурс]. URL: https://space.skyrocket.de/doc_sdat/aerocube-8-impact.htm. (дата обращения: 20.10.2020).

9. Guillaume T. OUFTI-2 educational CubeSat project of University of Liège // Belgium OUFTI-2 educational CubeSat project of University of Liège, Belgium. 2017, May.

10. Радиационные условия на геостационарной орбите / И. П. Безродных, Е. И. Морозова, А. А. Петрукович и др. Вопросы электромеханики. Тр. НПП ВНИИЭМ. 2010. Т. 117, № 4. С. 33–42.

11. Дюпон Д. Ядерные взрывы на орбите // В мире науки (Scientific American). 2004. № 9. С. 62–70.

12. Лобановский Ю. И. Цена космоса: сколько стоит выход на орбиту? [Электронный ресурс]. URL: http://www.synerjetics.ru/article/cost.pdf (дата обращения: 25.10.2020).

13. Вайтузин О. П., Кузнецов А. А. Изучение микростркуры металлов методом компьютерной оптической микроскопии / Сиб. гос. аэрокосмич. ун-т. Красноярск, 2006. 100 с.

14. Pliny, C. P. S. (circa 70). Natural History Book 33, 21.

15. Agricola G. (1556). De Re Metallica Trans Hoover, H. C. and Hoover, L. H., Dover Publications, N. Y. 1950 Book XIII.

16. Берт Р. О., Миллза К. Технология гравитационного обогащения : пер. с англ. Е. Д. Бачевой. М. : Недра, 1990. 574 с.

17. Anon (1979). British-developed laboratory separator aids small-scale mineral studies. Min. Mag, Jan. P. 45–48.

18. Шохин В. Н., Лопатин А. Г. Гравитационные процессы обогащения. М. : Недра, 1980. С. 256–257.

Danilenko Evgeniya Grigor'evna – Master's Student; Reshetnev Siberian State University of Science and Technology. E-mail: evg.danilenko@mail.ru.

Telegin Sergey Vladimirovich – Cand. Sc., Associate Professor of the Department of Technical Physics; Reshetnev Siberian State University of Science and Technology. E-mail: sey_62@mail.ru.

Даниленко Евгения Григорьевна – магистрант; Сибирский государственный университет науки и технологий имени академика М. Ф. Решетнёва. E-mail: evg.danilenko@mail.ru.

Телегин Сергей Владимирович – кандидат технических наук, доцент кафедры технической физики; Сибирский государственный университет науки и технологий имени академика М. Ф. Решетнёва. E-mail: sey_62@mail.ru.

STUDY OF STRUCTURAL PROPERTIES OF BISMUTH PYROSTANNATE BY RAMAN AND IR SPECTROSCOPY

L. V. Udod[1,2*], O. B. Romanova[2], S. S. Aplesnin[1,2], V. V. Kretinin[1]

[1]Reshetnev Siberian State University of Science and Technology
31, Krasnoyarskii rabochii prospekt, Krasnoyarsk, 660037, Russian Federation
[2] Kirensky Institute of Physics, FRC KSC Siberian Branch of the Russian Academy of Sciences
50, Akademgorodok, Krasnoyarsk, 660036, Russian Federation
*E-mail: luba@iph.krasn.ru

Chromium-substituted bismuth pyrostannates with a pyrochlore structure were synthesized by the solid-phase reaction method. The X-ray structural analysis performed at room temperature showed that the samples $Bi_2(Sn_{1-x}Cr_x)_2O_7$, $x = 0; 0.05, 0.1$ are single-phase and belong to the Pc monoclinic structure. Polymorphic transformations of the synthesized samples were studied by Raman and IR spectroscopy. IR spectra were obtained at the temperature range 110–525 K and frequencies 350–1100 cm^{-1}. Raman spectra were measured at room temperature at frequencies of 100–3000 cm^{-1}. Heterovalent substitution of Sn^{4+} for Cr^{3+} modifies the spectra of pure $Bi_2Sn_2O_7$. The crystal structure of $Bi_2Sn_2O_7$ consists of two oxygen sublattices: SnO_6 and Bi_2O'. Chromium ions substituted tin ions in the SnO_6 oxygen octahedra, distorting the local structure in the vicinity of bismuth ions. Phonon modes are softening in the vicinity of phase transitions. A shift of the phase boundaries of polymorphic transitions is observed for $Bi_2(Sn_{1-x}Cr_x)_2O_7$, $x = 0.05, 0.1$. The frequencies of stretching vibration modes were determined from IR and Raman spectra. The substitution of chromium for tin ions resulted in the appearance of two new modes at frequencies of 581 and 822 cm^{-1} in the Raman spectra. The absence of an inversion center in the crystal structure of $Bi_2(Sn_{1-x}Cr_x)_2O_7$ is confirmed by Raman spectroscopy. IR spectra of chromium-substituted samples consist of complex lines, which decompose into 2 and 3 Lorentzian lines. The softening and broadening of optical absorption modes are associated with the electronic contribution. Impurity states of electrons form polarons.

Keywords: bismuth pyrostannate, crystal structure, phase transitions, IR spectroscopy, Raman spectroscopy, X-ray structural analysis.

ИССЛЕДОВАНИЕ СТРУКТУРНЫХ СВОЙСТВ ПИРОСТАННАТА ВИСМУТА МЕТОДОМ РАМАН И ИК СПЕКТРОСКОПИИ

Л. В. Удод[1,2*], О. Б. Романова[2], С. С. Аплеснин[1,2], В. В. Кретинин[1]

[1] Сибирский государственный университет науки и технологий имени академика М. Ф. Решетнева
Российская Федерация, 660037, г. Красноярск, просп. им. газ. «Красноярский рабочий», 31
[2]Институт физики им. Л. В. Киренского СО РАН – обособленное подразделение ФИЦ КНЦ СО РАН
Российская Федерация, 660036, г. Красноярск, Академгородок, 50, стр. 38
* E-mail: luba@iph.krasn.ru

Методом твердофазной реакции синтезированы хромзамещенные пиростаннаты висмута со структурой пирохлора. Рентгеноструктурный анализ, выполненный при комнатной температуре, показал, что образцы $Bi_2(Sn_{1-x}Cr_x)_2O_7$, $x = 0; 0,05, 0,1$ однофазные и принадлежит к моноклинной структуре Pc. Полиморфные превращения синтезированных образцов изучались методами Раман и ИК спектроскопии. ИК-спектры получены в температурном диапазоне 110–525 K, интервале частот 350–1100 $см^{-1}$. Спектры Рамановского рассеяния измерялись при комнатной температуре на частотах 100–3000 $см^{-1}$. Гетеровалентное замещение Sn^{4+} на Cr^{3+} видоизменяет спектры чистого $Bi_2Sn_2O_7$. Кристаллическая структура $Bi_2Sn_2O_7$ состоит из двух кислородных

подрешеток: SnO_6 и Bi_2O'. Ионы хрома замещают ионы олова в кислородных октаэдрах SnO_6, искажая локальную структуру в окрестности ионов висмута. Вблизи фазовых переходов происходит смягчение фононных мод. Для $Bi_2(Sn_{1-x}Cr_x)_2O_7$, 0,05, 0,1 наблюдается смещение фазовых границ полиморфных переходов. Из ИК и Раман спектров определены частоты мод валентных колебаний. В Рамановских спектрах замещение ионов олова хромом привело к появлению двух новых мод на частотах 581 и 822 см$^{-1}$. Отсутствие центра инверсии в кристаллической структуре $Bi_2(Sn_{1-x}Cr_x)_2O_7$ подтверждается Раман спектроскопией. ИК спектры хромзамещенных образцов состоят из сложных линий, которые разлагаются на 2 и 3 линии Лоренцовой формы. Смягчение и уширение спектров поглощения связывается с электронным вкладом. Примесные состояния электронов образуют поляроны.

Ключевые слова: пиростаннат висмута, кристаллическая структура, фазовые переходы, ИК спектроскопия, Раман спектроскопия, рентгеноструктурный анализ.

Introduction. Bismuth pyrostannate $Bi_2Sn_2O_7$ belongs to the pyrochlore family, which is interesting for its physical properties. These compounds exhibit well-known structural phase transitions of the displacement type in oxygen-octahedral structures, which are usually accompanied by sharp changes in dielectric, mechanical, optical, and other properties.

Three structural modifications were found in polymorphic $Bi_2Sn_2O_7$. Above 900 K, the compound has a cubic structure with small displacements of Bi^{3+} ions from the ideal pyrochlore structure and belongs to the γ-phase. In the temperature range 390–900 K, the β-phase with an orthorhombic structure is realized. At room temperature, $Bi_2Sn_2O_7$ is in a noncentrosymmetric monoclinic structure (α-phase) with space group *P1c1* [1]. Recently, a low-temperature transition at $T = 140$ K from the monoclinic structure to the lower triclinic system has been discovered [2].

In most cases, the crystal structure of bismuth pyrostannate is cubic with a lattice constant of about 1.0 nm and eight formula units per unit cell. The large A-ion is located in 16d-positions and is eight-fold coordinated by oxygen ions, while the smaller B-ion is located in the octahedral environment of oxygen (16c-positions) and has sixfold coordination. The pyrochloric structure $A_2B_2O_6O'$ is consists of two sublattices: B_2O_6 and A_2O'. The B_2O_6 sublattice is formed of BO_6 – octahedra connected by an oxygen B – O – B bridge at an angle of 135° into zigzag chains, all B – O bonds are equivalent. The A cation forms the A_2O' sublattice from the A – O' chains. Cations A and B in the structure of pyrochlores form a sublattice of tetrahedra connected by corners.

The structure of $Bi_2Sn_2O_7$ is well described by two interpenetrating oxide sublattices. The Sn_2O_6 sublattice consists of SnO_6 octahedra connected by vertices to form hexagonal rings. In the Bi_2O' sublattice, the Bi^{3+} cation is tetrahedrally coordinated by O' anions with linear O'−Bi−O' bonds.

It was found that the transitions to the α- and β-phases occur with the rotation of Bi_2O' tetrahedra, which displace Bi ions to the top of the SnO_6 oxygen octahedron of the α-phase and the edge in the β-phase [3]. Bismuth ions in their electronic structure have a lone pair of $6s^2$ electrons. These electrons cause mobility of Bi^{3+} and O^{2-} in Bi_4O', which leads to distortion of the ideal structure of pyrochlore. Correlated displacements of Bi^{3+} can lead to phase transitions into complex ordered structures, which in turn lead to changes in macroscopic properties.

In the region of structural phase transitions, anomalies on the curves of temperature dependences of dielectric and electrical properties of $Bi_2Sn_2O_7$ are observed [1; 4].

Bismuth pyrostannate is a dielectric. Substitution of tin ions by 3-d elements in $Bi_2Sn_2O_7$ causes distortion of the crystal structure and a shift in phase transitions. For example, heterovalent substitution of Bi^{3+} and Sn^{4+} ions in $Bi_2Sn_2O_7$ leads to a change in the temperature of the α→β transition [5–7].

In the region of the α→β structural phase transition, the compound $Bi_2(Sn_{1-x}Cr_x)_2O_7$, $x = 0.1$ completely changes the conductivity type from hopping (Mott conductivity) to the Poole-Frenkel tunnel emission type. The conductivity of $Bi_2(Sn_{1-x}Cr_x)_2O_7$, $x = 0.15$ at the α→β transition is mixed, some of the domains of the compound carry out charge transfer according to the Mott conductivity type, and the other according to the Poole-Frenkel type. The ratio between these phases is approximately 50×50 [5; 8].

An electronic transition with a change in the conductivity type from the hopping to the tunnel emission Poole-Frenkel type at the α→β structural transition is observed at isovalent substitution of $Bi_2(Sn_{0.9}Mn_{0.1})_2O_7$.

Substitution of manganese for tin ions changed the type of thermal effects during structural phase transitions from exothermic to endothermic [7]. Anomalies of the dielectric constant are observed in the region of the α→β transition. For example, the real part of the dielectric constant $Re(\varepsilon)$ $Bi_2(Sn_{0.9}Mn_{0.1})_2O_7$ has an inflection point at 418 K and a sharp rise above 700 K, the imaginary part $Im(\varepsilon)$ exhibits a maximum at $T = 425$ K and an increase that begins from $T \sim 700$ K [7].

Anomalies of the dielectric constant in the temperature range of phase transitions are also observed in chromium-substituted pyrostannates. In the $Bi_2(Sn_{1-x}Cr_x)_2O_7$ system, a broad maximum in $Re(\varepsilon)$ and $Im(\varepsilon)$ at about 420 K is observed with their further increase near the β→γ transition [9].

The structural α→β transition is accompanied by anomalies in the temperature behavior of the magnetic susceptibility. In the compound $Bi_2(Sn_{0.95}Mn_{0.05})_2O_7$ [10] antiferromagnetic exchange prevails, and in $Bi_2(Sn_{1-x}Cr_x)_2O_7$ ferromagnetic exchange dominates [5; 11–12].

The absence of an inversion center in bismuth pyrostannate is a prerequisite for the existence of ferroelectric

order at low temperatures. Theoretical calculations carried out from first principles confirm this assumption. In $Bi_2(Sn_{0.8}Fe_{0.2})_2O_7$ magnetoelectric interaction up to 300 K was found [13–14]. An external electric field leads to deformation of the crystal lattice and to the formation of electric polarization.

The magnetic field-induced electric polarization is an even function of the magnetic field, with the exception of the 140–160 K structural phase transition region, where the linear magnetoelectric effect predominates. The magnetic field-induced electrical polarization decreases with heating. The structural phase $\alpha \rightarrow \beta$ transition and the transition from a noncentrosymmetric to a centrosymmetric structure are accompanied by maxima in the temperature dependence of the dielectric constant and thermoelectric power.

Cationic doping changes the structure of pyrochlore and the basic physical properties of the compounds, since the structural and physical properties are correlated with each other. This group of compounds can be potentially in demand as materials for electrochemical devices, electronic devices of a new generation due to the relatively low synthesis temperatures of doped bismuth pyrostannates and a significant increase in their thermal stability. The possibility of distributing atoms of doping elements over two equivalent crystallographic positions increases the variability of the properties of compounds, due to the different nature of the doping element, affects the defectiveness of the cationic and anionic sublattices, and the transport properties of ions (in particular, mobile oxygen O').

At polymorphic transitions in a wide temperature range, the electric polarization can be controlled by the magnetic field. Multiferroics, which include substituted bismuth pyrostannates, are widely used in electronics and telecommunication technologies. They can be used as polarizers in a wide frequency range from 10^{10}–10^{15} Hz, for magnetic memory devices and spin electronics, in magnetic random access memory, which combines the speed of semiconductor electronics and non-volatility. Multiferroics serve as the basis for the creation of ME elements of spintronics, in microwave devices as valves, modulators.

Based on the information presented, the purpose of this work is to study the effect of replacing Sn^{4+} ions with Cr^{3+} ions on the structural properties by X-ray diffraction analysis and IR, Raman spectrometry.

Experimental results and discussion. *Synthesis and X-ray structural analysis.* The study of the structural properties by X-ray diffraction analysis, Raman and IR spectroscopy was carried out on polycrystalline samples. Compounds of complex oxide $Bi_2(Sn_{1-x}Cr_x)_2O_7$, x = 0; 0,05, and 0.1 were obtained by solid state reaction method according to the following reaction:

$$2(1 - x)SnO_2 + xCr_2O_3 + Bi_2O_3 \rightarrow Bi_2(Sn_{1-x}Cr_x)_2O_{7-x}$$

A mixture of oxides SnO_2, Cr_2O_3 and Bi_2O_3 in a stoichiometric ratio was ground for a long time in an agate mortar, pressed into tablets, placed in an oven and kept at a temperature from 973 to 1223 K, the holding time varied from 8 to 24 hours [11; 12].

X-ray structural analysis was performed on the synthesized samples. X-ray powder diffraction patterns of $Bi_2(Sn_{1-x}Cr_x)_2O_{7-x}$, x = 0; 0.05, 0.1 were carried out at room temperature on a Bruker D8 ADVANCE diffractometer using a VANTEC linear detector and Cu-Kα radiation. During the experiment, different sizes of the primary beam slits were used: 0.6 mm in the range of angles 2Θ = 5–70° and 2 mm in the range of 70–120°. The scanning step is 0.016° and remained constant in all areas, the exposure time at each step is 1.5 and 1 s for the ranges 5–70° and 70–120°, respectively. The standard deviations of the intensities of all points of the X-ray diffraction pattern were calculated, and then the intensities and standard deviations of all points of the high-angle part were multiplied by a normalizing factor of 0.45. All peaks corresponded to the monoclinic cell of the *Pc* α-phase $Bi_2Sn_2O_7$ [15]. The crystal structure contains 32 Bi^{3+} ions, 32 Sn^{4+} ions, and 112 O^{2-} ions in the independent part of the cell (fig. 1). All Bi^{3+} ions are coordinated by 8 O^{2-} ions and form distorted cubes, while Sn^{4+} ions are coordinated by 6 O^{2-} ions and form octahedra, which are connected by vertices.

The coordinates of all 176 atoms were fixed, since the number of coordinates alone, 528, is comparable to the number of observed reflections. Nevertheless, even the fixed coordinates of the atoms made it possible to correctly describe all the present reflections, and the refinement yielded low uncertainty factors (tab. 1, fig. 2, *a*).

A linear decrease of the unit cell volume with an increase in the concentration of the substitution ion (fig. 2, *b*) confirms the single-phase nature of the $Bi_2(Sn_{1-x}Cr_x)_2O_7$ compositions, since the ionic radius IR (Cr^{3+}, CN=6) = 0.615 Å is less than the radius of the IR ion (Sn^{4+}, CN=6) = 0.69 Å [16]. Cr^{3+} ions preferably occupy octahedral positions.

IR spectroscopy. Studies of $Bi_2(Sn_{1-x}Cr_x)_2O_7$ by IR spectroscopy were performed on a Fourier transform spectrometer Vertex 80 v with a spectral resolution of 1 cm^{-1} in the temperature range 110–525 K, the frequency range 350–1100 cm^{-1}. The studies were carried out on a sample in the form of a tablet with a diameter of 13 mm in a KBr matrix.

The absorption bands of the IR spectra of $Bi_2Sn_2O_7$ in the frequency range of 100–1000 cm^{-1} are usually attributed to the stretching vibrations of the crystal lattice ions. These compounds have seven active IR modes, stretching and bending [17] and concern only vibrations of oxygen atoms occupying two crystallographic positions in the crystal structure of $A_2B_2O_6O'$.

IR absorption spectra at room temperature in the frequency range 350–1200 cm^1 for $Bi_2(Sn_{1-x}Cr_x)_2O_7$, x = 0; 0.05 are shown in fig. 3.

The IR spectrum of $Bi_2Sn_2O_7$ contains 4 main vibration modes: 521, 615, 726 and a broad complex mode in the region at 800 cm^{-1} (tab. 2). The stretching vibration mode *w* = 521 is attributed to stretching vibrations of oxygen in the SnO_6 octahedron and splits into two lines at 518 and 525 cm^{-1}. The IR spectra of pyrochlore compounds have very weak absorption bands in the frequency range 800–1100 cm^{-1}, which were identified as an additional complex structural mode of the A–O' long bond

in the A_2O' sublattice. The difference in bond lengths is 20 % between 2.351 Å and 1.961 Å, and the displacement of the O' anion and the A cation within the domain leads to the shortening of one A – O' bond and lengthening of the other [18]. According to this model, the vibrations of the short A – O' bond correspond to phonon modes at about 850 cm^{-1} and vibrations of the long bond at 483 cm^{-1}.

The substitution of tin by chromium ions led to a modification of the IR spectrum, which also contains four distinct groups of lines in the frequency ranges 370–440, 480–560, 580–680, 820–920 cm^{-1}.

All lines of this spectrum are complex and consist of several lines: the frequency range 370–440, 480–560, 580–680 cm^{-1} contains 2 lines, and 820–940 cm^{-1} – 3 lines.
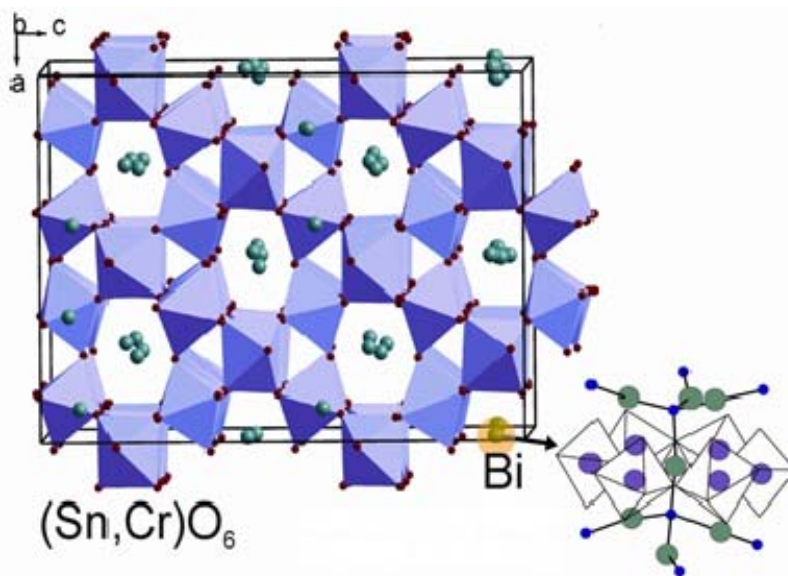
Fig. 1. $Bi_2(Sn_{1-x}Cr_x)_2O_{7-x}$, $x = 0$; 0.05, 0.1 crystal structure. The BiO_8 fragment is shown separately. There are Sn ions in the center of octahedra. Color code: O atoms are at the vertices of the blue octahedra, O′ atoms are dark blue

Рис. 1. Кристаллическая структура $Bi_2(Sn_{1-x}Cr_x)_2O_{7-x}$, $x = 0$; 0.05, 0.1. Подрешетка BiO_8 выделена отдельно. В центре октаэдров находятся ионы Sn. Атомы О находятся в вершинах голубых октаэдров. Атомы О′– темно голубые

а   *б*
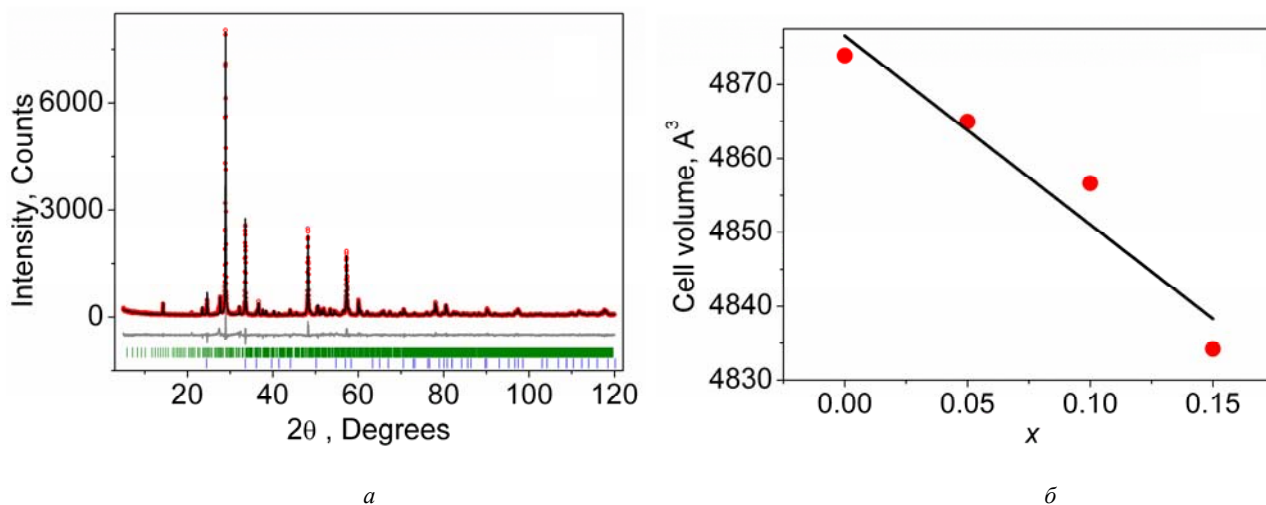
Fig. 2. Difference XRD pattern of $Bi_2(Sn_{1-x}Cr_x)_2O_7$ (*a*). Cell parameters of $Bi_2(Sn_{1-x}Cr_x)_2O_7$ (*b*)

Рис. 2. Разностная рентгенограмма $Bi_2(Sn_{1-x}Cr_x)_2O_7$ (*a*). Параметры ячейки $Bi_2(Sn_{1-x}Cr_x)_2O_7$ (*б*)

Table 1

The main parameters experiments and refinement results of Bi$_2$(Sn$_{1-x}$Cr$_x$)$_2$O$_7$

X	0.05	0.1
Space group	*Pc*	*Pc*
a, Å	15.0634 (13)	15.075 (1)
b, Å	15.1055 (12)	15.0823 (1)
c,Å	21.381 (2)	21.3589 (13)
β, °	89.924 (7)	89.905 (4)
V, Å3	4865.0 (7)	4856.6 (5)
2θ interval, °	5–90	5–90
R$_{wp}$, %	13.93	13.62
R$_p$, %	10.21	10.06
R$_B$, %	5.08	5.56
χ^2	1.75	1.70

This is agree with the X-ray structural data for Bi$_2$(Sn$_{0.95}$Cr$_{0.05}$)$_2$O$_7$. The vibration frequency of ions is determined by the symmetry of the crystal lattice.

The frequency range 370–440 cm^{-1} of the IR spectrum of Bi$_2$(Sn$_{0.95}$Cr$_{0.05}$)$_2$O$_7$ (fig. 3) contains a set of lines with frequencies of 378, 416 cm^{-1}. The mode at a frequency of 382 cm^{-1} is a stretching Bi – O mode of the ideal pyrochlore structure [12]. The 416 cm^{-1} line corresponds to oxygen vibrations in the SnO$_6$ octahedron.

The next frequency range 490–540 cm^{-1} at room temperature contains two broadened lines with frequencies of 506, 526 cm^{-1} (fig. 3), corresponding to stretching vibrations of the Bi – O' bond in Bi$_2$Sn$_2$O$_7$.

In the frequency range 610–640 cm^{-1}, the IR spectrum of Bi$_2$(Sn$_{0.95}$Cr$_{0.05}$)$_2$O$_7$ at room temperature has a broadened line, which consists of two lines (fig. 3) with frequencies of 618 and 632 cm^{-1}. IR absorption in this frequency range is attributed to stretching vibrations of the Sn – O bond of the oxygen octahedron SnO$_6$ in the pyrochlore structure [12].

Low-intensity absorption is observed in the high-frequency range 850–920 cm^{-1}. The absorption spectrum has a shoulder at 863 cm^{-1} and a broadened line consisting of 2 lines with frequencies of 878 and 894 cm^{-1}. In the Bi$_2$(Sn$_{0.95}$Cr$_{0.05}$)$_2$O$_7$ solid solution, the substitution of tin by chromium distorts the local structure in the vicinity of bismuth ions, and the vibrations of the Bi – O' – Cr bonds correspond to these frequencies. In Bi$_2$Sn$_2$O$_7$, the lone electron pairs of Bi^{3+} are shortened due to the overlap of Bi 6s electron pairs and d-orbitals of Sn^{4+}. The ionic radii of Sn^{4+}, Cr^{3+} and Bi^{3+} are 0.067, 0.064, 0.120 nm respectively. Chromium ions predominantly occupy octahedral positions; therefore, it can be assumed that chromium replaces tin ions in SnO$_6$, distorting the nearest environment.

Almost all vibration frequencies decrease monotonically with increasing temperature, except for the vibration frequency of the Sn-O bond at 630 cm^{-1}. A slight softening of the frequencies at 878 and 894 cm^{-1} upon heating and a decrease in their intensity is observed at a temperature of 330 K. This is possibly due to the electronic contribution to the absorption spectrum. Impurity states of

electrons (holes) form a bound state with phonons – a polaron. At a certain value of the parameter of the electron-phonon interaction, a quasigap is formed in impurity polaron states. With increasing temperature, the chemical potential falls into the forbidden polaron subband and the intensity of thermal transitions decreases at T = 330 K.

In the vicinity of a temperature of 260 K, another transition in the absorption intensity was found. IR absorption reaches a maximum at a frequency of 508 cm^{-1}, corresponding to the vibration of a single Bi-O' bond. It is possible that a center of symmetry appears in one of the phases, i.e. a centrosymmetric – noncentrosymmetric phase transition is realized. This assumption is supported by the presence of a maximum dielectric constant at 260 K 11].

Raman spectroscopy. Micro-Raman scattering spectra were measured in backscatter geometry at room temperature through a 50x microscope objective using a Renishawin Via micro-Raman spectrometer equipped with an argon laser (514.5 nm, maximum power 10 MW). The spectral signal was scattered by a 2400 groove/mm diffraction grating on a Peltier-cooled CCD detector with a resolution of 1 cm^{-1}.

The absence of a center of symmetry in the α-phase is also confirmed by Raman scattering spectra. Experimental data of Raman spectroscopy Bi$_2$(Sn$_{1-x}$Cr$_x$)$_2$O$_7$, x = 0, 0.1 are shown in fig. 4 in the frequency range 100–1000 cm^{-1} at room temperature. The spectrum of Bi$_2$Sn$_2$O$_7$ consists of a number of broad bands and is consistent with the spectrum data [19]. The ideal pyrochlore structure A$_2$B$_2$O(1)$_6$O(2) with a space group $Fd\bar{3}m$ has several types of vibrations $\Gamma_R = A_{1g} + E_g + 4F_{2g}$. In this view, the six main Raman modes are active. The spectra shown in fig. 4 have a number of spectral lines that differ from the ideal pyrochlore structure, as a result of a decrease in symmetry (tab. 2).

Bismuth pyrostannate with symmetry $Pc\left(C_s^2\right)$ has a larger number of active modes $\Gamma_R = 526A' + 527A''$. In the frequency range 100–200 cm^{-1} for Bi$_2$(Sn$_{1-x}$Cr$_x$)$_2$O$_7$, x = 0, bending (F$_{1u}$) O-Bi-O, 148 cm^{-1} and stretching (F$_{1u}$) Bi-SnO$_6$, 188 cm^{-1} vibrations are active [6].

In the intermediate region of the spectrum of $Bi_2Sn_2O_7$, 200–400 cm^{-1} some modes correspond to active vibrations of IR spectroscopy for pyrochlores with low symmetry. The spectral line at 211 cm^{-1} is predominantly described by stretching vibrations (F_{1u}) along the Bi-SnO_6 bond. Vibrations with frequencies of 274, 382 cm^{-1} are defined as stretching (F_{1u}) O-Sn-O and stretching (F_{1u}) Bi-O. Within this range, there are two modes that correspond to the ideal pyrochlore structure, 225 (F_{2g}) and 248 cm^{-1} (E_g). The mode (F_{2g}) is associated with the shift of oxygen O1 in the SnO_6 polyhedron. Four groups of vibrations are observed in the Raman spectrum of $Bi_2Sn_2O_7$ above 400 cm^{-1}. Vibrations of 535 and 400 cm^{-1} are classified as stretching O-Sn-O (A_{1g}) and Sn-O (F_{2g}).
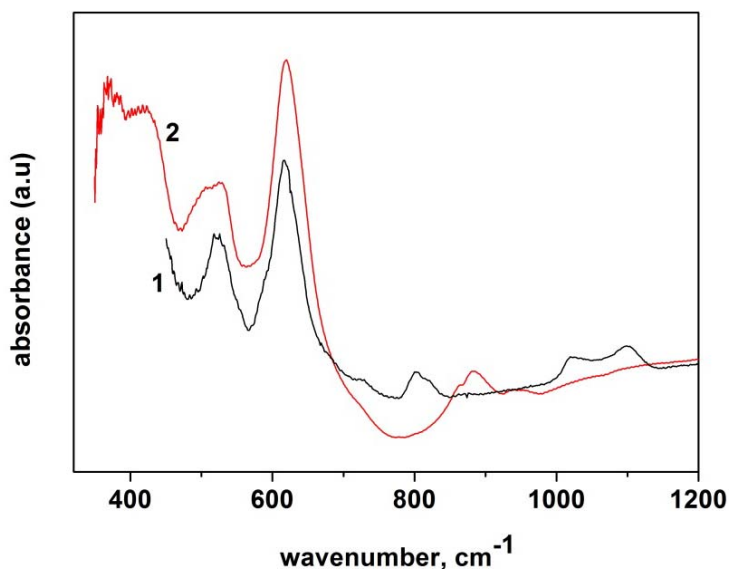
Fig. 3. IR spectra of $Bi_2(Sn_{1-x}Cr_x)_2O_7$. Curve 1 corresponds to $x = 0$, curve 2 corresponds to $x = 0.05$

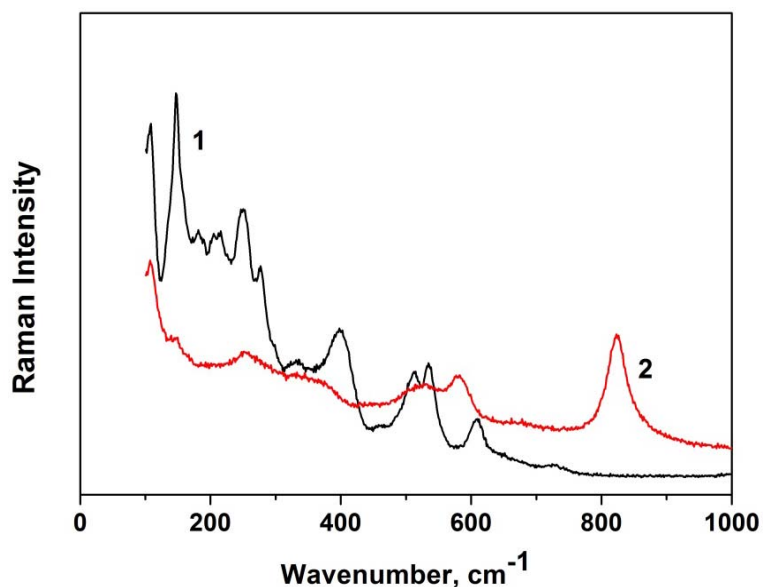Рис. 3. ИК спектры $Bi_2(Sn_{1-x}Cr_x)_2O_7$. Кривая 1 относится к $x = 0$, кривая 2 относится к $x = 0{,}05$

Fig. 4. Raman scattering spectrum of $Bi_2(Sn_{1-x}Cr_x)_2O_7$. Curve 1 corresponds to $x = 0$, curve 2 corresponds to $x = 0.05$

Рис. 4. Спектры Рамановского рассеяния $Bi_2(Sn_{1-x}Cr_x)_2O_7$. Кривая 1 относится к $x = 0$, кривая 2 относится к $x = 0{,}05$

Table 2

Vibration modes of Raman and IR spectroscopy of $Bi_2(Sn_{1-x}Cr_x)_2O_7$

Raman modes (cm^{-1})		IR modes (cm^{-1})		correspondence
$X = 0$	$X = 0.1$	$X = 0$	$X = 0.05$	
108	108			A_{2u}
148	144 broad			Flexural O-Bi-O (F_{1u})
181				Bi-SnO$_6$ (F_{1u})
208				
215				F_{1u}
225				F_{2g}
248	251			E_g
274				Flexural O-Sn-O (F_{1u})
332			353	F_{1u}
			382	Stretching Bi – O′
400			416 broad	Flexural O в SnO′$_6$(F_{2g})
			507	Bi-O'
512		518		Stretching SnO$_6$ octahedron (A_{1g})
534	523	525	526	Flexural O' (A_{1g})
	581			Stretching Bi-O(F_{2g})
608				(F_{2g})
		615	619	Stretching Sn–O
			632	
		726		
		801		Overtone or combination
	822	820	863, 883	

The substitution of tin ions by chromium led to a decrease in the number and intensity of spectral lines of the Raman spectrum, as well as to the appearance of two new modes at frequencies of 581 and 822 cm^{-1}. The spectral line 581 cm^{-1} exists in the optical spectra of compounds with an ideal pyrochlore structure and refers to stretching vibrations of the Bi-O bond. The high-frequency spectral line 822 cm^{-1} does not have an unambiguous interpretation, and it is defined as an "overtone or combined" band (combination band) or mode (F_{2g}) [6].

Substitution of tin by Cr^{3+} ions does not change the space symmetry group and leads to the absence of some spectral lines in the spectrum of $Bi_2(Sn_{1-x}Cr_x)_2O_7$, x = 0.1 in comparison with $Bi_2Sn_2O_7$. Perhaps this is due to an increase in the local symmetry of bismuth pyrostannate at a disordered arrangement of Cr^{3+} ions.

Conclusion. At room temperature, bismuth pyrostannate $Bi_2(Sn_{1-x}Cr_x)_2O_7$, x = 0; 0.05, 0.1 refers to the monoclinic structure of *Pc*. Chromium ions replace tin ions in SnO$_6$ octahedra. In The IR absorption spectra four frequency regions with two absorption lines in each region, and three lines in the high-frequency region were revealed. The softening of frequencies and the type of vibration mode associated with the valence bonds of bismuth and tin at structural transitions have been established. The absence of an inversion center in doped bismuth stannates is confirmed by Raman spectra. In chromium-substituted pyrostannates, the phase boundaries of the structural transitions inherent in $Bi_2Sn_2O_7$ are shifted.

References

1. Udod L. V., Aplesnin S. S., Sitnikov M. N., Molokeev M. S. Dielectric and Electrical Properties of Polymorphic Bismuth Pyrostannate $Bi_2Sn_2O_7$. *Physics of the Solid State*. 2014, Vol. 56, P. 1315–1319.

2. Udod L. V., Aplesnin S. S., Sitnikov M. N., Romanova O. B., Molokeev M. N. Phase transitions in bismuth pyrostannate upon substitution of tin by iron ions. *J. Alloys and Compounds*. 2019, Vol. 804, P. 281–287.

3. Lewis J. W., Payne J. L., Evans I. R., Stokes H. T., Branton J. Campbell and John S. O. Evans. An Exhaustive Symmetry Approach to Structure Determination: Phase Transitions in $Bi_2Sn_2O_7$. *J. Am. Chem. Soc*. 2016, Vol. 138, P. 8031−8042.

4. Udod L. V., Sitnikov M. N., Aplesnin S. S., Molokeev M. S. Electrical and Dielectrical Propeties of Gas-Sensor Resistive Type $Bi_2Sn_2O_7$. *Solid State Phenomena*. 2014, Vol. 215, P. 503–506.

5. Aplesnin S. S., Udod L. V., Sitnikov M. N. Electronic transition, ferroelectric and thermoelectric properties of bismuth pyrostannate $Bi_2(Sn_{0.85}Cr_{0.15})_2O_7$. *Ceramics International*. 2018, Vol. 44, P. 1614–1620.

6. Aplesnin S. S., Udod L. V., Sitnikov M. N., Kretinin V. V., Molokeev M. S., Mironova-Ulmane N. Dipole glass in chromium-substituted bismuth pyrostannate. *Mater. Res. Express.* 2018, Vol. 5, P. 115202.

7. Aplesnin S. S., Udod L. V., Sitnikov M. N., Molokeev, M. S., Tarasova L. S., Yanushkevich K. I. Magnetic, Dielectric, and Transport Properties of Bismuth Pyrostannate $Bi_2(Sn_{0.9}Mn_{0.1})_2O_7$. *Physics of the Solid State.* 2017, Vol. 59, P. 2268–2273.

8. Aplesnin S. S,, Udod L. V., Loginov Y. Y., Kretinin V. V., Masyugin A. N. Influence of cation substitution on dielectric and electric properties of bismuth stannates $Bi_2Sn_{1.9}Me_{0.1}O_7$ (Me=Cr, Mn). *IOP Conf. Series: Materials Science and Engineering.* 2019, Vol. 467, P. 012014.

9. Udod L. V., Aplesnin S. S., Sitnikov M. N. Magnetic Properties of Bismuth Pyrostannate Doped with 3D Ions. *Inorganic Materials: Applied Research.* 2020, Vol. 11, P. 809–814.

10. Udod L. V., Aplesnin S. S., Sitnikov M. N., Eremin E. V., Molokeev M. S. Effect of Mn Doping on Magnetic and Dielectric Properties of $Bi_2Sn_2O_7$. *Sol. St. Phenomena.* 2015, Vol. 233–234, P. 105.

11. Aplesnin S. S., Udod L. V., Sitnikov M. N., Eremin E. V., Molokeev M. S., Tarasova L. S., Yanushkevich K. I., Galyas A. I., Correlation of the Magnetic and Transport Properties with Polymorphic Transitions in Bismuth Pyrostannate $Bi_2(Sn_{1-x}Cr_x)_2O_7$. *Phys. Sol. St.* 2015, Vol. 57, P. 1627–1632.

12. Aplesnin S. S., Udod L. V., Sitnikov M. N., Shestakov N. P. $Bi_2(Sn_{0.95}Cr_{0.05})_2O_7$: Structure, IR spectra, and dielectric properties. *Ceramics International.* 2016, Vol. 42, P. 5177–5183.

13. Aplesnin S. S., Udod L. V., Sitnikov M. N., Romanova O. B. Dielectric and transport properties, electric polarization at the sequential structural phase transitions in iron-substituted bismuth pyrostannate. *Ceramics International.* 2020. Available at: https://doi.org/10.1016/j.ceramint.2020.08.287 (accessed 25.10.2020).

14. Udod L. V., Aplesnin S. S., Sitnikov M. N., Romanova O. B., Bayukov O. A., Vorotinov A. M., Velikanov D. A., Patrin G. S. Magnetodielectric effect and spin state of iron ions in substituted bismuth pyrostannate. *European Physical Journal Plus.* 2020. DOI: 10.1140/epjp/s13360-020-00781-2.

15. Evans I. R., Howard J. A. K., Evans J. S. O. α-$Bi_2Sn_2O_7$ – a 176 atom crystal structure from powder diffraction data. *J. Mater. Chem.* 2003, Vol. 13, P. 2098–2103.

16. Shannon R. D. Revised effective ionic radii and systematic studies of interatomic distances in halides and chalcogenides. *Acta Cryst. A.* 1976, Vol. 32 (5), P. 751–767.

17. Chen M., Tanner D. B., Nino J.C. Infrared study of the phonon modes in bismuth pyrochlores. *Phys. Rev. B.* 2005, Vol. 72, P. 054303-8.

18. Moens L., Ruiz P., Delmon B., Devillers M. Co-operation effects towards partial oxidation of isobutene in multiphasic catalysts based on bismuth pyrostannate. *Appl. Catal. A: Gen.* 1998, Vol, 171, P. 131.

19. Silva R. X., Paschoal C. W. A., Almeida R. M., M. Carvalho Castro Jr., Ayalac A. P., Auletta J. T., Lufaso M. W. Temperature-dependent Raman spectra of $Bi_2Sn_2O_7$ ceramics. *Vibrational Spectroscopy.* 2013, Vol. 64, P. 172–177.

Библиографические ссылки

1. Диэлектрические и электрические свойства полиморфного пиростаната висмута $Bi_2Sn_2O_7$ / Л. В. Удод, Аплеснин С. С., Ситников М. Н. и др. // Физика твердого тела. 2014. Т. 56 (7). С. 1267–1271.

2. Phase transitions in bismuth pyrostannate upon substitution of tin by iron ions / L. V. Udod, S. S. Aplesnin, M. N. Sitnikov et. al. // J. Alloys and Compounds. 2019. Vol. 804. P. 281–287.

3. An Exhaustive Symmetry Approach to Structure Determination: Phase Transitions in $Bi_2Sn_2O_7$ / J. W. Lewis, J. L. Payne, I. R. Evans at. al. // J. Am. Chem. Soc. 2016.Vol. 138, P. 8031−8042.

4. Electrical and Dielectrical Propeties of Gas-Sensor Resistive Type $Bi_2Sn_2O_7$ / L.V. Udod, M. N. Sitnikov, S. S. Aplesnin et. al. // Solid State Phenomena. 2014. Vol. 215. P. 503–506.

5. Aplesnin S. S., Udod L. V., Sitnikov M. N. Electronic transition, ferroelectric and thermoelectric properties of bismuth pyrostannate$Bi_2(Sn_{0.85}Cr_{0.15})_2O_7$ // Ceramics International. 2018. Vol. 44. P. 1614–1620.

6. Dipole glass in chromium-substituted bismuth pyrostannate / S. S. Aplesnin, L. V. Udod, M. N. Sitnikov et. al. // Mater. Res. Express. 2018. Vol. 5. P. 115202.

7. Магнитные, диэлектрические и транспортные свойства пиростанната висмута $Bi_2(Sn_{0.9}Mn_{0.1})_2O_7$ / С. С. Аплеснин, Л. В. Удод, М. Н. Ситников и др. // Физика твердого тела. 2017. Т. 59 (11). С. 2246–2251.

8. Influence of cation substitution on dielectric and electric properties of bismuth stannates $Bi_2Sn_{1.9}Me_{0.1}O_7$ (Me=Cr, Mn) / S. S. Aplesnin, L. V. Udod, Y. Y. Loginov et. al. // IOP Conf. Series: Materials Science and Engineering. 2019. Vol. 467. P. 012014.

9. Udod L. V., Aplesnin S. S., Sitnikov M. N. Magnetic Properties of Bismuth Pyrostannate Doped with 3D Ions // Inorganic Materials: Applied Research. 2020. Vol. 11 (4). P. 809–814.

10. Effect of Mn Doping on Magnetic and Dielectric Properties of $Bi_2Sn_2O_7$ / Udod L. V., S. S. Aplesnin, M. N. Sitnikov et. al. // Sol. St. Phenomena. 2015. Vol. 233–234. P. 105.

11. Корреляция магнитных и транспортных свойств с полиморфными переходами в пиростаннате висмута $Bi_2(Sn_{1-x}Cr_x)_2O_7$ / С. С. Аплеснин, Л. В. Удод, М. Н. Ситников и др. // Физика твердого тела. 2015. Т. 57 (8). С. 1590–1595.

12. $Bi_2(Sn_{0.95}Cr_{0.05})_2O_7$: Structure, IR spectra, and dielectric properties / S. S. Aplesnin, L. V. Udod, M. N. Sitnikov et. al. // Ceramics International. 2016. Vol. 42. P. 5177–1583.

13. Dielectric and transport properties, electric polarization at the sequential structural phase transitions in iron-substituted bismuth pyrostannate / S. S. Aplesnin, L. V. Udod, M. N. Sitnikov et. al. // Ceramics Interna-

tional. 2020 [Электронный ресурс]. URL: https://doi.org/10.1016/j.ceramint.2020.08.287 (дата обращения: 25.10.2020).

14. Magnetodielectric Effect and Spin State of Iron Ions in Substituted Bismuth Pyrostannate / L. Udod, S. Aplesnin, M. Sitnikov et. al. // European Physical Journal Plus. 2020. DOI: 10.1140/epjp/s13360-020-00781-2.

15. Evans I. R., Howard J. A. K., Evans J. S. O. α-$Bi_2Sn_2O_7$ – a 176 atom crystal structure from powder diffraction data // J. Mater. Chem. 2003. Vol. 13. P. 2098–2103.

16. Shannon R. D. Revised effective ionic radii and systematic studies of interatomic distances in halides and chalcogenides // ActaCryst. A, 1976. Vol. 32 (5). P. 751–767.

17. Chen M., Tanner D. B., Nino J. C. Infrared study of the phonon modes in bismuth pyrochlores // Phys. Rev. B 2005. Vol. 72. P. 054303-8.

18. Cooperation effects towards partial oxidation of isobutene in multiphasic catalysts based on bismuth pyrostannate / L. Moens, P. Ruiz, B. Delmon et. al. // Appl. Catal. A: Gen. 1998. Vol. 171. P. 131.

19. Temperature-dependent Raman spectra of $Bi_2Sn_2O_7$ ceramics / Silva R. X., C. W. A. Paschoal, R. M. Almeida, Carvalho M., Jr. Castro // Vibrational Spectroscopy. 2013. Vol. 64. P. 172–177.

Udod Lubov Viktorovna – Cand. Sc., Associate Professor; Reshetnev Siberian State University of Science and Technology; Kirensky Institute of Physics, FRC KSC Siberian Branch of the Russian Academy of Sciences. E-mail: luba@iph.krasn.ru.

Romanova Oksana Borisovna – Cand. Sc., Researcher; Kirensky Institute of Physics, FRC KSC Siberian Branch of the Russian Academy of Sciences. E-mail**:** rob@iph.krasn.ru.

Aplesnin Sergey Stepanovich – Dr. Sc., Professor, Head of the Department of Physics; Reshetnev Siberian State University of Science and Technology; Kirensky Institute of Physics, FRC KSC Siberian Branch of the Russian Academy of Sciences. E-mail: aplesnin@sibsau.ru,

Kretinin Vasily Vasilievich – student of the Department of Physics; Reshetnev Siberian State University of Science and Technology. E-mail: kretinin.vasya@yandex.ru.

Удод Любовь Викторовна – кандидат физико-математических наук, доцент; Сибирский государственный университет науки и технологий имени академика М. Ф. Решетнева; Институт физики им. Л. В. Киренского СО РАН – обособленное подразделение ФИЦ КНЦ СО РАН. E-mail: luba@iph.krasn.ru.

Романова Оксана Борисовна – кандидат физико-математических наук, научный сотрудник; Институт физики им. Л. В. Киренского СО РАН – обособленное подразделение ФИЦ КНЦ СО РАН. E-mail: rob@iph.krasn.ru.

Аплеснин Сергей Степанович – доктор физико-математических наук, профессор, заведующий кафедрой физики; Сибирский государственный университет науки и технологий имени академика М. Ф. Решетнева; Институт физики им. Л. В. Киренского СО РАН – обособленное подразделение ФИЦ КНЦ СО РАН. E-mail: aplesnin@sibsau.ru, apl@iph.krasn.ru.

Кретинин Василий Васильевич – студент; Сибирский государственный университет науки и технологий имени академика М. Ф. Решетнева. E-mail: kretinin.vasya@yandex.ru.

DEVELOPMENT OF SEM METHOD FOR ANALYSIS OF ORGAN-CONTAINING OBJECTS USING INVERSE OPALS

O. V. Shabanova[1*], I. V. Nemtsev[2,3], A. V. Shabanov[3]

[1] Special Designing and Technological Bureau "Nauka" KSC SB RAS
50, Akademgorodok, Krasnoyarsk, 660036, Russian Federation
[2] Federal Research Center
Krasnoyarsk Science Center of the Siberian Branch of the Russian Academy of Sciences
50, Akademgorodok, Krasnoyarsk, 660036, Russian Federation
[3] L.V. Kirensky Institute of Physics SB RAS
50, building 38, Akademgorodok, Krasnoyarsk, 660036, Russian Federation
*E-mail ollach@yandex.ru

The purpose of this study is to test the possibility of using inorganic macroporous structures of inverse opal in sample preparation for scanning electron microscopy of biological objects.

As an absorbent substrate we used silica inverse opals prepared by a sol-gel method to study the biological objects. The process of manufacturing the inverse opal involves a complex multi-stage technological process. First, we synthesized submicron spherical particles from polymethylmethacrylate by the method of emulsifier-free emulsion polymerization of methylmethacrylate in an aqueous medium in the presence of a diazoinitiator. This method can be used to obtain an ensemble of particles with high monodispersity, the average size of which can vary in the range from 100 to 500 nm. Then, by self-assembly technique, we deposited the beads of polymethylmethacrylate into ordered matrices (templates), mainly with a face-centered cubic lattice. The resulting mesoporous structures, called artificial opals or colloidal crystals, had lateral dimensions of about 10 × 10 × 2 mm. Then we heat-treated the opals to 120 °C to harden the template before being impregnated with the precursor. Further, we impregnated the opals with silica sol with a particle size distribution from 1 to 5 nm, obtained by hydrolysis of tetraethoxysilane in the presence of hydrochloric acid, and then, after curing and drying the impregnating composition in air at room temperature, we multi-stage fired them up to 550 °C at normal pressure in the air atmosphere to remove all organic components. As a result, the macroporous metamaterial (the so-called inverse opals) with an open system of pores up to 400 nm in size, occupying about 80 % of the volume, were obtained.

We studied lactic acid bacteria of cucumber brine and human red blood cells with TM4000 Plus, SU3500 and S-5500 scanning electron microscopes. Auxiliary substance for the sample preparation was ionic liquid VetexQ EM (Interlab LLC). We showed that it is possible to use the inverse opal as an absorbent substrate for sample preparation and rapid analysis in scanning electron microscopy without pre-drying, chemical treatment, or temperature exposure. To improve imaging in the electron microscope, we used sputter coater to cover the inverse opal surface with a thin film of platinum. The use of ionic liquid in combination with the absorbent porous medium allows preserving an original shape of the biological structures. Using the human red blood cells and lactic acid bacteria, we showed that it is possible to carry out of the morphological analysis of the cells using various scanning electron microscopes. We found that on the basis of the inverse opal, there is a fundamental possibility of creating the absorbent substrate suitable for repeated use in the study of the biological objects. At the same time, trace remnants of previous samples remaining after annealing the plate do not introduce significant distortions when conducting new series of observations. In this study, we obtained high-quality electronic micrographs of the biological objects with high resolution and contrast. At the same time, due to the use of the inverse opals as the absorbent substrate, time and financial costs for research are reduced.

Keywords: scanning electron microscopy, mesoporous structure, inverse opal, lactic acid bacteria, erythrocyte.

РАЗРАБОТКА ЭЛЕКТРОННО-МИКРОСКОПИЧЕСКОГО МЕТОДА АНАЛИЗА ОРГАНСОДЕРЖАЩИХ ОБЪЕКТОВ С ИСПОЛЬЗОВАНИЕМ ИНВЕРСНЫХ ОПАЛОВ

О. В. Шабанова[1*], И. В. Немцев[2,3], А. В. Шабанов[3]

[1]Специальное конструкторско-технологическое бюро «Наука»
Российская Федерация, 660036, г. Красноярск, Академгородок, 50, стр. 45
[2]Федеральный исследовательский центр
«Красноярский научный центр Сибирского отделения Российской академии наук»
Российская Федерация, 660036, г. Красноярск, Академгородок, 50
[3]Институт физики им. Л. В. Киренского СО РАН
Российская Федерация, 660036, г. Красноярск, Академгородок, 50, стр. 38
*E-mail: ollach@yandex.ru

Целью данного исследования является апробация возможности применения неорганических макропористых структур инверсного опала при пробоподготовке для сканирующей электронной микроскопии биообъектов.

Изготовленные золь-гель способом инверсные опалы на основе кремнезёма применялись в качестве впитывающей подложки для изучения биологических образцов. Изготовление инверсного опала представляет собой сложный многоступенчатый технологический процесс. Сначала методом безэмульгаторной эмульсионной полимеризации метилметакрилата в водной среде в присутствии диазоинициатора были синтезированы субмикронные сферические частицы из полиметилметакрилата. Таким способом можно получать ансамбль частиц с высокой монодисперсностью, средний размер которых может варьироваться в диапазоне от 100 до 500 нм. Затем методом самосборки субмикросферы полиметилметакрилата осаждались в упорядоченные матрицы (шаблоны) преимущественно с гранецентрированной кубической решёткой. Полученные мезопористые структуры, называемые искусственными опалами или коллоидными кристаллами, имели размеры порядка 10 ×10 × 2 мм. Затем опалы подвергались термической обработке до 120 °C для упрочнения шаблона перед пропиткой прекурсором. Далее опалы пропитывались золем кремнезёма с размером частиц от 1 до 5 нм, полученным путём гидролиза тетраэтоксисилана в присутствии соляной кислоты и затем, после отверждения и сушки пропитывающего состава на воздухе при комнатной температуре, подвергались многоступенчатому обжигу до 550 °C при нормальном давлении в воздушной атмосфере для удаления всех органических компонентов. В результате получались образцы макропористых метаматериалов (так называемые, инверсные или инвертированные опалы) с открытой системой пор размером до 400 нм, занимающих около 80 % объёма.

В сканирующих электронных микроскопах TM4000 Plus, SU3500 и S-5500 с использованием макропористых структур были исследованы молочнокислые бактерии и красные кровяные тельца. Для улучшения визуализации использовались системы напыления металлов для покрытия поверхности инверсного опала тонкой плёнкой платины. Вспомогательным веществом в пробоподготовке выступала ионная жидкость VetexQ EM (Interlab LLC). Показано, что инверсный опал можно использовать как впитывающую подложку для пробоподготовки и экспресс-анализа в сканирующей электронной микроскопии без предварительной сушки, химической обработки или температурного воздействия биообъектов. Использование ионной жидкости в сочетании с впитывающей пористой средой позволяет сохранить первоначальную форму биологических структур. Показана возможность изучения морфологических особенностей биоструктур на примере эритроцитов человека и молочнокислых бактерий. Экспериментально установлено, что впитывающую подложку на основе инверсного опала можно использовать многократно при исследовании биологических объектов. Следовые остатки предыдущих проб, оставшиеся после отжига пластины, не вносят существенных искажений при проведении новых серий наблюдений. В нашем исследовании были получены высококачественные электронные микрофотографии биообъектов с высоким разрешением и контрастом. При этом за счёт использования инверсных опалов в качестве впитывающей подложки обеспечивается сокращение временных и финансовых затрат на исследования.

Ключевые слова: сканирующая электронная микроскопия, мезопористая структура, инверсный опал, молочнокислая бактерия, эритроцит.

Introduction. Electron microscopy in the field of studying biological objects (cells, cell organelles, bacteria, viruses, biogenic macromolecules, etc.) allows solving a number of research problems to determine the structure, morphology, chemical composition, contact interaction with each other, etc. with high contrast and resolution [1–3].

Scanning electron microscopy (SEM) is used to study the morphology of individual biological objects and their groups [4; 5]. Transmission electron microscopy (TEM) works with thin sections of samples [6]. SEM sequentially scans the surface of the object, registering for each point such processes as the generation of back-scattered electrons, secondary electrons, characteristic X-ray emission, and others. TEM captures an image by scattering electrons passing through a thin sample, allowing structural features within a biological object to be investigated.

The stage of preparing samples for research plays a key role in electron microscopy. The traditional approach to sample preparation of biological objects for electron microscopy is reduced to repeating natural processes that have been going on for millions of years. Chemical sub-

stitution of certain organic compounds for minerals is an alternative to fossilization. Replacing water with wax or epoxy is similar to making amber with inclusions. Drying at the critical point is close to mummification, and the cryofixation method makes it possible to stop all biochemical processes in the sample relatively quickly and avoid morphological changes inherent in chemical fixation (but it has its own limitations) [4].

The bases of the latest techniques, without doubt, are devices with concentrated water vapor in the observation chamber: the partial pressure of the gas does not allow the liquid to boil. Unfortunately, this equipment is not widely used at present.

Another area is the use of salts that are liquid at room temperature. These are very heavy organic compounds that do not boil under vacuum in the working chamber of a conventional electron microscope (10^{-2}–10^{-3} Pa). The ionic liquid, covering the sample, retains its shape and successfully conduct the electric current.

Thus, it is known that in order to obtain the most poisonous natural compound (botulinum toxin), a microfilter is needed. Bacteria are concentrated on it when pumping a suspension. Subsequent extraction from the accumulated layer of unicellular organisms allows obtaining the required chemical compound [7].

The idea of separating a biofluid from microscopic objects suspended in it, therefore, has more than one decade and has been successfully implemented on an industrial scale [8–10]. For the electron microscopy, this approach allows to reduce the waiting interval between the stages "object in a living environment" – "object under an electron beam" to several minutes. The main delay is caused by the time it takes to achieve the required vacuum in the microscope sample chamber.

In this regard, of particular interest are inverse opal materials (IOM) [11–13] that are inorganic macroporous structures with a pore size ≥ 50 nm [14–17].

The purpose of this paper is to assess the possibility of using IOM in the study of biological objects using the example of lactic acid bacteria and human erythrocytes.

The main part. The process of obtaining IOM is described in the papers [18; 19]. Briefly, suspensions of submicron spherical particles were synthesized by the method of emulsifier-free emulsion polymerization of methyl methacrylate in an aqueous medium in the presence of a diazo initiator. Particle size distribution, or monodispersity, did not exceed 6 %. After the deposition of polymethyl methacrylate balls by self-assembly into a mesoporous structure [15; 20–22] with a cubic face-centered packing [23; 24], the dispersion medium was removed; the resulting matrices (templates) were impregnated with silica sol [25]. After curing the impregnation at room temperature and drying at 75–80 °C, the samples were subjected to multistage firing to remove polymer components. The inorganic part of the material (SiO_2) remained in the form of a three-dimensional imprint of the matrix (fig. 1).

To effectively remove the charge of the sample surface in the SEM chamber, a platinum film with a thickness of 2–6 nm was deposited on the surface of inverse opal using the K575XD turbo-pumped dual head sputter coater (Emitech Quorum, UK) and the ACE200 metal vacuum deposition system (Leica, Germany). To visualize morphological features and X-ray elemental mapping the following SEMs were used: TM4000 Plus, SU3500 and S-5500 (Hitachi, Japan).

It should be noted that more than 80 % of the inverse opal volume is occupied by interconnected voids (fig. 1, on the left). Under the influence of capillary forces, the liquid surrounding the samples is absorbed into it. Therefore, salts and organic compounds evaporated under vacuum are hidden inside the volume of the porous substrate.

The fig. 1 (on the right) represents the EDS spectrum of inverse opal. The spectrum contains peaks associated with carbon, oxygen, silicon and copper. The high carbon content in the spectrum can be characterized as follows. Firstly, it is well known that electron probe microanalysis is not accurate for low atomic number elements such as C, B, N, O, etc. Secondly, in most cases, apparently, the inevitable contamination of the inner walls of the vacuum chamber with carbon occurs. In addition, a double-sided electrically conductive carbon tape was used to mount the sample for operation in the SEM. The presence of copper is due to the copper substrate for the SEM.

The absence of crystals of salts, fat spots, carbohydrates and other things allows one to observe the surface of cells without artifacts (fig. 2).

In fig. 2 lactic acid bacteria did not change their shape under vacuum. Usually, after drying, only "deflated" shells can be observed. Sometimes organic objects in the electron microscope chamber explode, leaving an imprint on the mineral substrate. In fig. 3 area 1 is damaged lactic acid bacteria. Their shell is macerated ("wrinkled" during the drying process). Area 2 is the trace left by the bacteria.

The liquid forms a drop if it comes in contact with a hydrophobic surface. Its drying and retraction leads to destruction of the upper layers of fragile inverse opal (fig. 4). These distortions go up to domain boundaries. There is an assumption that due to the polydomain nature, the chips do not cause through cracks.

Physiologically, human erythrocytes enter narrow capillaries, and therefore their shape very easily changes under mechanical stress. In practice, this leads to deformation of the cells on the surface. Erythrocytes are imprinted into the pores of the IOM, as seen in fig. 5 (dark rounded spots are traces of blood cells).

The darkened zones recorded in the micrograph are caused not only by the penetration of biological fluids into the porous structure, but also by the carbon deposit left after annealing by the flame of previous samples.

For comparison (fig. 6). represents a blood sample on an aluminum substrate, washed with excess gasoline.

Fig. 6 shows erythrocytes adhered to the surface, as well as substances dissolved in blood plasma, which hinder a qualitative study of cell morphology. Due to the low adhesive capacity, a significant part of the erythrocytes was washed off with the flushing liquid.

A completely different picture is given by the use of an ionic liquid (fig. 7) [5]. Objects retain their three-dimensional shape, protrude above the substrate level and are visible even at low magnifications.
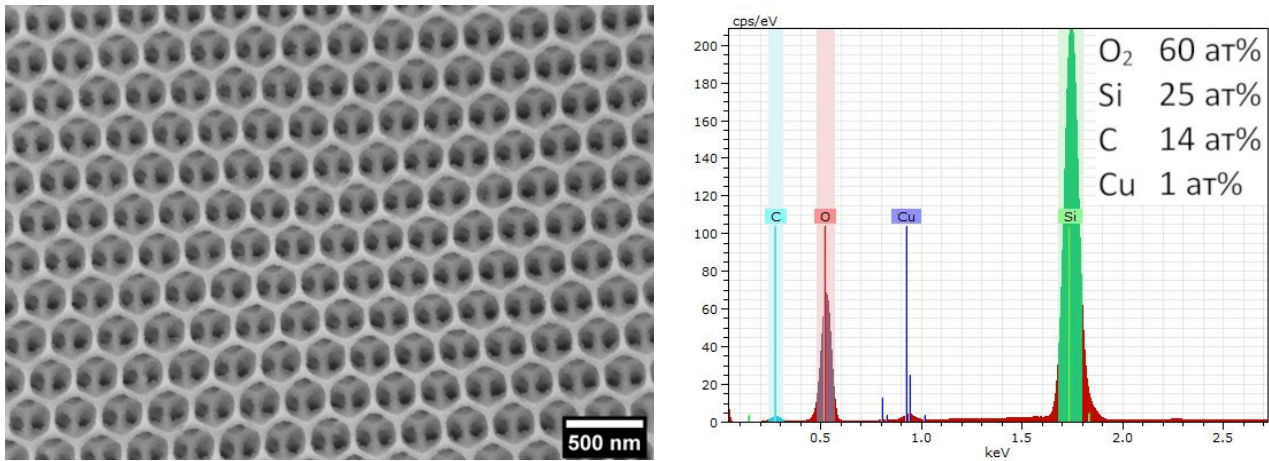
Fig. 1. On the left is an electronic micrograph of an inverse opal based on silicon (IV) oxide. S-5500 microscope, 3 kV, secondary electrons; on the right – an EDS spectrum of the sample. The insert shows the molar content of the elements. The high carbon content is due to the imperfection (shortcoming) of the vacuum in the working chamber of the SEM (residual contamination), copper – from the working substrate of the SEM)

Рис. 1. Слева – электронная микрофотография инверсного опала на основе оксида кремния (IV). Электронный микроскоп S-5500, 3 кВ, вторичные электроны. Справа – ЭДС-спектр образца. На вставке приведено молярное содержание элементов. Высокое содержание углерода обусловлено неидеальностью вакуума в рабочей камере РЭМ (остаточные загрязнения, медь – от рабочего столика РЭМ)
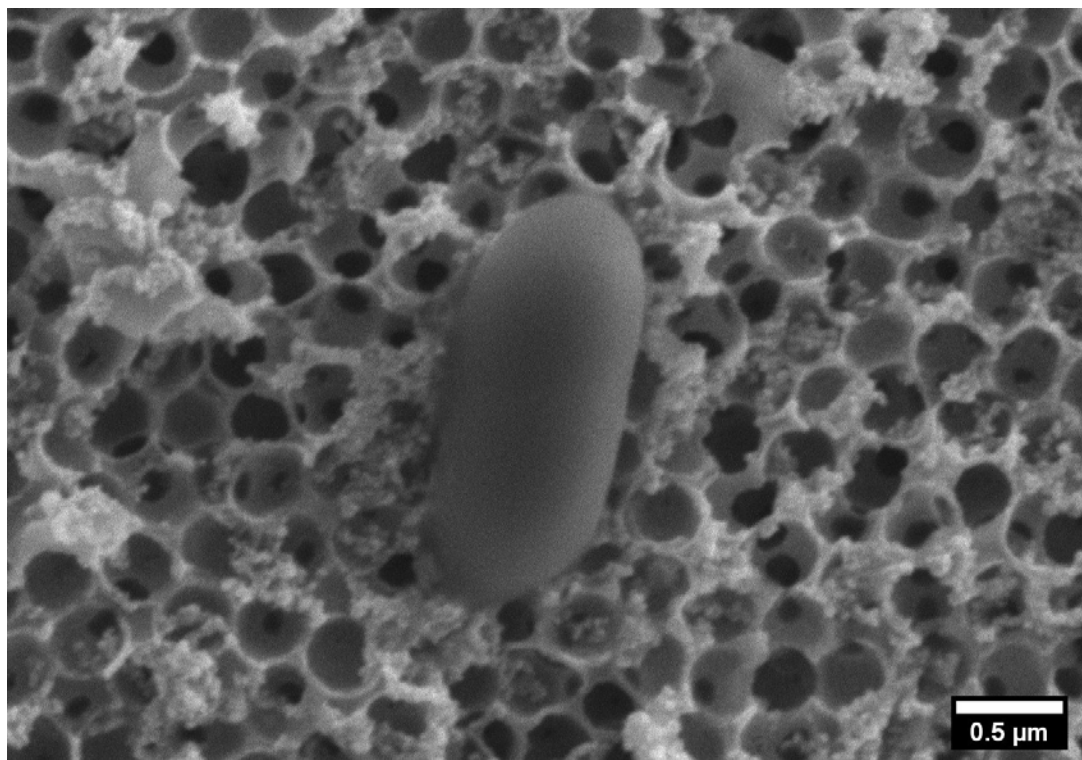

Fig. 2. SEM image of lactic acid spores on surface of inverted silica opal.
SU3500 microscope, 5 kV, secondary electrons

Рис. 2. Электронная микрофотография споры молочнокислой бактерии
на поверхности инвертированного опала из кремнезёма.
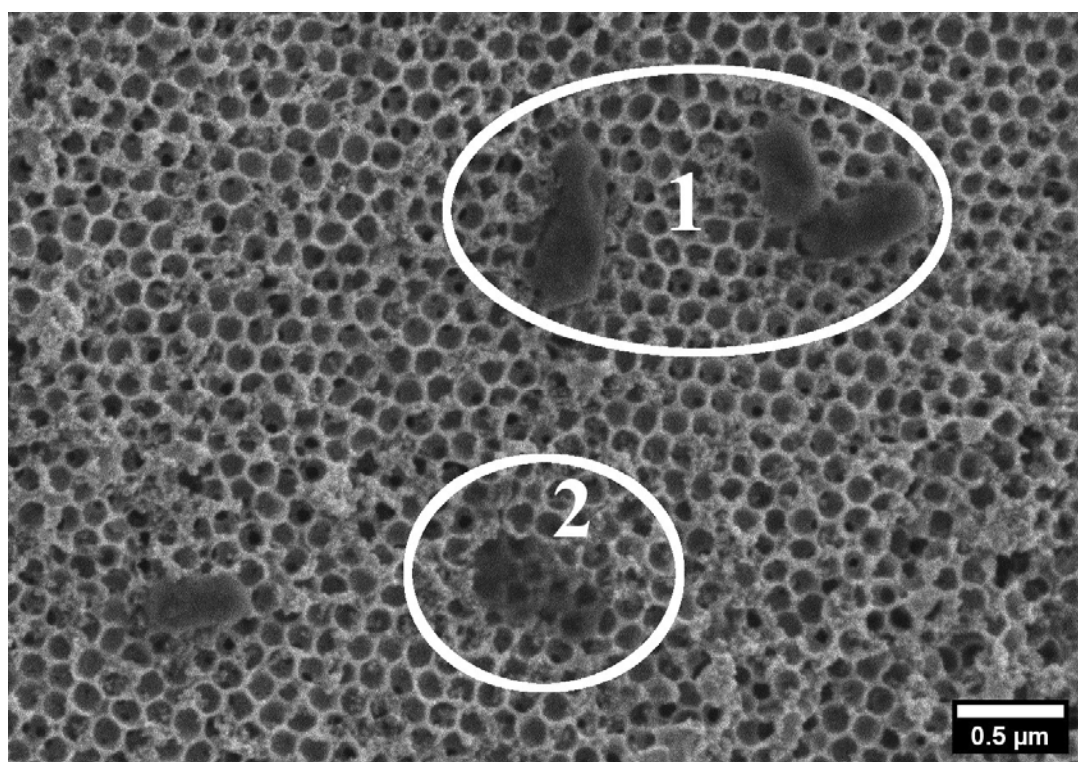Микроскоп SU3500, 5 кВ, вторичные электроны

Fig. 3. An electron micrograph of lactic acid bacteria damaged during vacuuming on surface
of an inverted silicon oxide opal. SU3500 microscope, 1.5 kV, secondary electrons

Рис. 3. Электронная микрофотография молочнокислых бактерий, повреждённых во время вакуумирования,
на поверхности инвертированного опала из оксида кремния. Микроскоп SU3500, 1,5 кВ, вторичные электроны
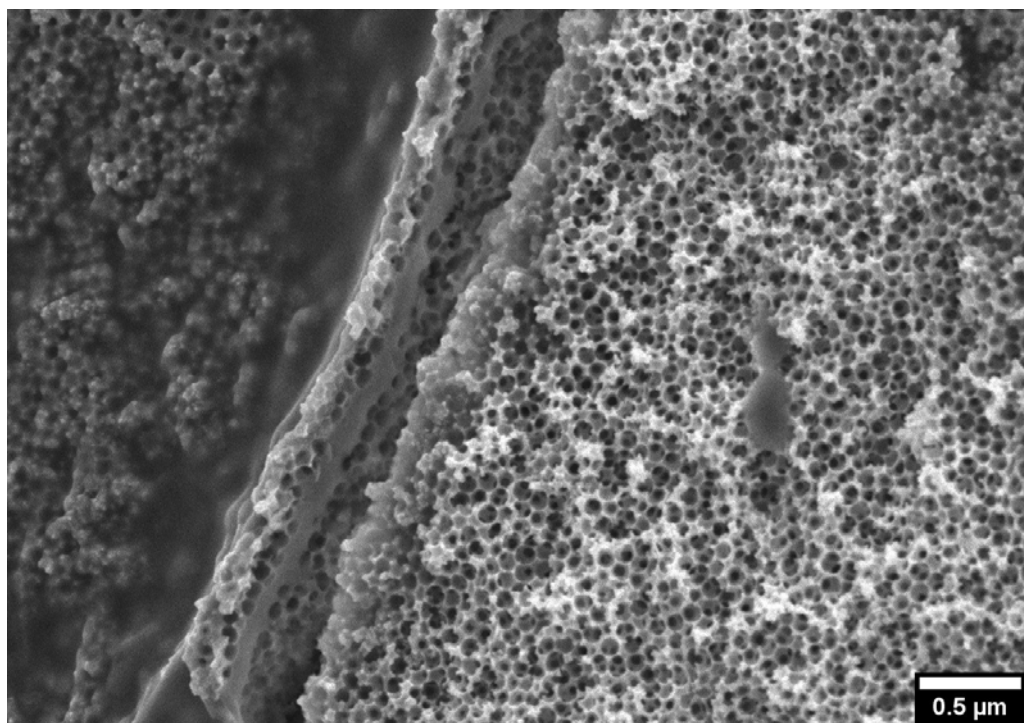

Fig. 4. A local crack on surface of an inverted silica opal caused by deformation during drying
of an organic film. SU3500 microscope, 5 kV, secondary electrons

Рис. 4. Локальная трещина на поверхности инвертированного опала из оксида кремния, обусловленная
деформированием при высыхании плёнки органического происхождения.
Микроскоп SU3500, 5 кВ, вторичные электроны
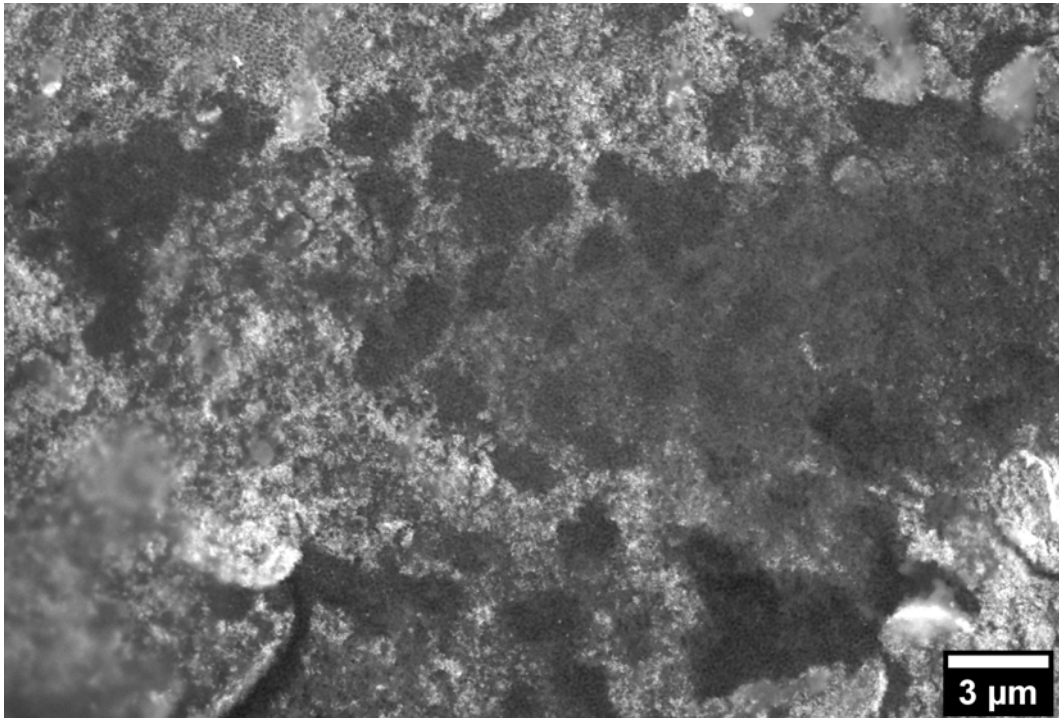
Fig. 5. Traces of human red blood cells on surface of inverted silica opal.
TM4000 Plus microscope, 20 kV, back-scattered electrons

Рис. 5. Следы эритроцитов человека на поверхности инвертированного опала из оксида кремния.
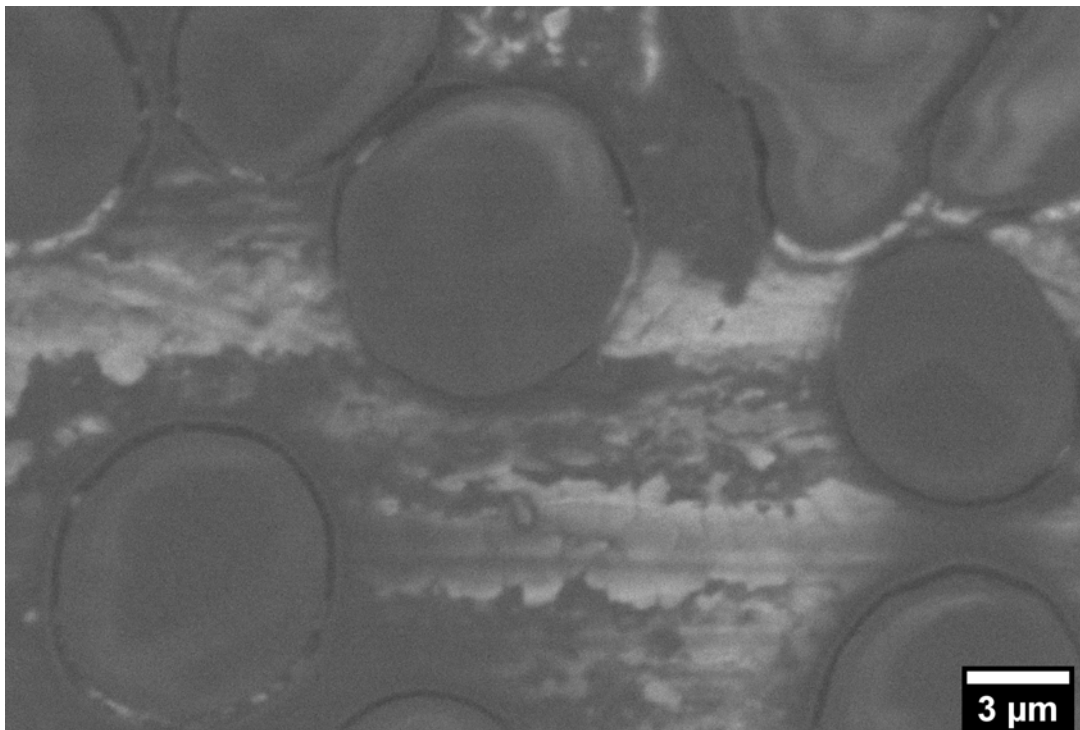Микроскоп TM4000 Plus, 20 кВ, обратно-отражённые электроны

Fig. 6. SEM image of red blood cells on surface of aluminum foil.
TM4000 Plus microscope, 5 kV, back-reflected electrons

Рис. 6. Электронная микрофотография эритроцитов на поверхности алюминиевой фольги.
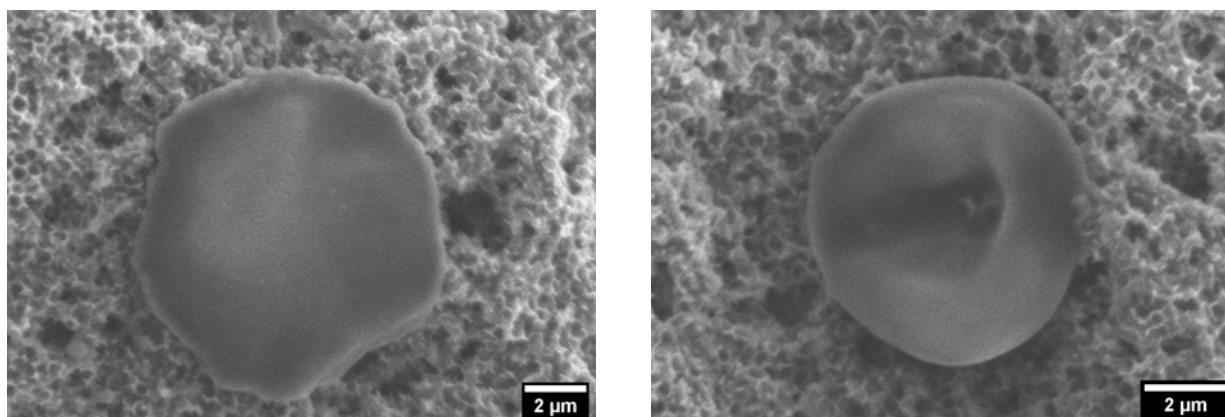Микроскоп TM4000 Plus, 5 кВ, обратно-отражённые электроны

Fig. 7. Red blood cells after treatment with an ionic liquid on surface of an inverted silica opal.
On the left is an erythrocyte that resembles a stellate (acanthocyte) in shape, on the right – it resembles
a target-shaped (platycyte). SU3500 microscope, 5 kV, secondary electrons

Рис. 7. Эритроциты после обработки ионной жидкостью на поверхности инвертированного опала
из оксида кремния. Слева – эритроцит, напоминающий по форме звёздчатый (акантоцит), справа – имеющий сходство
с мишеневидным (платицитом). Микроскоп SU3500, 5 кВ, вторичные электроны

Under the influence of the current, the ionic liquid can both boil and decompose. Therefore, there is an instrumental limitation on the maximum possible magnification that does not cause destruction of the object. In connection with the above, optimization of the SEM observation parameters (currents, voltages, vacuum levels) and obtaining conductive coatings is the goal of further research.

Conclusion. During the study of biological objects using scanning electron microscopy, the morphological features and elemental composition of the inverse opal structure of silica, lactic acid bacteria, as well as human red blood cells were studied. A technique has been developed for the preparation of biological samples using an ionic liquid in a complex (in combination as a whole) with an absorbent macroporous material, which makes it possible to preserve the original shape and structure of biological structures unchanged.

The possibility of express sample preparation for the subsequent express study of biological objects in a liquid has been experimentally shown. The principal possibility of multiple use of macroporous structures based on inverse opal from silica for the study of biological samples has been demonstrated empirically. The exceptional fragility of inverse opal has been demonstrated, which makes it impossible to use it as a biological filter for the separation of liquid biological media.

References

1. Scherr J. et al. Smart Molecular Nanosheets for Advanced Preparation of Biological Samples in Electron Cryo-Microscopy. *ACS Nano. NLM (Medline).* 2020. Vol. 14, № 8. P. 9972–9978.

2. Golinejad S., Mirjalili M. H. Fast and cost-effective preparation of plant cells for scanning electron microscopy (SEM) analysis. *Anal. Biochem. Academic Press Inc.* 2020. Vol. 609. P. 113920.

3. Souza J. B. et al. Pair Distribution Function from Electron Diffraction in Cryogenic Electron Microscopy: Revealing Glassy Water Structure. *J. Phys. Chem. Lett. American Chemical Society.* 2020. Vol. 11, № 4. P. 1564–1569.

4. Mironov A. A., Komissarchik Ya. Yu., Mironov V. A. *Metody elektronnoy mikroskopii v biologii i meditsine* [Electron microscopy methods in biology and medicine]. Saint-Petersburg: Russian Academy of Sciences, 1994. Samizdat. 400 p.

5. Zhuravlev O. E., Ivanova A. I., Grechishkin R. M. Preparation of samples for SEM studies using an ionic liquid. *J. Surf. Investig.* 2015, Vol. 9, No. 5, P. 904–907.

6. Khatanova N. A., Brovkina E. A. *Prosvechivayushchaya elektronnaya mikroskopiya tverdykh tel i biologicheskikh ob"ektov* [Transmission electron microscopy of solids and biological objects]. Moscow, faculty of physics, Moscow state University Publ., 2005, 190 p.

7. Sakaguchi G. Clostridium botulinum toxins. *Pharmacol. Ther. Pergamon.* 1982, Vol. 19, No. 2, P. 165–194.

8. Bechhold H. Kolloidstudien mit der Filtrationsmethode. *Zeitschrift für Elektrotechnik und Elektrochemie.* Wiley-Blackwell, 1907, Vol. 13, No. 32, P. 527–533.

9. Gerhardt P., George R., Murray E. Manual of methods for general bacteriology. Ed.-in-chief Philipp Gerhardt; ed. R. G. E. Murray et al. Ghent University Library. Washington, American society for microbiology, 1981. 524 p.

10. Tribe M. A. et al. Basic Biology Course Unit 1: Volume 2, Electron Microscopy and Cell Structure: Tribe, Michael A., Eraut, Michael R., Snook, Roger K., Tallan, Irwin: 9780521209076: Amazon.com: Books. Cambridge: Cambridge University Press, 1975, 117 p.

11. Waterhouse G. I. N., Waterland M. R. Opal and inverse opal photonic crystals: Fabrication and characterization. *Polyhedron*. 2007, Vol. 26, No. 2, P. 356–368.

12. Xin L., Liu X. Black TiO$_2$ inverse opals for visible-light photocatalysis. *RSC Adv. Royal Society of Chemistry*. 2015, Vol. 5, No. 88, P. 71547–71550.

13. Zhang Y. S., Zhu C., Xia Y. Inverse Opal Scaffolds and Their Biomedical Applications. *Adv. Mater.* 2017, Vol. 29, No. 33, P. 1701115–1701140.

14. Wang G. et al. Fabrication of Elastic Macroporous Polymers with Enhanced Oil Absorbability and Antiwaxing Performance. *Langmuir. NLM (Medline)*. 2020, Vol. 36, No. 36, P. 10794–10802.

15. Cuadrado-Collados C. et al. Well-defined meso/macroporous materials as a host structure for methane hydrate formation: Organic versus carbon xerogels. *Chem. Eng. J.* Elsevier B.V., 2020, Vol. 402, P. 126276.

16. García Schejtman S. D. et al. Redefining the chemistry of super-macroporous materials: When dendritic molecules meet polymer cryogels. *Polym. Chem. Royal Society of Chemistry*. 2020, Vol. 11, No. 27, P. 4507–4519.

17. Son Y. et al. Calendering-Compatible Macroporous Architecture for Silicon-Graphite Composite toward High-Energy Lithium-Ion Batteries. *Adv. Mater. Wiley-VCH Verlag*. 2020, Vol. 32, No. 37, P. 2003286.

18. Nemtsev I. V. et al. Angle-resolved reflection spectroscopy of high-quality PMMA opal crystal. *Photonics Nanostructures – Fundam. Appl.* 2018, Vol. 28, P. 37–44.

19. Nemtsev I. V. et al. Morphology stability of polymethylmethacrylate nanospheres formed in water – acetone dispersion medium. *Appl. Phys. A. Springer Berlin Heidelberg*. 2019, Vol. 125, P. 738–750.

20. Muramoto N. et al. Preparation of periodic mesoporous organosilica with large mesopores using silica colloidal crystals as templates. *Nanoscale. Royal Society of Chemistry (RSC)*. 2020.

21. Wellia D. V. et al. Mesoporous Materials for Degradation of Textile Dyes. Springer, Cham, 2020, P. 255–288.

22. Li C. et al. Self-assembly of block copolymers towards mesoporous materials for energy storage and conversion systems. *Chem. Soc. Rev. NLM (Medline)*. 2020, Vol. 49, No. 14, P. 4681–4736.

23. Shabanova O. V., Shabanov A. V., Nemtsev I. V. Research of conditions of synthesis of nanoscale monodisperse spherical particles of poly-methylmethacrylate. *Sib. J. Sci. Technol.* 2011, Vol. 4, No. 37, P. 201–205.

24. Nemtsev I. V., Shabanova O. V., Shabanov A. V. Electron microscopy investigation of polymethylmethacrylate spherical particles & artificial opals based on it. *Sib. J. Sci. Technol.* 2012, Vol. 1, No. 41, P. 126–129.

25. Stober W., Fink A., Ernst Bohn D. Controlled Growth of Monodisperse Silica Spheres in the Micron Size Range 1. *J. Colloid Interface Sci.* 1968, Vol. 26, P. 62–69.

Библиографические ссылки

1. Scherr J. et al. Smart Molecular Nanosheets for Advanced Preparation of Biological Samples in Electron Cryo-Microscopy // ACS Nano. NLM (Medline). 2020. Vol. 14, No. 8. P. 9972–9978.

2. Golinejad S., Mirjalili M. H. Fast and cost-effective preparation of plant cells for scanning electron microscopy (SEM) analysis // Anal. Biochem. Academic Press Inc. 2020. Vol. 609. P. 113920.

3. Pair Distribution Function from Electron Diffraction in Cryogenic Electron Microscopy: Revealing Glassy Water Structure / J. B. Souza et al. // J. Phys. Chem. Lett. American Chemical Society. 2020. Vol. 11, No. 4. P. 1564–1569.

4. Миронов А. А., Комиссарчик Я. Ю., Миронов В. А. Методы электронной микроскопии в биологии и медицине. Самиздат. СПб. : Российская академия наук, 1994. 400 p.

5. Журавлев О. Е., Иванова А. И., Гречишкин Р. М. Препарирование объектов для РЭМ-исследований с помощью ионной жидкости // Поверхность. Рентгеновские, синхротронные и нейтронные исследования. Akademizdatcenter Nauka. 2015. Vol. 9. P. 45–48.

6. Хатанова Н. А., Бровкина Е. А. Просвечивающая электронная микроскопия твердых тел и биологических объектов. М. : Физический факультет МГУ, 2005. 190 p.

7. Sakaguchi G. Clostridium botulinum toxins // Pharmacol. Ther. Pergamon. 1982. Vol. 19, No. 2. P. 165–194.

8. Bechhold H. Kolloidstudien mit der Filtrationsmethode // Zeitschrift für Elektrotechnik und Elektrochemie. Wiley-Blackwell. 1907. Vol. 13, No. 32. P. 527–533.

9. Gerhardt P., George R., Murray E. Manual of methods for general bacteriology / ed.-in-chief Philipp Gerhardt; ed. R. G. E. Murray et. al. Ghent University Library. Washington : American society for microbiology, 1981. 524 p.

10. Basic Biology Course Unit 1: Vol. 2, Electron Microscopy and Cell Structure / Tribe Michael A., Eraut Michael R., Snook Roger K., Tallan Irwin: 9780521209076: Amazon.com: Books. Cambridge: Cambridge University Press, 1975. 117 p.

11. Waterhouse G. I. N., Waterland M.R. Opal and inverse opal photonic crystals: Fabrication and characterization // Polyhedron. 2007. Vol. 26, No. 2. P. 356–368.

12. Xin L., Liu X. Black TiO$_2$ inverse opals for visible-light photocatalysis // RSC Adv. Royal Society of Chemistry. 2015. Vol. 5, No. 88. P. 71547–71550.

13. Zhang Y. S., Zhu C., Xia Y. Inverse Opal Scaffolds and Their Biomedical Applications // Adv. Mater. 2017. Vol. 29, No. 33. P. 1701115–1701140.

14. Fabrication of Elastic Macroporous Polymers with Enhanced Oil Absorbability and Antiwaxing Performance / G. Wang et al. // Langmuir. NLM (Medline). 2020. Vol. 36, No. 36. P. 10794–10802.

15. Well-defined meso/macroporous materials as a host structure for methane hydrate formation: Organic versus carbon xerogels / C. Cuadrado-Collados et al. // Chem. Eng. J. Elsevier B. V. 2020. Vol. 402. P. 126276.

16. Redefining the chemistry of super-macroporous materials: When dendritic molecules meet polymer cryogels / S. D. García Schejtman et al. // Polym. Chem.

Royal Society of Chemistry. 2020. Vol. 11, No. 27. P. 4507–4519.

17. Calendering Compatible Macroporous Architecture for Silicon-Graphite Composite toward High-Energy Lithium-Ion Batteries / Y. Son et al. // Adv. Mater. Wiley-VCH Verlag. 2020. Vol. 32, No. 37. P. 2003286.

18. Angle-resolved reflection spectroscopy of high-quality PMMA opal crystal / I. V. Nemtsev et al. // Photonics Nanostructures – Fundam. Appl. 2018. Vol. 28. P. 37–44.

19. Morphology stability of polymethylmethacrylate nanospheres formed in water – acetone dispersion medium / I. V. Nemtsev et al. // Appl. Phys. A. Springer Berlin Heidelberg. 2019. Vol. 125. P. 738–750.

20. Preparation of periodic mesoporous organosilica with large mesopores using silica colloidal crystals as templates / N. Muramoto et al. // Nanoscale. Royal Society of Chemistry (RSC). 2020.

21. Mesoporous Materials for Degradation of Textile Dyes / D. V. Wellia et al. Springer, Cham, 2020. P. 255–288.

22. Self-assembly of block copolymers towards mesoporous materials for energy storage and conversion systems / C. Li et al. // Chem. Soc. Rev. NLM (Medline). 2020. Vol. 49, No. 14. P. 4681–4736.

23. Шабанова О. В., Шабанов А. В., Немцев И. В. Исследование условий получения наноразмерных монодисперсных сферических частиц полиметилметакрилата // Сибирский журнал науки и технологий. 2011. Т. 4, № 37. P. 201–205.

24. Немцев И. В., Шабанова О. В., Шабанов А. В. Исследование сферических частиц полиметилметакрилата и искусственных опалов на их основе методом растровой электронной микроскопии // Сибирский журнал науки и технологий. 2012. Т. 1, № 41. P. 126–129.

25. Stober W., Fink A., Ernst Bohn D. Controlled Growth of Monodisperse Silica Spheres in the Micron Size Range 1 // J. Colloid Interface Sci. 1968. Vol. 26. P. 62–69.

Shabanova Olga Vilgelmovna – junior researcher; Special Designing and Technological Bureau "Nauka" "Krasnoyarsk Science Center of the Siberian Branch of the Russian Academy of Sciences". E-mail: ollach@ya.ru.

Nemtsev Ivan Vasilyevich – researcher; Federal Research Center "Krasnoyarsk Science Center" of the Siberian Branch of the Russian Academy of Sciences. E-mail: ivan_nemtsev@mail.ru.

Shabanov Alexander Vasilyevich – PhD, senior researcher; место работы. L. V. Kirensky Institute of Physics of the Siberian Branch of the Russian Academy of Sciences. E-mail: alexch_syb@mail.ru.

Шабанова Ольга Вильгельмовна – младший научный сотрудник; Специальное конструкторско-технологическое бюро «Наука». E-mail: ollach@ya.ru.

Немцев Иван Васильевич – научный сотрудник; Федеральный исследовательский центр «Красноярский научный центр Сибирского отделения Российской академии наук». E-mail: ivan_nemtsev@mail.ru.

Шабанов Александр Васильевич – кандидат физико-математических наук, старший научный сотрудник; Институт физики им. Л. В. Киренского Сибирского отделения Российской академии наук. E-mail: alexch_syb@mail.ru.

PRODUCTION OF FINLY DESPERSED POWDER FROM GRAPHITE BY ELECTROLYSIS

I. Y. Shestakov[1*], A. V. Kupryashov[1], V. D. Utenkov[1], I. A. Remizov[2]

[1] Reshetnev Siberian State University of Science and Technology
31, Krasnoyarskii rabochii prospekt, Krasnoyarsk, 660037, Russian Federation
[2]Siberian Federal University
79, Svobodniy Av., Krasnoyarsk, 660041, Russian Federation
*E-mail: yakovlevish@mail.ru

Multifunctional coating is a multi-layer structure applied to the surface of an aircraft to protect it from external influences. The main tasks of the multifunctional coating are: restoration of properties, overall dimensions, mass of the surface of the product, which were violated under operating conditions; changing the initial physical, mechanical and chemical properties of the product surface to ensure the specified operating conditions. Today multifunctional coatings based on micro glass spheres with applied tungsten are widely used in aerospace engineering. However, this coating has a number of disadvantages: the coating layers heterogeneity; the composition contains a harmful and dangerous component – a fluorone dye. In this article it is suggested to replace the main component of a multifunctional coating with finely dispersed graphite powder obtained by electrolysis. For this purpose, the equipment based on the principle of a diaphragm electrolyzer was constructed. The main elements of the device are a stainless steel cathode and a graphite anode immersed in an aqueous solution. As a result of anodic processes, a finely dispersed graphite powder was obtained. The average particle size of the resulting graphite particles is 4 microns. This finely dispersed graphite powder can be used as the main component of a multifunctional coating in aircraft, since it has an even homogeneous structure, as well as higher values of the main mechanical properties of a multifunctional coating.

Keywords: multifunctional coating, fine graphite powder, electrochemical action, molecular oxygen, diaphragm electrolyzer.

ПОЛУЧЕНИЕ МЕЛКОДИСПЕРСНОГО ПОРОШКА ИЗ ГРАФИТА ЭЛЕКТРОЛИЗОМ

И. Я. Шестаков[1*], А. В. Купряшов[1], В. Д. Утенков[1], И. А. Ремизов[2]

[1]Сибирский государственный университет науки и технологий имени академика М. Ф. Решетнева
Российская Федерация, 660037, г. Красноярск, просп. им. газ. «Красноярский рабочий», 31
[2]Сибирский федеральный университет,
Российская Федерация, 660041, г. Красноярск, просп. Свободный, 79
*E-mail: yakovlevish@mail.ru

Многофункциональное покрытие – это многослойная структура, нанесенная на поверхность летательного аппарата для защиты от внешних воздействий. Основными задачами мультифункционального покрытия являются: восстановление свойств, габаритных размеров, массы поверхности изделия, которые были нарушены в условиях эксплуатации; изменение исходных физико-механических и химических свойств поверхности изделия, для обеспечения заданных условий эксплуатации. Сегодня в аэрокосмической технике широко применяются многофункциональные покрытия на основе микростеклосфер с нанесённым вольфрамом. Такое покрытие обладает комплексом недостатков: неоднородность слоёв покрытия; в составе имеется вредный и опасный компонент – флуороновый краситель. Предлагается использовать в качестве основного компонента многофункционального покрытия мелкодисперсный графитовый порошок, полученный электролизом. Для этого создано устройство, с разделением анодного и катодного пространства путем использования диафрагмы. Основными элементами установки являются катод из нержавеющей стали и графитовый анод, погружённый в водный раствор. В результате анодных процессов получен мелкодисперсный порошок из графита. Средний размер полученных частиц графита составляет 4 мкм. Данный мелкодисперсный графитовый порошок мож-

но использовать в качестве основного компонента многофункционального покрытия в летательных аппаратах, так как он обладает ровной однородной структурой, а также более высокими значениями основных механических свойств многофункционального покрытия.

Ключевые слова: многофункциональное покрытие, мелкодисперсный графитовый порошок, электрохимическое воздействие, диафрагменный электролизёр.

Introduction. The main purpose of a multifunctional (functional gradient) coating in aerospace engineering is thermal protection, protection against ionizing, electromagnetic and radio radiation and laser beam reflection. The secondary purpose of a multifunctional coating in rocketry is to increase strength and rigidity of product external parts, as well as to protect them from corrosion and erosion [1].

Multifunctional coating structure and composition description. Multifunctional coating structure is rather complicated. It consists of four main components such as: a catalyst, a fluorone dye, a low-molecular polymer, and dispersed filler [2–4].

The main component of the multi-functional coating is a dispersed filler: micro-glass spheres modified with tungsten, that is, hollow particles of micro-glass spheres, on the surface of which a tungsten coating is applied. Micro glass spherical particles have various shapes: sphere, cube, parallelepiped, flake, cylinder, hexagon, various fibers, etc. [5–7]. Fig. 1 shows a schematic cross-section of the multi-functional coating layer, where you can see various shapes of microspheres and the chaotic arrangement of dispersed filler particles in the layer.

This filler is compatible with a low-molecular polymer. It is dispersed (emulsified) in the polymer to form a homogeneous composite mass [8–9]. Fig. 2 shows the outer appearance form of the dispersed filler modified with tungsten.

Multifunctional coating which consists of the described above components is actively used in aerospace engineering today [10], however there are many disadvantages: a dangerous and harmful component Rhodamine 6G [11], components high price, high labor cost for obtaining a composite mixture, heterogeneity of the coating layers (due to the variety of forms of dispersed filler, see fig. 1), which involves additional machining operations to obtain a layer of multifunctional coating of a given thickness.

Scientific research main idea. These disadvantages can be eliminated by using dispersed carbon filler [12] made on the basis of graphite with a hexagonal crystal structure.

Graphite is an allotropic form of carbon. It has a hexagonal crystal lattice. In a single crystal carbon atoms are arranged in parallel layers (basic planes). In each layer, the atoms are bound together by a strong home polar bond, due to this structure; graphite has anisotropy of physical and electrical properties [13].

Graphite powder was obtained by electrochemical method of – the anodic oxidation of high-strength fine-dispersed dense graphite of the MPG-6 brand. It is a widely used form of industrial graphite [14]. It is a dispersed modification of hexagonal polymorphic carbon. Unlike coarse-grained graphite, it is characterized by a powdery fine-dispersed structure. Basic physical and chemical characteristics are presented in table.

It can be seen from table that in comparison with the micro-glass sphere with deposited tungsten ($\approx$0.62 g/cm^3) the density of MPG-6 graphite is much higher. It means that the main mechanical properties (breaking stress at separation, ultimate strength, hardness) of the multifunctional graphite-based coating will be of higher values in comparison with the coatings used today in aerospace engineering.
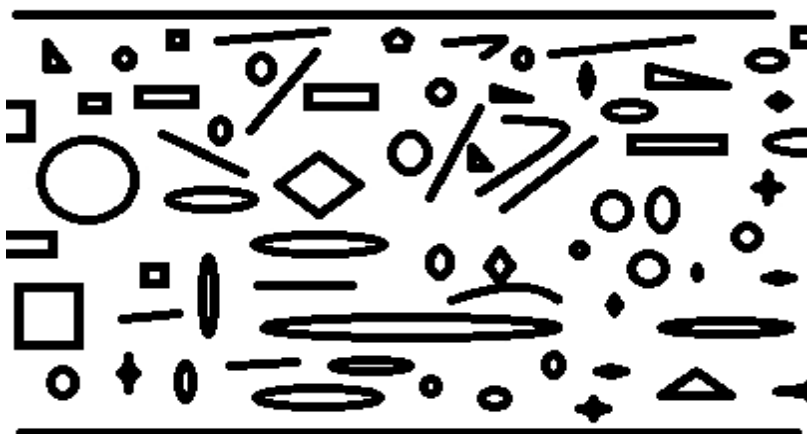

Fig. 1. Schematic section of one layer of a multifunctional coating
with micro glass spheres in the composition

Рис. 1. Схематичный срез слоя многофункционального покрытия
с микростеклосферами

Fig. 2. The appearance of the dispersed filler modified with tungsten

Рис. 2. Внешний вид дисперсного наполнителя,
модифицированного вольфрамом

Basic physical and chemical characteristics and properties of grade MPG-6 graphite

№ п/п	Параметр	Значение
1	Mass fraction of ash, not more than %	0.02
2	Density, g / cm^3	1.65
3	Thermal conductivity coefficient W / m×K	95
4	Tensile strength at compression, MPa, not less	73
5	Tensile strength at bending, MPa, not less	34.3
6	Hazard class according to GOST 12.1.007	4 (low risk)

Scientific research description. For the graphite powder production a special device was created, fig. 3 shows its schematic diagram The unit consists of a cylindrical body (*1*), inside which the electrodes: cathode (*2*), anode (*3*) are placed. Between the electrodes there is a cylindrical perforated container (*4*), with a canvas cloth inside (*5*), which acts as a diaphragm. A graphite electrode of the MPG-6 brand is used as the anode. Current leads (*7*) and the anode (*3*) are installed on the cover. The cold tap water which has been kept for 8–10 hours in an open glass container at room temperature is used a working medium.

A perforated container with a diaphragm is coaxially installed in a container with a cathode. After that some water is poured into the near-cathode and near-anode space up to the same level. Then a cover with the anode is installed and voltage is applied to the electrodes. The process of electric current transfer starts by ions moving to the electrodes in the electrolyte and electrons in the external circuit. Positively charged ions migrate to the cathode, and negatively charged ions migrate to the anode under the influence of the electric field. The electron transition takes place on the electrodes. The cathode releases electrons into the solution and reduction processes occur in the near-electrode space. The processes of elec-

tron transfer from reacting particles to the electrode – oxidation takes place in the near-anode space [15–18].

Anodic oxidation and cathodic reduction form the basis of the electrolysis process that occurs in the device. In the first six minutes when the electric current is passing through the anode, the C^{4+} ion is formed from carbon atoms [19; 20]:

$$C^0 - 4e \rightarrow C^{4+} \tag{1}$$

A hydrate shell is formed around C^{4+} ions. The hydrated ions formed stay in the water:

$$C^{4+} + H_2O \rightarrow C(H_2O)_n \tag{2}$$
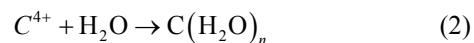
Immediately after the unit is switched off, the cover with the anode is removed and the end of the anode is placed on the film. The obtained water solution is dried; as a result, graphite particles (a fine powder) remain on the film.

Scientific research results. The graphite powder was examined with a digital microscope. The photo of the graphite powder obtained using a digital microscope is shown in fig. 4.

As we see in fig. 4, the particles of the obtained powder reach the desired size of 0.004 mm.
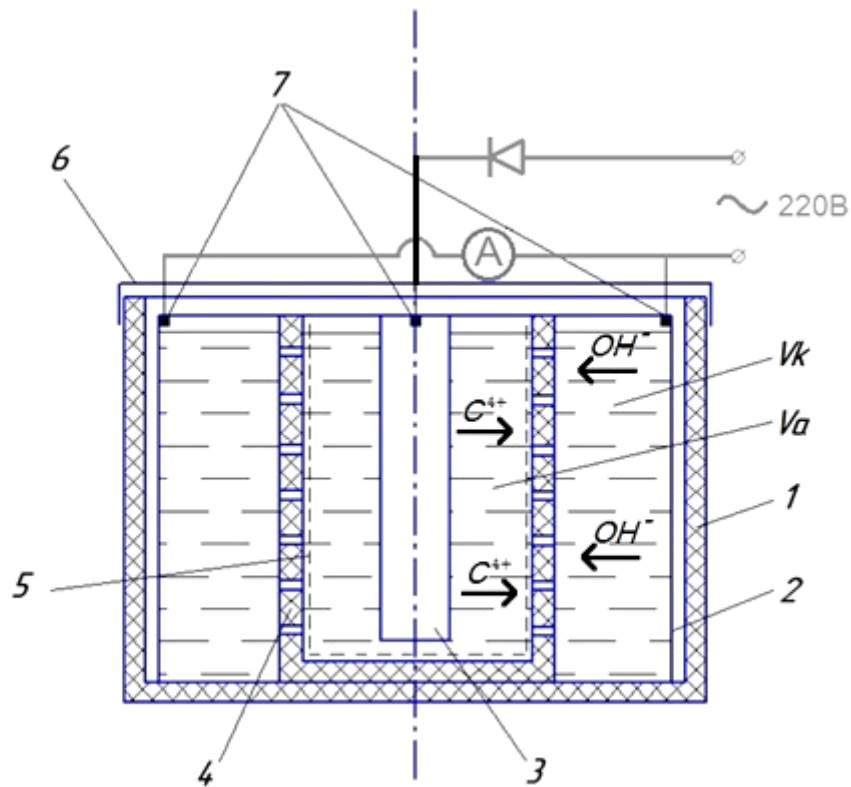
Fig. 3. Schematic diagram of the device:
1 – fluoroplastic device body; *2* – stainless steel cathode; *3* – graphite anode;
4 – cylindrical perforated container; *5* – tarpaulin-based fabric; *6* – plastic cover;
7 – current leads; V_k – cathode space volume; V_a – anode space volume

Рис. 3. Принципиальная схема устройства:
1 – корпус из фторопласта; *2* – катод из нержавеющей стали; *3* – анод из графита;
4 – цилиндрическая перфорированная ёмкость; *5* – брезентовая ткань; *6* – крышка;
7 – токоподводы; V_k – объём прикатодного пространства; V_a – объём прианодного
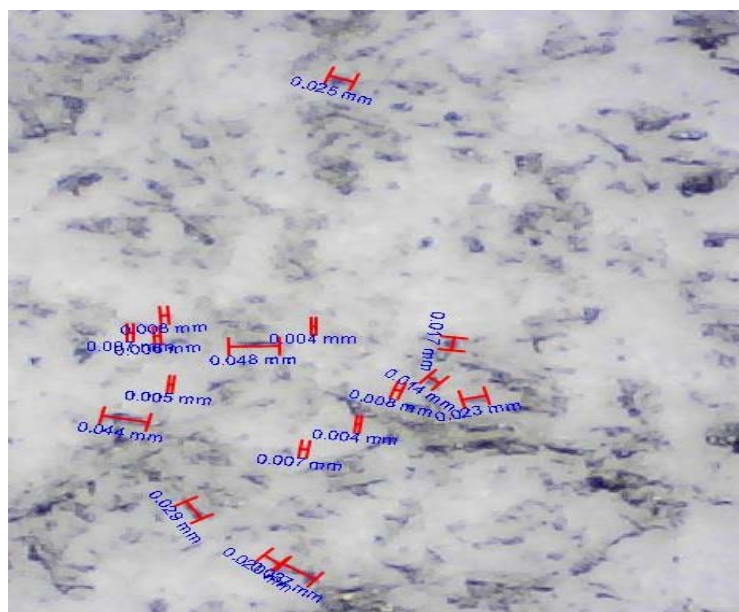пространства

Fig. 4. A photograph of the graphite powder obtained during the experiment

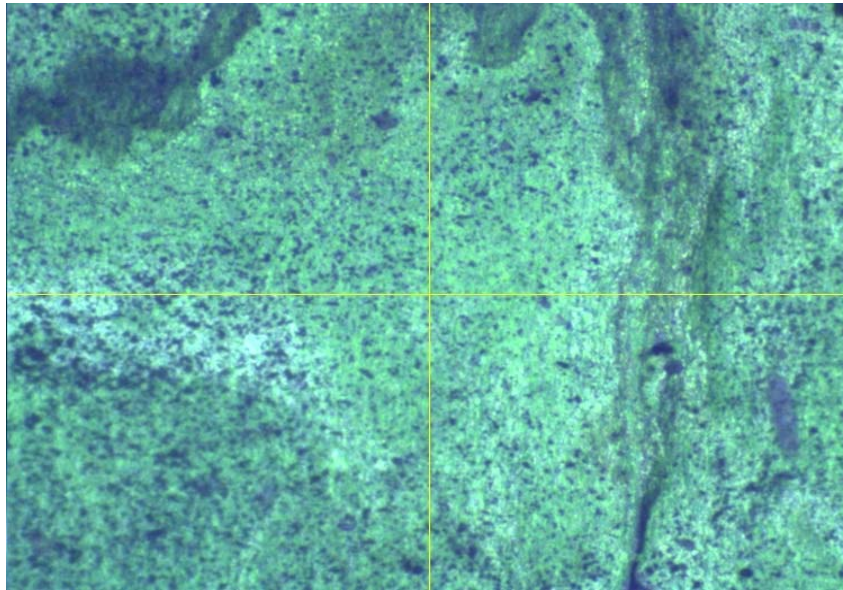Рис. 4. Графитовый порошок, полученный в ходе эксперимента

Fig. 5. A graphite powder image, magnified up to 0.001 mm

Рис. 5. Снимок графитового порошка, с увеличением до 0,001 мм

Fig. 5 shows the image obtained with a video measuring device of the TESA-VISIO 300GL laser principle with a magnification of up to 0.001 mm.

In fig. 5 the granular microstructure of the powder can be seen, which means that the particles have a suitable hexagonal shape. Due to such form of the graphite powder particles the multifunctional coating will have a smooth uniform structure, since the particles are tightly bound to each other.

The smooth, uniform surface structure of the multifunctional coating layers eliminates the necessity of using the extraction-photometric quality determination method with the use of the xanthene (fluorone) dye – Rhodamine 6G, a toxic and dangerous component.

Conclusion. In fig. 5, there is a granular structure of the powder, which means that the particles have an almost regular octagonal shape. The multifunctional coating will have a smooth uniform structure, due to the graphite powder particles form as the particles are tightly bound to each other.

The smooth, uniform surface structure of the multifunctional coating layers eliminates the necessity of using the extraction-photometric quality determination method with the use of the xanthene (fluorone) dye – Rhodamine 6G, a toxic and dangerous component.

Thus, the dispersed carbon filler (graphite powder obtained by electrolysis from MPG-6 graphite with a particle size of approximately 0.004 mm) provides the following advantages:

1. Elimination of the 2nd hazard class toxic substance – Rhodamine 6G from the multifunctional coating composition.

2. Higher values of the main multifunctional coating mechanical properties, due to the high particle density of the main component (1.65 g/cm^3 for graphite powder, in comparison with micro-glass spheres modified with tungsten ≈0.62 g/cm^3).

3. The main component lower cost of (≈9500 rubles/kg for graphite powder, compared to 103000 rubles/kg for micro glass spheres modified with tungsten).

4. Labor cost reduction in the production the multifunctional coating by eliminating mechanical processing (saving up to 10 % of the total labor intensity of the multifunctional coating production), due to the smooth homogeneous structure of the main component.

References

1. Kupryashov A. V., Shestakov I. Ya. [Multifunctional coating in modern rocket and space technology]. *Materialy XIX Mezhdunar. nauch. konf.* [Volume of the XIX-th International Scientific Conference of bachelor students, master students, post-graduate students and young scientists]. Krasnoyarsk, SibSU, 2020, P. 310–311.

2. Kernozhitskiy V. A., Kolychev A. V., Okhochinskiy D. M. *Termoemissionnyi sposob teplovoi zashchity chastei letatel'nykh apparatov pri ikh aerodinamicheskom nagreve* [Thermal emission method of thermal protection of aircraft parts during their aerodynamic heating]. Patent RF, No. 2404087, 2010.

3. Orlov V. G., Savvateeva O. A., Shumov A. E. *Teplozashchitnoe pokrytie* [Heat protective coating]. Patent RF, No. 2631302, 2017.

4. Zhukov A. V., Mushenko V. D., Baratova T. N. *Kataliticheskaya smes' dlya otverzhdeniya siloksanovykh kauchukov* [Catalyst mixture for curing silicone rubbers]. Patent RF, No. 2424260, 2011.

5. Kolosova A. S., Sokol'skaya M. K., Vitkalova I. A. [Fillers for modification of modern polymer composite materials]. *Fundamental'nye issledovaniya*, 2017, No. 10, P. 459–465 (In Russ.).

6. Babaevskiy P. G. *Napolniteli dlya polimernykh kompozitsionnykh materialov* [Fillers for polymer composite materials]. Moscow, Khimiya Publ., 1981, 736 p.

7. Bondaletova L. I., Bondaletov V. G. *Polimernye kompozitsionnye materialy (chast' 1)* [Polymer composite materials (part 1)]. Tomsk, Tomsk State Polytechnic University Publ., 2013, 118 p.

8. Zaponov A. E. [Theoretical and experimental study of the processes of chemical decomposition of a modified low-molecular-weight stirosil polymer in a continuous field of laser radiation]. *Humanitarian Bulletin of the Military Academy of Strategic Rocket Troops.* 2018, No. 11 (43), P. 295–302 (In Russ.).

9. Ustinov A. S. [Method of applying fire-retardant composite material "liquid glass-graphite microparticles" on the surface of the fence]. *Scientific and Technical Journal of Information Technologies, Mechanics and Optics.* 2018, No. 6 (18), P. 1001–1007 (In Russ.).

10. Shaidurova G. I., Vasil'ev I. L., Karmanova L. I. [Development and confirmation of the working capacity of the repair composition for the external heat-protective coating]. *PNRPU Aerospace Engineering Bulletin.* 2014, No. 36, P. 49–63 (In Russ.).

11. Mittsel' Yu. A., Levshchin L. V., Golovina A. P. [Spectroscopic study of the state of rhodamine 6G molecules in non-polar solvents]. *Vestnik Moskovskogo Universiteta.* 1968, No. 1, P. 74–79 (In Russ.).

12. Leonov D. V. *Razrabotka poliamida-6 funktsional'nogo naznacheniya, modifitsirovannogo okislennym grafitom. Kand. Diss.* [Development of polyamide-6 functional purpose modified with oxidized graphite. Cand. Diss.]. Saratov, 2018. 163 p.

13. Koritskiy Yu. V., Pasynkova V. V., Tareeva B. M. *Spravochnik po elektrotekhnicheskim materialam* [Electrical Materials Handbook]. Leningrad, Energoatomizdat Publ., 1988, Vol. 3, 728 p. (In Russ.).

14. Pitukhin E. A., Ustinov A. S. [Investigation of the fire resistance limit of a composite material liquid glass-graphite micro particle]. *Scientific and Technical Journal of Information Technologies, Mechanics and Optics.* 2016, Vol. 16, No. 2, P. 277–283 (In Russ.).

15. Tarasevich M. R. *Elektrokhimiya uglerodnykh materialov* [Electrochemistry of carbon materials]. Moscow, Nauka Publ., 1984, 253 p.

16. Stankovic V. Electrochemical Engineering – its appearance, evolution and present status. Approaching an anniversary. *Journal of Electrochemical Science and Engineering.* 2012, No. 2, P. 1–14.

17. Chen G. Electrochemical technologies in wastewater treatment. *Separation and Purification Technology.* 2004, No. 38, P. 11–41.

18. Wright H. Electrochemical Engineering: Emerging Technologies and Applications. USA, Willford Press, 2016, 254 p.

19. Stolten D., Emonts B. Fuel Cell Science and Engineering: Materials, Processes, Systems and Technology. New York, John Wiley & Sons, 2012, 1268 p.

20. Yakimenko L. M. *Elektrodnye materialy v prikladnoi elektrokhimii* [Electrode materials in applied electrochemistry]. Moscow, Khimiya Publ., 1977, 264 p.

Библиографические ссылки

1. Kupryashov A. V., Shestakov I. Ya. Multifunctional coating in modern rocket and space technology // Молодежь. Общество. Современная наука, техника и инновации : материалы XIX Междунар. науч. конф. бакалавров, магистрантов, аспирантов и молодых ученых (20 мая 2020, г. Красноярск) ; под общ. ред. Ю. Ю. Логинова ; СибГУ им. М. Ф. Решетнева. Красноярск, 2020. С. 310–311.

2. Термоэмиссионный способ тепловой защиты частей летательных аппаратов при их аэродинамическом нагреве : пат. 2404087 C1 Рос. Федерация. №: 2009140802/11 / Керножицкий В. А., Колычев А. В., Охочинский Д. М. ; заявл. 03.11.2009 ; опубл. 20.11.2010, Бюл. № 32. 7 с.

3. Теплозащитное покрытие : пат. 2631302 C2 Рос. Федерация. №: 2015105402/15 / Орлов В. Г., Савватеева О. А., Шумов А. Е. и др.; заявл. 18.02.2015 ; опубл. 20.09.2017, Бюл. № 26. 6 с.

4. Каталитическая смесь для отверждения силоксановых каучуков : пат. 2424260 C2 Рос. Федерация. №: 2008120718/04 / Жуков А. В., Мушенко В. Д., Баратова Т. Н. ; заявл. 16.05.2008 ; опубл. 20.07.2011, Бюл. № 20. 6 с.

5. Наполнители для модификации современных полимерных композиционных материалов / А. С. Колосова, М. К. Сокольская, И. А. Виткалова и др. // Фундаментальные исследования. 2017. № 10. С. 459–465.

6. Наполнители для полимерных композиционных материалов: справ : пер. с англ. / под ред. П. Г. Бабаевского, М. : Химия, 1981. 736 с.

7. Бондалетова Л. И. Полимерные композиционные материалы. Ч. 1 / Л. И. Бондалетова, В. Г. Бондалетов. Томск : Изд-во Томского политехн. ун-та, 2013. 118 с.

8. Запонов А. Э. Теоретическое и экспериментальное исследование процессов химического разложения модифицированного низкомолекулярного полимера стиросил в непрерывном поле лазерного излучения // Вестник Военной академии РВСН им. Петра Великого. 2018. № 11 (43). С. 295–302.

9. Устинов А. С. Метод нанесения огнезащитного композитного материала «жидкое стекло–микрочастицы графита» на поверхности ограждения // Науч.-техн. вестник информационных технологий, механики и оптики. 2018. № 6 (18). С. 1001–1007.

10. Шайдурова Г. И., Васильев И. Л., Карманова Л. И. Разработка и подтверждение работоспособности ремонтного состава для наружного теплозащитного покрытия // Вестник ПНИПУ. Аэрокосмич. техн. 2014. № 36. С. 49–63.

11. Спектроскопическое изучение состояния молекул родамина 6Ж в неполярных растворителях / Ю. А. Митцель, Л. В. Лёвщин, А. П. Головина и др. // Вестник Московского ун-та. 1968. № 1. С. 74–79.

12. Леонов Д. В. Разработка полиамида-6 функционального назначения, модифицированного окисленным графитом : дис. … канд. техн, наук: 05.17.06. Саратов, 2018. 163 с.

13. Справочник по электротехническим материалам / под ред. Ю. В. Корицкого, В. В. Пасынкова, Б. М. Тареева. Т. 3 : 3-е изд., перераб. Л. : Энергоатомиздат. 1988. 728 с.

14. Питухин Е. А., Устинов А. С. Исследование предела огнестойкости композитного материала жид-

кое стекло–микрочастицы графита // Научно-технический вестник информационных технологий, механики и оптики. 2016. Т. 16, № 2. С. 277–283.

15. Тарасевич М. Р. Электрохимия углеродных материалов. М. : Наука, 1984. 253 с.

16. Stankovic V. Electrochemical Engineering – its appearance, evolution and present status. Approaching an anniversary // Journal of Electrochemical Science and Engineering. 2012. № 2. P. 1–14.

17. Chen G. Electrochemical technologies in wastewater treatment // Separation and Purification Technology. 2004. № 38. P. 11–41.

18. Wright H. Electrochemical Engineering: Emerging Technologies and Applications. Willford Press. 2016. 254 p.

19. Stolten D., Emonts B. Fuel Cell Science and Engineering: Materials, Processes, Systems and Technology // John Wiley & Sons. 2012. 1268 p.

20. Якименко Л. М. Электродные материалы в прикладной электрохимии. М. : Химия, 1977. 264 с.

Shestakov Ivan Yakovlevich – Dr. Sc., Associate Professor, Professor; Reshetnev Siberian State University of Science and Technology. E-mail: yakovlevish@mail.ru.

Kupryashov Andrey Viktorovich – graduate student; Reshetnev Siberian State University of Science and Technology. E-mail: KupryashovAndrey@yandex.ru.

Utenkov Viktor Dmitrievich – Cand. Sc., Associate Professor of the Department of Mechanical Engineering; Reshetnev Siberian State University of Science and Technology. Email: sibsau-tms@mail.ru.

Remizov Igor Anatolyevich – Cand. Sc., Associate Professor of the Department of Technical Mechanics; Siberian Federal University. Email: IRemizov@sfu-kras.ru.

Шестаков Иван Яковлевич – доктор технических наук, доцент, профессор кафедры электронной техники и телекоммуникаций; Сибирский государственный университет науки и технологий имени академика М. Ф. Решетнёва. E-mail: yakovlevish@mail.ru.

Купряшов Андрей Викторович – аспирант; Сибирский государственный университет науки и технологий имени академика М. Ф. Решетнёва. E-mail: KupryashovAndrey@yandex.ru.

Утенков Виктор Дмитриевич – кандидат технических наук, доцент кафедры технологии машиностроения; Сибирский государственный университет науки и технологий имени академика М. Ф. Решетнева. E-mail: sibsau-tms@mail.ru.

Ремизов Игорь Анатольевич – кандидат физико-математических наук, доцент кафедры технической механики; Сибирский федеральный университет. E-mail: IRemizov@sfu-kras.ru.